

**Exploiting Polymer Theory to Simulate the Rheology of Micellar Solutions and Polymer Glasses**

by

Weizhong Zou

A dissertation submitted in partial fulfillment  
of the requirements for the degree of  
Doctor of Philosophy  
(Chemical Engineering)  
in the University of Michigan  
2018

Doctoral Committee:

Professor Ronald G. Larson, Chair  
Professor Michael J. Solomon  
Professor Anish Tujeta  
Professor Robert M. Ziff

Weizhong Zou

[weizhong@umich.edu](mailto:weizhong@umich.edu)

ORCID iD: [0000-0002-8369-9229](https://orcid.org/0000-0002-8369-9229)

© Weizhong Zou 2018

## **Dedication**

In remembrance of his love, support, and guidance,  
I dedicate this dissertation to my grandfather,  
Zou, Qingyu (邹青云)

## **Acknowledgements**

This dissertation is the result of great collaboration with my many colleagues and friends at the University of Michigan, University of Cincinnati, and Procter and Gamble Company, through whom I have been educated and inspired. Specifically, I want to express my greatest thanks to the following individuals for their sustained help and support during my entire Ph. D studies: my advisor Prof. Ronald Larson, my former group member Dr. Xueming Tang, my collaborators at Procter and Gamble Company Dr. Mike Weaver and Dr. Peter Koenig. I am also grateful for useful discussions with Hanqiu Jiang, Dr. Karste Vogtt, and Prof. Gregory Beaucage at the University of Cincinnati, Prof. Suzanne Fielding at University of Durham, Prof. Mike Cates at University of Cambridge, Prof. Robert Hoy at University of South Florida, and Prof. Joerg Rottler at University of British Columbia. In addition, I am indebted to Chemical Engineering Department and Rackham Graduate School at University of Michigan, National Science Foundation (NSF), Extreme Science and Engineering Discovery Environment (XSEDE), and Procter and Gamble Company (P&G), without their funding (CBET-1500377, CBET-0853662, DMR-0906587, DMR-1403335), fellowship (2016 Rackham Predoctoral Fellowship), and resource, my work and this dissertation would certainly not exist.

## Table of Contents

Dedication .....	ii
Acknowledgements .....	iii
List of Tables .....	vi
List of Figures .....	viii
List of Appendices .....	xiv
Abstract .....	xv
Chapter 1: Introduction .....	1
Chapter 2: A Mesoscopic Simulation Method for Predicting the Rheology of Semi-dilute Wormlike Micellar Solutions.....	12
I. Introduction.....	12
II. Definitions.....	13
III. Theory .....	15
IV. Modeling .....	27
V. Simulation Testing .....	33
VI. Analysis and Discussion .....	33
VII. Conclusions and Final Comments.....	48
Chapter 3: Determination of Characteristic Lengths and Times for Wormlike Micelle Solutions from Rheology using a Mesoscopic Simulation Method.....	49
I. Introduction.....	49
II. Model Review .....	50
III. Experimental Section .....	56
IV. Data Fitting Procedure .....	57
V. Results and Discussion .....	65
VI. Conclusions.....	75

Chapter 4: Multi-Scale Modeling of the Effects of Salt and Perfume Raw Materials on the Rheological Properties of Commercial Thread-like Micellar Solutions.....	77
I. Introduction.....	77
II. Multi-scale Modeling and Packing Argument .....	79
III. Experiments and Simulation Set Up .....	85
IV. Effect of Salt .....	89
V. Effect of PRM Addition.....	99
VI. Conclusions.....	108
Chapter 5: Mesoscopic Modeling on the Rheology of Partially Unentangled and Branched Micelle Solutions .....	111
I. Introduction.....	111
II. Experimental Section .....	115
III. Modeling and Simulation.....	116
IV. Result and Analysis.....	121
V. Discussion .....	127
VI. Conclusion .....	129
Chapter 6: A Hybrid Brownian Dynamics/constitutive Model for Yielding, Aging, and Rejuvenation in Deforming Polymeric Glasses .....	131
I. Introduction.....	131
II. Model Review .....	133
III. Brownian Dynamic Simulations .....	136
IV. Results and Discussion .....	140
V. Conclusions.....	155
Chapter 7: Conclusion.....	157
Appendices.....	163
Bibliography .....	200

## List of Tables

Table 2.1 Experimental values of $l_p$ and $r_{cs}$ from the literature. ....	20
Table 2.2 “Standard” values of parameters.....	27
Table 2.3 Scaling laws for relaxation without CLFs. ....	36
Table 2.4 Scaling laws for relaxation with CLFs. ....	36
Table 2.5 Estimations for average micelle length.....	37
Table 2.6 Estimation of parameters for data from Oelschlaeger <i>et al.</i> (2010) and Khatory <i>et al.</i> (1993).....	46
Table 3.1 Estimation of parameters from fits in Fig. 3.9(b), (c), and (d). ....	65
Table 3.2 Sensitivity analysis, showing effect of variation in $l_p$ on best-fit values of other parameters for data of Fig. 3.9(d). ....	67
Table 3.3 The summary of insensitivity percentages for micellar parameters for combined mechanical & DWS data of Fig. 3.9(d). ....	69
Table 4.1 Composition of ACCORD. For each component, the CAS number, IUPAC name, common name, chemical structure, octanol/water partition coefficient, molecular weight, and its weight percentage in the mixture, are given. ....	86
Table 5.1 A comparative list of relaxation mechanisms and the associated characteristic times between entangled and unentangled micelles .....	118
Table 5.2 Standard values of micellar parameters for simulation predictions in Fig. 5.3 .....	123
Table 5.3 Values of micellar parameters for simulation predictions in Fig. 5.4.....	125
Table 6.1 Values of model parameters for simulation predictions in Fig. 6.1a.....	141
Table 6.2 Values of model parameters for simulation predictions in Fig. 6.4.....	149
Table B.1 Estimated parameters from best fits in Fig. B.3 with different imposed values of $d$ . ....	178
Table B.2 Parameter values obtained by best fitting rheological data, for imposed values of $G_N$ . .....	178
Table B.3 The same as Table B.2, except for imposed values of $\zeta$ . ....	179
Table B.4 The same as Table B2, except for imposed values of $L$ .....	179

Table B.5 The same as Table B.2, except for imposed values of $\alpha_e$ .....	181
Table B.6 The same as Table B.2, except for imposed values of $l_e$ .....	181
Table C.1 Coarse-grained DPD molecular mapping of surfactants and PRMs.....	184
Table C.2 15 PRMs added separately to BW-1EO at 15 mM, resulting in zero shear viscosities $\eta_0$ plotted in Fig. 4.10 and tabulated in Table C.3.....	185
Table C.3 Names of 25 PRMs, viscosities $\eta_0$ (in Pa · s) upon addition of each of the 25 PRMs at 15 mM to BW-1EO in the absence of ACCORD at 1.0 wt. % NaCl, and the corresponding $\log P_{OW}$ .....	187



## List of Figures

Figure 2.1 Loose and tight entanglement regimes. ....	23
Figure 2.2 Plateau modulus for loose and tight entanglement regimes and the crossover between them (for $T = 300\text{K}$ , $l_p = 25\text{nm}$ , and $d = 5\text{nm}$ ). ....	25
Figure 2.3 Diffusing method with end-hop process. ....	28
Figure 2.4 Pointers along discretized micelles. The shaded segments are the unrelaxed ones. ...	29
Figure 2.5 Breakage and rejoining depicted by pointer algorithm (a) Rejoining (b) Breakage. ..	29
Figure 2.6 Procedure for multiple breakage/rejoining cycles. ....	30
Figure 2.7 Reptation and CLF depicted by pointer algorithm (a) Reptation (b) CLFs. ....	31
Figure 2.8 Results of two traditional transformation methods for the normalized Cole-Cole plot using standard values of parameters. ....	33
Figure 2.9 Flowchart describing steps in the calculation. ....	34
Figure 2.10 Effect of double reptation on the normalized Cole-Cole plot. ....	35
Figure 2.11 “Dip” in the normalized Cole-Cole plot at high frequencies caused by Rouse modes as a function of the number $Z$ of entanglements. ....	35
Figure 2.12 Effect of model parameters on normalized Cole-Cole plots (a) $l_p$ (b) $\zeta$ (c) $L$ (d) $\alpha_e$ . 38	38
Figure 2.13 Definition of significant local rheological features in plots of (a) $G'$ and $G''$ versus frequency, and (b) Cole-Cole plot. ....	39
Figure 2.14 Empirical correlations for the dependences of $G'_{max}/G_N$ and $G''_{max}/G_N$ on $\zeta$ with other parameters fixed at standard values. ....	40
Figure 2.15 Empirical correlation for the dependence of $G''_{min}/G_N$ on dimensionless tube length $Z_t$ with other parameters fixed at standard values. ....	40
Figure 2.16 Empirical correlation for the dependence of $\omega_{max} \tau_{rep}$ on dimensionless breakage rate $\zeta$ for various values of $Z_t$ and other parameters set to standard values. ....	41
Figure 2.17 Extended empirical correlation for the dependence of $G''_{min}/G_N$ on average entanglement number $Z$ by varying $L$ and $l_e$ (or equivalently $\alpha_e = l_e/l_p$ ) with other parameters fixed at standard values. ....	42

Figure 2.18 Dominant relaxation mechanisms and five parameters ( $G_N, \zeta, d$ and $\tau_{rep}, l_p$ ) controlling the behavior in each of four different frequency ranges. ....	43
Figure 2.19 Schematic of simulation procedure to obtain micelle parameters from rheological behavior.....	44
Figure 2.20 Simulation results of the Pointer Algorithm fitted to rheological data in Oelschlaeger <i>et al.</i> (2010).....	45
Figure 2.21 Simulation results of the Pointer Algorithm fitted to rheological data in Khatory <i>et al.</i> (1993).....	46
Figure 3.1 Schematic of pointer algorithm, showing the creation and movement of pointers by breakage and rejoining (left), and reptation and CLFs (right).....	55
Figure 3.2 Molecular structure of (a) SLE1S and (b) CAPB.....	57
Figure 3.3 Illustration of local rheological features. Inset: Cole-Cole plot. ....	58
Figure 3.4 Extended empirical correlation for the dependence of $\omega_{max} \tau_{rep}$ on semi-flexibility coefficient $\alpha_e = l_e/l_p$ and dimensionless breakage rate $\zeta$ with $l_p = 25 \text{ nm}$ and $d = 5 \text{ nm}$ . ....	59
Figure 3.5 Extended empirical correlation for the dependence of $G''_{min}/G_N$ on average entanglement number ( $Z$ ) by varying average micelle length ( $L$ ) and semi-flexibility coefficient ( $\alpha_e$ ) with $l_p = 25 \text{ nm}$ and $d = 5 \text{ nm}$ . (a) $\zeta = 0.01$ ; (b) $\zeta = 0.05$ ; (c) $\zeta = 0.1$ .....	60
Figure 3.6 Temperature-dependent rheological data from reference [Buchanan <i>et al.</i> (2005)], showing temperature shifts of $G''_{max}, G''_{min}$ and $\omega_{max}$ . ....	62
Figure 3.7 Definition of frequency regions and associated fitting deviations. ....	63
Figure 3.8 Parameter map showing relationships between the five independent model parameters ( $G_N, \zeta, L, \alpha_e, d$ ) and the additional parameters ( $\tau_{rep}, Z, L_t, l_e, l_p, \zeta$ ) derived from them. ....	64
Figure 3.9 Experimental data and fitting results with $d = 4 \text{ nm}$ for WLM solution (6.67 wt% SLE1S, 3.10 wt% NaCl with solvent viscosity $\eta_s = 0.9 \text{ cP}$ at $25^\circ\text{C}$ ). ....	66
Figure 3.10 Sensitivity of fits to the value of $l_p$ for combined mechanical & DWS data in Fig. 3.9(d).....	68
Figure 3.11 The same as Fig. 3.10, except for mechanical data only shown in Fig. 3.9(b). The inset shows an enlarged view of the fitting near the minimum in $G''$ . ....	70
Figure 3.12 The dependence of characteristic micellar parameters on salt weight percentage through fits to the experimental data for SLE1S/CAPB/NaCl surfactant solutions with perfume. .....	71

Figure 3.13 Experimental and fitting results for SLE1S/CAPB/NaCl surfactant solutions with perfume and various salt weight fractions. ....	73
Figure 3.14 Three different sequences in reversible scission scheme. ....	74
Figure 3.15 Stress relaxation behaviors for reversible scission scheme with three different sequences, depicted in Fig. 3.14. (a) Reptation with CLFs; (b) Pure reptation (i.e., no CLFs)....	74
Figure 3.16 Pointer algorithm with end-interchange and bond-interchange schemes.....	74
Figure 3.17 Stress relaxation behaviors for different breakage schemes for fixed surfactant volume fraction with the sequence used as defined in the text.....	75
Figure 4.1 Structures of surfactants and perfume raw materials (PRMs) used in this study .....	87
Figure 4.2 Snapshot of an equilibrated periodic wormlike micelle in a DPD simulation. ....	89
Figure 4.3 Salt curves for 11 wt. % and 9.5 wt. % formulations with 1 wt. % ACCORD (solid symbols) and without ACCORD (open symbols). ....	90
Figure 4.4 (a) Storage and (b) loss moduli for BW-1EO at different salt weight fractions.....	91
Figure 4.5 Normalized Cole-Cole plots for (a) BW-1EO and (b) BW-3EO. ....	92
Figure 4.6 Master curves of frequency-dependent moduli obtained by time-temperature superposition (TTS), shifted to 25 °C at salt concentrations of (a) 1.0 wt. %, and (b) 2.0 wt. % NaCl for BW-1EO. ....	93
Figure 4.7 (a) Zero shear viscosity $\eta_0$ , (b) average micelle length $L$ , (c) plateau modulus $G_N$ , and (d) breakage time $\tau_{br}$ for various salt weight fractions for BW-1EO at 20.0, 22.0, 23.5, and 25.0°C. ....	94
Figure 4.8 (a) Scission free energy $E_s$ vs. T at various salt concentrations for BW-1EO. (b) Viscosity activation energy $E_v$ , and terminal relaxation time activation energy $E_r$ .....	96
Figure 4.9 Normalized DPD bead number density radial distributions of head, tail, and water as functions of radial distance from COM. ....	98
Figure 4.10 Zero shear viscosities $\eta_0$ of BW-1EO in the presence of ACCORD and 0.7% NaCl on addition of each of 15 PRMs at 15 mM plotted against $\log P_{OW}$ , of the added PRM. ....	99
Figure 4.11 (a) Dependence of $\eta_0$ on concentration of dipropylene glycol (DPG), cumene, linalool, and isopropyl myristate (IPM) in BW-1EO containing ACCORD and 0.7 wt. % NaCl. (b) Estimated average micelle length $L$ , (c) scission free energy $E_s$ , and (d) average breakage time $\tau_{br}$ , inferred from the Pointer Algorithm, vs. PRM concentration.....	101

Figure 4.12 Storage $G'$ and loss moduli $G''$ vs. frequency for (a) BW-1EO and (b) BW-3EO, at various linalool concentrations. ....	103
Figure 4.13 Plot of $\eta_0$ (colored open diamonds connected by dash-dotted line, left axis) and surfactant packing distance (colored open triangles connected by dashed line, right axis) for BW-1EO upon addition of 15 mM dipropylene glycol (DPG), cumene, linalool, and isopropyl myristate (IPM) vs. their $\log P_{OW}$ for 11 wt. % BW-1EO in 0.7 wt. % NaCl. ....	104
Figure 4.14 Bead number count within a shell of 0.1 nm width as a function of radial distance to the spine of the micelle of tail, head, water and an additional PRM, namely (a) DPG, (b) linalool, (c) cumene, and (d) IPM as functions of radial distance to the COM. ....	105
Figure 4.15 Normalized DPD bead number count of tail, head, and additional linalool within a shell of 0.1 nm width as a function of radial distance to the COM of the wormlike micelles. ..	107
Figure 5.1 The chemical structure for (a) SLE1S (b) CAPB. ....	115
Figure 5.2 The combined rheological response (from mechanical rheometry at low frequencies and DWS at high frequencies) for WLM solutions with constant surfactant (SLE1S+CAPB) concentrations. ....	121
Figure 5.3 Effect of micellar parameters on normalized storage and loss modulus for partially unentangled micelles: (a) $\zeta$ , (b) $Z$ , (c) $l_p$ , (d) $\alpha_e$ .....	123
Figure 5.4 The evolution of micelle ensemble showing the equilibrate composition with average strand length $L_{st} = 2.2 \mu\text{m}$ and branching level $\beta = 0.09$ per $\mu\text{m}$ by the end of the simulation. ....	125
Figure 5.5 (a) The micelle size distribution and number of branched junctions contained in micelles with different sizes, (b) strand length distributions for equilibrated ensemble shown in Fig. 5.4. ....	125
Figure 5.6 The predicted rheological behaviors for micelle systems with same	
Figure 6.1 Simulation fits to experimental data from Lee <i>et al.</i> (2009) (a) and the effects of $G^s$ (b), $t_w$ (c), and $\mu$ (d) on the evolution of strain and segmental relaxation time $\tau_s$ for uniaxial extension with constant load ( $\Sigma_z^{ext} = 16 \text{ MPa}$ ), which is removed at time $t = 9375 \text{ s}$ . ....	143
Figure 6.2 Plots of the ensemble averaged extension $\lambda_e$ (a, left axis) and orientation angle $\theta$ (a, right axis) of chain segments, represented by individual springs of the bead-spring model, as well as the number percentage (b, left axis) and the corresponding averaged orientation angle (b, right axis) of nearly fully extended springs for the simulation results shown in Fig. 6.1a. ....	144

Figure 6.3 Effects of $\Sigma_z^{ext}$ (a), $G^p$ (b), $\alpha$ (c), and $R_0$ (d) on the hardening associated strain-plateau and incomplete strain recovery. ....	147
Figure 6.4 Sensitivities of simulation results to $N_K$ with $N_{sp}$ fixed and $G^p$ and $\alpha$ adjusted to keep the predictions nearly the same (a), and $N_{sp}$ with $N_{K,sp}$ fixed and $\alpha$ adjusted to keep the predictions nearly the same (b). ....	150
Figure 6.5 Mechanical response of polymeric glass under uniaxial extension with constant strain rates ( $\epsilon$ ): Stress (a) and $\tau^s/t_w$ (b). ....	150
Figure 6.6 Mechanical response of polymeric glass under simple shear with constant shear stress ( $\Sigma_{xz}^{ext}$ ) with stress removed at time $t = 9375$ s: $\Sigma_{xz}^{ext} \leq \Sigma_{xz,c}^{ext}$ (a) and $\Sigma_{xz}^{ext} \geq \Sigma_{xz,c}^{ext}$ (b). ....	153
Figure 6.7 Mechanical response of polymeric glass under two successive uniaxial extensions, both at a constant rate ( $= 10^{-4} \text{ s}^{-1}$ ). ....	154
Figure A.1 The initialization of genetic algorithm. ....	166
Figure A.2 Flowchart of genetic algorithm. ....	167
Figure A.3 Normalized Cole-Cole plot for standard values of parameters obtained from genetic algorithm-aided Fourier transform. ....	168
Figure A.4 The same as Fig. A.3, except with $\zeta = 0.05$ . ....	169
Figure A.5 The same as Fig. A.4, except that a constraint method is used. ....	169
Figure A.6 Relaxation function with CLFs and reptation for monodisperse ensemble for $Z = 33.5$ , $\tau_{rep} = 1\text{s}$ , $\alpha_e = 2$ , $l_p = 30\text{nm}$ and $d = 3\text{nm}$ . ....	171
Figure A.7 Family of normalized Cole-Cole plots for different values of $\zeta$ with standard values of other parameters. ....	172
Figure A.8 Family of normalized Cole-Cole plots for different values of $Z_t$ with standard values of other parameters. ....	173
Figure B.1 Flowchart showing data fitting procedure. ....	175
Figure B.2 Evolution of the allowed modification range for $l_p$ represented by gray regions. ...	177
Figure B.3 Best fits for WLM solution (6.67 wt% SLE1S, 3.10 wt% NaCl with solvent viscosity $\eta_s=0.9$ cP at 25°C) with different imposed values of $d$ showing the inability of rheology to determine micelle diameter. ....	178

Figure B.4 Fitting results showing sensitivity of best fits to imposed values of $G_N$ with $d = 4 \text{ nm}$ for WLM solution (6.67 wt% SLE1S, 3.10 wt% NaCl with solvent viscosity $\eta_s=0.9 \text{ cP}$ at $25^\circ\text{C}$ ).	179
Figure B.5 The same as Fig. B.4, except that variation is made in $\zeta$ .	180
Figure B.6 The same as Fig. B.4, except that variation is made in $L$ .	180
Figure B.7 The same as Fig. B.4, except that variation is made in $\alpha_e$ .	181
Figure B.8 The same as Fig. B.4, except that variation is made in $l_e$ .	182
Figure C.1 Viscosities of 8.0 wt. % BW-1EO in the absence of ACCORD at 1.0 wt. % NaCl on addition of each of 25 PRMs (from Table C.3) at 15 mM plotted against $\log P_{OW}$ , of the PRM.	185
Figure D.1 The simulation flow chart for generating the linear rheological behaviors.	189
Figure D.2 A flow chart illustrating the procedure to merge the mechanical rheometrical data with those from DWS.	190
Figure D.3 (a) The 3-arm branched architecture of micelles and (b) the corresponding analogy to the Kirchhoff circuit system.	191
Figure D.4 The intermicellar reactions between branched clusters: (a) breakage (b) recombination.	193
Figure D.5 The relaxation of branched micelles represented by the evolutions of pointers in the presence of sprouting and constrained diffusion.	194
Figure E.1 Illustration of bead-spring chain and the forces exerted on beads $j$ and $j - 1$ . Note that $\mathbf{F}_j^f$ is the friction force defined as $\mathbf{F}_j^f = \zeta_b \nabla \mathbf{v}^T \cdot \mathbf{r}_j$ .	196
Figure E.2 Illustration of the insensitivity of simulation results to the value of $\eta$ and simulation time step $\Delta t$ . The parameters are the standard values listed in Table 6.1.	199

## List of Appendices

Appendix A: Genetic Algorithm and Simulation Details .....	164
I. Pre-factor for Modulus in Loose-entanglement Regimes .....	164
II. Genetic Algorithm for Converting to Frequency Domain .....	165
III. Simulation Testing Details.....	170
IV. Cole-Cole Plots for a Wide Range of $\zeta$ and $Z_t$ .....	172
V. Functional Forms for Micelle Parameters.....	172
Appendix B: Data Fitting Procedure and Sensitivity Study .....	174
I. Detailed Data Fitting Procedure.....	174
II. Sensitivity Studies for Micelle Parameters .....	177
Appendix C: DPD parameters, Effect of Individual PRMs, Scission Enthalpy and Entropy ....	183
I. DPD Forcefield Parameters and Molecular Mapping.....	183
II. Additional PRMs and Their Effects on Viscosity.....	185
Appendix D: Simulation Procedure for Unentangled Micelles and Branching-associated Kinetics .....	188
I. Simulation Procedure.....	188
II. Data Merging .....	189
III. Branching-associated Kinetics.....	190
Appendix E: Brownian Dynamics Simulation for Bead-spring Chains .....	196
I. Equations of Bead-spring Chain .....	196
II. Simulation Algorithm .....	197

## **Abstract**

Exhibiting different rheological (viscoelastic) behaviors, micellar solutions and polymeric glasses are at the center of many applications.

For micellar solutions, I have developed a mesoscopic simulation model, drawing from concepts developed for entangled polymer melts, to account for linear rheology of different micelle structures (linear and branched micelles). Through a “pointer” algorithm I developed, this new model tracks boundaries between relaxed and unrelaxed parts of micelles that are diffusing in entanglement tubes, and uses polymer-like mechanisms along with intermicellar reactions (breakage and reformation) to compute rheology, which allows, for the first time, not only quantitative prediction of flow behaviors but also estimation of important micelle properties from rheological measurement with much greater accuracy than ever before.

For polymeric glasses, by treating the short glassy segments as “solvent” for the slow-relaxing polymeric part, a hybrid model has been developed that combines a constitutive model of the glassy solvent with Brownian dynamics simulations of polymers, whose relaxation is coupled to the glassy dynamics through the drag coefficient. This hybrid model successfully captures numerous behaviors of polymeric glass (yielding, strain hardening, recovery, physical aging, and flow rejuvenation) under various types of deformations as well as the effects of polymer pre-orientation, whose results prove to be consistent with observations from both experiments and molecular level simulations.



## Chapter 1: Introduction

Known as fundamental building blocks for numerous soft materials, surfactants, more generally, amphiphiles which have both solvophilic and solvophobic groups, are at the center of many industrial formulations either as mixtures or as individual component. [Crothers, *et al.* (2016); Kunieda *et al.* (2001); Huang *et al.* (2016); Gao *et al.* (2016); Lin *et al.* (2001)] For instance, in most shampoos and body-washes, surfactants comprise about 90% dry mass of the products as cleaning agents. Above a critical concentration (i.e., the first CMC), these surfactant molecules aggregate to form a variety of self-assembled structures in the solution, referred to as micelles. As revealed by electron microscopy, such structures include small spheroids, ellipsoids, short rods or long worms, [Lequeux (1996)] bilayers, [Nagarajan (1989)], and ordered phases that depend on type and concentration of salt, [Candau *et al.* (1993); Wang and Larson (2009)] surfactant, [Hassan *et al.* (1998); Gomez *et al.* (2010)], temperature, and solvent. [Bruce *et al.* (2002); Jusufi *et al.* (2008)] The versatility in micellar morphologies is the result of the delicate balance on the incompatibility between the solvophilic and the solvophobic parts of the molecule under the presence of selective solvents, where a specific packing geometry, also known as spontaneous curvature, is favored. Given the relative facileness in tuning the non-covalent interactions between surfactant molecules, transitions between different types of micellar structures can be induced by the addition of simple electrolytes, cosurfactants, or strongly binding counterions (so-called hydrotropes). [Kaler *et al.* (1989); Villeneuve *et al.* (1999); Wang *et al.* (2016)] Such changes in micellar structure sometimes accompany with prominent gains in viscoelasticity indicating the existence of large micellar structure, in particular, the transient network of entangled wormlike micelles (WLMs), which have commonly been practiced in the realm of detergent-related industries. [Adamy (2016); Oelschlaeger *et al.* (2012); Zhao *et al.* (2015)]

However, most of studies on micelles have simply focused on solutions containing a single species of surfactant at relatively low concentration along with one species of anionic hydrotrope or inorganic salt. [Cates and Fielding (2006); Lawrence (1994); Maitland (2000);

Rhein *et al.* (2006); Wheeler *et al.* (1996)] For example, sodium dodecyl sulfate (SDS), has been investigated extensively in the concentration range between the first CMC at 0.008 M and the second CMC at 0.069 M, and over this concentration range, the majority of the micelles are small spheres or ellipsoids. [Kodama *et al.* (1972); Yasunaga *et al.* (1967)] WLM solutions composed of anionic surfactants at concentrations far above the second CMC are studied less frequently, even though those concentration ranges are more relevant to practical applications, and in those ranges the micelle solutions exhibit viscoelastic properties. Thus, mixed surfactants are usually used in practice because of the lower cost of polydisperse mixtures and their improved performance over that of the single-surfactant solutions: [Scamehorn (1986)] The addition of the ionic surfactant sodium lauryl ether sulfate (SLES) to an SDS solution enhances the viscosity of the mixture at low total surfactant concentration;<sup>23</sup> Superior interfacial tension reduction is obtained upon addition of the zwitterionic surfactant cocamidopropyl betaine (CAPB) to an SDS solution; [Danov *et al.* (2004); Galvan-Miyoshi *et al.* (2008); Hines *et al.* (1998)] Sharp drops in both the first and second CMCs are obtained in mixtures of CAPB and SLES, with one to three ethylene oxide (EO) monomers, compared to those seen in each of the individual surfactant components, as determined through experimental measurements using rheometry and SAXS. [Christov *et al.* (2004); Eguchi *et al.* (2007); Naruse *et al.* (2009)] Although the addition of cationic surfactants to anionic surfactants boosts viscosity enormously at low surfactant concentrations, the formation of an insoluble complex can limit the range of practicable formulations, and so it is often avoided. [Scamehorn (1986); Schurbert *et al.* (2003)]

Besides the fundamental interest on detailed interactions among surfactants, great efforts have been made for WLM solutions over decades to better understand the coupling between their complex rheological properties and the microstructure as well as their topology at mesoscale level. It is now well-accepted that the interplay between structural energy and system entropy brings two types of topological defects to the cylindrical body: end-caps and junctions, resulting in micelles with finite length and formation of branched structures, respectively. [Dan and Safran (2006)] The latter is thought to enable percolation and phase separation with the emergence of an interconnected network when temperature is increased. [Zilman *et al.* (2004); Zilman and Safran (2002)] As directly visualized via cryo-TEM, [Clausen *et al.* (1992); Lin (1996)] these WLMs have a diameter of 3-5 nm whilst their contour length can reach a few micrometers in the semi-dilute regime giving rise to the occurrence of entanglements and a transition to branched clusters

can eventually take place with high level of salt. [Padalkar *et al.* (2002); Yusof *et al.* (2012)] These structures and their size control the flow properties of the surfactant solution, which is crucial in applications, for example, in shampoos, for which careful design of the formulation is needed to achieve a product that is neither too runny nor too viscous. While much is known about their structures and flow behaviors, the complex dependencies of micellar structures on various types and concentrations of surfactant, salt, and additives (for instance, hydrotropes), make such solutions difficult to characterize and design for different applications. Such complexity can be simply illustrated by a so-called “salt curve” where, with increasing salt concentration, an increase in viscosity caused by the growth of long wormlike micelles and subsequent decrease caused by micelle branches are observed.

Thus, to unveil the basic property-structure relationships behind different flow behaviors of WLMs, a rich variety of theories and models are therefore proposed, which generally falls into two categories: thermodynamic or rheological. The thermodynamic models can well predict the “inverted” micellar phase behavior on the basis of a complex balance between mixing entropy and enthalpic/curvature energy, where the spontaneous curvature, is introduced to explain the temperature induced evolution of micelle morphology. [Dan and Safran (2006); Tlusty and Safran (2000)] While for rheological models, the main concept relies on the analogy between cylindrical micelles and polymer chains with the “flow” of topological defects, i.e., the evolving spatial distribution of chain-ends and branched junctions, which resembles binary fluid in the sense that their competition corresponds to a shift of micellar connectivity. [Zilman and Safran (2002); Drye and Cates (1992)] However, WLMs are subjected to constantly breaking and reforming in thermal equilibrium with their surfactant “monomers”, [Kalur *et al.* (2005); Feng and Han (2016)]: they are capable to break, reform, and exchange materials, and hence display pronounced fluidity than conventional polymers, [Lequeux and Candau (1994); Waton and Zana (2007)] which prevents them from mechanical degradation and hence being a desirable candidate as heat-transfer fluids and fracturing liquids. [Barhoum *et al.* (2012)] However, when the applied flow rate is high enough to disturb the equilibrium WLM structures, which in turn modify the flow itself, a rich variety of nonlinear rheological features would appear including localization of stress, heterogeneous shear bands, and flow induced phase separation etc. [Gallor *et al.* (2013); Cardiel *et al.* (2014)]

As nourished by the continuing development of instrument science and technology, experimental characterization of micelle structure has significantly contributed to the development of the theory of WLM dynamics. The value of the persistence length was measured by Porte *et al.* (1980), who showed that elongated micelles should be thought of as semi-flexible polymerlike chains, rather than as rods. Since then, many important measurement methods have been applied to micellar solutions: SANS (small angle neutron scattering) [Marignan *et al.* (1989); Appell and Marignan (1991)], birefringence [Shikata *et al.* (1994); Decruppe and Lerouge (1999)], DLS/SLS (dynamic/static light scattering) [Brown *et al.* (1989); Nemoto *et al.* (1995)], cryo-TEM (cryogenic transmission electron microscopy) [Clausen *et al.* (1992)], NSE (neutron spin echo) [Nettesheim and Wagner (2007)], DWS (diffusing wave scattering), [Galvan-Miyoshi *et al.* (2008)] ultrasonic velocimetry, [Gallot *et al.* (2013)] and micro-cantilevers. [Youssry *et al.* (2012)] Although these measurements supply vital inputs to micelle characterization, quantitative estimates and comparisons of the determined micellar characteristic lengths from those methods still remain challenging. The difficulties, to a large extent, rest on the gaps between individual methods in probing the structure beyond specific length scales or concentrations, which can hardly be overcome by a simple combination of several aforementioned characterization measurements. Since the rheology of WLM solutions appears to be rather sensitive to subtle changes in either length scales or lifetime of the microstructure, once coupled with an appropriate model, it can offer an indispensable route in micelle characterization. Remarkable efforts had thereafter been made to deduce characteristic information of the “living” behavior as well as micellar structure from experimental measurements on viscoelastic behaviors of WLMs, [Angelescu *et al.* (2003); Chellamuthu and Rothstein (2008); Ouchi *et al.* (2006)] among them, the model of Cates and coworkers was a great success in estimating micelle length which is otherwise inaccessible from non-rheological measurements. [Cates (1987); Candau and Cates (1990); Granek (1994)]

Within the framework of polymer “tube model” [Doi and Edwards (1986)] and reptation theory [de Gennes (1979)], in 1987, Cates put forward a model to explain the unique Maxwellian (i.e., single-exponential) stress relaxation behavior observed for simple surfactants that form WLMs such as cetyltrimethylammonium (CTA) surfactants [Turner and Cates (1991); Lequeux (1992)] in which diffusion of WLMs is limited to “tube”-like region by entanglements. The original Cates model is based on the interplay of two mechanisms: i.e., breakage/rejoining and

reptation. Imposition of a small step strain on entangled WLMs takes their conformations out of equilibrium, producing a stress. In the absence of breakage, micelle segments can only relax the stress by diffusing curvilinearly, or “reptating,” out of the initial tube, which leads to a loss of original, oriented tube segments as the micelle vacates them. This reptation motion is now well understood for ordinary “dead” polymers [Doi and Edwards (1986); Likhtman and McLeish (2002)], where no breakage or rejoining exists. For living WLMs, micellar breakage accelerates the relaxation by creating new ends. To address this effect, a dimensionless breakage time is defined: [Cates (1987)] When this dimensionless time decreases below unity, which is usually the case for WLM solutions, the relaxation spectrum is narrowed, since for a high breakage rate the distance that a micelle segment must travel to diffuse out of its tube becomes independent of the tube length. As a result, the polydispersity in micelle length distribution has little effect on the relaxation: All tube segments are lost at the same rate and the stress relaxes mono-exponentially.

In summary, the original Cates model rests on several assumptions [Cates (1987); Candau *et al.* (1989)], namely, (i) Micelles break with a uniform probability per unit length. (ii) Successive breakage and rejoining events are uncorrelated, and breakage is unimicellar while rejoining is bimicellar. (iii) Micelle relaxation occurs through reptation. (iv) Tube rearrangement or constraint release (CR) is neglected. Although the above model limits relaxation mechanisms of micelles to reptation assisted by breakage and rejoining, the approximate single exponential relaxation behavior, which reveals itself in a nearly semicircular Cole-Cole plot (i.e., the cross-plot of loss modulus  $G''$  against storage modulus  $G'$ ), can be successfully reproduced. Nevertheless, in experiments, deviations from the semicircle are always observed after a minimum is reached on the high frequency side of the Cole-Cole plot [Granek (1994)], implying that some relaxation mechanisms are missing from the original theory. Cates and coworkers, therefore, added breathing fluctuations or CLFs, which describe time dependent changes in the length of the tube contour, as well as high frequency Rouse modes [Dealy and Larson (2005)], subsequently into the model. [Granek and Cates (1992); Granek (1994)] Using this modified model, the micelle length can be determined from the observed minimum in Cole-Cole plot at high frequency. [Granek (1994)] Besides adding high frequency relaxation dynamics into the original model, Granek and Cates (1992) also developed a simulation method based on the

“Poisson renewal process,” where correlations of micelle length between breakage and rejoining events are neglected and micelle lengths are assumed to follow a Poisson distribution.

Since then, a lot of emphasis have been thrown on applying the Cates model to micellar systems composed of cationic, anionic, zwitterionic, or nonionic surfactants. [Barhoum *et al.* (2012)] Not surprisingly, shortcomings are found due to the lack of description on micelle rigidity, branches, as well as a complete spectrum of relaxation mechanism, all of which can be severely impacted by temperature, salt level, and the presence of hydrotropes, therefore resulting in discrepancies between theory and experiments. [Zhao *et al.* (2015); Feng and Han (2016); Lonetti *et al.* (2011); Cardiel *et al.* (2014)] For example, the micelle length extracted from rheological data using Cates model is usually a fraction of a micron, which is shorter than one would expect based on the rather high value of micelle scission energy (i.e., the free energy of creating two additional end caps) [Larson (2012)]. Hence, the accuracy of the model is questionable to estimate micellar parameters from rheological responses ( $G'$  and  $G''$  curves) Moreover, different approximations that are made when using the predictive ability of Cates model further complicates the rigorous interpretation of the micellar structure. However, when compared to other models and simulations in this area, [Yan *et al.* (2016); Padding *et al.* (2009); Acharya *et al.* (2006); Aniansson and Wall (1974)] the concept underlying the Cates model maintains its attractiveness and by supplemented with an adequate amount of physics, I believe, a sophisticated method can be established for quantitative estimation of micellar properties from rheology which can hardly be obtained otherwise.

Motivated by the work of Cates on unbranched WLMs, I developed a novel fast “pointer” simulation method that includes recent advances of polymer theories to describe relaxation of micelles, where “pointers” are used to track boundaries between relaxed and un-relaxed portions of wormlike micelles from time to time. This simulation model for the first time allows not only quantitative prediction of flow behaviors but also estimation of important micelle properties with much greater accuracy than ever before, which is now used by Procter and Gamble scientists to help them understand and eventually design improved surfactant formulations. In what follows, Chapter I focuses on both the theoretical and the computational development of the method, starting with descriptions of currently understood polymer relaxation mechanisms, followed by the novelty of the method in detail, including the pointer algorithm and the genetic algorithm (GA) that converts results from the time to the frequency domain. After introducing the two

experimental methods used to obtain rheological data from WLM solutions, Chapter II describes a detailed data-fitting procedure that yields properties of WLMs on the basis of empirical relationships between micellar parameters and local rheological behaviors. The sensitivity studies (i.e., analyses on the sensitivity of estimated parameters to error or noise), fitting results for various micellar solutions as well as the effect of different breakage mechanisms are also discussed there. In Chapter III, I report the success of the method in multiscale modeling of two types of commercial surfactant solutions and describe the effects of added salts and perfume raw materials (PRMs) on the viscoelastic properties through systematical studies on micellar properties inferred from rheology as well as through molecular simulations using dissipative particle dynamics (DPD) and molecular “packing parameter” concept. By connecting the surfactant packing at the molecular scale to micellar properties at the mesoscale, and these, in turn, to the rheological properties at the macroscopic scale, an approach for achieving a fundamental understanding of the structure–property relationships of commercial surfactant solutions is established. To extend the above success in modeling unbranched but well-entangled WLMs, Chapter IV contains the decisive progress being made on two more challenging topics: to include the effects of both micelle branches and unentangled micelle rods in the model. By simulating systems with different level of branched and unentangled micelles, this extended simulation method is capable to predict the change in rheology therefore to allow the characterization of solutions at various surfactant and salt concentrations.

The accomplishments of these work enable, for the first time, modeling of the flow behaviors of micelle solutions across the whole range of surfactant and salt concentrations that is typically used in micelle-based industrial applications. The above simulation method demonstrates good accuracy of the estimations of micelle parameters from rheometric data compared to that from neutron scattering. This implies that instead of conducting expansive and time consuming experiments such as neutron scattering, it is possible to obtain accurate estimates of micelle characteristic parameters and therefore the flow properties of shampoos using much cheaper and faster rheometric measurements combined with this simulation model. A recent application of this simulation method to 120 different commercial shampoo formulations prepared by Procter and Gamble shows the great success of the method in analyzing quantitatively how surfactant chemistry affects micelle microstructure and how it manifests in solution macroscopic properties. To the best of my knowledge, no such model has ever before

been developed for wormlike micelle solutions, and as complemented by molecular dynamic simulations this method is now deployed at Procter and Gamble to guide the design of shampoo formulations. Hence, with the aforementioned novelty, robustness and success, this method, I believe, would eventually become a standard technique in characterization of micelle solutions.

As a different research direction, I also worked on another topic, namely development of rheological model for mechanical response of polymeric glasses under deformation. Lacking long-range order, a glass is an amorphous solid conventionally formed by supercooling a liquid to the point of arresting molecular motion without crystallization, resulting in a non-equilibrium jammed state. [Debenedetti and Stillinger (2001)] This non-equilibrium, amorphous, structure of the glass is crucial to controlling the common characteristics of this type of material: hardness, brittleness, transparency, low conductivity, and soft magnetism. [Osborne and Lacks (2004); Greer (1995)] On the macroscopic scale, the transformation of the liquid to the glass appears within a narrow range of temperatures approximated by what is referred to as the glass transition temperature. Although the ability to form a glass is not restricted to a specific class of atoms or molecules, polymers, however, with a great diversity of local length scales and a broad range of characteristic times, can be easily cooled to form glasses with impact resistance and toughness [Lee *et al.* (2009)] that are significantly higher than that of colloidal or metallic glasses. Such advantages in mechanical properties make polymeric glasses widely-used in the manufacturing with applications being found in a variety of fields: printing and packaging, optics, surface protection and coatings, etc.

Unlike WLM solutions, the rheological modelling of polymeric glasses are greatly challenged by their complex behaviors: Under deformation, polymeric glasses show a linear elastic response at small strain followed by yielding at larger strains where the energetic barriers to plastic flow are overcome. [Boyce *et al.* (1988); Hoy (2011)] After yielding, strain-softening, and a drop in stress with an increase of strain, may also occur, signaling inhomogeneous deformation and strain localization (crazing, necking, and shear banding etc.). [Fielding *et al.* (2012) and (2013)] The degree of softening and the magnitude of the yield stress are known to depend on the thermomechanical history of polymeric glasses. [Klompfen *et al.* (2005); Wendlandt *et al.* (2005)] In many respects polymeric glasses are similar to other glasses: they show a slow evolution towards equilibrium known as physical ageing, and many show non-Arrhenius temperature dependence of relaxation as well as the decoupling of translational and



rotational diffusion as the material is cooled deeply into the glass, indicating increasing local heterogeneity. [Schweizer and Saltzmann (2004); Chen *et al.* (2009)] However, it has been generally accepted that the long-chain feature of polymer molecular structure greatly alters the mechanical responses of polymeric glasses relative to non-polymer ones. [Wendlandt *et al.* (2005); Hoy and O'Hern (2010)] At very large strains, the polymeric glass enters the hardening regime, a phenomenon unique to polymeric glasses where strain localization is greatly suppressed. [Hoy and Robbins (2008)]

Understanding the above behaviors is of great importance in the manufacturing of polymeric glass to achieve designed mechanical properties. [Arruda *et al.* (1993)] Through techniques such as neutron and X-ray scattering, [Hansen and McDonald (1986)] nuclear magnetic resonance (NMR), [Loo *et al.* (2000)] birefringence, [Arruda *et al.* (1993)] and optical photo-bleaching, [Lee *et al.* (2009)] it has been learned that stress can enhance local mobility in the glass by either deforming the potential energy landscape or by introducing mechanical disorder. [Debenedetti and Stillinger (2001); Chen and Schweizer (2010)] The resulting decrease in structural (or segmental) relaxation time is known as mechanical rejuvenation. [Lee *et al.* (2009)] However, when strain hardening begins, the local mobility of the polymeric glass decreases and the material becomes highly anisotropic due to the orientation of polymers under large deformation. [Wendlandt *et al.* (2005); Arruda *et al.* (1993)] A sophisticated model is thereof required to characterize the above complex, and non-monotonic behavior of deforming polymeric glasses. In general, most existing models of polymeric glasses fall into one of two generic categories, i.e., kinetic or thermodynamic. [Chen and Schweizer (2007)] For thermodynamic models, configurational entropy is the major concern: it drives local structure rearrangements within a cooperative region. Although it is hard to give a clear definition of the configurational entropy and the mapping to the real molecules, [Chen *et al.* (2009)] some of these models predict the observed decoupling of translational and rotational motion for different types of glasses. Kinetic models show much greater diversity: some relate molecular rearrangement to plastic deformation through excited small clusters of “defects” or of “free volume” whose concentration is controlled by the competition between ageing and rejuvenation. Others introduce a state variable carrying structural information which determines the structural relaxation of material functions. In these models, a polymeric glass is assumed to be a

continuously deformed material with the time evolution of the state variable controlled by ageing and rejuvenation.

Since most of the aforementioned models are greatly challenged by the non-monotonic, complex dependence of the segmental relaxation time on the deformation of the polymeric glass, especially during strain hardening and strain reversal. [Lee *et al.* (2009); Hoy and O'Hern (2010)] Given the blurred boundaries between melts and glasses at the molecular level, the generic fluid point of view (i.e., that any liquid exhibits solid-like behavior on time scales much shorter than the material relaxation time) is favored for the characterization of ageing and rejuvenation: the polymeric glass becomes more solid-like through ageing, but fluidizes upon rejuvenation. Using this concept, a so-called “fluidity” equation [Moorcroft *et al.* (2011)] was used by Fielding, Cates and Larson [Fielding *et al.* (2012) and (2013)] to account for the time-evolution of the segmental relaxation time for polymeric glasses under deformation. In this model, the dynamics follow a “two-time-scale” scenario: [Berthier *et al.* (2000)] the macroscopic behavior is controlled by both a local segmental mode and a separate larger-scale, slower, polymeric mode, where these two modes contribute additively to the overall stress with their relaxation times being coupled by a proportionality relationship. Since ageing and rejuvenation reflect local dynamics, and weakly depend on the type of glass, [Klompen *et al.* (2005); Chen *et al.* (2009); Thureau and Ediger (2002)] their effects on the segmental relaxation time are accounted for in an isotropic and additive fashion with a constant ageing rate and a deformation-controlled rate of rejuvenation, respectively. Therefore, the non-monotonic dependence of structural relaxation time on deformation under creep (constant stress) conditions is explained by the competition between ageing and rejuvenation: in the post-yield regime, strain-induced rejuvenation dominates, causing relaxation time to decline. However, as massive deformation builds up rapidly with the onset of strain hardening, and rejuvenation thereafter is suppressed. As a result, relaxation time undergoes a rapid rise indicating the “victory” of ageing, even under a fixed load.

To achieve even qualitative predictions from the above two mode model for the uniaxial creep experiment reported by Lee and coworkers, [Lee *et al.* (2009)] the value of polymeric modulus is required to be an order of magnitude larger than the experimentally determined rubbery modulus. However, during the unloading, this high value needs to be reduced back closer to the rubbery modulus by arbitrarily introducing a so-called “crinkle factor” in order to

capture the recoil behavior. Nonlinear elasticity [Wendlandt *et al.* (2005); Hoy and Robbins (2008); Larson (1990)] and the formation of “kinks” (i.e., the multiple-folded nearly fully stretched subsection of chains) [Fielding *et al.* (2012) and (2013); Larson (1990)] are thought to cause the above consequences. [Larson (1990)] Since the model represents the polymer as a simple two-bead dumbbell, does not naturally describe the effect of conformation change in polymers, an appropriate treatment that avoids both the artificially high polymer modulus and the “crinkle factor” requires a more realistic polymer model for local chain relaxation. Such model should also be able to account for intramolecular cooperativity, including chain connectivity, stiffness, and finite extensibility. Thus, in the last chapter of this dissertation, i.e., in Chapter V, I present a hybrid model for polymeric glasses under deformation that combines a minimal model of segmental dynamics, borrowed from the early work of Fielding *et al.*, with a beads-and-springs model of a polymer, solved by Brownian dynamics (BD) simulations. This coarse-graining allows simulations that are much faster than molecular dynamics and successfully capture the entire range of mechanical response including yielding, plastic flow, strain-hardening, and incomplete strain recovery. By representing polymers as bead-spring chains, this hybrid model improves upon the estimation of the small elastic recoil seen experimentally without the use of artificial parameters required previously. [Fielding *et al.* (2012)] With appropriate choice of parameters, predictions of creep, recovery, and segmental relaxation are found to be in good agreement with experimental data of a typical polymeric glass (i.e., polymethylmethacrylate, PMMA) under uniaxial extension. [Lee *et al.* (2009)] This new model shows dramatic differences in behavior of the segmental relaxation time between extensional creep and steady extension, and between extension and shear. The non-monotonic response of the segmental relaxation time to extensional creep and the small elastic recovery after removal of stress are shown to arise from sub-chains that are trapped between folds, and that become highly oriented and stretched at strains of order unity, connecting the behavior of polymeric glasses under creep to that of dilute polymer solutions under fast extensional flows. At last, this model is also capable to clarify the effects of a commonly used method in solid phase polymer processing, i.e., the effects of polymer pre-stress in the parallel or orthogonal direction on the subsequent response to extensional deformation by investigating the evolution of polymer conformation at mesoscale level.

## Chapter 2: A Mesoscopic Simulation Method for Predicting the Rheology of Semi-dilute Wormlike Micellar Solutions

### I. Introduction

Surfactant solutions with various self-assembled structures have been intensively studied in recent years. Such structures include small spheroidal micelles, long wormlike micelles [Lequeux (1996)], ellipsoids, bilayers [Nagarajan (1989)], and ordered phases, that depend on type and concentration of salt [Candau *et al.* (1993); Wang and Larson (2009)], surfactant [Hassan *et al.* (1998); Gomez *et al.* (2010)], temperature, and solvent [Bruce *et al.* (2002); Jusufi *et al.* (2008)]. Above the critical micelle concentration (CMC), surfactant molecules aggregate to form equilibrium spherical micelles. While changes in equilibrium structure are induced in a variety of ways [Michels and Waton (2003); Terech *et al.* (1992); Helgeson *et al.* (2010); Oelschlaeger *et al.* (2009)], a transition from spheroid to wormlike micelles often occurs with increasing salt concentration, and further increases can result in micelle branching and network formation [Ilgenfritz *et al.* (2004)]. With the widespread use of micelles and surfactant solutions [Rosen (1989); Siritwatwechakul *et al.* (2004)], extensively attention has been paid to determining the properties of micelle-solvent systems using computer simulations [Shang *et al.* (2009)], theoretical modeling [Cates and Candau (1990)] or advanced experimental techniques [Kuperkar *et al.* (2008)].

It has long been noted that the rheological properties of wormlike micellar solutions have similarities to those of long polymers [Candau *et al.* (1993); Cates and Candau (1990)]. A number of theories that exploit those similarities have been developed [Wittmer *et al.* (1998); Grmela *et al.* (2010); Rothstein (2003)] that treat wormlike micelles as living/equilibrium polymers, which incessantly break and rejoin in thermal equilibrium. Using the tube concept for entangled polymer, Cates and coworkers [Cates and Candau (1990); Cates (1987); Turner and Cates (1991)] developed a model that qualitatively or semi-quantitatively predicts the rheology of wormlike micellar solutions and allows properties of micelles, such as their length and rate of breakage, to be inferred from rheology. Despite its successes, there remain gaps [Lequeux

(1992); van der Schoot and Wittmer (1999); Larson (2011)] in the theory, as discussed in this paper. Meanwhile, over the past twenty years since the introduction of Cates' model, many improvements have been developed for more accurate description of the rheology of entangled polymer solutions and melts [Dealy and Larson (2005)]. It is therefore time to consider if those new developments might be exploited to improve upon Cates' model for wormlike micelles.

In this paper, we describe a novel simulation method for extending Cates' model by including additional physics known to be important in entangled polymer solutions but neglected in the earlier theories. In what follows, Section II defines needed terminology, Section III focus on the theoretical development of our method, starting with a brief review of Cates' model, followed by descriptions of currently understood polymer relaxation mechanisms, and ending with the mathematics underlying our simulation method. Section IV describes the computational part of our method in detail, including the pointer algorithm, and the genetic algorithm that converts results from the time to the frequency domain. After several simulation tests in Section V, Section VI contains analyses and discussions of relaxation mechanisms, parameters, and compares results from our method with those from Cates' model using two different procedures. At the end of Section VI, our simulation method is applied to experimental data to estimate characteristic parameters of some experimental semi-dilute micellar solutions. Conclusions and future work are presented in Section VII.

## II. Definitions

To avoid confusion, we first present definitions of following parameters:

1.  $L, L_t, \langle L \rangle$  and  $\langle L_t \rangle$

$L$  is the (contour) length of a specific micelle, while  $L_t$  is the corresponding tube length. The relationship between tube length and micelle (contour) length can be found in the next section. Here,  $\langle \cdot \rangle$  denotes an ensemble average over the distribution of micelle lengths or tube lengths.

2.  $\tau_{rep}$  and  $\bar{\tau}_{rep}$

Here,  $\tau_{rep}$  is the characteristic reptation time for a micelle of length  $L$  and curvilinear diffusion coefficient  $D_c$ , given in Eq. (2.12).  $\bar{\tau}_{rep}$  is the value of  $\tau_{rep}$  for a micelle of average

length  $\langle L \rangle$ . In general, an overbar means that the given micelle parameter is evaluated for a micelle of length  $\langle L \rangle$ .

### 3. $a$ and $d$

Here  $a$  is the tube diameter, while  $d$  is the micelle diameter.

### 4. $b_K$ and $l_p$

The Kuhn length ( $b_K$ ) is defined using:

$$\langle R^2 \rangle_0 = N_K b_K^2 = b_K L = a L_t \quad (2.1)$$

where  $\langle R^2 \rangle_0$  is the mean-square end-to-end distance of a micelle and  $N_K$  is the number of Kuhn steps in the micelle. Note that the persistence length ( $l_p$ ) is equal to  $b_K/2$ .

### 5. $Z$ and $Z_t$

$Z$  is the number of entanglements for a micelle with length  $L$ , while  $Z_t$  donates the ratio of micelle tube length to the entanglement length ( $l_e$ ):

$$Z \equiv \frac{L}{l_e}, \quad Z_t \equiv \frac{L_t}{l_e} \quad (2.2)$$

Here the entanglement length  $l_e$  is the length of micelle per entanglement. We discuss later how to estimate this.

### 6. $\xi$ , $\zeta$ , $\zeta$ , and $\zeta_K$

Here  $\xi$  is the excluded volume screening length (or blob/mesh size), which has units of length and in a good solvent is related to the persistence length and entanglement length by [Cates (1988); Granek and Cates (1992)]:

$$\xi = l_p^{0.4} l_e^{0.6} \quad (2.3)$$

The dimensionless breakage rate  $\zeta$  is a ratio of two time constants, namely the breakage time to the reptation time, given in Eq. (2.6). The drag coefficient per unit micelle length  $\zeta$  is given by [Morse (1998)]:

$$\zeta = \frac{2\pi\eta_s}{\ln(\xi/d)} \quad (2.4)$$

Finally,  $\zeta_K$  is the drag coefficient per micelle Kuhn step with units of force per unit velocity, which is related to  $\zeta$  by Eq. (2.5). Note that both of these drag coefficients are used in this paper.

$$N_K \zeta_K = \zeta L \quad (2.5)$$

### 7. $\bar{\tau}_{br}, \tau, \tau_R$ and $\tau_e$

Here,  $\bar{\tau}_{br}$  is the average micelle breakage time, and is related to the average micelle reptation time ( $\bar{\tau}_{rep}$ ) by the dimensionless breakage rate  $\zeta$ :

$$\zeta \equiv \frac{\bar{\tau}_{br}}{\bar{\tau}_{rep}} \quad (2.6)$$

We take  $\tau$  to be the stress relaxation time, defined as the inverse of the crossover frequency ( $\omega_{cross}$ ) of the storage modulus ( $G'$ ) with the loss modulus ( $G''$ ).  $\tau_R$  is Rouse rotational time given by:

$$\tau_R = \frac{\zeta_K N_K^2 b_K^2}{3\pi^2 k_B T} \quad (2.7)$$

Here, again,  $\zeta_K$  is drag coefficient per Kuhn step;  $k_B$  is Boltzmann's constant; and  $T$  is the temperature. The equilibration time ( $\tau_e$ ) is the Rouse time of a chain segment between entanglements. For monodisperse chains, the relationships [Larson *et al.* (2003)] among  $\tau_{rep}, \tau_e$  and  $\tau_R$  are given by:

$$\tau_{rep} = 3Z\tau_R = 3Z^3\tau_e \quad (2.8)$$

All these time constants will be used in this paper.

### 8. $\alpha_e$

The semi-flexibility factor  $\alpha_e$  is defined as the ratio of entanglement length to persistence length:

$$\alpha_e \equiv \frac{l_e}{l_p} \quad (2.9)$$

Note in the early work of Cates [Cates (1987)], the parameter  $\alpha$  ( $\equiv \bar{Z}^{-1}$ ) was introduced to approximate the influence of contour length fluctuations (CLFs), which were called ‘‘breathing fluctuations’’.

## III. Theory

Here we first briefly review the tube model and reptation theory.

## 1. Tube model and reptation theory

In the well-entangled regime, the motion of an individual chain-like molecule is confined to a “tube”-like region by topological constraints imposed by its neighbors [Dealy and Larson (2005); Doi and Edwards (1986)]. The tube length is no greater than the chain length and the so-called tube diameter ( $a$ ) is the length of a tube segment or a “tube Kuhn length”. For the so-called “loosely” and “tightly entangled” regimes (defined shortly),  $a$  is determined by the entanglement length ( $l_e$ ):

$$\text{Loose entanglements: } a^2 = N_e b_K^2 = 2l_e l_p \quad (2.10a)$$

$$\text{Tight entanglements: } a = l_e \quad (2.10b)$$

Here,  $N_e$  is the number of Kuhn steps in a single tube segment. By combining Eq. (2.1) with Eq. (2.10a), we can obtain an important relationship involving tube length ( $L_t$ ) and chain length ( $L$ ) for the loosely entangled regime:

$$l_e L_t = aL \quad (2.11)$$

In the tube, a micelle “chain” can alter its conformation by diffusing along the curvilinear path of the tube, which is a process known as “reptation” [de Gennes (1979)]. Any part of the chain that diffuses out of the tube instantly achieves an equilibrium conformation. (While this is not strictly true in the tight entanglement limit, wormlike micelles are typically close enough to being loosely entangled, and are long enough, that this approximation is a reasonable one even for tightly entangled micelles.) The reptation time and curvilinear diffusion coefficient  $D_c$  of a chain with length  $L$  are given by

$$\tau_{rep} = \frac{L_t^2}{\pi^2 D_c}, \quad D_c \equiv \frac{D_0}{L}, \quad D_0 = \frac{k_B T}{\zeta} \quad (2.12)$$

where  $D_0$  and  $\zeta$  are the diffusivity and drag coefficient per unit length of chain, respectively.

With these parameters, the fraction of tube remaining occupied at a time  $t$  after a small step deformation, which is proportional to the fraction of remaining stress ( $\mu$ ), for pure reptation, is:

$$\mu(t) = \frac{8}{\pi^2} \sum_{p=odd} p^{-2} \exp\left(\frac{-tp^2}{\tau_{rep}}\right) \quad (2.13)$$

The detailed derivation can be found in Doi and Edwards (1986). However, Eq. (2.13) is only accurate for monodisperse chains, and this formula assumes a fixed contour length and neglect of other high frequency motions [Likhtman and McLeish (2002)].



## 2. Cates' model

In 1987 Cates [Cates (1987)] put forward a model to address the “living” feature of micelle chains within the framework of tube model and reptation dynamics. The model successfully explained the nearly single-exponential shape of the stress relaxation function  $\mu(t)$  for simple surfactants that form wormlike micelles such as cetyltrimethylammonium (CTA) surfactants [Turner and Cates (1991); Lequeux (1992)]. The original Cates' model rests on several assumptions [Cates (1987); Candau *et al.* (1989)], namely:

- i. Micelles break with a uniform probability per unit length. The corresponding average breakage time ( $\bar{\tau}_{br}$ ) is defined as the lifetime of a micelle with average length  $\langle L \rangle$  :

$$\bar{\tau}_{br} = \frac{1}{k\langle L \rangle} \quad (2.14)$$

where  $k$  is the breakage rate per unit length. ii. Successive breakage and rejoining events are uncorrelated, and breakage is unimicellar while rejoining is bi-micellar. iii. Micelle relaxation occurs through reptation. iv. Tube rearrangement or constraint release (CR) is neglected.

Consistent with the above assumptions, the equilibrium statistical mechanics, based on a free energy containing translational entropy, and an end-cap free energy that is independent of micelle length, yields the following micellar length distribution [Cates (1987)]:

$$N(L) = \frac{k}{k'} \exp\left(\frac{-L}{\langle L \rangle}\right), \quad \frac{k}{k'} = \frac{\rho}{2\langle L \rangle^2} \quad (2.15a)$$

$$\rho = \int_0^{\infty} LN(L)dL \quad (2.15b)$$

Here  $N(L)dL$  is the number density of micelles with length  $L \pm dL/2$ ;  $\rho$  is the contour length of micelles per unit volume of solution;  $k$  is the rate constant for breakage; and  $k'$  is the rate constant for rejoining. See the original paper of Cates [Cates (1987)] for details.

According to assumptions iii and iv, the original Cates' model limits relaxation mechanisms of micelles to reptation assisted by breakage and rejoining. Note that by breaking, new ends are created, which helps to accelerate relaxation by reptation. For  $\bar{\tau}_{br} \gg \bar{\tau}_{rep}$ , breakage is slow compared to reptation, and the relaxation is dominated by reptation of polydisperse micelles; while for  $\bar{\tau}_{br} \ll \bar{\tau}_{rep}$ , the relaxation is controlled by the interplay of breakage/rejoining with reptation, which yields a nearly mono-exponential decay with stress relaxation time ( $\tau$ ):

$$\tau \sim \bar{\tau}_{rep} \zeta^{0.5}, \quad \zeta = \frac{\bar{\tau}_{br}}{\bar{\tau}_{rep}} \ll 1 \quad (2.16)$$

Thus, when Eq. (2.16) applies, the approximate single exponential relaxation produces a nearly semicircular ‘‘Cole-Cole’’ cross-plot of loss modulus ( $G''$ ) against storage modulus ( $G'$ ). Nevertheless, in experiments, an increase of  $G''$  is always observed after a minimum is reached on the right side (i.e., the high frequency side) of the Cole-Cole plot [Granek (1994)], implying that additional relaxation mechanisms are present at high frequencies. Cates and co-workers therefore added ‘‘breathing fluctuations’’ or contour length fluctuations (CLFs), which describe time dependent changes in the length of the tube contour.

The timescale of these ‘‘breathing fluctuations’’ relative to reptation is set by  $\bar{Z}$ , the number of entanglements for a micelle with average length  $\langle L \rangle$ , according to

$$\bar{\tau}_{breath} \sim \bar{Z}^{-1} \bar{\tau}_{rep} \quad (2.17a)$$

The stress relaxation time, when ‘‘breathing’’ is able to relax the entire wormlike micelle before reptation can, is given by:

$$\tau \sim \bar{\tau}_{rep} \bar{Z}^{-0.5} \zeta^{0.5}, \quad \zeta \leq \bar{Z}^{-3} \quad (2.17b)$$

An intermediate regime between breathing-dominated and reptation-dominated relaxation occurs when  $\zeta$  is comparable to  $\bar{Z}^{-1}$ :

$$\tau \sim \bar{\tau}_{rep} \bar{Z}^{0.25} \zeta^{0.75}, \quad \bar{Z}^{-3} \leq \zeta \leq \bar{Z}^{-1} \quad (2.17c)$$

To sum up, stress relaxation times under different conditions are given below:

$$\left\{ \begin{array}{l} \tau \sim \bar{\tau}_{rep}, \quad \zeta \geq 1 \\ \tau \sim \bar{\tau}_{rep} \zeta^{0.5}, \quad \bar{Z}^{-1} \leq \zeta \leq 1 \\ \tau \sim \bar{\tau}_{rep} \bar{Z}^{0.25} \zeta^{0.75}, \quad \bar{Z}^{-3} \leq \zeta \leq \bar{Z}^{-1} \\ \tau \sim \bar{\tau}_{rep} \bar{Z}^{-0.5} \zeta^{0.5}, \quad \zeta \leq \bar{Z}^{-3} \end{array} \right.$$

Note that the above formulas can be found in reference [Cates (1987)] except that we have replaced  $\alpha$  by its equivalent,  $\bar{Z}^{-1}$ .

By incorporating ‘‘breathing’’ along with high-frequency Rouse modes [Granek and Cates (1992); Granek (1994)], the deviation from a perfect semicircle at high frequency can be used to estimate the ratio of micelle entanglement length ( $l_e$ ) to average length ( $\langle L \rangle$ ):

$$\frac{G''_{min}}{G_N} = \left( \frac{l_e}{\langle L \rangle} \right)^{0.8} = \bar{Z}^{-0.8} \quad (2.18)$$

Here,  $G_N$  is the plateau modulus and  $G''_{min}$  is the local minimum of  $G''$  in the Cole-Cole plot at high frequency. Note that for micelle solutions with  $\bar{Z}^{-3} \leq \zeta \leq \bar{Z}^{-1}$ , as  $\zeta$  decreases, the minimum gets shallower [Cates (1987); Granek and Cates (1992); Granek (1994)]

until  $\zeta$  becomes comparable to  $\bar{Z}^{-3}$ , which only occurs for micelles with a large number of entanglements ( $\bar{Z}$ ).

Besides adding high frequency relaxation dynamics into the original model, Granek and Cates [Granek and Cates (1992)] also developed a simulation method based on the ‘‘Poisson renewal process.’’ By neglecting correlations of micelle length between breakage/rejoining events and assuming that micelle lengths follow a Poisson distribution (Eq. (2.15)), the relaxation modulus  $G(t)$  for wormlike micellar solutions can be described by extending Eq. (2.13) to polydisperse lengths. Using numerical simulations, the following stress relaxation time was obtained [Granek and Cates (1992)]:

$$\tau = 0.69\bar{\tau}_{rep}(\zeta^{1/2} + C\zeta^{2/3}) \quad (2.19)$$

where  $C$  is a correction coefficient accounting for effect of high frequency relaxation dynamics.

### 3. Experimental measurements and limitation of Cates’ model

Experimental characterization of micelle structure has significantly contributed to the development of the theory of thread-like micelle dynamics. The value of the persistence length was measured by Porte and coworkers [Porte *et al.* (1980)], who showed that elongated micelles should be thought of as semi-flexible polymer-like chains, rather than as rods. Since then, many important measurement methods have been applied to micellar solutions: SANS (small angle neutron scattering) [Marignan *et al.* (1989); Appell and Marignan *et al.* (1991)], birefringence [Shikata *et al.* (1994); Decruppe and Lerouge (1999)], DLS/SLS (dynamic/static light scattering) [Brown *et al.* (1989); Nemoto *et al.* (1995)], cryo-TEM (cryogenic transmission electron microscopy) [Clausen *et al.* (1992)], NSE (neutron spin echo) [Nettesheim and Wagner (2007)] and DWS (diffusing wave scattering) [Galvan-Miyoshi *et al.* (2008)]. Table 1.1 shows that the measured persistence lengths are typically in the range 20-50 nm, and the micelle diameter is approximately 4 nm.

Although these measurements supply inputs to Cates’ model, its predictive ability is limited by some shortcomings:

A. The average micelle length is not readily obtained from the above methods, and the value extracted from rheological data using Cates’ model is usually a fraction of a micron, which is shorter than one would expect based on the rather high value of micelle scission energy [Larson (2011)]. B. The model does not account for the effects of the persistence length ( $l_p$ ), nor

allow it to be estimated from rheological properties [Oelschlaeger *et al.* (2010)]. *C.* The accuracy of rheological predictions is questionable for solutions in the crossover region between “loose” and “tight” entanglements, as discussed below. *D.* The treatment of high frequency relaxation mechanisms is over-simplified and lacks consideration of micelle bending modes. *E.* The correlation of micelle length after a breakage/rejoining with that before such an event is neglected. *F.* Constraint release or tube rearrangement is neglected.

Table 2.1 Experimental values of  $l_p$  and  $r_{cS}$  from the literature.

Literature	Method	System	$l_p$ (nm)	$d/2$ (nm)
Marignan <i>et al.</i> (1989)	SANS	CPyBr/NaBr	~	1.85-2.4
Appell <i>et al.</i> (1991)	SANS	CPyClO <sub>3</sub> /NaBr	17±5	2±0.1
Gamez-Corrales <i>et al.</i> (1999)	SANS	CTAT/NaCl	38±2	2.1±0.05
Magid <i>et al.</i> (2000)	SANS	CTA26CIBz+CTAC/Na26CIBz+NaCl	17-34	1.76-2.25
Croce <i>et al.</i> (2003)	SANS	EHAC/KCl	~	2.1
Schubert <i>et al.</i> (2003)	SANS	CTAT+SDBS/NaTosylate	20-85	2.12-2.16
Kuperkar <i>et al.</i> (2008)	SANS	CTAB/NaNO <sub>3</sub>	~	2.28
Porte <i>et al.</i> (1980)	Birefringence	CPyBr/NaBr	20	3
Shikata <i>et al.</i> (1994)	Birefringence	CTAB/NaSal,	26	~
Appell <i>et al.</i> (1982)	SLS	CPyBr/NaBr	20±5	~
Imae <i>et al.</i> (1986)	SLS	CTAB/NaBr	42-53	2.3
Brown <i>et al.</i> (1989)	DLS	CTAB/Naphthalenesulfonate	36	~
Imae (1990)	DLS	C <sub>16</sub> TASal/NaSal	111-142	~
Nettesheim <i>et al.</i> (2007)	NSE	CTAB/NaSal	24	~
Willenbacher <i>et al.</i> (2007)	DWS	CPyCl/NaSal	31-34	~
Galvan <i>et al.</i> (2008)	DWS	CTAB/NaSal	29-45	~
Oelschlaeger <i>et al.</i> (2009)	DWS	CPyCl/NaSal	26-30	~
Oelschlaeger <i>et al.</i> (2010)	DWS	CTAB/KBr, CTAB/NaNO <sub>3</sub> , CTAB/NaClO <sub>3</sub>	40, 34, 29	~

Thus, an improved theory is desirable. In what follows, we present a more detailed description of micelle relaxation processes, and a simulation method that accounts for these details.

## 4. Relaxation theory

### A. Contour length fluctuations (CLFs)

Contour length fluctuations (CLFs) are Rouse-like fluctuations that allow the chain to wrinkle and un-wrinkle in its tube, vacating ends of the tube and relaxing stress [Dealy and

Larson (2005)]. CLFs lead to a shortening of reptation time ( $\tau_{rep}^F$ ), as estimated by Doi and Edwards (1986):

$$\tau_{rep}^F \approx \tau_{rep}^{NF} \left(1 - \frac{1.47}{\sqrt{Z}}\right)^2 \quad (2.20)$$

In the above, the superscript “*NF*” denotes the pure reptation, while “*F*” denotes the CLF-affected reptation. We note here that a more accurate expression (Eq. (2.21)) was derived by Likhtman and McLeish (2002):

$$\frac{\tau_{rep}^F}{\tau_{rep}^{NF}} = 1 - \frac{2C_1}{\sqrt{Z}} + \frac{C_2}{Z} + \frac{C_3}{Z^{1.5}} \quad (2.21)$$

where  $C_1 = 1.69$ ,  $C_2 = 4.17$ ,  $C_3 = -1.55$ .

Beyond this simple correction of the reptation time, Milner and McLeish (1998) developed a mathematical expression that accounts for the time-dependent relaxation produced by CLFs. By treating a linear chain as a two-armed star with fixed center, they obtained the following relationship for the shrinkage of the un-relaxed tube as a function of time:

$$\langle l_t^2 \rangle = \frac{4N_K b_K^2}{3\pi^{1.5}} \left(\frac{t}{\tau_R}\right)^{0.5} \quad (2.22)$$

Here  $l_t$  is the lost tube length at each end through fluctuations, and the brackets  $\langle \cdot \rangle$  denote an ensemble average. However, this formula leaves out the shrinkage of tube due to reptation, which becomes ever more important as relaxation progresses. To include contributions from both reptation and CLFs, we first take a time derivative of both sides of Eq. (2.22), and then use Eq. (2.22) to replace time  $t$  on the right side with  $\langle l_t^2 \rangle$ , giving:

$$\frac{d\langle l_t^2 \rangle}{dt} = \frac{8b_K^2 k_B T}{3\pi \zeta_K \langle l_t^2 \rangle} \quad (2.23)$$

where the definition of Rouse time ( $\tau_R$ ) (Eq. (2.7)) has been used in deriving the above equation. Substituting Eqs. (2.1), (2.5), and (2.12) into Eq. (2.23) yields:

$$\frac{d\langle l_t^2 \rangle}{dt} = \frac{16D_0 l_p}{3\pi \langle l_t^2 \rangle} \quad (2.24)$$

The advantage of Eq. (2.24) over Eq. (2.22) is that the former doesn't contain time  $t$  explicitly as Eq. (2.22) does, but instead describes the rate of loss of occupied tube due to CLFs. This allows us to add this rate to the rate of loss of tube length through reptation, as we describe later.

### B. Constraint release (CR)

In addition to the above mechanisms, chain relaxation can also occur due to motion of the surrounding chains, i.e., due to constraint release (CR). Because of its complexity, no general, rigorous theory has been developed for CR, especially for micelles or “living polymers” with breakage and rejoining kinetics. However, a simple model of CR, called double reptation [Dealy and Larson (2005)], has been found to capture much of its effect in ordinary polymers, especially when the length distribution is polydisperse, which is always the case for micellar solutions. Double reptation gives the following simple formula [Tuminello (1986); Tsenoglou (1987); des Cloizeaux (1988); Dealy and Larson (2005)] for CR effect on relaxation modulus ( $G(t)$ ):

$$G(t) = G_N \mu^2(t) \quad (2.25)$$

where  $\mu(t)$  is the relaxation function or the probability for a single chain to relax in a fixed entanglement matrix; i.e., in the absence of CR. Thus, as a simple but effective treatment of CR effects, double reptation is incorporated in our method.

### C. Rouse modes

For entangled solutions, long-range Rouse motions for monomers are impeded by topological constraints; the contribution of Rouse motions is thereby confined to a distance of order  $l_e$  along the chain. At such short length scales, its contribution is only significant at high frequencies. These high-frequency Rouse motions result in the following contributions to  $G'$  and  $G''$  [Wang *et al.* (2010)]:

$$G'(\omega) = G_N \frac{5(\omega\tau_e)^2}{4} \sum_i \frac{\phi_i}{Z_i} \sum_{p=Z_i}^{N_e Z_i} \frac{1}{(\omega\tau_e)^2 + 4\left(\frac{p}{Z_i}\right)^4} \quad (2.26a)$$

$$G''(\omega) = G_N \frac{5\omega\tau_e}{4} \sum_i \frac{\phi_i}{Z_i} \sum_{p=Z_i}^{N_e Z_i} \frac{2(p/Z_i)^2}{(\omega\tau_e)^2 + 4(p/Z_i)^4} \quad (2.26b)$$

where  $\phi_i$  is the volume fraction of micelles with length  $L_i$ ;  $\omega$  is the frequency;  $N_e$  is the number of Kuhn steps in a single tube segment ( $l_e/b_K$ ), which is here made an integer by rounding down, and  $\tau_e$  is the equilibration time. In the above,  $p$  is the mode number of the Rouse motions. Note that the lowest mode number for each chain is equal to the number of entanglements  $Z_i$  in the chain, since we are only accounting for Rouse motions localized to within a tube segment, as discussed in reference [Wang *et al.* (2010)]. In both Eqs. (2.26a) and (2.26b), the outer sum is a sum over a discrete distribution of micelle species indexed by “ $i$ ”.

The volume fraction ( $\phi_i$ ) of micelles with length  $L_i$  can be expressed in terms of the number density ( $N(L_i)$ ), where this number density distribution is now taken to be discrete, summing to unity.

$$\phi_i = N(L_i)L_i \frac{\pi d^2}{4} \quad (2.27)$$

#### D. Semi-flexibility and bending modes

##### 1) Entanglement regimes and semi-flexibility

For entangled chains, two different scenarios are depicted in Fig. 2.1 depending on the flexibility: case a) occurs when the chain can form a random-walk coil within a single tube segment of length  $a$ , while for case b) it can only bend slightly over this distance. The above two scenarios are called “loosely” and “tightly” entangled, respectively. Cates assumed that micellar solutions lie in the loosely entangled regime, which we are now finding to be inaccurate for some micellar solutions [Galvan-Miyoshi *et al.* (2008); Oelschlaeger *et al.* (2009); Oelschlaeher *et al.* (2010)].

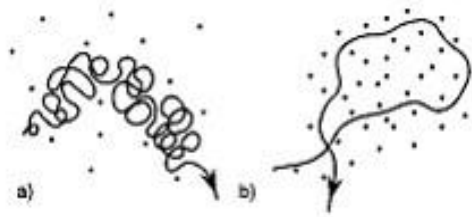


Figure 2.1 Loose and tight entanglement regimes [Reprinted with permission from Morse (1998a). Copyright 1998 American Chemical Society]

Therefore, in this paper both loosely and tightly entanglements are handled more carefully by introducing the parameter ( $\alpha_e$ ), which is the ratio of entanglement length to persistence length, as given by Eq. (2.9). Thus, in the loosely entangled regime ( $\alpha_e > 2$ ), the tube diameter ( $a$ ) is larger than the Kuhn length ( $b_K$ ). For the tightly entangled regime ( $\alpha_e < 1$ ),  $a$  is less than the persistence length ( $l_p$ ). And we take the crossover between these regimes to occur within the range  $1 \leq \alpha_e \leq 2$ . By applying Eqs. (2.10) and (2.11), the relationships between the micelle length ( $L$ ) and its corresponding tube length ( $L_t$ ) for these regimes are:

$$L_t \approx L, \quad \alpha_e < 2 \quad (2.28a)$$

$$L_t \approx L / \sqrt{0.5\alpha_e}, \quad \alpha_e > 2 \quad (2.28b)$$

Thus, in both the tight entanglement and crossover regimes ( $\alpha_e < 2$ ), the tube length is approximately equal to the micelle length.

Although the plateau modulus ( $G_N$ ) is often determined empirically by doubling the value of measured modulus at the crossover of  $G'$  and  $G''$  [Couillet *et al.* (2004)], it can also be calculated theoretically. In the loosely entangled regime,  $G_N$  can be derived from blob theory [Khatory *et al.* (1993); Heo *et al.* (2005)]:

$$G_N = A \frac{k_B T}{\xi^3} \quad (2.29)$$

where  $\xi$  is the mesh size (See Eq. (2.3)). Here we introduce a prefactor  $A$  which is absent from the original equation in Cates' paper [Turner and Cates (1991)]. The theoretical derivation of its value  $A = 9.75$  from established correlations for loosely entangled polymers is given in *Appendix A*.

On the other hand, in the tight entanglement regime  $G_N$  is given by [Morse (1998)]:

$$G_N = \frac{7}{5} \frac{\rho k_B T}{l_e} \quad (2.30)$$

where, as defined earlier,  $\rho$  is the micelle contour length per unit volume, which is related to micelle diameter ( $d$ ) and surfactant volume fraction ( $\phi$ ) by:

$$\rho = \frac{4\phi}{\pi d^2} \quad (2.31)$$

Since in many cases, micellar solutions lie between the tight and loose entanglement regimes, we here present a crossover formula to obtain the plateau modulus for any ratio ( $\alpha_e$ ) of entanglement length to persistence length, namely:

$$G_N = f(\alpha_e) \cdot 9.75 \frac{k_B T}{\alpha_e^{9/5} l_p^3} + [1 - f(\alpha_e)] \cdot \frac{28}{5\pi} \frac{\phi k_B T}{d^2 \alpha_e l_p} \quad (2.32a)$$

In the above, we take the weight function  $f(\alpha_e)$  to be:

$$f(\alpha_e) = \frac{\alpha_e^n}{n + \alpha_e^n} \quad (2.32b)$$

where the value  $n$  sets the steepness of the cross-over between the formulas for loose and tight entanglements (Eqs. (2.29) and (2.30)). Here, we set  $n = 3$  to give a relatively rapid, but smooth, crossover, as shown in Fig. 2.2 We note that at higher concentrations where one enters the tight entanglement regime, one might not expect the blob theory to be applicable. But the crossover formula, Eq. (2.32a), is designed to transition away from the prediction of the blob theory (Eq.



29) to that for tight entanglements (Eq. (2.30)) as the entanglements become tight, so the failings of the blob theory at high concentration should have negligible impact.

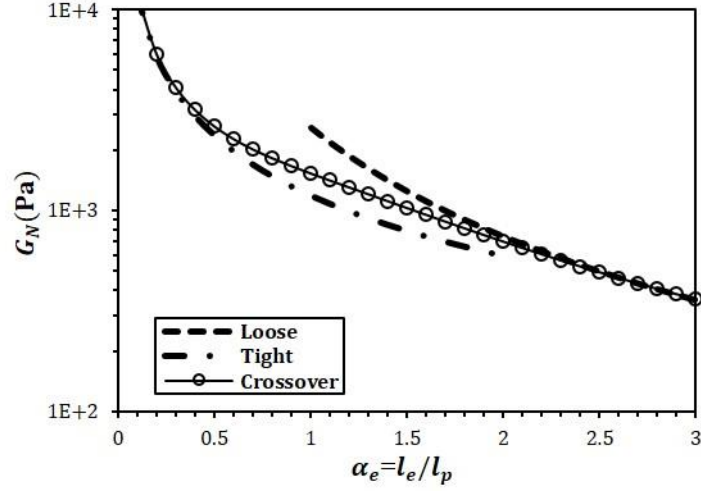


Figure 2.2 Plateau modulus for loose and tight entanglement regimes and the crossover between them (for  $T = 300\text{K}$ ,  $l_p = 25\text{nm}$ , and  $d = 5\text{nm}$ ).

## 2) Bending modes

The relaxation dynamics introduced in parts i through iii involve length scales larger than persistence length ( $l_p$ ), for which chains are flexible and high frequency relaxation dynamics is governed by Rouse modes. However, on length scales smaller than  $l_p$ , chain segments are effectively elastic rods [Morse (1998)], whose dynamics are governed by bending motions whose elastic modulus  $B(\omega)$  [Morse (1998); Pasquali *et al.* (2001)] was given by Morse and Macintosh [Morse (1998); Gittes and MacKintosh]:

$$B(\omega) = \frac{2^{3/4} k_B T}{l_p} (i\omega\tau_p)^{3/4}, \quad \tau_p = \frac{\zeta_{\perp} l_p^3}{k_B T} \quad (2.33a)$$

where  $\zeta_{\perp}$  is drag coefficient for perpendicular bending motion, given by Batchelor as [Batchelor (1971); Morse (1998)]:

$$\zeta_{\perp} = \frac{4\pi\eta_s}{\ln(0.6\xi/d)} \quad (2.33b)$$

Due to the short length scales over which it contributes to the modulus, bending is only important at frequencies ( $\omega > 1/\tau_p$ ) higher than those for flexible Rouse motions. Thus, contributions to the storage and loss modulus from bending motions are:

$$G'(\omega) = \text{Re} \left[ \frac{B(\omega) \cdot \rho}{15} \right], \quad G''(\omega) = \text{Im} \left[ \frac{B(\omega) \cdot \rho}{15} \right] + \omega \eta_s \quad (2.34)$$

where the definition of  $\rho$  is given by Eq. (2.31). Equations (2.33) and (2.34) yield a three-quarter power law for  $G''$  at high frequency, which has been confirmed experimentally by both Oelschlaeger's and Galvan's groups [Oelschlaeger *et al.* (2009); Galvan-Miyoshi *et al.* (2008); Oelschlaeger *et al.* (2010)].

## 5. Functional form of the modulus

The aim of our simulation method described in the following section is to predict linear viscoelasticity from micelle parameters, and, inversely, to devise a method to determine those parameters from rheological data. The latter methodology is valuable because some parameters are difficult to obtain from non-rheological measurements [Nettesheim and Wagner (2007); Schubert *et al.* (2003); Galvan-Miyoshi *et al.* (2008); Clausen *et al.* (1992); Shikata *et al.* (1994); Brown *et al.* (1989); Nemoto *et al.* (1995); Oelschlaeger *et al.* (2010); Appell *et al.* (1982); Willenbacher *et al.* (2007); Croce *et al.* (2003); Magid *et al.* (2000); Imae (1990); Imae and Ikeda (1986)]. Based on the relaxation mechanisms introduced above, the rheology of wormlike micellar solutions is controlled by five *independent* micelle parameters which can be taken to be: plateau modulus ( $G_N$ ), dimensionless breakage rate ( $\zeta$ ), average micelle length ( $\langle L \rangle$ ), semi-flexibility coefficient ( $\alpha_e$ ), and micelle diameter ( $d$ ). Detailed information about them and how other parameters, such as time scales, are derived from them, can be found in previous sections. Thus, with the above five *independent* parameters the functional form of the complex modulus  $G^*$  can be expressed as:

$$G^*(\omega) = \mathcal{F}[G_N \mu^2(t, \zeta, \langle L \rangle, \alpha_e, d)] + G^H(\omega) \quad (2.35)$$

Here the real and imaginary parts of  $G^*(\omega)$  are the storage ( $G'$ ) and loss ( $G''$ ) moduli, respectively. The dimensionless stress relaxation function  $\mu$  (fraction of un-relaxed tube segments in the absence of CR) is squared to allow for constraint release according to the “double reptation” ansatz (Eq. (2.25)).  $G^H(\omega)$  accounts for contributions from high frequency Rouse and bending modes (Eq. (2.26) and Eq. (2.34)), and also depends on the five parameters listed above. In practice, we only add these high frequency modes after we have Fourier transformed (denoted by operation  $\mathcal{F}[\cdot]$  in Eq. (2.35)) the time-dependent function into the frequency-dependent one. Note that the effect of experimental conditions (temperature  $T$ ,

surfactant volume fraction  $\phi$  and solvent or water viscosity  $\eta_s$ ) are implicitly included among the model parameters, although we don't count them among the five parameters listed above.

For use in what follows, we define in Table 2.2 a set of “standard” values of parameters to be used in example simulations.

Table 2.2 “Standard” values of parameters.

Section	Experimental conditions			Model parameters				
	$T$ (K)	$\phi$	$\eta_s$ (cP)	$l_p$ (nm)	$\zeta$	$\langle L \rangle$ (nm)	$\alpha_e$	$d$ (nm)
IV-3	300	0.1	0.891	15	0.005	$80l_p$	3	3
VI	300	0.1	0.891	25	0.05	$80l_p$	2	5

Note that persistence length ( $l_p$ ) can be used to obtain the plateau modulus ( $G_N$ ) once other micelle parameters ( $\zeta$ ,  $\langle L \rangle$ ,  $\alpha_e$  and  $d$ ) as well as temperature  $T$  and surfactant volume fraction  $\phi$  are known (see Eq. (2.32)).

## IV. Modeling

### 1. Polydispersity

In thermal equilibrium, wormlike micelles are polydisperse in length. Two simple approaches, i.e.: *A.* mean-field theory (MFT) and *B.* scaling theory, give relationships between average micelle length ( $\langle L \rangle$ ) and scission free energy ( $E$ ) [Cates (1988); Candau *et al.* (1989); Cates and Candau (1990)]:

$$\langle L \rangle_{MFT} = \phi^{0.5} \exp(E/2k_B T) \quad (2.36a)$$

$$\langle L \rangle_{scaling} \cong \phi^{0.6} \exp(E/2k_B T) \quad (2.36b)$$

The scaling result differs from that for MFT because of its inclusion of the excluded volume repulsion. Unfortunately, the above two equations cannot readily be used to extract average micelle length, since  $E$  is hard to determine from experiments.

In our simulation method, the exponential micelle length distribution (see Eq. (2.15)) is discretized into segments with segment length  $\Delta L \sim O(l_p)$ . The discretized distribution function relates the micelle length ( $m_i \Delta L$ , with  $m_i$  the number of segments in the micelle) to the corresponding number  $n_i$  of micelles with this length:

$$n_i = \text{Int}[num \cdot \exp(-m_i/M)] \quad (2.37)$$

Here “Int” is the integer function which rounds the argument down to nearest integer,  $num$  ( $num = 10,000$ ) is the total number of micelles in the simulation ensemble;  $M$  is the number of segments for a micelle with average length, so that  $m_i$  varies from 1 to several times  $M$ .

Note  $n_i, M, m_i, i$  are all integers in our simulation method, with the value of  $m_i$  determined by minimizing the error between continuous and discrete micelle length distributions.

## 2. Pointer algorithm

### A. Motivation

Since breakage/rejoining of micelles accelerates relaxation by creating new un-relaxed micelle ends, an appropriate treatment of micellar breakage/rejoining is the key element for any model of wormlike micellar solutions. In 1987, Cates [Cates (1987)] developed a particle diffusing method coupled with random end-hop processes to describe breakage/rejoining of micelles (See Fig. 2.3). His method is efficient, if only the curvilinear diffusivity (reptation) is included. Further improvements are attained by adding other relaxation dynamics (CLF and Rouse motion). A more sophisticated method was developed by Granek and Cates [Granek and Cates (1992)] in their “Poisson renewal” process, where a survival time for individual micelles is introduced to describe the occurrence of breakage/rejoining events. However, their model does not account for chain length correlations across breakage/rejoining events, nor does it include constraint release, or the crossover to tight entanglements. Thus, improvements are still required.

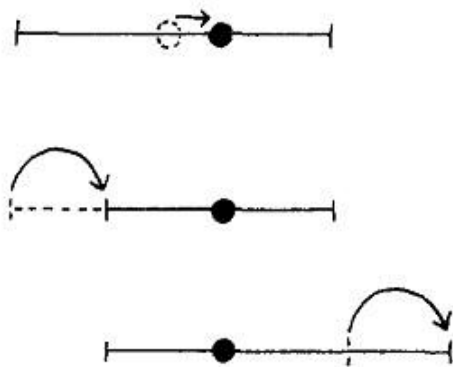


Figure 2.3 Diffusing method with end-hop process [Reprinted with permission from Cates (1987). Copyright 1987 American Chemical Society].

### B. Pointer algorithm

Here, we account for both the “living” feature of micelles and their polymer-like relaxation mechanisms using a large ensemble of around 10,000 wormlike micelles. Rather than dealing with all Kuhn segments in these chains, it is more efficient to track only the locations of pointers that separate the un-relaxed from the relaxed segments along a discretized micelle, as

illustrated in Fig. 2.4. Then, by summing the fraction of un-relaxed segments between the pointers for all micelles, the linear stress relaxation function ( $\mu$ ) in the absence of CR can be calculated.

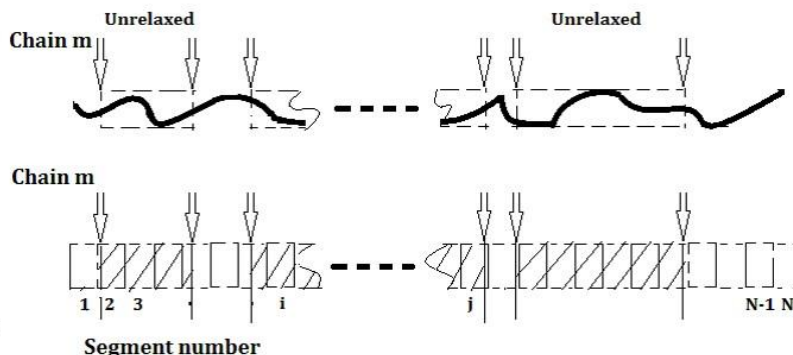


Figure 2.4 Pointers along discretized micelles. The shaded segments are the unrelaxed ones.

### C. Breakage and rejoining with pointer algorithm

With the above pointer algorithm, the breakage and rejoining of micelles can be described as creations and annihilations of pointers. When two chains fuse as shown in Fig. 2.5a, pointers do not disappear but are retained within the fused micelle to indicate the un-relaxed portions of the new, longer micelle. For micellar breakage (See Fig. 2.5b), a new pair of pointers is added, one at each new end created by the breakage. As the simulation proceeds, the number of pointers can increase, but eventually decreases due to the pointer annihilation process: when two pointers meet each other, both are removed, because the portion of the chain between them is completely relaxed. Since short chains relax very rapidly, the total number of pointers in the simulation is not enormous; it is comparable to the number of micelle ends ( $\sim 10,000$ ), which is much smaller than the total number of Kuhn segments ( $\sim 1,000,000$ ) in the micelle ensemble.

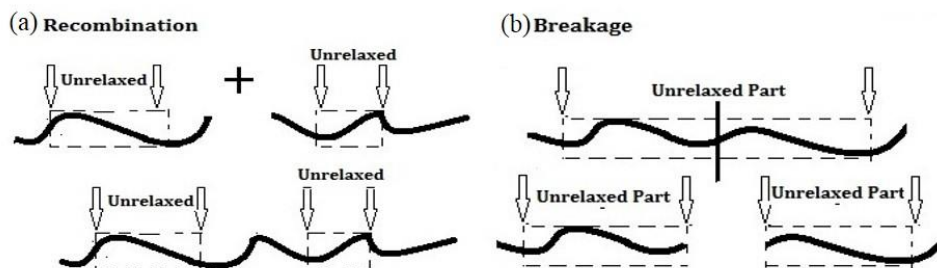


Figure 2.5 Breakage and rejoining depicted by pointer algorithm (a) Rejoining (b) Breakage.

The detailed simulation procedure for breakage and rejoining can be found in Fig. 2.6, where the total number of micelles in the ensemble is allowed to fluctuate. During each time step, every segment is given an equal probability to break. Thus, longer chains are more likely to break. Since rejoining is independent of micelle length, any two chain ends have an equal probability to fuse. To maintain upper and lower bounds on the exponential length distribution during the simulation, the shortest micelles (one-segment chains) are not allowed to break, while the longest micelle is not allowed to fuse with any other micelles. And also no new micelle formed by rejoining is allowed to have length greater than the longest one allowed. The above criterion is sensible since the longest chain breaks very quickly and so is not able to retain its length for very long. Since two sequential breakage/rejoining events cannot be allowed to occur within one time step, the simulation time step should not be larger than the average time required for one micelle in the whole ensemble to break/rejoin, which is:

$$\Delta t \leq \frac{\tau_{br}}{2 \cdot num} = \frac{\zeta \tau_{rep}}{2 \cdot num} \quad (2.38)$$

where  $num = 10,000$  is the total number of micelles in our simulation ensemble.

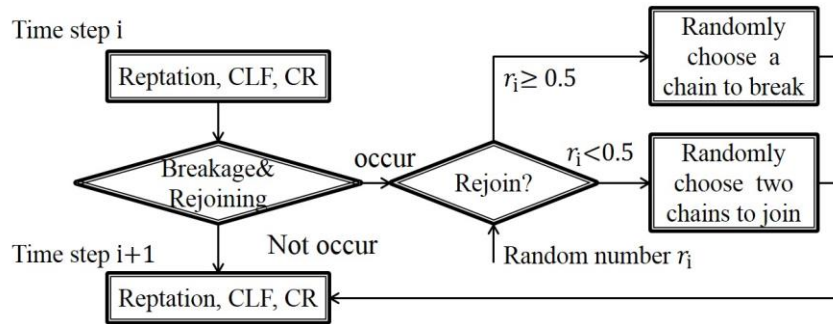


Figure 2.6 Procedure for multiple breakage/rejoining cycles.

The above breakage mechanism is the reversible scission scheme assumed in Cates' original model, as described in section III-2. However, additional “end-interchange” and “bond-interchange” schemes were suggested later by Turner and Cates (1992), which involve “three-arm” and “four-arm” intermediates. Although we do not consider these schemes in this paper, the pointer algorithm can readily be modified to include them as we hope to discuss in a future paper.

#### D. Relaxation with the pointer algorithm

With a pointer on each end of each micelle, the relaxation process induced by reptation is equivalent to the random movement of both two pointers on a micelle in the same direction and by the same amount, whose direction is uncorrelated from one time step to the next (See Fig. 2.7a). The distance ( $\Delta l_R$ ) of such a movement in a single time step is given by:

$$\Delta l_R = \sqrt{2D_c \Delta t} \quad (2.39)$$

Since the effect of contour length fluctuation (CLF) is significant at early times, we include its contribution by adding additional movement ( $\Delta l_F$ ) of the pointers (See Fig. 2.7b). However, Eq. (2.22) cannot be used throughout the simulation because it contains an explicit dependence on time  $t$ , and is not valid when reptation and breakage/rejoining are also occurring. Thus, we normally use Eq. (2.24), and deploy Eq. (2.22) only when Eq. (2.24) breaks down because a pointer reaches the end of a micelle. That is, we use

$$\Delta l_F^2 = \frac{16D_0 l_p \Delta t}{3\pi l^2}, \quad l \geq l_p \quad (2.40a)$$

$$\Delta l_F^2 = \frac{8L l_p}{3\pi^{1.5}} \left(\frac{\Delta t}{\tau_R}\right)^{0.5}, \quad l < l_p \quad (2.40b)$$

Here  $\Delta l_F$  is the CLF-induced additional movement of a pointer, whose sign is chosen always to reduce the size of unrelaxed region of the tube;  $l$  is the length of the relaxed end of a micelle during the current time step. Note that apart from making  $l$  large enough to switch to Eq. (2.40a), equation (2.40b) acts as the initialization for CLF, which has negligible effect on the overall relaxation process.

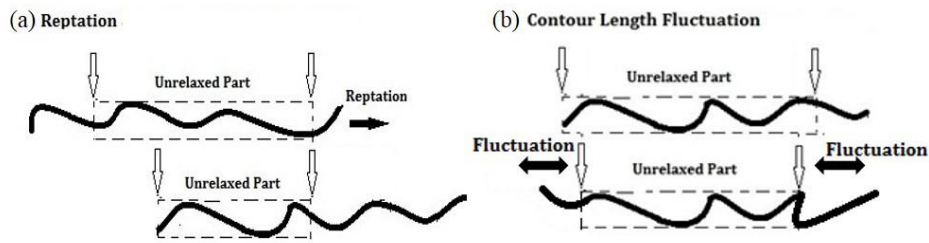


Figure 2.7 Reptation and CLF depicted by pointer algorithm (a) Reptation (b) CLFs.

To increase the accuracy, we apply an iterative method to Eq. (2.40a):

$$\Delta l_{F,i+1}^2 = \frac{16D_0 \Delta t l_p}{3\pi (l_i + \Delta l_{F,i}/2)^2}, \quad l_i \geq \Delta L \quad (2.40c)$$

To calculate  $\Delta l_{F,i+1}$ , 5 iterations are used, which we found gives nearly converged results that are insensitive to the time step.

#### *E. Other relaxation mechanisms (CR, Rouse and bending relaxation modes)*

For constraint release (CR), double reptation is applied according to Eq. (2.25). Since a direct simulation of high frequency behavior would require a tiny time step and huge computational cost, we add analytic forms for the Rouse and bending motions (Eq. (2.26) and Eqs. (2.33), (2.34)) to simulation results after they have been transformed to the frequency domain.

### 3. Genetic algorithm

To reduce the computational cost for post-simulation processing, the data is recorded in logarithmic time intervals, since the simulation data can span across several decades of time with typically millions of time steps. According to Eq. (2.38), the upper bound of the time step depends on the dimensionless breakage rate ( $\zeta$ ). In addition, early-time (high-frequency) behavior needs to be determined precisely, because for micellar solutions the high-frequency regime strongly affects the estimates of important microstructural small-length-scale parameters ( $l_e, l_p$  and  $d$ ), which in turn affect estimates of other parameters. However, the transformation from the time to the frequency domain is a classic ill-posed problem. Here, results (Fig. 2.8) from two traditional methods (classical Fourier transform Eq. (2.41a) and integral smoothing Eq. (2.41b)) are used to illustrate the difficulties with these transformations. The “standard” values of parameters used in this section can be found in Table 2.2.

$$G'(\omega) = G_N \omega \int_0^T \sin(\omega t) \mu(t) dt, \quad G''(\omega) = G_N \omega \int_0^T \cos(\omega t) \mu(t) dt \quad (2.41a)$$

$$G'(\omega) = G_N \int_0^1 \frac{\omega^2 t^2}{1 + \omega^2 t^2} d\mu(t), \quad G''(\omega) = G_N \int_0^1 \frac{\omega t}{1 + \omega^2 t^2} d\mu(t) \quad (2.41b)$$

As shown by Fig. 2.8, the classical Fourier transformation gives good results only at low frequencies ( $\omega < 500$ rad/s), above which large oscillations occur as a result of the ill-posedness of simple integral transform in Eq. (2.41a). On the other hand, although the integral smoothing method works reasonably well for broad distributions of relaxation times [Dealy and Larson (2005)], the height of the  $G''/G_N$  versus  $G'/G_N$  curves is underestimated when the distribution of relaxation times is narrow for small  $\zeta$ . This can be seen by comparing the height of the



normalized Cole-Cole plot in Fig. 8, where  $G''/G_N$  remains below 0.4 for integral smoothing, with that for classical Fourier transformation, where the height exceeds 0.45.

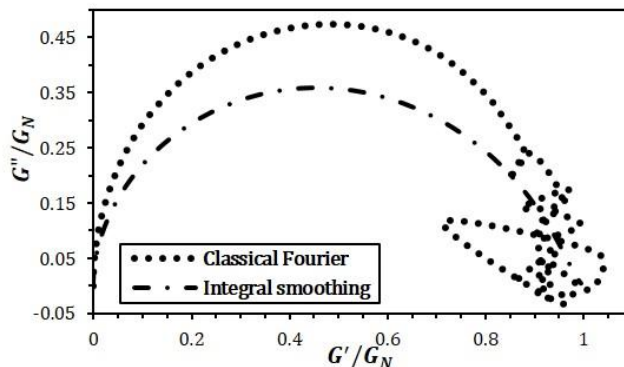


Figure 2.8 Results of two traditional transformation methods for the normalized Cole-Cole plot using standard values of parameters.

Fortunately, there are standard methods for solving ill-posed problems of the kind faced here. Such methods include Monte Carlo methods, annealing algorithms, and genetic algorithms. Here, we choose to develop a genetic algorithm because of its stability, non-locality and insensitivity to initial guess. A more detailed description of our genetic algorithm is given in *Appendix A*, which also shows that our genetic algorithm avoids the problems discussed above.

## V. Simulation Testing

We tested that the model gives the correct equilibrium distribution of micelle lengths, captures the relaxation dynamics of pure reptation and with added contour length fluctuations correctly, and converges with increasing simulation duration and ensemble size. Testing details are given in *Appendix A*.

## VI. Analysis and Discussion

We now address the relationships between rheological predictions ( $G'$  and  $G''$  curves) and the micelle parameters ( $G_N$ ,  $\zeta$ ,  $\langle L \rangle$ ,  $\alpha_e$  and  $d$ ). We will describe both the determination of linear rheology from micelle parameters, and, conversely, the extraction of micelle parameters from measured linear rheological properties. Standard values of parameters, given in Table 2.2, are used in this section. Note that the base of following logarithm functions (denoted as “log”) is 10.

## 1. From micelle parameters to rheology

### A. Simulation procedure

As described by Eq. (2.35), five important *independent* parameters ( $G_N$ ,  $\zeta$ ,  $\langle L \rangle$ ,  $\alpha_e$  and  $d$ ) are necessary to predict the rheology of wormlike micellar solutions over a wide frequency range. With these parameters as inputs, linear rheological behavior is obtained by simulating the time-dependent relaxation of a polydisperse micelle ensemble. A flowchart describing the sequence of calculations, and the flow of inputs and outputs for each calculation, is shown in Fig. 2.9.

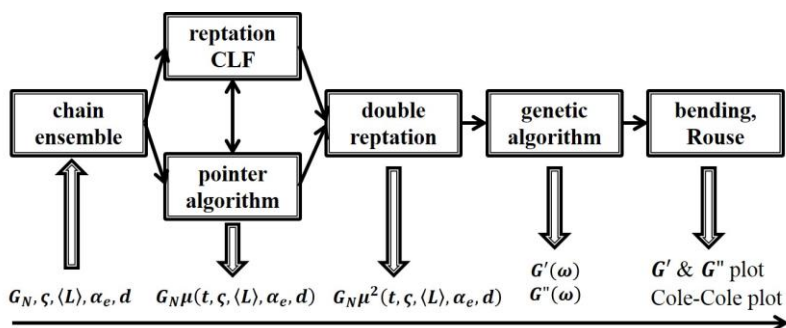


Figure 2.9 Flowchart describing steps in the calculation.

### B. Relaxation mechanisms with breakage/rejoining

By running simulations following the procedure depicted in Fig. 2.9, we can determine the effects of each relaxation mechanism on the rheology. Our simulations show that an increase in the parameter  $\alpha_e$  (ratio of micelle entanglement length to persistence length) speeds relaxation for fixed  $\zeta$  and  $\langle L \rangle$ . The reason is that increase in  $\alpha_e$  allows micelles to form coils within individual tube segments, thus reducing tube length ( $\langle L_t \rangle$ ) through Eq. (2.28), which speeds relaxation.

Since the characteristic time ( $\tau_R$ , Eq. (2.7)) for contour length fluctuations (CLFs) is typically 1~2 orders of magnitude lower than that for reptation (Eq. (2.8)), inclusion of CLFs adds short relaxation times to the relaxation process. Thus, a larger deviation from the Maxwell model (mono-exponential relaxation or perfect semi-circle in Cole-Cole plot) is expected when CLFs are present than when only pure reptation occurs. Note that the effects of some parameters ( $\langle L \rangle$  and  $\alpha_e$ ) cannot be observed in Cole-Cole plots, for these parameters mainly affect the overall relaxation rate, and the Cole-Cole plot contains no absolute frequency or time information.

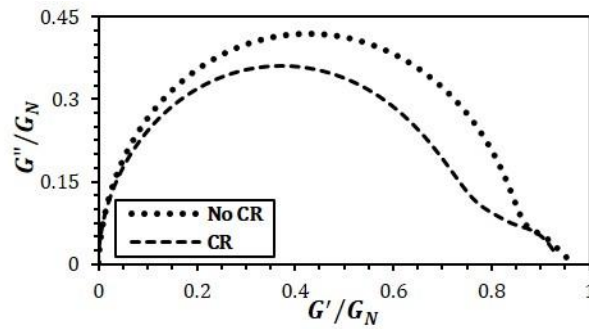


Figure 2.10 Effect of double reptation on the normalized Cole-Cole plot.

As with CLFs, double reptation increases deviations from the Maxwell model, in the latter case by squaring the stress relaxation function. The effect of double reptation can be easily seen in Fig. 2.10 by lowering height of the Cole-Cole semi-circle. Since fast local motions (Rouse and bending) are not affected by the slower relaxation dynamics discussed thus far, the contributions of Rouse and bending dynamics are simply added to the simulation results analytically. These high-frequency modes produce a “dip” in the Cole-Cole plot where  $G''$  goes through a minimum. Confirmed by simulations with large  $\alpha_e$  (for which micelle rigidity is insignificant), a smaller average number of entanglements ( $\bar{Z}$ ) yields a shallower “dip” and a shift of upturn towards lower frequency, which is leftward on a Cole-Cole plot [Granek (1994)] (Fig. 2.11). Note that, as shown by Fig. 2.11, local maxima are also observed at high frequencies ( $\omega > 1/\tau_e$ ) due to the truncation of the high frequency Rouse modes at the frequency at which micelle stiff cuts off these modes (Eq. 2.26b). However, this local maximum disappears when bending modes are added.

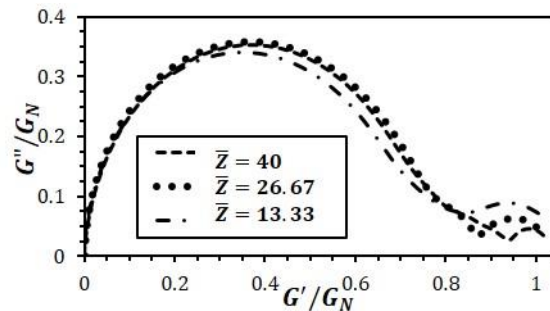


Figure 2.11 “Dip” in the normalized Cole-Cole plot at high frequencies caused by Rouse modes as a function of the number  $\bar{Z}$  of entanglements. The Rouse modes are cut off at a short time scale set by the stiffness of the micelles, as discussed in the text, but no bending modes are included.

### C. Scaling laws

Although our method is based on simulations, it is worthwhile to construct approximate scaling expressions for rheological features from the simulations and compare them with those obtained from Cates' model [Cates (1987)] without/with “breathing fluctuations” (CLFs). A general expression (Eq. (2.42)) for the stress relaxation time ( $\tau$ ) can be found with prefactor  $C$  and power law exponents ( $\beta$ ,  $\gamma$ , and  $\delta$ ) either determined by analytical theory from [Cates (1987); Granek (1994)] or from fits to simulation results with parameters varied over experimentally realistic ranges:

$$\tau = C \bar{\tau}_{rep}^\beta \zeta^\gamma \bar{Z}^\delta \quad (2.42)$$

Here  $\tau = 1/\omega_{cross}$ , as defined in Section II-7. Notice that the effect of  $\langle L \rangle$  and  $\alpha_e$  have been included implicitly in the above equation, since both  $\bar{Z}$  and  $\bar{\tau}_{rep}$  are functions of  $\langle L \rangle$  and  $\alpha_e$ . The scaling laws are shown in Table 2.3 and 2.4 for relaxations without/with CLFs respectively.

Table 2.3 Scaling laws for relaxation without CLFs.

Cates' model		Pointer Simulations	
$\tau \sim \bar{\tau}_{rep}$	$\zeta > 1$	$\tau \sim f(\bar{\tau}_{rep})$	$\zeta > 200$
$\tau \sim \bar{\tau}_{rep} \zeta^{0.5}$	$\zeta < 1$	$\tau \cong 1.50(\bar{\tau}_{rep})^{0.95} \zeta^{0.56}$	$\zeta < 10$

Notice that the simulation results can be described by simple power law dependencies on the relevant parameters in the regime:  $\zeta < 10$  (“living” micelles). For  $\zeta > 200$ , micelles are “dead”, whose rheological behavior (expressed as a functional dependence) is the same as in a classical polymer solution. Between these two regimes, we do not have a simple scaling formula. It is surprising that the Cates' formula  $\tau \sim \bar{\tau}_{rep} \zeta^{0.5}$  persists to remarkably high values of  $\zeta$ , apparently because the longer micelles in the ensemble are still able to break multiple times before relaxing, and these dominate the terminal relaxation time.

Table 2.4 Scaling laws for relaxation with CLFs.

Cates' model		Pointer Simulations	
$\tau \sim \bar{\tau}_{rep}$	$\zeta > 1$	$\tau \sim f(\bar{\tau}_{rep}, \bar{Z})$	$\zeta > 200$
$\tau \sim \bar{\tau}_{rep} \zeta^{0.5}$	$\bar{Z}^{-1} < \zeta < 1$	$\tau \cong 1.39(\bar{\tau}_{rep})^{1.03} \zeta^{0.62}$	$\bar{Z}^{-1.5} < \zeta < 10$
$\tau \sim \bar{\tau}_{rep} \zeta^{0.75} \bar{Z}^{0.25}$	$\bar{Z}^{-3} < \zeta < \bar{Z}^{-1}$	$\tau \cong 2.11(\bar{\tau}_{rep})^{1.03} \zeta^{0.74} \bar{Z}^{0.19}$	$\zeta < \bar{Z}^{-1.5}$
$\tau \sim \bar{\tau}_{rep} \zeta^{0.5} \bar{Z}^{-0.5}$	$\zeta < \bar{Z}^{-3}$	$\sim$	

Note that attainment of the fourth Cates regime ( $\zeta < \bar{Z}^{-3}$ ) requires much smaller values of both  $\zeta$  ( $\zeta \sim 10^{-3}$ ) and  $\bar{Z}$  ( $\bar{Z} \sim 10$ ) than are normally considered, and lies outside of the scope of our work here.

After incorporating the high frequency Rouse and bending motions, in early literature Cates' model has been used to obtain an estimation of the dimensionless average micelle length  $\bar{Z} = \langle L \rangle / l_e$  (Eq. (2.2)) from  $G''_{min}$ , the depth of the minimum in  $G''$  relative to the plateau

modulus (Eq. (2.18)). As described in more detail in the next section (Eq. (2.43b), Fig. 2.17), the corresponding correlation extracted from our simulations is shown here in Table 2.5.

Table 2.5 Estimations for average micelle length.

Cates' model	Pointer Simulations
$\frac{G''_{min}}{G_N} \sim \bar{Z}^{-0.8}$	$\frac{G''_{min}}{G_N} \cong C\bar{Z}_t^{-0.61}, 1 < \alpha_e < 3$

Note that  $\bar{Z}$  is greater than or equal to  $\bar{Z}_t$  (i.e., the micelle contour length is always equal to or larger than the tube length).

Thus, while the scaling results from our simulations are qualitative similar to those from Cates' model, they are quantitative significantly different.

#### D. Parameter analysis

In the above, we have assessed the effects of different relaxation mechanisms and parameters on stress relaxation time or on the depth of the minimum in  $G''$ . However, their effects on the relaxation curve over the entire frequency region have not yet been considered. Thus, in what follows we will discuss their effects on the normalized Cole-Cole plot by varying one parameter at a time, leaving others set at their corresponding standard values.

##### 1) Persistence length $l_p$

We note first that persistence length ( $l_p$ ) can be used to obtain the plateau modulus ( $G_N$ ) once other parameters ( $\langle L \rangle, \alpha_e, \zeta, d$  and  $T, \phi$ ) are known. To eliminate the influence of  $G_N$ , Cole-Cole plots normalized by  $G_N$  are shown in Fig. 2.12a for different values of  $l_p$ . According to Eqs. (2.33) and (2.34), the value of  $l_p$  affects the slope of the “upturn” in  $G''$  after it passes through a minimum and enters the high frequency region, as shown in Fig. 2.12a.

##### 2) Breakage time relative to reptation time $\zeta$

Figure 2.12b reveals that as  $\zeta$  decreases, the height of normalized Cole-Cole plot increases and, as expected, the plot becomes more semi-circular, approaching that for a Maxwell model. Thus, the parameter  $\zeta$  has a greater effect than any other parameter on the shape of normalized Cole-Cole plot before the upturn at high frequencies. Note in Fig. 2.12b that as long as  $\zeta$  is less than unity, its effect on the high-frequency upturn is small.

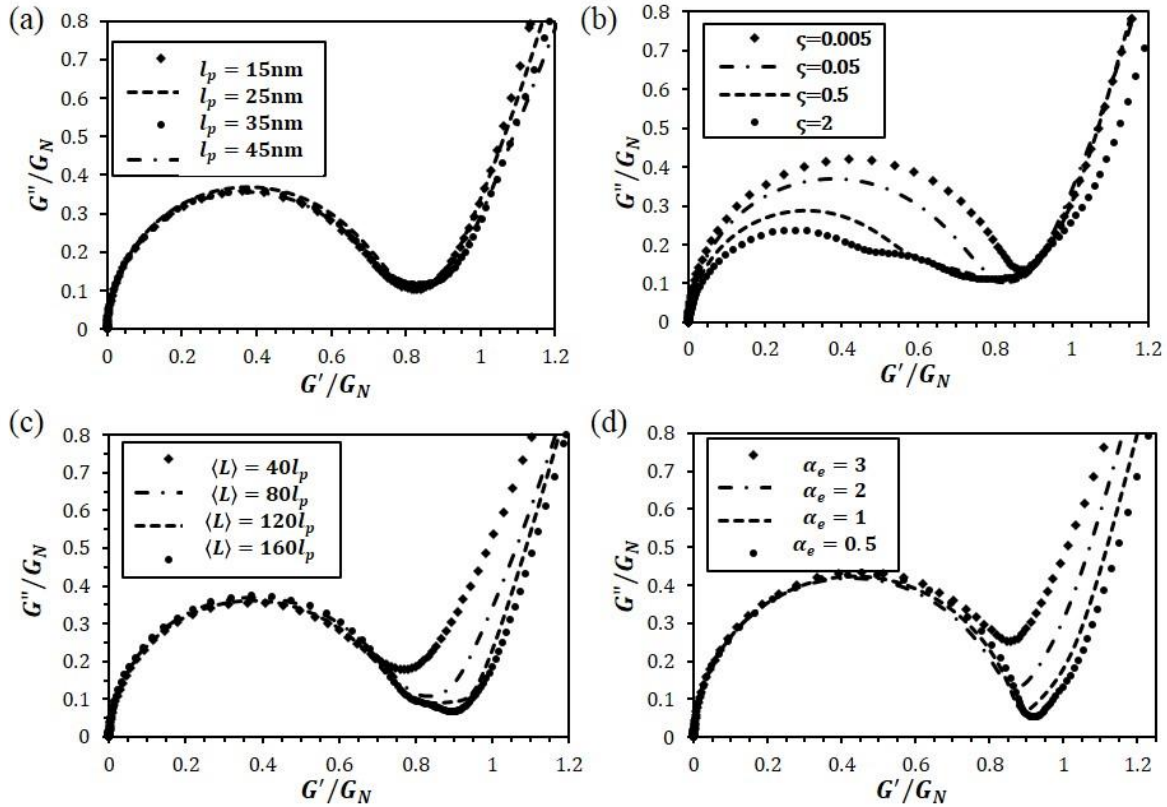


Figure 2.12 Effect of model parameters on normalized Cole-Cole plots (a)  $l_p$  (b)  $\zeta$  (c)  $\langle L \rangle$  (d)  $\alpha_e$ .

### 3) Average micelle length $\langle L \rangle$ and flexibility $\alpha_e$

The effects of average micelle length ( $\langle L \rangle$ ) and flexibility coefficient ( $\alpha_e$ ) on the normalized Cole-Cole plot are similar (see Figs. 2.12c and 2.12d). (The micelle length  $\langle L \rangle$  also has a large effect on the terminal relaxation time, but that effect does not show up in a Cole-Cole plot.) Both of them affect the minimum value of  $G''$  while holding the height of semicircle constant. A somewhat flat region around the minimum is also observed when the ratio of  $\langle L \rangle$  to  $l_p$  exceeds 100 and  $\alpha_e$  is no larger than 2. The reason for the flat region for  $\alpha_e < 2$  is that micelle stiffness suppresses Rouse modes which would otherwise cause a more gradual change in  $G''$  before the onset of bending modes. Thus, without Rouse modes, a deeper “dip” is expected and the upturn is postponed to higher frequency.

Thus, a qualitative look at the shape of normalized Cole-Cole plot gives a rough indication of the magnitude of  $\zeta$  and of either  $\langle L \rangle$  or  $\alpha_e$ . To determine these parameters more precisely, we turn next to development of a systematic method for inferring micelle parameters from rheological behavior.

## 2. From rheology to micelle parameters

### A. Empirical formulas

An iterative simulation procedure to estimate parameters from “global” rheological behavior is developed in this section. Since a proper starting point for further iterations can reduce the total number of iterations and improve the accuracy of final result significantly, we attempt to construct empirical formulas for good initial guesses of parameters through “local” features of rheological curves. Figures 2.13a and b give the same data but in different formats (frequency and Cole-Cole plot). The points  $(G'_{max}, G''_{max})$  and  $(G'_{min}, G''_{min})$  in Fig. 2.13b correspond to the same points donated as  $(\omega_{max}, G'_{max}, G''_{max})$  and  $(\omega_{min}, G'_{min}, G''_{min})$  in Fig. 2.13a. Note that the subscripts “max” and “min” represent the maximum and minimum in  $G''$ .

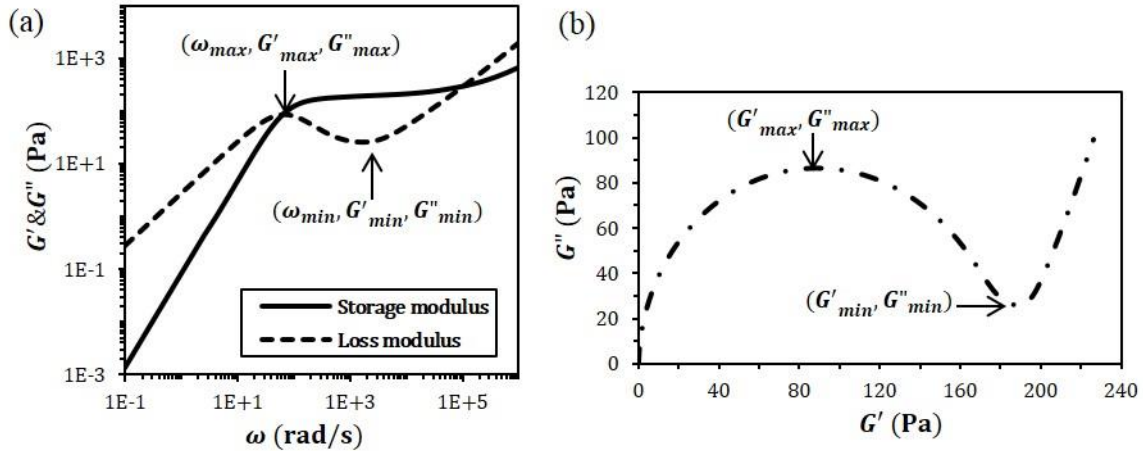


Figure 2.13 Definition of significant local rheological features in plots of (a)  $G'$  and  $G''$  versus frequency, and (b) Cole-Cole plot.

#### 1) $G_N$ versus $\zeta$

As mentioned above,  $\zeta$  controls the height of the normalized Cole-Cole semicircle, which is negligibly affected by other parameters. A family of curves shown in *Appendix A* (Fig. A.7) obtained by varying  $\zeta$  alone, give heights plotted in Fig. 2.14. Semi-log fits to the relationships between  $G''_{max}/G_N$  vs.  $\zeta$ , as well as  $G'_{max}/G_N$  vs.  $\zeta$  are obtained for  $\zeta$  between 0.001 and 2. As shown in Fig. 2.14, as  $\zeta$  increases, the difference between  $G'_{max}$  and  $G''_{max}$  increases, as the Cole-Cole plot deviates more and more from a semi-circle.

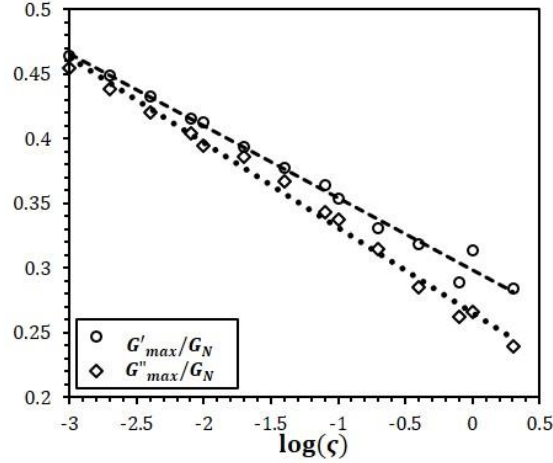


Figure 2.14 Empirical correlations for the dependences of  $G'_{max}/G_N$  and  $G''_{max}/G_N$  on  $\zeta$  with other parameters fixed at standard values.  $R^2$  values of the semi-log fits are as follows: 0.988 for the dashed line; 0.991 for the dotted line.

## 2) $G_N$ versus $\bar{Z}_t$

Motivated by an equation from Granek (1994) (Eq. (2.18)) that allows an estimation of  $\langle L \rangle$  from the ratio  $G''_{min}/G_N$ , we now examine the effect of a related quantity,  $\bar{Z}_t$  (Eq. (2.2)), on this “dip” ( $G''_{min}/G_N$ ) in a normalized Cole-Cole plot. From the family of curves (Fig. A.8 in Appendix A), we have obtained the power-law correlation ( $G''_{min}/G_N = C\bar{Z}_t^{-0.61}$ ) plotted in Fig. 2.15 with the prefactor  $C$  determined approximately in what follows: when  $\bar{Z}_t > 30$  the prefactor is set to be unity, and then it increases linearly to 1.5 when  $\bar{Z}_t = 10$ . The detailed expressions are given in Eq. (2.43b).

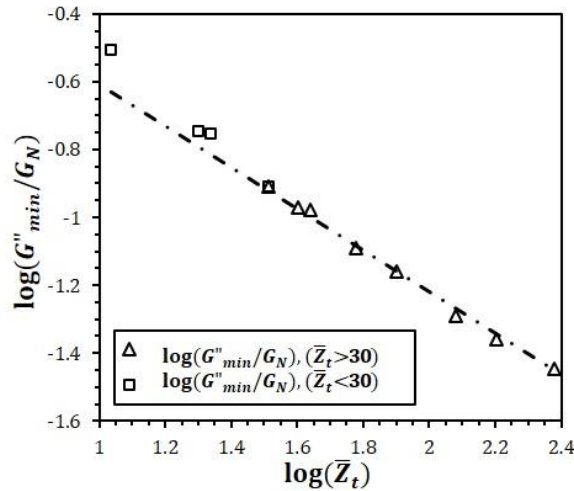


Figure 2.15 Empirical correlation for the dependence of  $G''_{min}/G_N$  on dimensionless tube length  $\bar{Z}_t$  with other parameters fixed at standard values.  $R^2$  value of log-log fit is 0.970.



3)  $\bar{\tau}_{rep}$  versus  $\zeta$

Since normalized Cole-Cole plots do not contain either frequency or time, they do not allow estimates of characteristic times such as  $\bar{\tau}_{rep}$ , which must instead be obtained from a frequency plot of  $G''$  by constructing an additional equation relating  $\bar{\tau}_{rep}$  to the dimensionless breakage rate ( $\zeta$ ) and specific frequency ( $\omega_{max}$ ). Our results are shown in Fig. 2.16, where a power-law formula, with exponent -0.63, for the dependence of  $(\omega_{max}\bar{\tau}_{rep})$  on  $\zeta$  and prefactor  $B$  is illustrated.

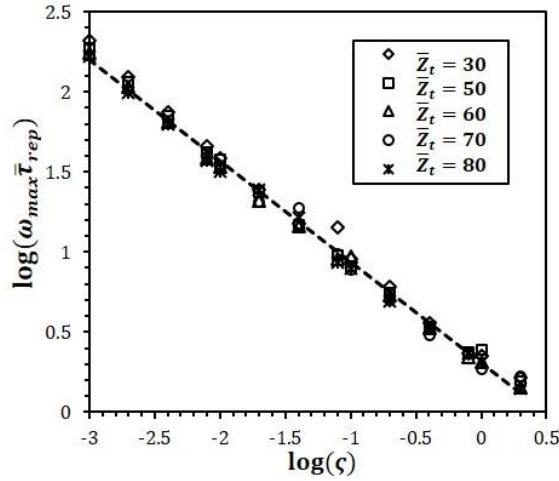


Figure 2.16 Empirical correlation for the dependence of  $(\omega_{max}\bar{\tau}_{rep})$  on dimensionless breakage rate  $\zeta$  for various values of  $\bar{Z}_t$  and other parameters set to standard values. The result can be approximated by Eq. (2.43c).

The above results can be summarized by the following empirical formulas:

$$\frac{G'_{max}}{G_N} = -0.0557 \log(\zeta) + 0.298, \quad \frac{G''_{max}}{G_N} = -0.0657 \log(\zeta) + 0.265, \quad \bar{Z} > 10 \quad (2.43a)$$

$$\frac{G''_{min}}{G_N} = C \bar{Z}_t^{-0.61}, \quad 1 < \alpha_e < 3, \quad \begin{cases} C = 1, \bar{Z}_t > 30 \\ C = \frac{7 - 0.1\bar{Z}_t}{4}, 30 > \bar{Z}_t > 10 \end{cases} \quad (2.43b)$$

$$\omega_{max}\bar{\tau}_{rep} = B\zeta^{-0.63}, \quad B = 2.1 \text{ for } 1 < \alpha_e < 3 \quad (2.43c)$$

Note that applications of the above correlations are limited to their stipulated regions, outside of which their accuracy cannot be guaranteed. The ranges considered are those needed for comparison to experiments described below. Extension of those correlations to a much wider range of  $\bar{Z}$  and  $\alpha_e$  will be taken up in future work. However, as one example, we note that the scaling law in Eq. (2.43b) is invalid in the “loose” entanglement limit, where  $\alpha_e$  is large.

However, by replacing  $\bar{Z}_t$  with  $\bar{Z}$  in Eq. (2.43b), scaling laws for  $G''_{max}/G_N$  vs.  $\bar{Z}$  valid over a wide range of  $\bar{Z}$  and  $\alpha_e$  varying from 8 (loosely entangled) to 0.4 (tightly entangled) can be obtained, as shown in Fig. 2.17.

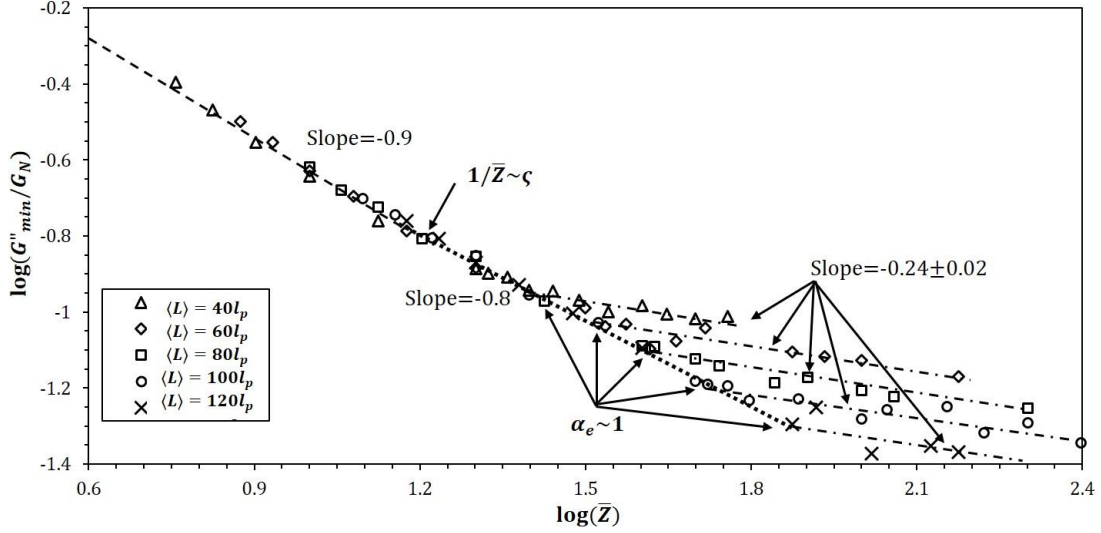


Figure 2.17 Extended empirical correlation for the dependence of  $G''_{min}/G_N$  on average entanglement number  $\bar{Z}$  by varying  $\langle L \rangle$  and  $l_e$  (or equivalently  $\alpha_e = l_e/l_p$ ) with other parameters fixed at standard values.

Now we try to sum up all the equations needed for an initial guess of micelle parameters. For simplicity, detailed expressions for each formula do not appear in this list, and we simply represent the functions by "A", "B", ..., "Q":

$$\begin{cases} xG'_{max} + (1-x)G''_{max} = A(G_N, \varsigma) \\ G''_{min} = B(G_N, \bar{Z}_t) \\ \omega_{max} = C(\varsigma, \bar{\tau}_{rep}) \end{cases} \quad (2.44a)$$

$$\begin{cases} \bar{Z}_t = F(\langle L \rangle, \alpha_e, l_p) \\ \bar{\tau}_{rep} = G(\langle L \rangle, \alpha_e, d, l_p) \\ G_N = H(\alpha_e, d, l_p) \end{cases} \quad (2.44b)$$

$$G^H(\omega) = Q(d, l_p, \omega) \quad (2.44c)$$

Equation group (2.44a) comes from empirical formulas in Eq. (2.43). The three equations in (2.44b) are derived theoretically by combining Eqs. (2.2), (2.9), (2.28); Eqs. (2.4), (2.12), (2.28); and Eq. (2.32); respectively, whose detailed expressions are given in *Appendix A*. The above two groups of equations are used to obtain initial guesses of parameters for the simulation procedure described below. Thus, Eqs. (2.44a) and (2.44b) consist of 6 equations involving 12 parameters including 4 ( $\omega_{max}, G'_{max}, G''_{max}, G''_{min}$ ) that can be extracted simply from

rheological curves, and 2 (micelle persistence length  $l_p$  and diameter  $d$ ) that are set to pre-assigned values initially. This leaves 6 unknown parameters ( $G_N, \zeta, \langle L \rangle, \alpha_e$  and  $\bar{\tau}_{rep}, \bar{Z}_t$ ) and 6 equations so that a unique solution is possible. Note that  $l_p$  and  $d$  can be updated during the simulation based on fitting Eq. (2.44c) to the high-frequency data. If high-frequency data are not available or are not adequate to fit  $l_p$  and  $d$  unambiguously, then these two parameters must be assigned values from sources other than rheological data, as discussed below. Definitions for all the above parameters can be found in Section II.

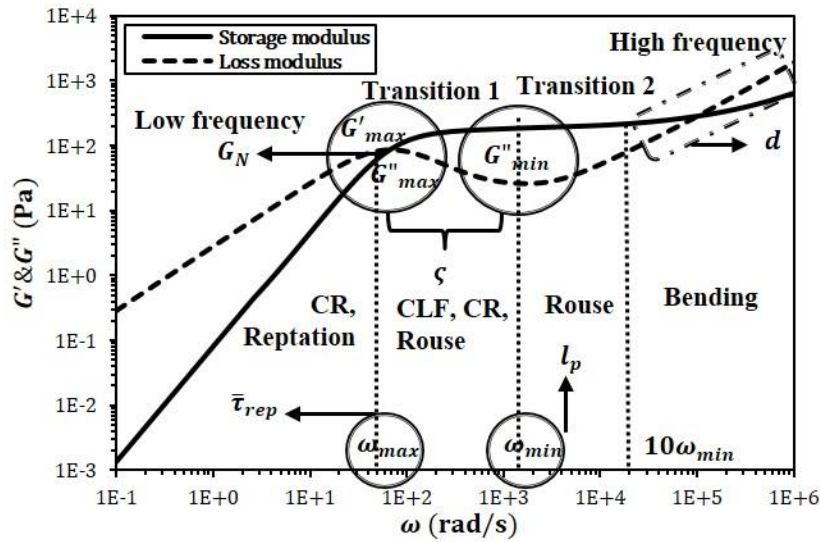


Figure 2.18 Dominant relaxation mechanisms and five parameters ( $G_N, \zeta, d$  and  $\bar{\tau}_{rep}, l_p$ ) controlling the behavior in each of four different frequency ranges. Note that this set of five parameters differs from the set of “five independent parameters” described above in that they include  $\bar{\tau}_{rep}$  and  $l_p$  rather than  $\langle L \rangle$  and  $\alpha_e$ . However, the set of five parameters extracted from this plot can be converted to our canonical five independent parameters using Eq. (2.44b). One should also note that a system dependent choice of  $10\omega_{min}$  as the start frequency for bending regime is made here.

### B. Parameter estimation

Although equation groups (Eqs. (2.44a) and (2.44b)) are applied to get the initial guess, these formulas have other uses. By dividing the frequency domain into four different ranges (low, transition 1, transition 2, and high frequency) with three specific frequencies ( $\omega_{max}, \omega_{min}$  and  $10\omega_{min}$ ), these formulas can tell us which parameters one can estimate by matching specific points or fitting data in each of these frequency ranges. The rheological parameters with their corresponding fitting features and the relaxation mechanisms that dominate in each frequency range are depicted in Fig. 2.18. An accurate estimate of a parameter can only be achieved by

fitting experimental data over a frequency range that contains the rheological features showing the greatest sensitivity to that parameter.

### C. Simulation procedure

Based on the analysis in parts A and B, the simulation procedure to extract parameters from rheological behavior is laid out in Fig. 2.19: rheological plots ( $G'$  &  $G''$  versus frequency) immediately offer us values of  $(\omega_{max}, G'_{max}, G''_{max}, G''_{min})$ . With the initial guesses of  $l_p$  and  $d$  as inputs, equations in Eqs. (2.44a) and (2.44b) can be solved for 6 parameters ( $G_N, \zeta, \langle L \rangle, \alpha_e$  and  $\bar{\tau}_{rep}, \bar{Z}_t$ ). Of these, 5 independent parameters ( $G_N, \zeta, \langle L \rangle, \alpha_e$  and the guessed  $d$ ) can be used to predict rheological curves based on the procedure in Fig. 2.9. The difference between simulated curves and the experimental ones ( $\Delta G^H, \Delta\omega_{max}, \Delta G'_{max}, \Delta G''_{max}, \Delta\omega_{min}$ , and  $\Delta G''_{min}$ ) can then be used as feedback to modify the original guess of these parameters for next iteration. Through optimization, we can get excellent fits with reasonable values of the parameters (shown below). Note that entanglement length ( $l_e$ ) and persistence length ( $l_p$ ) are not independent parameters. Their values can be obtained once micelle parameters ( $G_N, \zeta, \langle L \rangle, \alpha_e$  and  $d$ ) as well as temperature  $T$  and surfactant volume fraction  $\phi$  are known. Details of the iteration procedure and sensitivity of the fits to the parameter values will be addressed in a subsequent paper.

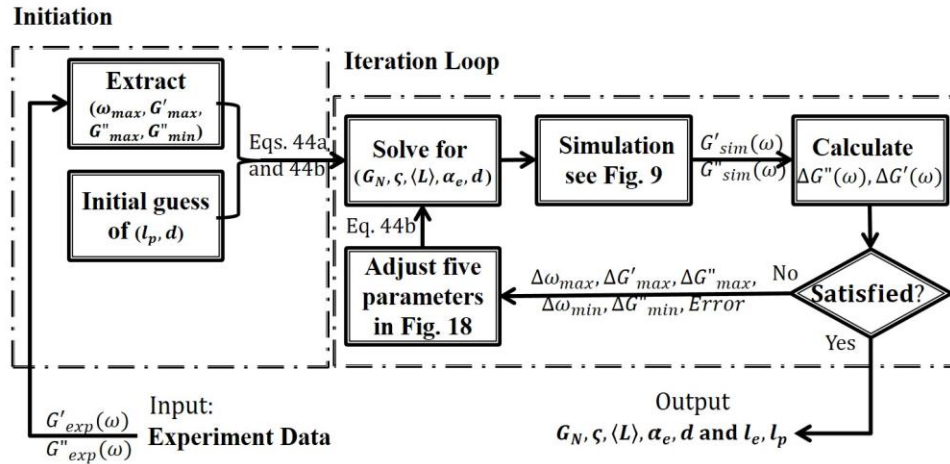


Figure 2.19 Schematic of simulation procedure to obtain micelle parameters from rheological behavior.

### D. Results and discussion

Finally, we present in Figs. 2.20 and 2.21 the results of the fitting (with  $R^2$  values of 0.97 and 0.92, respectively, for Figs. 2.20 and 2.21) to experimental data ( $c_{CTAB} = 0.35\text{mol/}$

L,  $c_{\text{NaClO}_3} = 0.6\text{mol/L}$ ,  $T = 303\text{K}$ ) from Oelschlaeger *et al.* (2010) and ( $c_{\text{CTAB}} = 0.15\text{mol/L}$ ,  $c_{\text{KBr}} = 1.5\text{mol/L}$ ,  $T = 308\text{K}$ ) from Khatory *et al.* (1993). Note that low frequency behaviors ( $\omega < 100\text{ rad/s}$ ) were measured by a mechanical rheometer in both cases, while diffusing wave spectroscopy (DWS) was used by Oelschlaeger *et al.* (2010) to obtain the high frequency data in Fig. 2.20.

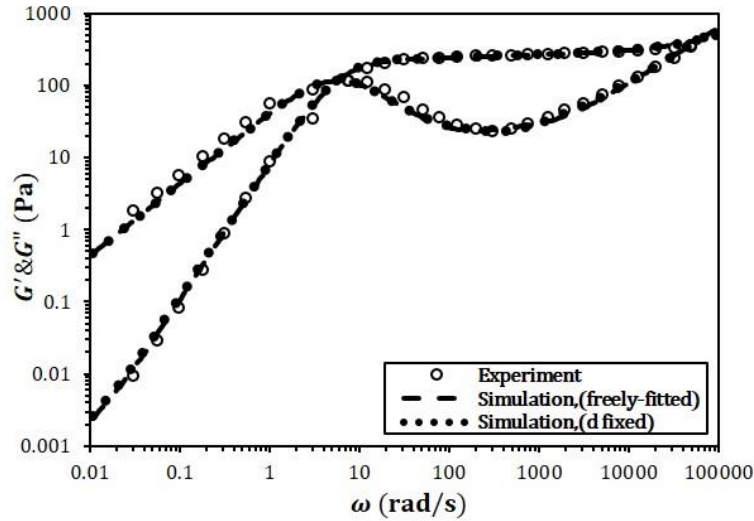


Figure 2.20 Simulation results of the Pointer Algorithm fitted to rheological data in Oelschlaeger *et al.* (2010).

As shown in Figs. 2.20 and 2.21, our simulation results successfully match the rheological behavior of micellar solutions in the low and transition frequency ranges. (The deviation at low frequencies in Fig. 2.21 is likely due to transducer error, since the slope in this region is steeper than the expected terminal slope of 2 for  $G'$ .) At high frequencies, an unexpectedly early upturn occurs in the data of Khatory *et al.* (1993) (the upturn frequency  $\omega_{min}$  is 10 times smaller than that for Oelschlaeger *et al.* (2010)), which makes our fitting much poorer in this region for the high-frequency mechanical data of Khatory *et al.* than for the high-frequency DWS data in Oelschlaeger *et al.* (2010). The high-frequency data in Khatory *et al.* can be better fit with the Pointer Algorithm, but only by using an unrealistically large value of the persistence length of around 200nm (In the simulation, the maximum value of  $l_p$  is set to 120nm). The pre-mature upturn in  $G''$  in the data of Khatory *et al.* (1993) might be due to the large salt-surfactant concentration ratio (around 10). Or perhaps the mechanical data

are unreliable at these frequencies. But, we have chosen not to force a fitting of these high-frequency data by using such an unrealistically high persistence length.

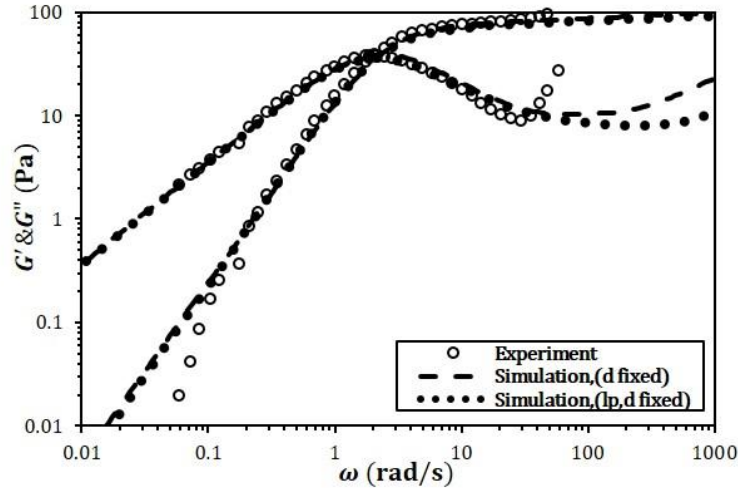


Figure 2.21 Simulation results of the Pointer Algorithm fitted to rheological data in Khatory *et al.* (1993).

The parameter values suggested by Oelschlaeger *et al.* (2010), Khatory *et al.* (1993) and obtained from our simulations with parameters either all freely fitted (in the case of Oelschlaeger *et al.* (2010)), or  $d$  alone fixed (in both the case of Oelschlaeger *et al.* (2010) and of Khatory *et al.* (1993)), or both  $d$  and  $l_p$  fixed (in the case of Khatory *et al.* (1993)) to what we consider realistic values ( $d = 4.4\text{nm}$  [Nettesheim and Wagner (2007)],  $l_p = 40\text{nm}$ ) are shown in Table 2.6.

Table 2.6 Estimation of parameters for data from Oelschlaeger *et al.* (2010) and Khatory *et al.* (1993).

Parameters	Oelschlaeger <i>et al.</i> (2010)			Khatory <i>et al.</i> (1993)		
	Literature	Simulation		Literature	Simulation	
		Freely-fitted	$d$ fixed		$d$ fixed	$d, l_p$ fixed
$G_N$ (Pa)	255	285	288	95	100	99
$\zeta$	~	1.13E-2	1.0E-2	0.79~1.23	1.52E-2	4.95E-2
$\langle L \rangle$ ( $\mu\text{m}$ )	0.24	5.35	5.15	0.66	6.88	5.77
$\alpha_e$	0.76	2.23	1.76	4.2	1.2	3
$d$ (nm)	4.4	3.8	4.4	~	4.4	4.4
$l_e$ (nm)	22.6	87	86	63.1	144	120
$l_p$ (nm)	29.8	39	49	15	120	40

Note that since high frequency zone is unreachable for data from Khatory *et al.* (1993), the micelle diameter cannot be estimated using our method. The value of  $d=4.4\text{nm}$  used in the simulation for this case is taken from SANS measurements [Nettesheim *et al.* (2007)].

In Table 2.6, for both data sets, an order of magnitude difference in estimated values of  $\langle L \rangle$  is seen between the values reported in the literature and those we have extracted from our simulations. Some of this difference (around a factor of 2) arises because we take into account the effect of CR. However, the main reason lies in the different frequency ranges we used for predicting  $\langle L \rangle$ : Cates [Cates and Candau (1990)] and Granek [Granek (1994)] rely on the transition region (i.e. the ratio  $G''_{min}/G_N$  used in Eq. (18)), while our estimate comes from the low frequency region which is more sensitive to the average micelle length than is the transition region. In addition, the longer micelle length obtained from our method leads to a smaller value of  $\zeta$  (the longer the micelle is, the faster it breaks and the smaller is the value of  $\zeta$ ). From the data of Oelschlaeger *et al.* (2010), by including bending modes in the simulation, the persistence length  $l_p$  and micelle diameter  $d$  can also be extracted from the high frequency behavior; the values we obtain are similar but not identical to the estimates obtained by Oelschlaeger *et al.* (2010). The difference might be the result of a larger predicted value of  $G_N$  than that for Oelschlaeger *et al.* (2010). Note also that the ratio ( $\alpha_e$ ) of  $l_e$  to  $l_p$  extracted from the data of Oelschlaeger *et al.* (2010) puts this solution close to, or in, the cross-over region ( $\alpha_e=2.23$  and  $1.76$ ) between tight and loose entanglements, showing that our cross-over formula may be important for modeling this solution. Note also that the estimated values for  $l_e$  and  $l_p$  for data from Khatory *et al.* (1993) in the second to last column in Table 2.6, when only the micelle diameter  $d$  is held fixed, cannot be taken seriously since  $l_p$  reaches the maximum value ( $l_p \leq 120\text{nm}$ ) that our simulation allows, which is still not high enough to fit the upturn.

By fixing the micelle diameter to an experimental value, rather than allowing it to be fit, the estimation of the persistence length for the data of Oelschlaeger *et al.* (2010) changes from 39 to 49 nm, which allows a good fitting behavior at high frequencies to be maintained. The values of other parameters change only slightly, which shows the robustness of their fitted values using our method. However, if data in the high frequency region is poor or missing as is the case for the data of Khatory *et al.* (1993), estimation of other parameters will depend on the value of persistence length assumed, as shown in Table 2.6. Thus, the results from fitting the data of Oelschlaeger *et al.* (2010) indicate that if high frequency data are available, four of the five parameters can be extracted using our method. The fifth parameter, the micelle diameter  $d$ , must be supplied from non-rheological data, but its value is known a priori well enough that the other parameters can be robustly extracted from the model. However, if high frequency data are not

available, or are unreliable, as appears to be the case for the data of Khatory *et al.* (1993), the persistence length must be supplied from non-rheological considerations, or else the value of  $\zeta$  cannot be robustly determined, as indicated by its sensitivity to the value of the persistence length shown in the last two columns of Table 2.6. However, the micelle length  $\langle L \rangle$  and especially the plateau modulus  $G_N$  are seen in Table 2.6 to be much less sensitive to an incorrect value of the persistence length  $l_p$ . A detailed analysis of the sensitivity of extracted parameter values to uncertainties in parameters or rheological data will be the focus of a later paper.

## VII. Conclusions and Final Comments

We have developed an algorithm based on Cates' model for wormlike micelles that we believe allows more accurate rheological predictions than before. We have included additional mechanisms beyond those of Cates' model, including constraint release by double reptation, reptation in the tight entanglement regime as well as in the cross-over between loose and tight entanglements, and bending modes at high frequency. Based on the most up-to-date theories of polymer dynamics and innovations in modeling, fits to rheological data using our pointer algorithm allow more micelle parameters (including micelle persistence length) to be estimated, and more accurate estimates to be obtained than was possible from the earlier approaches using Cates' method. The advantages of our simulation method are illustrated by obtaining micelle parameters from fits to  $G'$  &  $G''$  data by Oelschlaeger *et al.* (2010) over six decades of frequency with an average deviation of only 6%. We find significant differences between the best-fit micelle parameters derived from our algorithm and those obtained by the traditional method of Cates and coworkers, especially in the average micelle length, which is an order of magnitude larger than inferred from the traditional method. Future work will focus on an analysis of parameter sensitivity, and the effect of CR and high frequency data on parameter estimation. It will also be worthwhile to study the effect of salt concentration, concentration of surfactant, and temperature on the parameter values extracted by our method and to compare parameter values extracted from our rheological method with those obtained more directly from electron microscopy, neutron scattering, or other methods. We note that our method is limited to linear micelles and to linear viscoelasticity. Extension to branched micelles and nonlinear rheology is also highly desirable, but these remain as future tasks.



### **Chapter 3: Determination of Characteristic Lengths and Times for Wormlike Micelle Solutions from Rheology using a Mesoscopic Simulation Method<sup>1</sup>**

#### **I. Introduction**

Surfactant solutions containing self-assembled micelles and other structures are widely used in many applications, due to their various equilibrium aggregation states (oblate or prolate spheroids, short rods or long worms, disks) [Pérez *et al.* (2014)] and physicochemical properties (density, viscoelasticity, conductivity, solubility, surface tension) [Zdziennicka *et al.* (2012)]. Induced by changes in temperature, pH, type and concentration of surfactant and salt, morphology transitions between different structures have been extensively investigated [Bernheim-Groswasser *et al.* (2000); Baccile *et al.* (2012); Kusano *et al.* (2012); Yusof and Khan (2012)], leading, for example, to creation of micellar solutions whose rheological properties (viscoelasticity) are tunable by light [Ketner *et al.* (2007); Lu *et al.* (2013)], temperature [Kalur *et al.* (2005)], and additives [Sreejith *et al.* (2011); de Silva *et al.* (2013)]. When long wormlike micelles (WLMs) form, via reversible breaking and rejoining, the solution exhibits viscoelastic behavior through inter-micellar entanglements or networks [Cates and Candau (1990); Khatory and Kern *et al.* (1993)]. Applications of WLM solutions are found in shampoo and detergent formulations, drag reduction [Shi *et al.* (2014)], rheology modification [Beaumont *et al.* (2013)], colloid stabilization [James and Walz (2014)], and templated synthesis of nano-particles [Romano and Kurlat (2000)] and molecular sieves [Beck *et al.* (1992)].

Combinations of different experimental methods including traditional temperature jump (T-jump) experiments [Waton and Zana (2007)], mechanical rheometry [Khatory and Lequeux *et al.* (1993)], birefringence [Shikata *et al.* (1994)], light and neutron scattering [Imae and Ikeda (1986); Marignan *et al.* (1989); Jensen *et al.* (2013)], turbidity [Razak and Khan (2013)], and more recently diffusing wave spectroscopy (DWS) [Galvan-Miyoshi *et al.* (2008)], neutron spin echo (NSE) [Nettesheim and Wagner (2007)], and nuclear Overhauser effect spectroscopy

---

<sup>1</sup> The rheological measurements in this chapter are conducted by the former group member Xueming Tang as collaborated with Procter and Gamble scientists Mike Weaver and Peter Koenig.

(NOESY) [Padia *et al.* (2014)], are often needed to achieve a thorough characterization of micellar properties [Croce *et al.* (2003); Kuperkar *et al.* (2008)]. Theories have also been developed to extract information about micellar kinetics and thermodynamics from experimental data [Ilgenfritz *et al.* (2004); Babintsev *et al.* (2014)]. For WLMs, a particularly important theory is that of Cates and coworkers [Turner and Cates (1991)] which allows average micelle length and rate of breakage to be extracted from linear rheology. Although many improvements to the original Cates’ theory have been made [Granek and Cates (1992); Granek (1994)], shortcomings still exist, and continued efforts are required to make its predictions more quantitative [Larson (2012); Zou and Larson (2014)].

Our recently developed “pointer” simulation method [Zou and Larson (2014)] is capable, we believe, of estimating micellar parameters more quantitatively than is possible using previous methods based on Cates’ theory [Turner and Cates (1991)]. In what follows, after reviewing both Cates’ theory and our simulation model in Section II, we present a brief description of experimental methods and surfactant solutions used to obtain rheological data in Section III. Using improved empirical relationships between micellar parameters and local rheological behaviors, Section IV presents a detailed data-fitting procedure that yields properties of WLMs from rheological data, and Section V contains the associated sensitivity studies as well as fitting results for several micellar solutions. The effect of different breakage mechanisms and the possibility of branched micelle detection through our simulation method are also discussed in Section V. Conclusions are presented in Section VI.

## II. Model Review

### 1. Cates’ theory

Porte and coworkers [Porte *et al.* (1980)] suggested that WLMs be regarded as semi-flexible chains rather than as rigid rods, after the micelle persistence length was first measured in 1980. Since then, many similarities in rheology between WLM and polymer solutions have been noted [Candau *et al.* (1989); Cates and Candau (1990)]. However, a major difference between these two kinds of solutions is the “living” feature of micelles: i.e., their incessant and random breaking and rejoining at thermal equilibrium, which yields a Poisson exponential length distribution [Cates (1987)]:

$$N(L) \sim \exp(-L/\langle L \rangle) \tag{3.1}$$

where  $L$  is the length of an individual micelle, and  $\langle L \rangle$  is the average micelle length.

Using the polymer “tube model” [Doi and Edwards (1986)] and reptation theory [de Gennes (1979)], Cates in 1987 explained the unique Maxwellian (i.e., single-exponential) stress relaxation behavior observed for entangled WLM solutions in which diffusion of WLMs is limited to “tube”-like region by entanglements [Cates (1987)]. His theory is based on the interplay of two mechanisms: i.e., breakage/rejoining and reptation. Imposition of a small step strain on entangled WLMs takes their conformations out of equilibrium, producing a stress. In the absence of breakage, micelle segments can only relax the stress by diffusing curvilinearly, or “reptating,” out of the initial tube, which leads to a loss of original, oriented tube segments as the micelle vacates them. The characteristic time for reptation-induced relaxation depends on the curvilinear diffusivity ( $D_c$ ) of the micelle along the tube, and the length of the tube ( $L_t$ , which is proportional to the length of the micelle  $L$ ). For micelles with an average length  $\langle L \rangle$ , the reptation time ( $\bar{\tau}_{rep}$ ) is given by:

$$\bar{\tau}_{rep} = \frac{\langle L_t \rangle^2}{\pi^2 D_c}, \quad D_c \equiv \frac{k_B T}{\zeta \langle L \rangle} \quad (3.2)$$

where  $k_B$  and  $\zeta$  are Boltzmann’s constant and the longitudinal drag coefficient per unit length of the micelle, respectively.

The above relaxation mechanism is well understood for ordinary “dead” polymers [Doi and Edwards (1986); Likhtman and McLeish (2002)], where no breakage or rejoining exists. For “living” WLMs, micellar breakage accelerates the relaxation by creating new ends. To address this effect, a dimensionless breakage rate ( $\zeta$ ) is defined [Cates (1987)]:

$$\zeta \equiv \frac{\bar{\tau}_{br}}{\bar{\tau}_{rep}}, \quad \bar{\tau}_{br} = \frac{1}{k \langle L \rangle} \quad (3.3)$$

where  $\bar{\tau}_{br}$ , called the average breakage time, is the lifetime a micelle of average length survives before breakage, while  $k$  is the breakage rate per unit length.

When  $\zeta$  decreases below unity, the relaxation spectrum is narrowed, since for a high breakage rate the distance that a micelle segment must travel to diffuse out of its tube becomes independent of the tube length. For WLM solutions with  $\zeta \ll 1$ , the polydispersity in length distribution therefore has little effect on the relaxation: all tube segments are lost at the same rate and the stress relaxes mono-exponentially. In that case, the stress relaxation time (which is

approximated as the reciprocal of crossover frequency  $\omega_{cross}$  of the storage or elastic modulus  $G'$  with the loss or viscous modulus  $G''$ ) is given as [Cates (1987)]:

$$\tau \cong 1/\omega_{cross} \sim \bar{\tau}_{rep} \zeta^{0.5}, \quad \zeta \ll 1 \quad (3.4)$$

The ideal single exponential relaxation behavior, alluded to above, is captured by Cates' original theory, and reveals itself in a perfect semicircular Cole-Cole plot (of  $G''$  versus  $G'$ ) [Cates and Candau (1990)]. Deviations from the perfect semi-circle are observed experimentally [Turner and Cates (1991)], however, at high frequencies, implying that some relaxation mechanisms are missing from the original theory. Thus, “breathing” fluctuations, also called “contour length fluctuations” (CLFs) and high frequency Rouse modes [Dealy and Larson (2005)] were subsequently incorporated into the theory [Granek and Cates (1992); Granek (1994)]. Using the modified theory, the average micelle length  $\langle L \rangle$  can be estimated from the observed minimum in  $G''$  ( $G''_{min}$ ) at high frequency by [Granek (1994)]:

$$\frac{G''_{min}}{G_N} = \left( \frac{l_e}{\langle L \rangle} \right)^{0.8} = \bar{Z}^{-0.8} \quad (3.5)$$

where,  $l_e$  is the micelle entanglement length, and  $\bar{Z}$  is the number of entanglements for micelles with average length  $\langle L \rangle$ .  $G_N$  is the plateau modulus, which can be calculated theoretically from [Cates (1988)]:

$$G_N \cong \frac{k_B T}{l_e^{1.8} l_p^{1.2}} \quad (3.6)$$

where  $l_p$  is the micelle persistence length.

By assuming WLMs have a persistence length of 15 nm, a method [Turner and Cates (1991)] was developed to determine the average micelle length ( $\langle L \rangle$ ) and dimensionless breakage rate ( $\zeta$ ) indirectly from rheological data, since these quantities are essentially impossible to obtain directly from other experiments. However, as we discussed in our earlier work [Zou and Larson (2014)], the accuracy of the method is limited by the assumptions of both the theory and the approximations used to extract micelle parameters from individual features of the rheological curves ( $G'$  and  $G''$ ), and by possible inaccuracy in the assumed value of the persistence length. Hence, it is desirable to overcome these limitations, by developing a more advanced predictive model, discussed next.

## 2. Simulation model

We extended Cates' theory by developing a simulation-based mesoscopic model [Zou and Larson (2014)] for entangled WLM solutions, allowing more quantitative estimates of multiple characteristic micellar parameters. The new model includes important physics neglected in the earlier Cates' theories [Cates (1987); Cates (1988); Turner and Cates (1991); Granek and Cates (1992); Granek (1994)], i.e.: tube rearrangement, micelle semi-flexibility, and high-frequency bending modes. Derived from the expression for CLF-induced relaxation of linear polymers [Milner and McLeish (1997); Milner and McLeish (1998)], the rate of loss of tube segments at the ends of tubes is represented in a time-implicit form in our model to facilitate the addition of contributions from reptation [Zou and Larson (2014)]. The effect of tube rearrangement (i.e., disentanglement-induced relaxation due to the motion of neighboring micelles) is accounted for using "double reptation" [Tuminello (1986); des Cloizeaux (1988)]. Unlike classical polymers, which are flexible enough to coil up within their tubes, WLMs are relatively rigid: they only bend slightly in thin tubes due to a large persistence length (10~300 nm). The semi-flexibility of WLMs is characterized by the ratio of micelle entanglement length ( $l_e$ ) to persistence length ( $l_p$ ) as:

$$\alpha_e \equiv \frac{l_e}{l_p} \quad (3.7)$$

If  $\alpha_e > 2$ , micelles coil up in the tube, which implies that the micelle length is larger than its tube length (Eq. (3.8a)). Otherwise, the micelle length is approximately equal to its tube length (Eq. (3.8b)).

$$L \approx L_t \cdot \sqrt{0.5\alpha_e}, \quad \alpha_e > 2 \quad (3.8a)$$

$$L \approx L_t, \quad \alpha_e \leq 2 \quad (3.8b)$$

The former is called the loosely entangled regime, while the latter one, with  $\alpha_e < 1$ , is the tightly entangled regime. A crossover between these regimes occurs in the range  $1 \leq \alpha_e \leq 2$ . Detailed information about these regimes can be found in references [Morse (1998a and 1998b)]. A formula to calculate the plateau modulus ( $G_N$ ) for any  $\alpha_e$  is [Zou and Larson (2014)]:

$$G_N = f(\alpha_e) \cdot 9.75 \frac{k_B T}{\alpha_e^{9/5} l_p^3} + [1 - f(\alpha_e)] \cdot \frac{28}{5\pi} \frac{\phi k_B T}{d^2 \alpha_e l_p} \quad (3.9a)$$

where  $\phi$  is the volume fraction of surfactant, and  $d$  is the micelle diameter. To get a smooth crossover from loosely (first term) to tightly (second term) entangled regimes, the weighting function  $f(\alpha_e)$  is taken to be [Zou and Larson (2014)]:

$$f(\alpha_e) = \frac{\alpha_e^3}{3 + \alpha_e^3} \quad (3.9b)$$

Note that while this functional form is arbitrary, in the middle of the cross-over the predictions for  $G_N$  from each of the two regimes differ by a factor of less than two, and the cross-over formula (Eq. (3.9a)) gives a value roughly halfway between the two limits. Hence the exact functional form is unlikely to matter much.

Bending motions, where micelle segments behave as bendable elastic rods, dominate on length scales smaller than the persistence length, as is revealed in rheological experiments by a three-quarters power law of modulus versus frequency at high frequencies (See Eq. (3.10a)) [Galvan-Miyoshi *et al.* (2008); Oelschlaeger *et al.* (2009)]. Like the high-frequency Rouse modes [Wang *et al.* (2010)], bending motions [Gittes and MacKintosh (1998)] are incorporated analytically by the following additive contributions to  $G'$  and  $G''$  [Zou and Larson (2014)]:

$$G'(\omega) = Re \left[ i^{\frac{3}{4}} \right] \frac{\rho}{15} \frac{k_B T}{l_p} (2\omega\tau_p)^{\frac{3}{4}}, \quad G''(\omega) = Im \left[ i^{\frac{3}{4}} \right] \frac{\rho}{15} \frac{k_B T}{l_p} (2\omega\tau_p)^{\frac{3}{4}} + \omega\eta_s \quad (3.10a)$$

$$with \quad \rho = \frac{4\phi}{\pi d^2}, \quad \tau_p = \frac{\zeta_{\perp} l_p^3}{k_B T} \quad (3.10b)$$

In the above, “ $Re[\cdot]$ ” and “ $Im[\cdot]$ ” refer to real and imaginary parts, “ $i$ ” is the imaginary unit, and  $\rho$  is the micelle contour length per unit volume, which is related to the micelle diameter ( $d$ ) and surfactant volume fraction ( $\phi$ ) by Eq. (3.10b). Note that Eq. (3.10b) involves a constant  $\zeta_{\perp}$  describing the drag coefficient for perpendicular bending motions [Morse (1998b)], which should be distinguished from the longitudinal drag coefficient  $\zeta$  for reptation in Eq. (3.2), i.e.:

$$\zeta = \frac{2\pi\eta_s}{\ln(\alpha_e^{0.6} l_p/d)}, \quad \zeta_{\perp} = \frac{4\pi\eta_s}{\ln(0.6\alpha_e^{0.6} l_p/d)} \quad (3.11)$$

where  $\eta_s$  is the solvent viscosity.

Apart from relaxation mechanisms, innovations in modeling breakage/rejoining and converting data from time to frequency enable fast simulations with an ensemble of 5000 WLMs by our mesoscopic method. Using pointers to track the locations of the ends of unrelaxed tube segments along discretized micellar chains, the number of pointers and their relative positions vary with time: pointers can be created by breakage, and moved and finally annihilated by chain

relaxation through reptation and CLFs. By summing the fraction of unrelaxed tube segments, the time-dependent stress relaxation function ( $\mu(t)$ ) can be calculated and squared to incorporate constraint release using the double reptation ansatz. Although largely empirical, we use double reptation since it has proven to be accurate for polydisperse polymers, and because no general, rigorous theory has been developed for constraint release in micelles with incessant breakage and rejoining. A schematic of the above procedure (called the “pointer algorithm”) is shown in Fig. 3.1, details of which can be found in our previous paper [Zou and Larson (2014)].

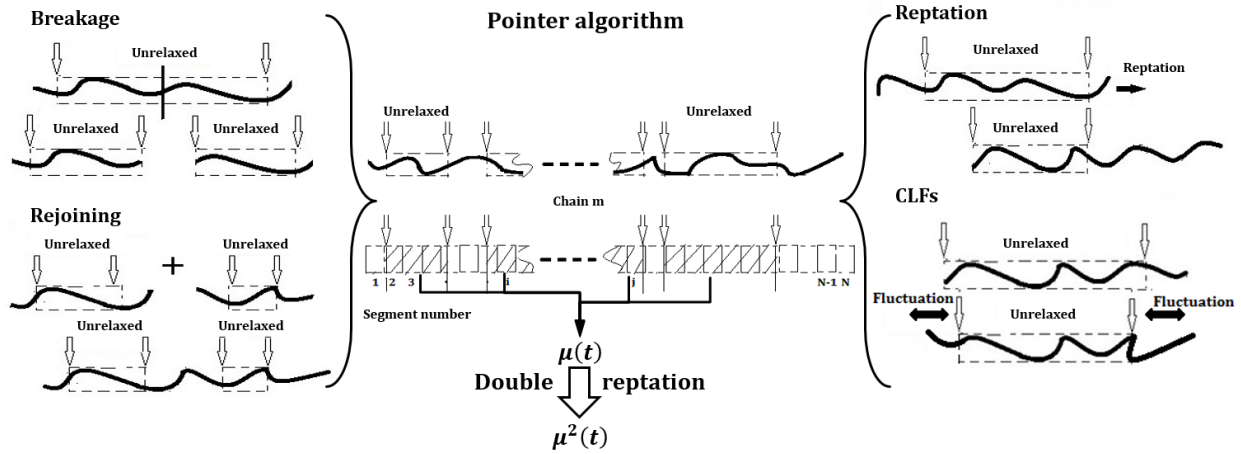


Figure 3.1 Schematic of pointer algorithm, showing the creation and movement of pointers by breakage and rejoining (left), and reptation and CLFs (right). In the center panel, the hatched zones represent unrelaxed tube segments.

Due to the failure of traditional Fourier transform methods as micellar parameters vary, a modified genetic algorithm (GA) is applied to facilitate the transformation of  $\mu^2(t)$  to the frequency domain with high frequency relaxation mechanisms added through an analytical function  $G^H$  [Zou and Larson (2014)]. Hence, our simulation model can be expressed in the following functional form:

$$G^*(\omega) = G_N \mathcal{F}[\mu^2(t, \varsigma, \langle L \rangle, \alpha_e, d)] + G^H(\omega, G_N, \langle L \rangle, \alpha_e, d) \quad (3.12)$$

where  $G^*(\omega)$  is the complex modulus, whose real and imaginary parts are  $G'(\omega)$  and  $G''(\omega)$ , respectively. The operator  $\mathcal{F}[\cdot]$  denotes the time-to-frequency transformation through a modified GA. On the right side of the above equation, the first term accounts for contributions from low frequency relaxation mechanisms: reptation, CLFs, and tube re-arrangement; while the second term represents analytical expressions for high frequency Rouse and bending motions.

According to Eq. (3.12), five characteristic parameters are used to predict the rheological behavior of WLM solutions, i.e.: plateau modulus ( $G_N$ ), dimensionless breakage rate ( $\zeta$ ), average micelle length ( $\langle L \rangle$ ), semi-flexibility coefficient ( $\alpha_e$ ), and micelle diameter ( $d$ ). Temperature ( $T$ ), surfactant volume fraction ( $\phi$ ), and solvent viscosity ( $\eta_s$ ), are known experimental parameters and not counted here as model parameters. Thus, by fitting rheological data with our simulation model, estimates for the five micellar parameters ( $G_N, \zeta, \langle L \rangle, \alpha_e, d$ ) can be obtained.

### III. Experimental Section

The WLM solutions used in this paper are aqueous solutions of SLE1S (sodium lauryl ether sulfate, Fig. 3.2(a)) and a mixture of SLE1S and CAPB (cocamidopropyl betaine, Fig. 3.2(b)) at 25°C. A simple salt (sodium chloride, NaCl) is added to both solutions, while the latter one also contains a 1 wt% perfume mixture. Due to the complexity of these commercial materials, a weight percentage instead of molar concentration is used here. An 11 wt% SLE1S/CAPB solution contains 9.85 wt% SLE1S and 1.15 wt% CAPB, where SLE1S is an abbreviation for commercial sodium lauryl ether sulfate with one ethoxyl group on average (but with polydispersity about this average); and CAPB is the co-surfactant. The perfume mixture consists of six organic components with their corresponding weight percentages i.e.: 1. synambran (CAS number: 6790-58-5, 10.7 wt%); 2. linalool (CAS number: 78-70-6, 23.3 wt%); 3. allylamylglycolate (CAS number: 67634-00-8, 13.5 wt%); 4. beta-ionone (CAS number: 14901-07-6, 11.5 wt%); 5. heliotropin (CAS number: 120-57-0, 15.4 wt%); and 6. undecavertol (CAS number: 81782-77-6, 25.6 wt%). The rheological properties of samples were measured by a TA Instruments DHR3 controlled-stress rheometer with TRIOS software using a 60mm Aluminum, 2 degree-cone. The cone geometry was inertially corrected prior to measurement, and the air bearing mapped in precision mode as prescribed in the TRIOS software. The frequency spectrum was collected using either 1% or 10% strain amplitude from 0.1 to 500 rad/s, but edited to include only data where the raw phase angle was below the 180 degree limit in TRIOS software. For these samples this usually limited the frequency spectrum to 250-316 rad/s, and abrupt changes in moduli (most easily indicated in tan delta) would be rejected. For the former solution, diffusing wave spectroscopy (DWS) is also applied to get the high frequency behavior (1~ 150,000 rad/s). The wavelength of light and the diameter of beads used in DWS are 532 nm and 630 nm, respectively. The beads are made of IDC polystyrene latex from Life



Technologies (cat# S37495) with hydrophobic surface, which are stabilized with a low level of sulfate charges and surfactant free. The WLM solution samples for DWS measurement were mixed with 0.5 wt% beads before adding salt to ensure good mixing prior to thickening with salt. After 12 hours equilibration, samples were measured in 5 mm glass cells on LS Instruments RheoLab II system. The transport mean free path  $l^*$  ( $= 580 \mu\text{m}$ ) was determined from the control sample with the same-size beads in water. Details about DWS can be found in references [Buchanan *et al.* (2005); Galvan-Miyoshi *et al.* (2008); Oelschlaeger *et al.* (2009)]. Samples were both prepared and measured at the Procter & Gamble company.

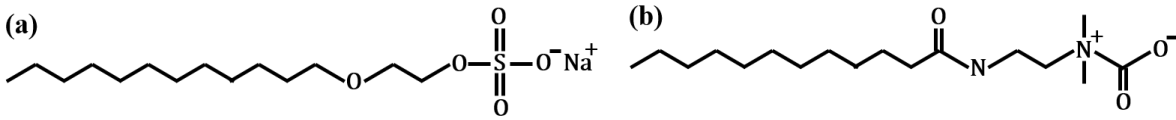


Figure 3.2 Molecular structure of (a) SLE1S and (b) CAPB.

#### IV. Data Fitting Procedure

##### 1. Empirical correlations

As shown in our previous paper [Zou and Larson (2014)], empirical relationships between local rheological features and micellar parameters are constructed from simulation results using the pointer algorithm to obtain good initial guesses of WLM properties. These features are the local maximum and minimum values of  $G''$  along with the corresponding frequencies, denoted as  $(\omega_{max}, G''_{max})$  and  $(\omega_{min}, G''_{min})$ , respectively. Motivated by the work Cates and coworkers [Turner and Cates (1991); Granek (1994)],  $G''_{max}/G_N$ , or the height of the semi-circle on the normalized Cole-Cole plot, is related to the dimensionless breakage rate ( $\zeta$ ), while the “dip” at high frequencies (i.e.,  $G''_{min}/G_N$ ) is related to the dimensionless average tube length ( $\bar{Z}_t$ , defined in Eq. (3.13b)). Instead of using the stress relaxation time ( $\tau$ , Eq. (3.4)),  $\omega_{max}$  is introduced to extract the characteristic time (i.e., reptation time,  $\bar{\tau}_{rep}$ ) from the frequency information. An illustration for these local features is shown in Fig. 3.3, along with empirical correlations for the above quantities, given in our previous paper [Zou and Larson (2014)], and repeated here as Eq. (3.13), given below.

$$\omega_{max} \bar{\tau}_{rep} = B \cdot \zeta^{-0.63}, \quad B = 2.1, \quad 1 < \alpha_e < 3 \quad (3.13a)$$

$$\frac{G''_{min}}{G_N} = C \bar{Z}_t^{-0.61}, \quad \bar{Z}_t = \frac{\langle L_t \rangle}{l_e}, \quad 1 < \alpha_e < 3 \quad (3.13b)$$

$$\frac{G''_{max}}{G_N} = -0.0657 \log(\zeta) + 0.265, \quad \bar{Z} = \frac{\langle L \rangle}{l_e} > 10 \quad (3.13c)$$

Since the above correlations are only accurate over a limited range of  $\alpha_e$  and  $\bar{Z}$  (average entanglement number), their corresponding extensions are achieved by replacing the prefactor  $B$  with a function of  $\alpha_e$  for Eq. (3.13a) and  $\bar{Z}_t$  with  $\bar{Z}$  for Eq. (3.13b) in what follows. Note that “log” and “ln” denote the logarithmic base of 10 and  $e$ , respectively.

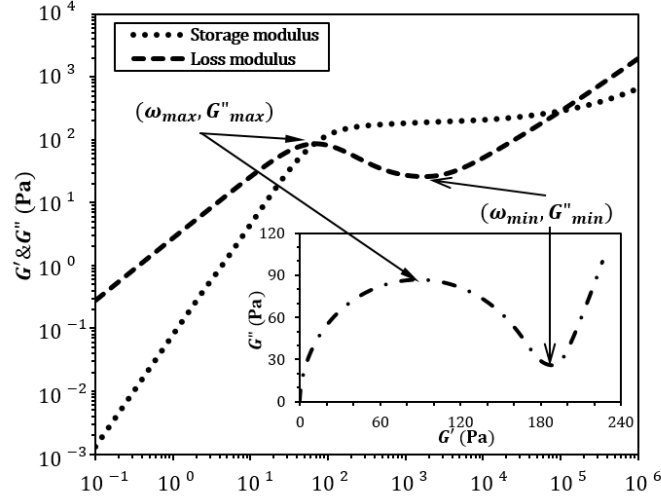


Figure 3.3 Illustration of local rheological features. Inset: Cole-Cole plot.

By fixing  $\zeta$  ( $= 0.05$ ), a log-log plot of  $\omega_{max} \bar{\tau}_{rep}$  versus  $\alpha_e$  is obtained in Fig. 3.4(a), with a power law exponent of 3. From Fig. 3.4(b), the dependence of  $\omega_{max} \bar{\tau}_{rep} \alpha_e^{-3}$  on  $\zeta$  and the associated prefactor are obtained by the slope and intercept with  $\log(\zeta) = 0$ , respectively, according to the linear fit on the log-log plot. The extended formula, covering the experimentally relevant range of  $\alpha_e$  (0.3~8) is given in Eq. (3.14a).

By plotting  $G''_{min}/G_N$  against  $\bar{Z}$  logarithmically in Fig. 3.5, the exponent of the power law correlation between these two quantities is obtained in each of three regions whose range depends on the specific value of  $\zeta$ . When  $\bar{Z}$  is small, WLMs are short and loosely entangled, and the exponent is -1 (denoted by the slope of solid lines in Fig. 3.5). Once  $\bar{Z}$  becomes larger than a critical value ( $\bar{Z}_c$ ), the exponent changes to -3/4, shown by the slope of dashed lines in Fig. 3.5, which is close to the power-law prediction of Cates and coworkers (-0.8, Eq. (3.5)). Micelle semi-flexibility ( $\alpha_e$ ) has no effect on this power law dependence: the data points for micelles with different  $\langle L \rangle$  and  $\alpha_e$  merge onto common curves (denoted by dashed lines in Fig. 3.5).

However, if WLMs are entangled tightly enough ( $\alpha_e < 1.5$ ), deviations from the above common curves appear as dash-dotted parallel lines with a slope of  $-1/5$  in Fig. 3.5. Note that the range of the first region ( $\bar{Z} < \bar{Z}_c$ ) varies with  $\zeta$ : an increase of  $\zeta$  decreases  $\bar{Z}_c$ , thus limiting its range. The relationship between  $\bar{Z}_c$  and  $\zeta$  is given in Eq. (3.14b).

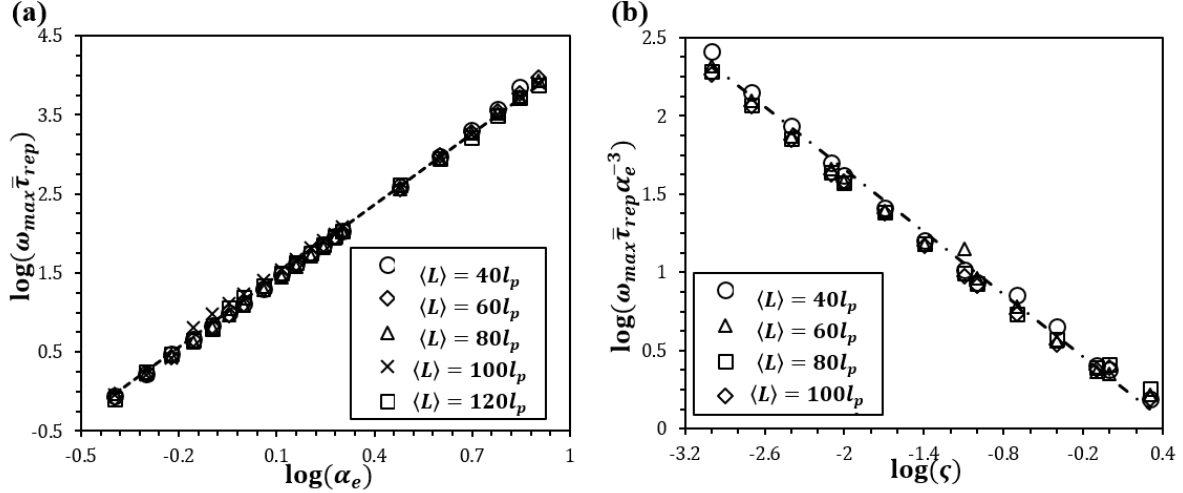


Figure 3.4 Extended empirical correlation for the dependence of  $\omega_{max}\bar{\tau}_{rep}$  on semi-flexibility coefficient  $\alpha_e = l_e/l_p$  and dimensionless breakage rate  $\zeta$  with  $l_p = 25 \text{ nm}$  and  $d = 5 \text{ nm}$ . (a) The linear fit (dashed line) on the log-log plot has a slope of 3 with  $R^2 = 0.999$  for fixed  $\zeta = 0.05$ ; (b) The linear fit (dash-dotted line) on the log-log plot has a slope of  $-2/3$  and intercept of  $\log 2$  when  $\log(\zeta) = 0$  with  $R^2 = 0.995$ . Note that data in the above figures all come from simulations.

The above-extended empirical correlations are summed up as:

$$\omega_{max}\bar{\tau}_{rep} = 2\alpha_e^3\zeta^{-2/3} \quad (3.14a)$$

$$\frac{G''_{min}}{G_N} = C\bar{Z}^{-a} \text{ with } \bar{Z}_c = \zeta^{-3/4} \begin{cases} a = 1, C \cong \zeta^{-1/4}, (\bar{Z} \leq \bar{Z}_c \text{ and } \alpha_e > 1.5) \\ a = 3/4, C \cong \zeta^{-1/16}, (\bar{Z} > \bar{Z}_c \text{ and } \alpha_e > 1.5) \\ a = 1/5, C \cong \zeta^{-1/16} \left(\frac{2\langle L \rangle}{3l_p}\right)^{-11/20}, (\alpha_e \leq 1.5) \end{cases} \quad (3.14b)$$

$$\frac{G''_{max}}{G_N} = -0.0657 \log(\zeta) + 0.265 \quad (3.14c)$$

Note that the above correlations (Eq. (3.14)) are all based on simulation results with  $10^{-3} < \zeta < 10$ ,  $0.3 < \alpha_e < 8$  (these ranges encompass the values typical of actual WLM solutions), and well-defined local maximum and minimum  $G''_{max}$  and  $G''_{min}$ , but are nearly independent of micelle persistence length  $l_p$  and diameter  $d$  which have only a small effect on data normalized by  $G_N$  at frequencies below that at which  $G''$  has its minimum,  $G''_{min}$  [Zou and

Larson (2014)]. If there is no well-defined maximum and minimum in  $G''$ , the crossover frequency ( $\omega_{cross}$ ) and the corresponding  $G''(\omega_{cross})$  will be treated as  $\omega_{max}$  and  $G''_{max}(=G''_{min})$ , respectively. This situation usually occurs for WLM solutions with  $\bar{Z} \ll \bar{Z}_c$ . (Where there is a maximum in  $G''$ , the crossover point ( $G''_c$ ) is only about a few percent of the plateau modulus ( $G_N$ ), and we therefore don't expect there to be a large difference in results obtained using the cross-over point, instead of the maximum in  $G''$ .)

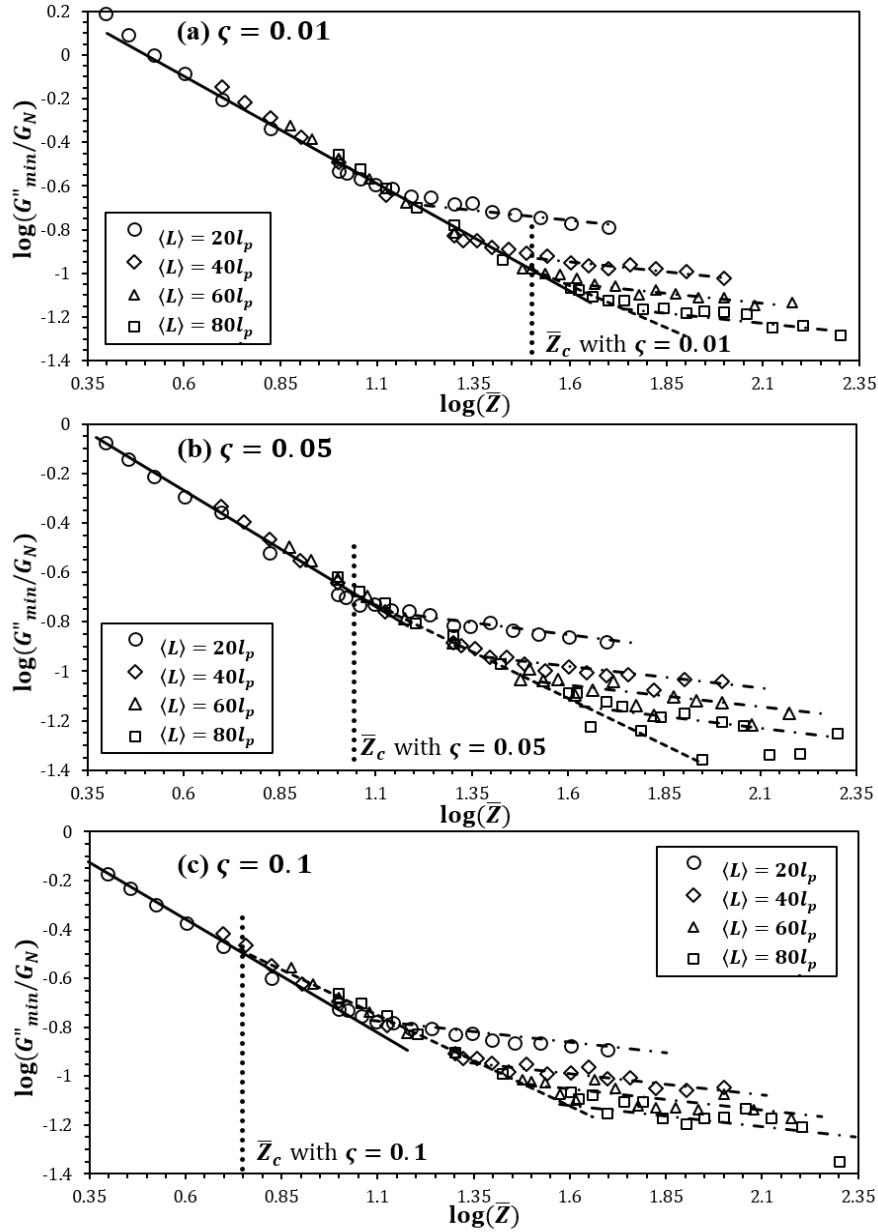


Figure 3.5 Extended empirical correlation for the dependence of  $G''_{min}/G_N$  on average entanglement number ( $\bar{Z}$ ) by varying average micelle length ( $\langle L \rangle$ ) and semi-flexibility coefficient ( $\alpha_e$ ) with  $l_p = 25 \text{ nm}$

and  $d = 5 \text{ nm}$ . (a)  $\zeta = 0.01$ ; (b)  $\zeta = 0.05$ ; (c)  $\zeta = 0.1$ . Note in the above figures that the slope of solid lines, dashed lines, and dot-dashed lines are -1, -3/4, and -1/5 respectively, and all the data are from simulations.

The empirical correlations in Eq. (3.14) are useful for inferring the properties of WLM solutions from rheological data ( $G'$  and  $G''$ ). As an example, we consider the temperature-dependent rheological data in Fig. 6 from reference [Siriwatwechakul *et al.* (2004)], which is for a 2 wt% erucyl bis (hydroxyethyl) methylammonium chloride (EHAC) surfactant solution with added 4 wt% potassium chloride (KCl) salt. From the lowest temperature (25°C, denoted by circles) to the highest one (45°C, denoted by squares), the value of  $G''_{min}$  triples while  $G''_{max}$  and  $G_N$  (plateau modulus, denoted by the magnitude of the plateau region for  $G'$ ) remain constant. A frequency shift is also observed with around a 30-fold increase of  $\omega_{max}$ .

Since  $G''_{max}$  ( $\cong 2 \text{ Pa}$ ) and  $G_N$  ( $\cong 5 \text{ Pa}$ ) remain unchanged, according to Eq. (3.14c),  $\zeta$  can be taken as a constant, which is approximately equal to 0.01. Assuming the solution lies in the loosely entangled regime ( $\alpha_e > 2$ ), then  $\bar{Z} < 0.5\langle L \rangle/l_p$ , and if  $\zeta = 0.01$ , as shown by the solid line in Fig. 3.5(a), the power-law dependence of  $G''_{min}/G_N$  on  $\bar{Z}$  (Eq. (3.14b)) is in the regime where the exponent is -1, which means:

$$\bar{Z} \sim 1/G''_{min}$$

Based on Eqs. (3.2), (3.7), (3.8a) and the definition of  $\bar{Z}$  given in Eq. (3.13c), we can also find:

$$\bar{\tau}_{rep} \sim \langle L \rangle \langle L_t \rangle^2 \sim \bar{Z}^3 l_p^3 \alpha_e^2$$

For a constant  $G_N$ , according to Eq. (3.9), for the loosely entangled regime ( $f(\alpha_e) \approx 1$ ):

$$\alpha_e \sim l_p^{-5/3}$$

Then, substituting the above relationships for  $\bar{Z}$ ,  $\bar{\tau}_{rep}$ ,  $\alpha_e$  into Eq. (3.14a), yields:

$$\omega_{max}/G''_{min}^3 \sim l_p^{-14/3}$$

With an approximate 30-fold and 3-fold increase in  $\omega_{max}$  and  $G''_{min}$ , respectively, the above qualitative correlation implies that there is little change in micelle persistence length ( $l_p$ ) from 25°C to 45°C. Thus, in this case temperature has little effect on  $l_p$ , which is confirmed by the collapse of the data for  $G''$  at high frequencies (shown by the solid line in Fig. 3.6, which is a region influenced by persistence length, and would therefore show a shift with temperature if  $l_p$  were temperature dependent.)

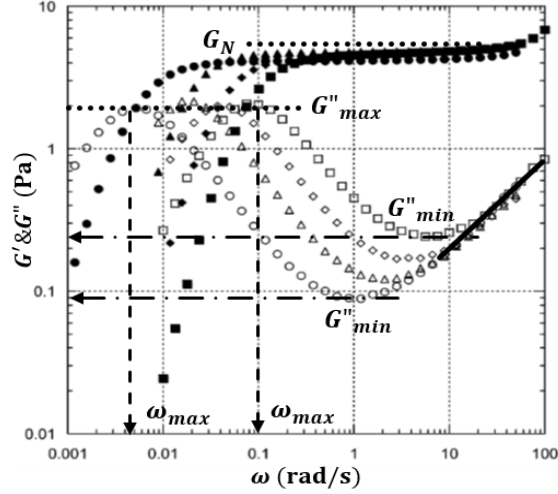


Figure 3.6 Temperature-dependent rheological data from reference [Buchanan *et al.* (2005)], showing temperature shifts of  $G''_{max}$ ,  $G''_{min}$  and  $\omega_{max}$ . Circles:  $T = 25^\circ\text{C}$ ; triangles:  $T = 35^\circ\text{C}$ ; diamonds:  $T = 40^\circ\text{C}$ ; squares:  $T = 45^\circ\text{C}$ .

## 2. Data fitting procedure

For quantitative analyses of WLM properties, we develop an iterative experimental data fitting procedure to achieve accurate estimates of micellar parameters with low fitting errors. The procedure relies heavily on empirical correlations (Eq. (3.14)) as well as theoretical equations (Eqs. (3.2), (3.8), (3.9)). Fitting deviations are calculated separately within each of the four frequency domains depicted in Fig. 3.7 (low frequency, transition 1, transition 2, and high frequency):

$$\varepsilon_i = \frac{1}{2N_i} \sum_{j=1}^{N_i} \left\{ \ln \left[ \frac{G'^{fit}(\omega_{i,j}^{exp})}{G'^{exp}(\omega_{i,j}^{exp})} \right] + \ln \left[ \frac{G''^{fit}(\omega_{i,j}^{exp})}{G''^{exp}(\omega_{i,j}^{exp})} \right] \right\}, i = 1, \dots, 4 \quad (3.15a)$$

$$\text{with } \omega_{1,N_1}^{exp} = \omega_{max}^{exp}, \omega_{2,N_2}^{exp} = \omega_{min}^{exp}, \omega_{3,N_3}^{exp} = 10\omega_{min}^{exp} \quad (3.15b)$$

where superscripts *exp* and *fit* represent data points from experiment and simulation, respectively.  $N_i$  is the number of data points in each frequency range. Note that the above error is not a least-squares error, but is a net deviation in the logarithmic ratio of fitted to experimental results, averaged over each frequency domain. We use this measure of error because it allows us to use the net deviation direction (positive or negative) in that domain to better determine how to adjust fitting parameters (See *Appendix B* for details) that are most important for that domain and hence quickly reach an optimal fit (i.e. within around 12 iterations). Such a rapidly converging method is needed because each iteration requires a separate simulation of the relaxation of 5000 micelles and takes 2~3 hours on a single CPU. However, the method does require a separate

measure of error averaged over each of four separate domains to prevent positive deviations in one domain from cancelling negative ones in another. The key to the success of this method is the monotonic behavior of  $G''$  within each domain and the dominant effect of just one or two fitting parameters in each domain.

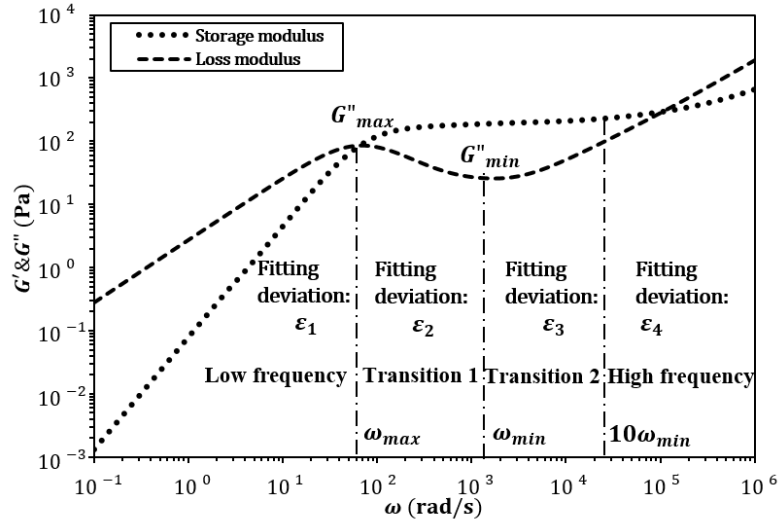


Figure 3.7 Definition of frequency regions and associated fitting deviations.

Besides the overall goodness of fit represented by the values of  $\varepsilon_i$  in Eq. (3.15), differences between experimental and predicted local features, i.e., the values of  $(\omega_{max}, G''_{max})$  and  $(\omega_{min}, G''_{min})$ , can also help iterate to a better estimation of parameters, as alluded to above. Although they are not included in the set of five model fitting parameters  $(G_N, \zeta, \langle L \rangle, \alpha_e, d)$  listed in Eq. (3.12), other micellar parameters  $\bar{\tau}_{rep}, \bar{Z}$  (defined in Eq. (3.2) and (3.13c)) as well as  $\langle L_t \rangle, l_e, l_p, \zeta$  (Eqs. (3.7), (3.8), (3.11)) need to be determined during parameter modification. A “map” (Fig. 3.8) is established for that purpose, which shows how all the additional parameters  $(\bar{\tau}_{rep}, \bar{Z}, \langle L_t \rangle, l_e, l_p, \zeta)$  can be derived from the five *independent* model parameters  $(G_N, \zeta, \langle L \rangle, \alpha_e, d)$  along with theoretical relationships (Eqs. (3.2), (3.3), (3.7), (3.8), (3.9), and (3.11)) and known experimental parameters  $(T, \phi, \eta_s)$ .

The flowchart of the data fitting procedure is laid out in *Appendix B* (Fig. B.1). At the end of each simulation (details of which can be found in our previous paper [Zou and Larson (2014)]), fitting deviations  $(\varepsilon_1, \varepsilon_2, \varepsilon_3, \varepsilon_4)$  are calculated through Eq. (3.15) and predicted local feature-related points are obtained. Using the parameter “map” (See Fig. 3.8), the five independent model parameters  $(G_N, \zeta, \langle L \rangle, \alpha_e, d)$  from the last round of simulation are converted

into  $(G_N, \zeta, \bar{\tau}_{rep}, \bar{Z}, l_p)$  for further modifications: two different routes are taken in alternating steps to minimize both the overall fitting deviations and the difference in local features between experimental points  $(\omega_{min}^{exp}, G_{min}^{exp}, \omega_{min}^{exp}, G_{min}^{exp})$  and simulated ones  $(\omega_{max}^{fit}, G_{max}^{fit}, \omega_{min}^{fit}, G_{min}^{fit})$ , respectively. Detailed equations used to determine the values of five model parameters for the next round of simulation are also derived in Appendix A. The fitting deviations and differences in local features are also used to constrain the modified values of  $\zeta, \bar{\tau}_{rep}, l_p$  within ranges of limited width (Eq. (B.8), Fig. B.2 in *Appendix B*), leading to more stable convergence. The code and an example input file can be found under our website: <http://cheresearch.engin.umich.edu/larson/software.html>.

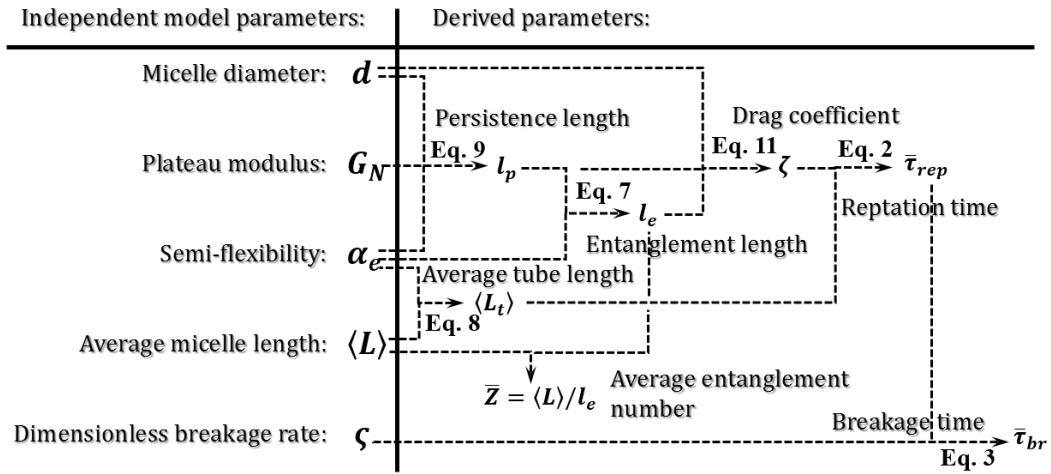


Figure 3.8 Parameter map showing relationships between the five independent model parameters ( $G_N, \zeta, \langle L \rangle, \alpha_e, d$ ) and the additional parameters ( $\bar{\tau}_{rep}, \bar{Z}, \langle L_t \rangle, l_e, l_p, \zeta$ ) derived from them. Arrows point towards quantities derived from the equations given. Dashed lines connect to the input parameters required by the given equation.

After ~6-8 iterations, the simulated curves typically have average fitting deviations (Eq. (3.15)) around 10% for each frequency range. In general, 12 iterations are used to achieve the best fit with less than 10% average fitting deviations and the least difference of local-feature points. The computational time is around 6-12 hours for a single processor. Since the above procedure is based on the empirical correlations in Eq. (3.14), in case a well-defined local maximum and minimum are missing, the following substitutions are made:  $\omega_{max}$  ( $= \omega_{cross}$ ),  $G_{max}''$  ( $= G_{cross}''$ ),  $\omega_{min}$  ( $= 2\omega_{max}$ ), and  $G_{min}''$  ( $= G_{max}''$ ). As explained in our previous work [Zou and Larson (2014)], our method is incapable of determining micelle diameter ( $d$ ) from fitting rheological data, but a reasonably accurate value for  $d$  can be supplied from other



measurements, for instance small angle neutron scattering (SANS) [Marignan *et al.* (1989)], or from molecular modeling.

## V. Results and Discussion

### 1. Fitting results

Experimental data and the corresponding fits to mechanical rheometric data, DWS data, and a combination of these two data sets, i.e., mechanical data at low frequencies (<50 rad/s) and DWS data at high frequencies (>50 rad/s), for the same WLM solution (6.67 wt% SLE1S, 3.10 wt% NaCl with solvent viscosity  $\eta_s=0.9$  cP at 25°C) are given in Fig. 3.9 with resulting estimates of parameters shown in Table 3.1. The persistence length ( $l_p$ ) over 100 nm is obtained for these micelles formed by SLE1S, which is much greater than that for the classical CTAB or CPyCl [Chen *et al.* (2006)]. The reason for this greater value of  $l_p$ , we believe, is due to the larger micelle diameter resulting from the larger headgroup and the longer average tail length of SLE1S surfactant molecule, since the estimation of  $l_p$  strongly depends on micelle diameter (See Table B.1 in *Appendix B*). We note that in classic beam theory, a solid cylinder has a bending modulus that scales as the fourth power of its diameter, and so a modest 20% increase in diameter can double the persistence length. While micelles are not solid cylinders, by analogy, a steep dependence of persistence length on micelle diameter might nevertheless be expected.

Table 3.1 Estimation of parameters from fits in Fig. 3.9(b), (c), and (d).

Parameters	Mechanical data	DWS data	Combined data
$G_N$ (Pa)	115	105	115
$\zeta$	2.49	1.16	1.82
$\langle L \rangle$ ( $\mu\text{m}$ )	1.45	1.60	1.59
$\alpha_e$	1.35	1.41	1.36
$d$ (nm)	4	4	4
$l_e$ (nm)	155	161	153
$l_p$ (nm)	116	114	112

Note: the value of  $d = 4$  nm used in simulations for the WLM solution is taken from SANS measurement by our collaborators Karsten Vogt and Gregory Beaucage at the University of Cincinnati.

According to Fig. 3.9(a), mechanical rheometric data overlaps well with that for DWS in the frequency range from 10 rad/s to 50 rad/s. Mismatches at low and high frequencies are attributed to errors in DWS and mechanical rheometry, respectively, which lead to differences in

parameter estimates as shown in Table 3.1. For the parameters  $G_N$ ,  $\zeta$ , and  $\alpha_e$ , the values extracted from DWS data alone deviate more from the values obtained from the combined data than do the values from the mechanical data alone. This suggests a greater importance of low frequency behavior than of high frequency behavior on estimations of these parameters. The over six frequency-decade fit to the combined data (Fig. 3.9(d)) with less than 5% absolute average deviation between predicted and measured data points suggests that the viscoelastic behaviors of micelle solutions are well depicted by our simulation method. Although little difference is observed for estimates of all parameters obtained from mechanical and combined data sets (even the persistence length is hardly changed when the DWS data are included as shown by Table 1), the accuracies of estimations (i.e. insensitivity percentage discussed later) vary with parameters and availability of high-frequency data (i.e. the data beyond  $\omega_{min}$ ). Thus, while fits using the mechanical data only were adequate for the data of Fig. 3.9, in general, high-frequency data are important to extract an accurate value of  $l_p$ , as is demonstrated in the following sensitivity study.

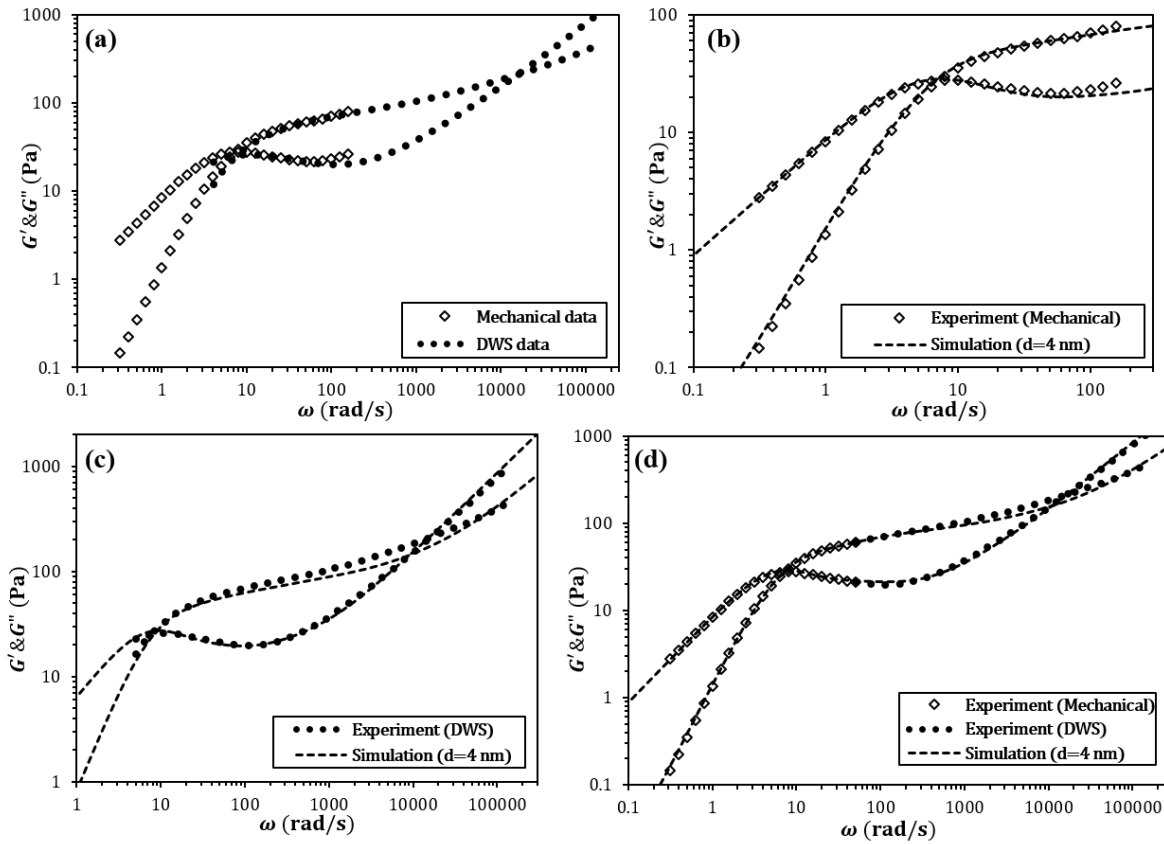


Figure 3.9 Experimental data and fitting results with  $d = 4 \text{ nm}$  for WLM solution (6.67 wt% SLE1S, 3.10 wt% NaCl with solvent viscosity  $\eta_s = 0.9 \text{ cP}$  at  $25^\circ\text{C}$ ). (a) Experimental data; (b) Fits for mechanical rheometric data; (c) Fits for DWS data; (d) Fits for combined data.

## 2. Sensitivity study

Here, the sensitivity of parameter determination to error or noise is assessed by a constrained fitting procedure. For this purpose, the combined (mechanical & DWS) experimental data (Fig. 3.9(d)) is used with its best-fit parameters shown in Table 3.1. Starting from these best-fit values, we take each parameter, one at a time, and artificially change its value to a new one that deviates from its best-fit value by a given percentage. Then, holding this one parameter value fixed, we adjust the other parameters to obtain constrained best fits to the rheological data. An exception is the value of  $d$ , which we hold at 4 nm according to SANS measurements, since its value cannot be accurately determined from rheology as discussed earlier. This inability of rheology to determine micelle diameter is illustrated by Fig. B.3 in *Appendix B* with the corresponding fitted parameters given in Table B.1, where no significant difference is observed among fitting curves for micelle diameter varying between 3 nm and 4.5 nm (the range encompass the values typical of actual WLM solutions). Based on this constrained fitting, the deviation between experimental and fitted curves is a measure of the sensitivity of the fit to the value of the constrained parameter. As an illustration, the effect of varying micelle persistence length ( $l_p$ ) is given below.

Table 3.2 Sensitivity analysis, showing effect of variation in  $l_p$  on best-fit values of other parameters for data of Fig. 3.9(d).

Parameters	70% $l_p$	80% $l_p$	90% $l_p$	Best-fit $l_p$	110% $l_p$	120% $l_p$	130% $l_p$	140% $l_p$	150% $l_p$
$G_N$ (Pa)	138.5	121	114	115	108	104	97.5	95	92
$\zeta$	15.58	2.06	1.10	1.82	1.53	0.96	0.76	0.93	0.69
$\langle L \rangle$ ( $\mu\text{m}$ )	0.927	1.59	1.80	1.59	1.58	1.83	1.92	1.73	1.87
$\alpha_e$	1.516	1.497	1.446	1.363	1.341	1.304	1.288	1.261	1.238
$l_e$ (nm)	119	134	146	153	165	176	188	198	208
$l_p$ (nm)	78.5	89.5	101	112	123	135	146	157	168
$\varepsilon_{max}$	20.8%	16.2%	9.6%	4.1%	5.3%	5.6%	10.7%	14.8%	19.5%

Note that the error ( $\varepsilon_{max}$ ) is the absolute maximum from the four average fitting derivations ( $\varepsilon_1, \varepsilon_2, \varepsilon_3, \varepsilon_4$ , defined in Eq. (3.15)). By varying  $l_p$  from its unconstrained best-fit value, the maximum average fitting deviation occurs in the high frequency region, as shown by Fig. 3.10.

As shown by Table 3.2 and Fig. 3.10, a variation of  $l_p$  from its best-fit value drives all the other parameters ( $G_N, \zeta, \langle L \rangle, \alpha_e, l_e$ ) away from their unconstrained best-fit values in order to optimize the goodness of the constrained fit. With an increase in variation of  $l_p$  from its best-fit value, poorer fits are obtained at high frequencies (i.e., in the transition 2 and the high-frequency

regions; see Fig. 3.7). A similar analysis is performed for other parameters  $G_N$ ,  $\zeta$ ,  $\langle L \rangle$ ,  $\alpha_e$ , and  $l_e$  with their corresponding fits as given in Appendix B. We here define the “insensitivity percentage” for a given parameter to be the maximum percentage variation in that parameter which can be allowed, while retaining an absolute maximum average fitting error ( $\varepsilon_{max}$ , defined in the note of Table 3.2) of no more than 10% among all the four frequency regions. Note that a higher value of the “insensitivity percentage” implies a lower sensitivity of the fit to that parameter value. The “insensitivity percentage” can therefore be taken as an estimate of the “likely error” in that parameter value. We give the insensitivity percentages in Table 3.3.

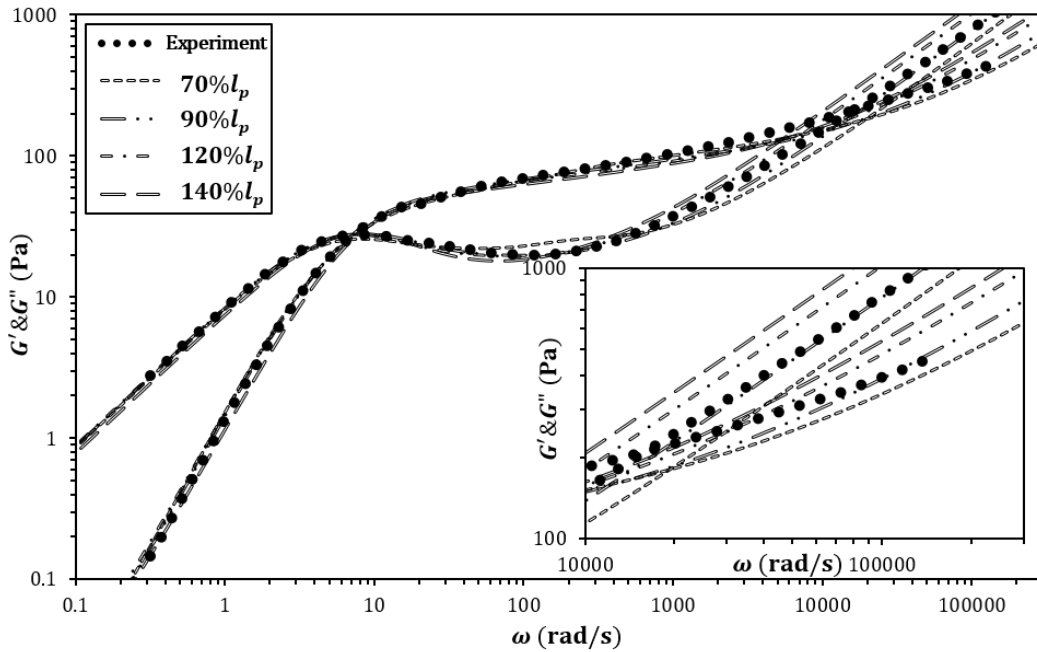


Figure 3.10 Sensitivity of fits to the value of  $l_p$  for combined mechanical & DWS data in Fig. 3.9(d). Each curve results from a best fit of other parameters, with  $l_p$  constrained at a given percentage of the unconstrained best-fit value. The inset shows an enlarged view of the high-frequency fitting.

If high-frequency DWS data are not available, and fittings must be made to mechanical rheometric data alone, Fig. 3.11 shows that there is a larger insensitivity percentage ( $\pm 20\% \sim \pm 30\%$ ) in persistence length  $l_p$  than is the case when fits are made to combined mechanical & DWS data, as in Fig. 3.10. As shown by Fig. 3.10 and 3.11, a larger  $l_p$  leads to a somewhat smaller  $\omega_{min}$  causing the minimum in  $G''$  to shift to a lower frequency, due to a greater contribution of bending modes (Eq. (3.10)) with an increase of  $l_p$ . An analytical expression for  $\omega_{min}$  can be found in reference [Granek (1994)]. This shift in  $\omega_{min}$  and the

corresponding shift in  $G''_{min}$ , if available from mechanical data, are in principle adequate to determine the value of  $l_p$  from mechanical data alone. However, compared to the large changes in the high-frequency data, to which the value of  $l_p$  is most sensitive, the effect of varying  $l_p$  on  $\omega_{min}$  is modest (Fig. 3.10 and 3.11). Thus, the greater uncertainty in predicting  $l_p$  from mechanical data alone arises from the importance of the high frequency data in securing an accurate estimate of  $l_p$  (See Fig. 3.10 at high frequencies). In addition, mechanical rheometric measurements are problematic at the upper range of their frequency, and fitting these data precisely sometimes require such a small  $l_p$  that deviations occur in fits to the lower-frequency mechanical data, as shown by the line for  $60\%l_p$  in Fig. 3.11, which gives a best fit to the data near the minimum in  $G''$ , but fails at lower frequency. Thus, DWS data should, if possible, be combined with the mechanical data for a more accurate and confident estimation of  $l_p$ , especially when the mechanical data do not reach frequencies high enough to resolve the local minimum in  $G''$ , or the highest-frequency mechanical data cannot be well fit without producing a poor fit at lower frequency.

Table 3.3 The summary of insensitivity percentages for micellar parameters for combined mechanical & DWS data of Fig. 3.9(d).

Parameter	Insensitivity percentage	Regions most sensitive to parameter	
		$G'(\omega)$	$G''(\omega)$
$G_N$	$\pm 10\%$	Transition 1 & 2	Transition 1
$\zeta$	$\pm 20\% \sim \pm 30\%$	Low frequency	Low frequency
$\langle L \rangle$	$\pm 30\%$	Low frequency, Transition 1	Low frequency, Transition 1
$\alpha_e$	$\pm 2.5\% \sim \pm 5\%$	Transition 1 & 2	Transition 1
$l_e$	$\pm 5\% \sim \pm 10\%$	Transition 1 & 2	Transition 1, High frequency
$l_p$	$\pm 10\% \sim \pm 20\%$	High frequency	Transition 2, High frequency

While DWS data are very helpful to determine an accurate and trustworthy value of  $l_p$ , the data overlap between mechanical rheometry and DWS measurements becomes unsatisfactory in various cases, for instance, at low surfactant concentration. A vertical shift of the DWS data (which is typically high frequency data) is often made in the literature to line up the DWS data with the mechanical data [Willenbacher *et al.* (2007); Oelschlaeger *et al.* (2009); Oelschlaeger *et al.* (2010);], but the validity of this remains unclear. A detailed discussion of the relationship between mechanical rheometry (macro-rheology) and particle-related DWS (micro-rheology) can be found in Buchanan *et al.* (2005).

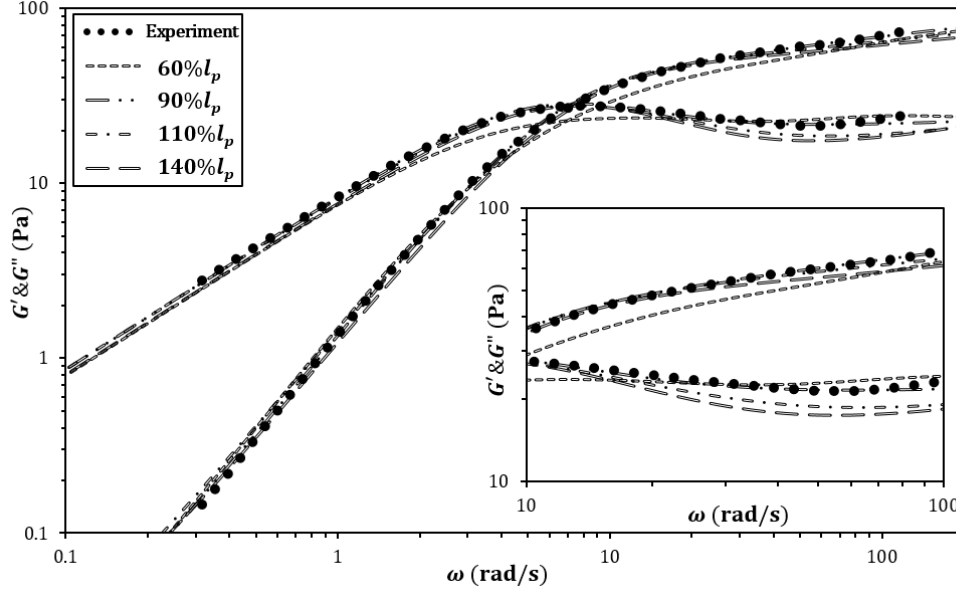


Figure 3.11 The same as Fig. 3.10, except for mechanical data only shown in Fig. 3.9(b). The inset shows an enlarged view of the fitting near the minimum in  $G''$ .

### 3. Effect of salt

By effectively screening out the electrostatic interaction between surfactant charged headgroups, added salt greatly affects the rheological properties of micellar solutions, which is reflected in a sharp rise of the zero shear viscosity ( $\eta_0$ ) with increasing salt concentration ( $c_s$ ) at low salt concentration, followed by a decrease in  $\eta_0$  at high salt concentration. This non-monotonic dependence of  $\eta_0$  on  $c_s$  is referred to as a “salt curve.” The growth of WLMs and formation of micelle branches is believed to cause the increase and the subsequent decrease in viscosity, respectively [Khatory and Kern *et al.* (1993)]. However, shifts of the salt curve are often observed when other additives (alcohols, perfumes, and organic solvents) are added to the surfactant-salt solutions because of their partial or complete incorporation into micelles [Fischer and Fieber (2009); Parker and Fieber (2013)].

In what follows, using our data fitting procedure, we extract micellar parameters from the rheological data ( $G'$  and  $G''$ ) for SLE1S/CAPB surfactant solutions at 11 wt% of surfactants plus co-surfactants and 1 wt% perfume (detailed components are given in Section III), with added NaCl varying from 0.63 wt% to 2 wt%. The salt curve and salt concentration-dependent micellar properties are shown in Fig. 3.12 (where the positions of the zero shear viscosity maxima are indicated by arrows), while the measured mechanical data and the corresponding fitting curves

can be found in Fig. 3.13. These data sets do not include DWS measurements, which limits somewhat the accuracy of the parameters extracted as we discussed above.

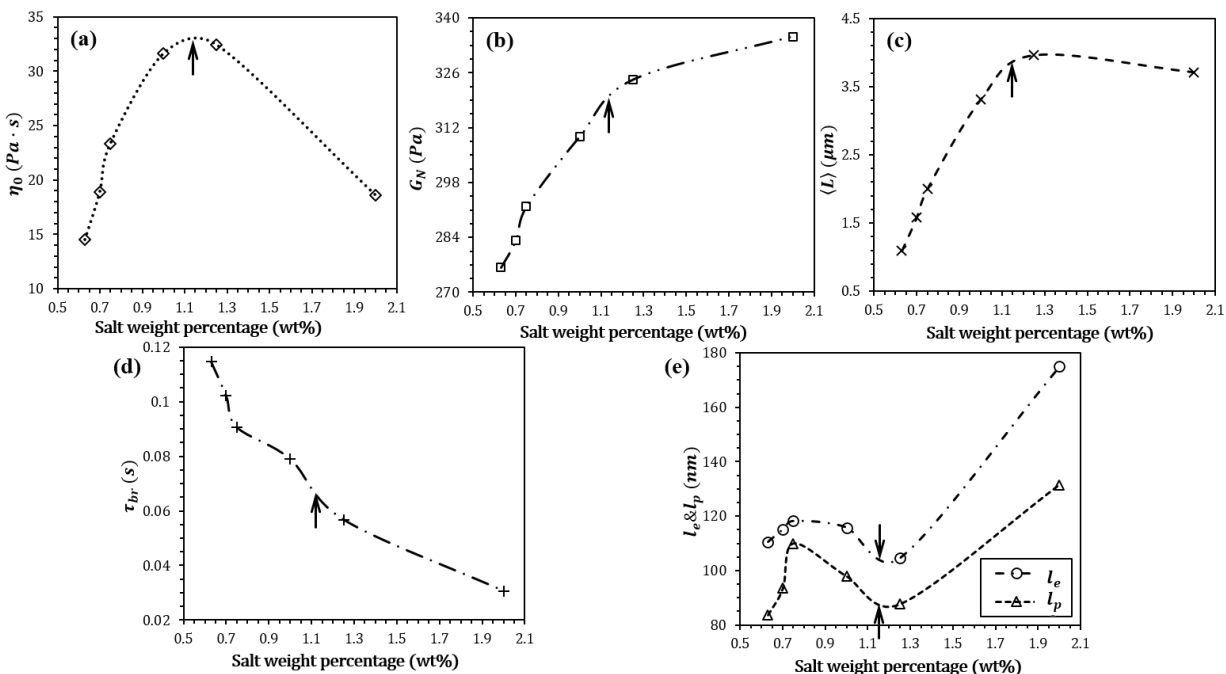


Figure 3.12 The dependence of characteristic micellar parameters on salt weight percentage through fits to the experimental data for SLE1S/CAPB/NaCl surfactant solutions with perfume. (a) Zero-shear viscosity,  $\eta_0$ ; (b) plateau modulus,  $G_N$ ; (c) average micelle length,  $\langle L \rangle$ ; (d) average breakage time,  $\bar{\tau}_{br}$ ; (e) micelle entanglement length,  $l_e$  and persistence length  $l_p$ . Notice the positions of zero shear viscosity maxima are indicated by arrows in all the above subfigures.

According to Fig. 3.12, both the plateau modulus  $G_N$  and the average breakage time  $\bar{\tau}_{br}$  ( $= \bar{\tau}_{rep}\zeta$ , Eq. (3.3)) show monotonic dependences (Fig. 3.12(b) and (d)) on salt weight fraction:  $G_N$  increases with added salt while  $\bar{\tau}_{br}$  decreases. This monotonic decrease of  $\bar{\tau}_{br}$  with salt concentration has also been reported in the literature [Nakamura and Shikata (2006); Parker and Fieber (2013)]. According to our results, these solutions fall into the fast breakage regime with  $\bar{\tau}_{br} \ll \bar{\tau}_{rep}$ , and therefore  $\zeta \ll 1$  (Eq. (3.3)), when the salt fraction is greater than 0.75 wt%. An increase in average micelle length ( $\langle L \rangle$ ) is also observed before the solution reaches the maximum on its salt curve, and beyond that, the apparent “length”  $\langle L \rangle$  decreases slightly (Fig. 3.12(c)). Since our method does not distinguish branched from linear micelles, the “micelle length”  $\langle L \rangle$  at high salt concentration is only an apparent length, and its value more likely reflects the spacing between branch points as much or even more than the micelle length [Khatory and Kern *et al.* (1993)]. We are currently working on an extension of our simulation method to

branched micelles, which should help overcome this limitation and may provide a quantitative interpretation on the rheological scaling behavior for  $G_N$  and other parameters as we did in Fig. 3.12. With a larger surfactant fraction (11 wt%) than in the previous solution (6.67 wt%, Fig. 3.9(a)), higher values of  $\omega_{min}$  (the frequency where  $G''$  reaches a local minimum) are observed (Fig. 3.13(a)-(f)) causing poorer resolution of  $\omega_{min}$ , from which micelle entanglement length ( $l_e$ ) and persistence length ( $l_p$ ) are extracted. Therefore, the possible errors in  $l_e$  and  $l_p$  for these samples are likely greater than for the mechanical data for the 6.67% SLE1S solution in Section V.2, which we found had likely errors (or insensitivities) of 20%~30%. Thus, the non-monotonic dependences of  $l_e$  and  $l_p$  on salt concentration given in Fig. 3.12(e) might be spurious, especially since  $l_p$  is expected to decrease monotonically with increasing salt concentration based on the predictions of Oelschlaeger *et al.* [Oelschlaeger *et al.* (2009) and (2010)]. The poorer model fits in Fig. 3.13(e) and (f), especially at high frequencies may be due to the presence of branching in those samples.

#### 4. Breakage mechanisms

Finally, in this section, the details of micellar breakage mechanisms and their effects on stress relaxation are discussed. As suggested by Turner and Cates (1992), three different micellar breakage schemes may occur in WLM solutions: reversible scission, end-interchange, and bond-interchange, whose existence is studied by simulation and experimental work [Yamamoto and Hyodo (2005); Nakamura and Shikata (2006)]. Reversible scission is a uni-micellar, while the other two (end- and bond-interchange) are bi-micellar, and involve the formation of three- and four-arm intermediates, respectively. With the aid of pointer algorithm (Fig. 3.1), reversible scission can be modeled by three different sequences of breakage, rejoining and relaxation events, as shown in Fig. 3.14.



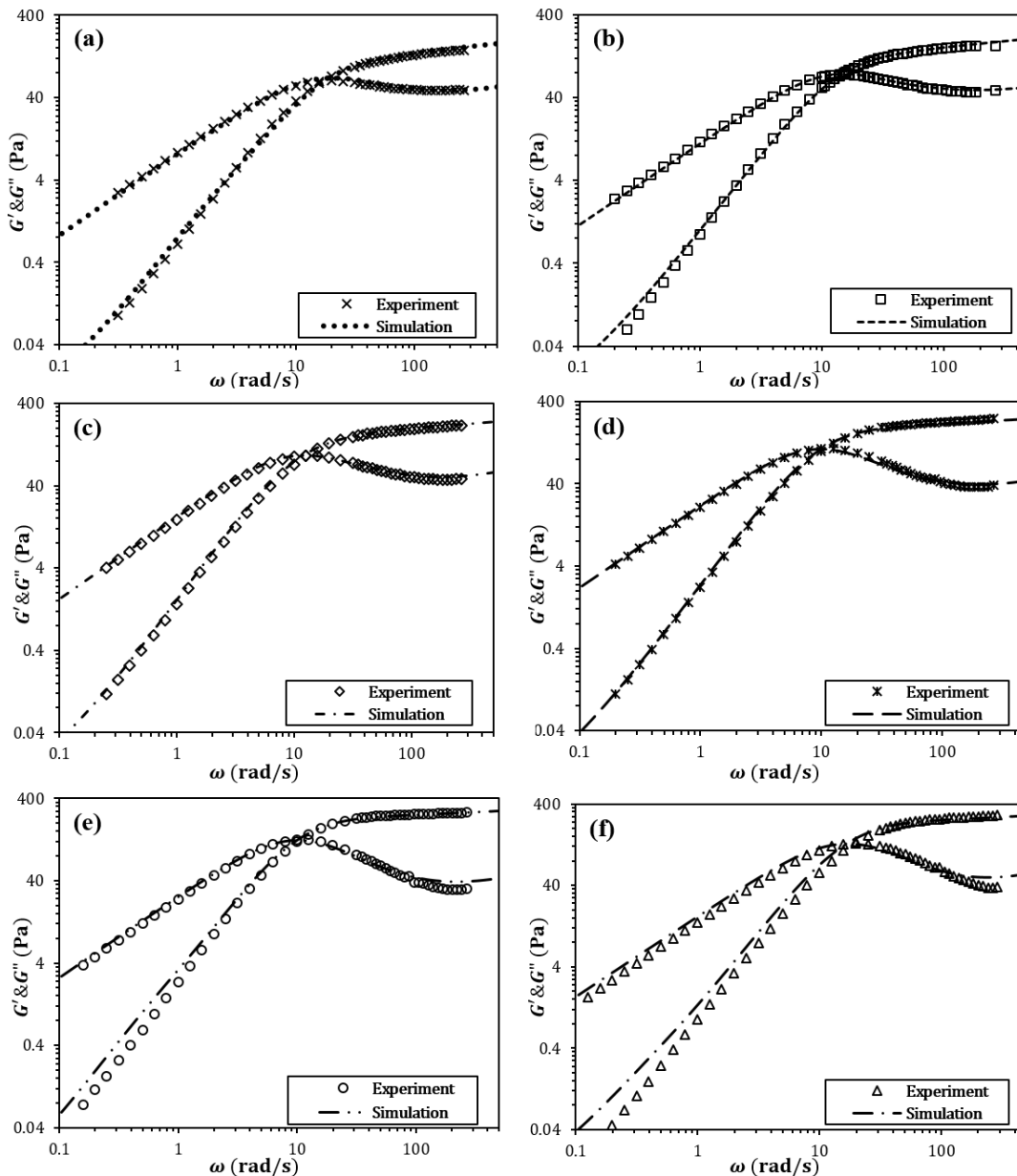


Figure 3.13 Experimental and fitting results for SLE1S/CAPB/NaCl surfactant solutions with perfume and various salt weight fractions. (a) 0.63 wt% NaCl; (b) 0.7 wt% NaCl; (c) 0.75 wt% NaCl; (d) 1.0 wt% NaCl; (e) 1.25 wt% NaCl; (f) 2.0 wt% NaCl. The fitting parameters are given in Fig. 3.12.

From Fig. 3.14, sequence 1 allows the total number of WLMs to fluctuate by randomly choosing a breakage or rejoining event after the relaxation, while sequences 2 and 3 are based on a regular cycle of breakage and rejoining. With a large enough ensemble, the above three sequences should give the same relaxation behavior, which is indeed shown in Fig. 3.15.

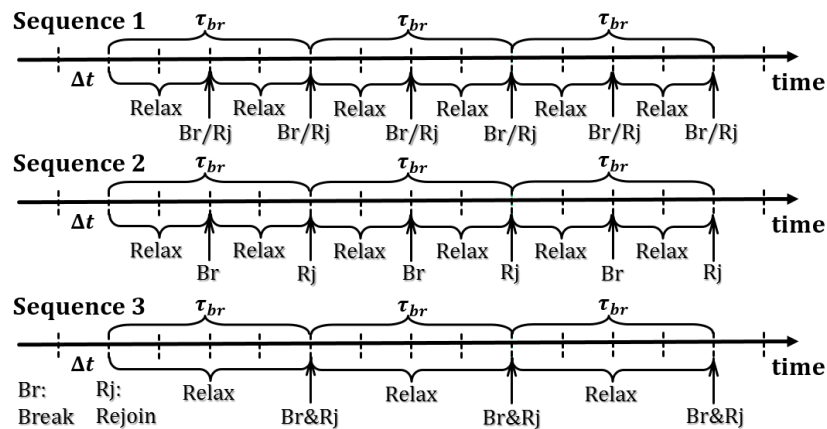


Figure 3.14 Three different sequences in reversible scission scheme.

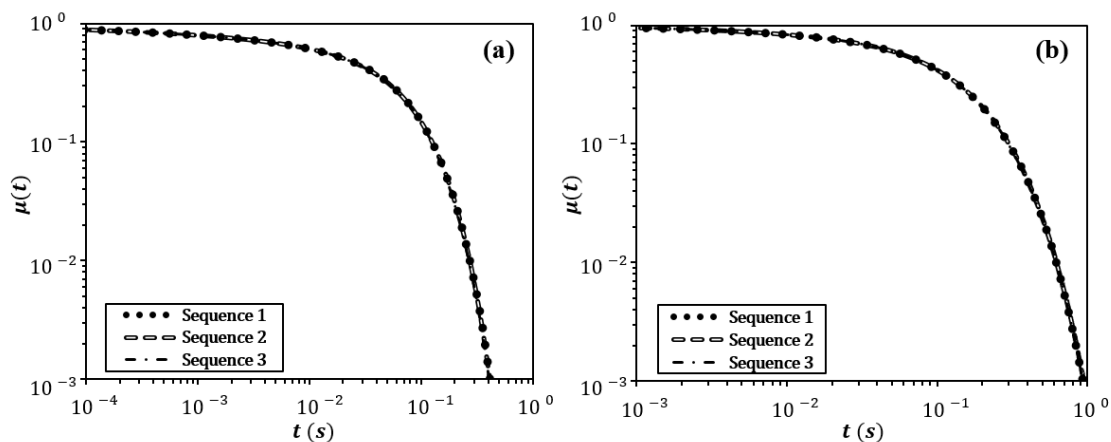


Figure 3.15 Stress relaxation behaviors for reversible scission scheme with three different sequences, depicted in Fig. 3.14. (a) Reptation with CLFs; (b) Pure reptation (i.e., no CLFs).

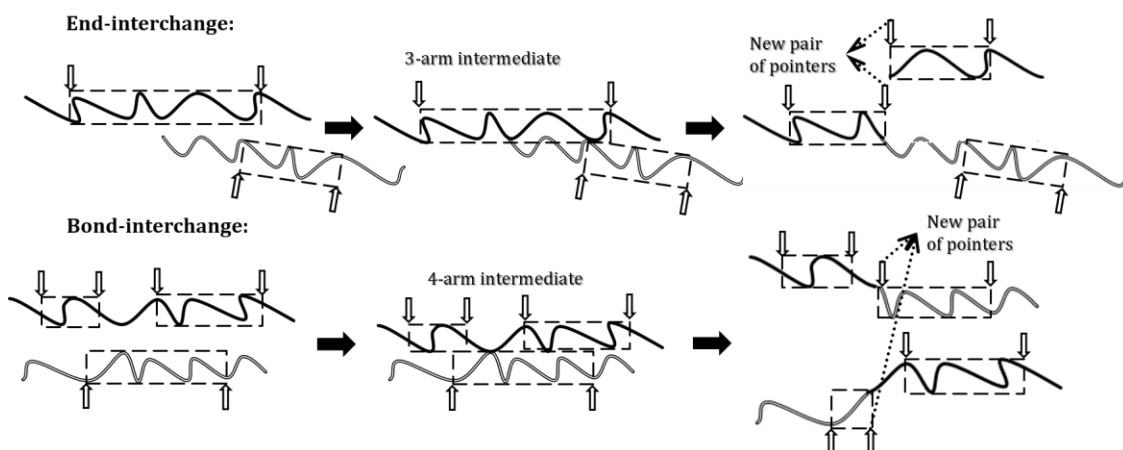


Figure 3.16 Pointer algorithm with end-interchange and bond-interchange schemes.

By extending our pointer algorithm to accommodate end- and bond-interchange (Fig. 3.16) with sequence 3, we find in Fig. 3.17 that pure end- and bond-interchange scheme only

produce a modest 10% and 30% increase, respectively, of the stress relaxation time ( $\tau$  defined in Eq. (3.4)) for a high breakage rate ( $\zeta = 0.05$ ) with fixed surfactant volume fraction ( $\phi = 0.1$ ). Although the precise mechanism by which micelles break and rejoin should affect the dependence of micelle length and therefore viscoelasticity on surfactant concentration, for a fixed surfactant concentration considered here, such effects are not probed.

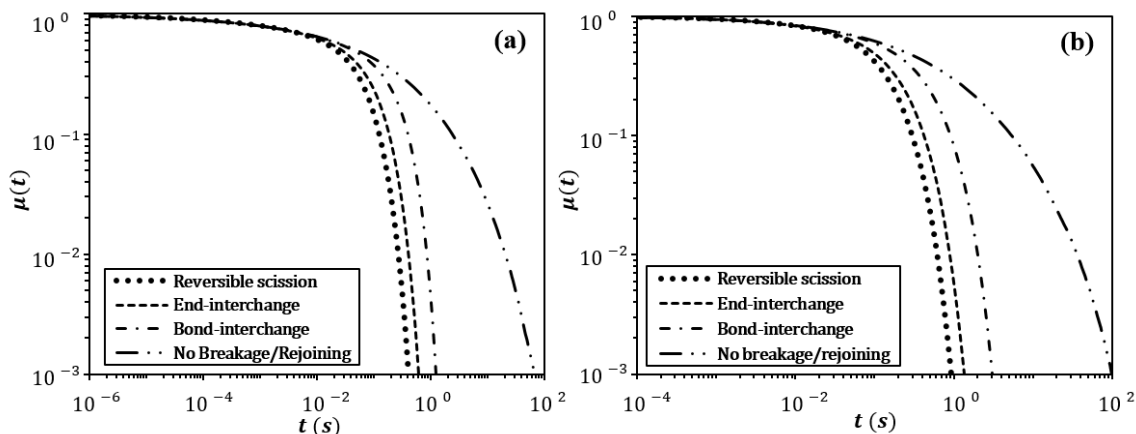


Figure 3.17 Stress relaxation behaviors for different breakage schemes for fixed surfactant volume fraction with the sequence used as defined in the text. (a) Reptation with CLFs; (b) Pure reptation (i.e., no CLFs).

## VI. Conclusions

We have established improved empirical relationships and an associated data-fitting procedure to allow quantitative estimation of micellar characteristic lengths (average micelle length  $\langle L \rangle$ , entanglement length  $l_e$ , and persistence length  $l_p$ ) and times (average breakage time  $\bar{\tau}_{br}$ , and reptation time  $\bar{\tau}_{rep}$ ) to be extracted from rheological data using our recently developed simulation method for entangled WLM solutions. We were able to obtain fits to  $G'$  &  $G''$  data with less than 5% absolute average deviation over a six-decade frequency range, including high frequency data obtained from diffusing wave spectroscopy (DWS). A comparison of fitted micellar parameters were made between DWS data and mechanical rheometric data for WLM solution, and this indicates the importance of low-frequency data in estimating the plateau modulus  $G_N$ , the dimensionless breakage rate  $\zeta$ , and the semi-flexibility coefficient  $\alpha_e$ . The accuracy of our simulation method was demonstrated by sensitivity studies for different micellar parameters. By applying our method to examine effects of added salt concentration, we observed monotonic and non-monotonic dependences of different micellar parameters on salt

concentration, as well as poorer fits at high salt weight fraction where branched micelles predominate. Finally, three different micellar breakage schemes (reversible scission, end-interchange, and bond-interchange) and their rather modest effect on the stress relaxation for fixed surfactant concentration were discussed.

## Chapter 4: Multi-Scale Modeling of the Effects of Salt and Perfume Raw Materials on the Rheological Properties of Commercial Thread-like Micellar Solutions<sup>2</sup>

### I. Introduction

Surfactants are widely used in consumer products including detergents, health and personal care products, and foodstuffs, and in industrial applications including oil recovery and drug delivery. [Cates and Fielding (2006); Kralova and Sjoblom (2009); Lawrence (1994); Maitland (2000); Rehage and Hoffmann (1988); Rhein *et al.* (2006); Zana and Kaler (2007)] Many of these surfactant solutions contain elongated micelles and are viscoelastic, which is of great importance, especially in design of consumer products such as shampoos and body washes. Extensive studies of the rheology of micellar solutions have been carried out over the past three decades, both to satisfy scientific interest and in hopes of improving their design for applications. Many studies have focused on relatively simple solutions containing a single species of cationic surfactant along with one species of anionic hydrotrope or inorganic salt. [Cates and Fielding (2006); Zana and Kaler (2007); Candau *et al.* (1989); Cappelaere *et al.* (1994); Wheeler *et al.* (1996)]

In most cleaning products, including personal-care products, anionic surfactants predominate. The simplest and most common of these, sodium dodecyl sulfate (SDS), has been investigated extensively in the concentration range between the first critical micelle concentration (CMC) at 0.008 M and the second CMC at 0.069 M, over which concentration range the majority of the micelles are small spheres or ellipsoids.<sup>20,21</sup> Wormlike micelle solutions composed of anionic surfactants at concentrations far above the 2nd CMC are studied less frequently, even though those concentration ranges are more relevant to practical applications, and exhibit viscoelastic properties.

In practical applications, mixed surfactants are usually used because of the lower cost of polydisperse mixtures and improved performance over that of the single-surfactant solutions.

---

<sup>2</sup> This chapter results from the collaboration with the former group member Xueming Tang as well as Procter and Gamble scientists Peter Koenig, Shawn McConaughy, Mike Weaver, David Eike, and Michael Schmidt. These individuals contributed a lot to the molecular level simulations and rheological measurements shown in this chapter.

[Scamehorn (1986)] The addition of the ionic surfactant sodium lauryl ether sulfate (SLES) to an SDS solution enhances the viscosity of the mixture at low total surfactant concentration.

[Acharya *et al.* (2006)] Superior interfacial tension reduction is obtained upon addition of the zwitterionic surfactant cocamidopropyl betaine (CAPB) to an SDS solution. [Danov *et al.* (2004); Galvan-Miyoshi *et al.* (2008); Hines *et al.* (1998); Sarmiento-Gomez *et al.* (2010)] Sharp drops of both the 1st and 2nd CMC are obtained in mixtures of CAPB and SLES having one to three ethylene oxide (EO) monomers over that seen in each of the individual surfactant components, as determined through experimental measurements using rheometry and SAXS. [Christov *et al.* (2004); Eguchi *et al.* (2007); Naruse *et al.* (2009)] Here the EO groups connect the alkane tails to the negatively charged sulfate head groups within an SLES molecule. Although the addition of cationic surfactant to anionic surfactants boost viscosity enormously at low surfactant concentrations, the formation of an insoluble complex can limit the range of practicable formulations, and so is often avoided. [Scamehorn (1986); Schubert *et al.* (2003)]

Earlier studies of simple surfactant solutions containing at most two species of surfactants have provided insights into the structure-property relationships of wormlike micelle solutions. However, such systems are oversimplified relative to commercial surfactant mixtures, which contain many species, as well as polydispersity within individual species, such as in SLEnS. In addition, perfumes used in commercial mixtures contain a few dozen distinct small organic molecules, each named a “perfume raw material” (PRM). One of the main challenges in applications of complex fluids such as surfactant solutions is to measure accurately their microstructure at the molecular scale so that these microstructures can be designed for optimal performance of the product. To address this issue and accelerate formulation development, we here report our efforts at multiscale modeling and its use in the prediction of rheological properties of two commercial body wash formulations. Specifically, here we systematically study the effects of salts and PRMs on the viscoelastic properties of body washes, and estimate the corresponding micellar properties through application of the “Pointer Algorithm,” [Cates and Candau (1990); Larson (2012)] a simulation method that we use to infer micelle length, breakage time and other properties from their rheology, as well as through molecular simulations using Dissipative Particle Dynamics (DPD) and through application of the molecular “packing parameter” concept. [Israelachvili *et al.* (1976)] By connecting the surfactant packing at the molecular scale to micellar properties at the mesoscale, and these, in turn, to the rheological

properties at the macroscopic scale, we develop an approach for achieving a fundamental understanding of the structure-property relationships of commercial surfactant solutions.

## II. Multi-scale Modeling and Packing Argument

### 1. Micellar-scale model

Cryo-TEM measurements of body washes verify the formation of entangled networks of wormlike micelles. The solutions are viscoelastic and their rheology is similar to that of entangled polymer solutions. One difference is that wormlike micelles break and recombine rapidly. By combining the theories considering polymer reptation and micellar fast reversible scission, Cates developed a reptation-reaction model to estimate linear micellar characteristic time and length parameters. [Cates and Fielding (2006); Cates and Candau (1990); Khatory *et al.* (1993); Cates (1987); Granek and Cates (1992)] The frequency-dependent linear rheological moduli predicted by the Cates model in the fast-breakage limit are given by a single-relaxation-time Maxwell model. Zou and Larson (2014) extended the Cates model by including important physics neglected in the previous model and using “pointers” to track relaxation dynamics in ensembles containing thousands of micelles. This “Pointer Algorithm” allows estimates of multiple micellar parameters from fits of the predictions to the rheology of entangled wormlike micelles. [Español and Warren (1995)] We will use the Pointer Algorithm here to extract micelle parameters, including average micelle length, breakage time, etc. from rheological data we obtain for several commercial body washes.

Once the average micelle length is obtained from such simulations, the scission free energy  $E_s$  (i.e., the free energy of creating two additional end caps), can be determined from the dependence of the average micelle aggregation number  $\langle n \rangle$  on temperature as [Larson (1999)]

$$\langle n \rangle \approx \frac{\rho_s \pi d^2 \langle L \rangle N_A}{4 \bar{M}_s} \approx 2 \chi^{0.5} \exp\left(\frac{E_s}{2k_B T}\right) \quad (4.1a)$$

Here,  $\chi$  is the mole fraction of the surfactant, and the exponent 0.5 is derived from the law of mass action, assuming activity coefficients of unity for individual surfactant molecules and micellar species. To derive the above expression, which is slightly more precise than the scaling law of Cates and Candau, [Cates and Candau (1990); Vogtt *et al.* (2017)] which uses surfactant volume fraction  $\phi$  instead of mole fraction  $\chi$ , we note that for cylindrical micelles containing surfactant with surfactant density  $\rho_s = 1.1 \text{ g/cm}^3$  (which we take from the mass density of the

surfactant crystal) and diameter  $d = 4$  nm,  $\langle n \rangle$  can be expressed in terms of the average micelle length  $\langle L \rangle$  as:

$$\langle n \rangle = \frac{\rho_s V_s}{\bar{M}_s} N_A = \frac{\pi d^2 \langle L \rangle N_A}{4 \bar{M}_s} \quad (4.1b)$$

Here  $N_A$  is the Avogadro number and  $\bar{M}_s = 345$  g/mol is the average molecular weight of the surfactant, which we take as the weight-averaged molecular weight of the components. SLE1S (molecular weight = 346 g/mol) and CAPB (molecular weight = 342 g/mol), with the weight fractions of these two being 9.85/11 and 1.15/11, respectively. We neglect the small contributions of salt and perfume molecules to the mole fraction of surfactant  $\chi$ . Substituting the above equation into Eq. (4.1a), yields:

$$\langle L \rangle \approx \frac{8 \bar{M}_s \chi^{0.5}}{\rho_s \pi d^2 N_A} \exp\left(\frac{E_s}{2k_B T}\right) \quad (4.2)$$

Here the mole fraction  $\chi$  is obtained as 0.64 for 11 wt. % surfactant solutions (i.e.,  $\chi = [w_s/\bar{M}_s]/[w_s/\bar{M}_s + (1 - w_s)M_w] = 0.64$  with  $w_s = 0.11$ ). To limit our analyses to the regime of cylindrical micelles, we apply Eq. (4.2) only over a set of four temperatures separated by intervals of 1 or 2 degrees within a narrow range from 20.0 to 25.0 °C. We note that if the molar volume of the surfactant is set equal to that of water, the simpler expression of Cates is obtained. Similar to the scission energy, we express the temperature dependence of the terminal relaxation time  $\tau$  and zero-shear viscosity  $\eta_0$  in Arrhenius forms involving terminal relaxation time and viscosity activation energies  $E_r$  and  $E_v$ , respectively: [Cates and Candau (1990)]

$$\tau \sim \eta_s \exp\left(\frac{E_r}{k_B T}\right), \quad \eta_0 \sim \eta_s \exp\left(\frac{E_v}{k_B T}\right) \quad (4.3)$$

where  $\eta_s$  is the solvent viscosity which itself is a function of temperature. These activation energies can also be extracted from the corresponding rheological curves.

## 2. Dissipative particle dynamics (DPD) simulations

To describe the structure of cylindrical micelles in a computationally efficient way, coarse-grained dissipative particle dynamics (DPD) simulations using a soft repulsive potential are applied here. [Español and Warren (1995); Groot and Warren (1997)] In the DPD simulations used here, three to five heavy atoms are lumped into one quasi-particle or bead, which interacts with other beads via pairwise forces, and obeys Newton's equations of motion. The pairwise interparticle force contains three contributions,



$$f_i = \sum_{j \neq i} (F_{ij}^C + F_{ij}^D + F_{ij}^R) \quad (4.4)$$

where  $F_{ij}^C$  is a conservative force defined by a purely repulsive (harmonic) soft-core potential sensitive to chemical identity,  $F_{ij}^D$  is a dissipative force and  $F_{ij}^R$  is a random force. The latter two forces take into account the fluctuation and dissipation of energy and serve as the Langevin thermostat. The conservative force  $F_{ij}^C$  determines the thermodynamics of the DPD system and the soft potential allows for larger time steps of picoseconds instead of the femtoseconds used in traditional MD simulations.

$$\begin{aligned} F_{ij}^C &= -a_{ij} \omega^C(r_{ij}) \hat{r}_{ij} \\ F_{ij}^D &= -\gamma \omega^D(r_{ij}) (v_{ij} \cdot \hat{r}_{ij}) \hat{r}_{ij} \\ F_{ij}^R &= -\sigma \omega^R(r_{ij}) \xi_{ij} \Delta t^{-1/2} \hat{r}_{ij} \end{aligned} \quad (4.5)$$

Here  $a_{ij}$ ,  $\gamma$  and  $\sigma$  are parameters that determine the strength of these forces. The parameters  $\sigma$ ,  $\gamma$  are chosen such that they will obey the dissipation-fluctuation theorem with  $\sigma^2 = 2\gamma$  and  $\sigma = 3$ . The repulsive parameters  $a_{ij}$  are dependant on the chemical identity of beads  $i, j$ .  $\hat{r}_{ij}$  is a unit vector in the direction of  $r_{ij}$  and  $r_{ij} = |r_i - r_j|$ , while  $v_{ij} = v_i - v_j$  is the relative velocity between beads  $i$  and  $j$ .  $\xi_{ij}$  is a Gaussian distributed random variable with zero mean and unit variance and  $\Delta t$  is the integration time step.  $\omega^C$ ,  $\omega^D$  and  $\omega^R$  are the weight functions:

$$\omega^C(r_{ij}) = \omega^R(r_{ij}) = \begin{cases} 1 - \frac{r_{ij}}{r_{cut}} & \text{if } 0 \leq r_{ij} \leq r_{cut} \\ 0 & \text{if } r_{ij} > r_{cut} \end{cases} \quad (4.6a)$$

$$\omega^D = (\omega^R)^2 \quad (4.6b)$$

where  $r_{cut}$  is the truncation distance.

Since its introduction by Hoogerbrugge and Koelman in 1992, [Hoogerbrugge and Koelman (1992)] DPD has been improved significantly by Español and Warren [Español and Warren (1995)] and then by Groot and Warren. [Groot and Warren (1997)] Recently, Liyana Arachchi *et al.*, [Liyana-arachchi *et al.* (2015)] introduced a revision of the Groot and Warren DPD equation of state (rGW-EOS) that improves it for low bead number densities and allows for beads of different number densities to be used in a simulation. Different bead number densities correspond to different effective sizes of beads. This formalism does not change the cutoff distance  $r_{cut}$ ; however the conservative repulsion parameter  $a_{ii}$  for beads of the same type  $i$  now depends on the chemical species associated with  $i$ .

Liyana Arachchi *et al.* [Liyana-arachchi *et al.* (2015)] also provide for a more systematic determination of parameters  $a_{ij}$  for distinct types  $i, j$  determined from infinite dilution transfer free energies as determined for instance using COSMOtherm.

In this Chapter, we used a water model lumping three water molecules into one bead with a volume of  $90.05 \text{ \AA}^3$ . We set the bead number density of water molecules to 5.0. This results in a definition of the DPD length scale of  $r_{cut} = 7.6 \text{ \AA}$ . We set the repulsion parameter between water molecules to  $a_{ii} = 15.0$ . The number densities of other beads are determined from comparing their molar volume to the molar volume of the water beads. Molar densities are computed using the empirical model implemented in COSMOtherm. [Klamt *et al.* (2010); Klamt (2011)] The repulsion parameters  $a_{ii}$  for like interactions are determined from the respective number density following the rGW-EOS. The repulsion parameters  $a_{ij}$  for unlike interactions are computed from the infinite dilution transfer free energy approach previously described. [Liyana-arachchi *et al.* (2015)]

To describe some of the more complex molecules in the simulations described here, multiple beads have to be used. The validity range of the rGW-EOS allows for beads comprising on the order of 3-5 heavy atoms (the definition of the beads used in this work is contained in Table C.1 in *Appendix C*). To determine the size of the beads, the molar volume is derived from related model compounds by subtracting the molar volume of terminating groups. For instance, the molar volume of a C3 bead describing a propylene functionality is obtained by subtracting the molar volume of ethane from the molar volume of pentane. As another example, some of the isomers found in dipropylene glycol are symmetric in nature. The volumes of the corresponding beads are determined as half of the molar volume of the parent compound.

To determine the interaction parameters for these beads, the weights are assigned to the respective parent compound for COSMOtherm calculations, resulting in only the molecular surface that corresponds to the bead to be considered for the transfer free energies.

For the parameterization of harmonic bond and angles potentials, ensemble distributions were matched to atomistic Monte-Carlo simulations using the COMPASS force field implemented in Biovia Materials Studio.

To our knowledge, no systematic approach has been described for the parameterization of charged beads in DPD. Given that most ions in aqueous solutions possess a hydration shell, we make the strong assumption that the interactions aside from the electrostatic charge are

dominated by the hydration shell. We hence define the  $\chi_{ij}$  parameters describing the interactions of ions with other beads as identical with water interacting with said bead. An ionic bead interacting with another ionic bead would then have a  $\chi_{ij}$  parameter identical to that for a water bead with itself. In addition, integer electrostatic charges are assigned to the beads following their formal electrostatic charges. To prevent singularities in electrostatic forces and energies for the soft core potential, electrostatic charges are described as Gaussian charge clouds centered at the respective bead as suggested by Groot. [Groot (2003)] If the width of the charge distributions are identical for all beads, a standard particle-mesh Ewald scheme can be used to compute the interaction if the real-space cutoff is set to 0.0 (See *Appendix C*). For these simulations, we used a homogeneous relative dielectric constant of  $\epsilon_0 = 80$  and a standard deviation of  $\sigma_{ES} = 0.8/\sqrt{2}$  for the Gaussian charge distributions.

We used LAMMPS to apply this model in simulations of canonical ensembles at constant pressure and constant temperature with semi-isotropic pressure coupling ( $p_{ref} = 41.9, \tau_p = 15\tau$ ) with a time step of  $\tau = 0.015$  DPD units to study the effects on micelle properties of salts in the two formulations BW-1EO and BW-3EO (defined below) and the effects of four PRMs in BW-1EO. All DPD parameters used for the simulations are provided as supplementary materials.

Using a combination of the Pointer Algorithm and the DPD molecular model, we seek to assess quantitatively the changes in rheological properties that result from the addition of salts and PRMs and thereby build a fundamental understanding of the structure-property relationships of surfactant formulations. We used LAMMPS to apply this model in simulations of canonical ensembles at constant pressure and constant temperature with semi-isotropic pressure coupling ( $p_{ref} = 41.9, \tau_p = 15\tau$ ) with a time step of  $\tau = 0.015$  DPD units to study the effects on micelle properties of salts in the two formulations BW-1EO and BW-3EO (defined below) and the effects of four PRMs in BW-1EO. Detailed DPD parameters and the molecular mapping are listed in Table C.1 in Supporting Information. Using a combination of the Pointer Algorithm and the DPD molecular model, we seek to assess quantitatively the changes in rheological properties that result from the addition of salts and PRMs and thereby build a fundamental understanding of the structure-property relationships of surfactant formulations.

### 3. Packing argument and octanol/water partition coefficient.

#### A. Packing arguments

At concentrations above the 1st CMC in solution, surfactants self-assemble into diverse structures including spherical, global, and cylindrical micelles as well as ordered phases. [Zana and Kaler (2007); Imae *et al.* (1985); Larson (1999); Israelachvili *et al.* (1976); Groot (2003)] These self-assembled structures depend on the concentration and chemical structures of the surfactants, the nature of the counter ions, the presence of salts and/or other surfactants, pH, temperature and pressure. [Zana and Kaler (2007); Larson (1999)] Israelachvili and coworkers proposed a packing argument based on the dimensionless “packing parameter”  $p$  to predict the shape of the micelles, which is defined as [Israelachvili *et al.* (1976)]

$$p = \frac{V}{l_c a_0} \quad (4.7)$$

where  $V$  is the occupied volume of the hydrophobic tail,  $l_c$  is the tail length, and  $a_0$  is the area occupied by the hydrophilic heads on the micelle surface.

Generally, the hydrophobic tails are wrapped within the hydrophilic heads, giving them limited access to their environment. Therefore the tail volume  $V$  and tail length  $l_c$  are typically taken to be constant, while the head group area  $a_0$  can change, for example with ionic strength. Using the packing parameter  $p$ , the effects of salts and non-hydrophobic PRMs on micellar properties can be easily explained, at least qualitatively. For example, as salt is added into the micellar solution, the electrostatic repulsions between the surfactant heads are screened out, resulting in a decrease of  $a_0$  and an increase of  $p$ , which flattens the micelle surface, leading, for example, to a transition from spherical to elongated cylindrical micelles. Similarly, addition of a hydrophobic perfume that swells the tails increases  $V$ , also resulting in a similar transition. However, as we shall see, large, very hydrophobic, PRMs can penetrate deeply into the hydrophobic core of the micelle, segregated from the tails and swelling the micelle radius, effectively changing not only  $V$  but also  $l_c$ , which can lead, perhaps surprisingly, to a decrease in  $p$ , and a transition towards spherical micelles.

#### B. Octanol/water partition coefficient

PRMs are essential ingredients for fragrances in body washes formulated to meet consumers' preferences. The effects of a single PRM are often studied and correlated with the

value of its octanol/water partition coefficient,  $P_{OW}$ , which is the concentration ratio of the PRM in hydrophobic octanol to that in the hydrophilic water phase (See Eq. (4.8)). [Bradbury *et al.* (2013); Penfold *et al.* (2008); Saito *et al.* (2003); Suratkar and Mahapatra (2000); Tokuoka *et al.* (1994); Zhou and Zhu (2005)] The logarithm,  $\log P_{OW}$ , is often used as a hydrophobicity parameter. In this paper we use the logP values as computed by the Consensus algorithm implemented in ACD/Percepta version 14.02 by Advanced Chemistry Development, Inc. (ACD/Labs, Toronto, Canada). Approximating the hydrophobic surfactant tail region and the hydrophilic surfactant head region by the octanol phase and water phase, respectively, we obtain

$$\log P_{OW} = \log \left( \frac{[PRM]_{Octanol}}{[PRM]_{Water}} \right) \cong \log \left( \frac{[PRM]_{Tail\ region}}{[PRM]_{Head\ region} + [PRM]_{Water}} \right) \quad (4.8)$$

However, the above approximation neglects geometric constraints, especially in the tightly packed surfactant tail region, which might restrict access of PRMs to the micelle core or cause a significant change of the surfactant packing within micelles.

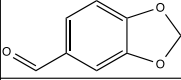
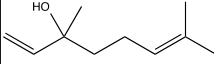
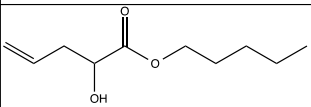
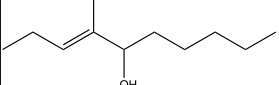
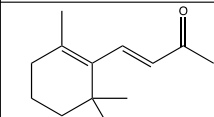
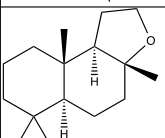
### III. Experiments and Simulation Set Up

#### 1. Materials

Two body wash formulations, “BW-1EO” and “BW-3EO” with a simple salt (sodium chloride, NaCl) and PRM (if added), were tested. Raw industrial grade surfactants, analytical grade salts and PRMs, and Milli-Q water were used in both formulations. Due to the complexity of these commercial materials, weight percentage (wt. %) instead of molar concentration is used here. An 11 wt. % BW-1EO aqueous solution is a mixture of 9.85 wt. % SLE1S, 1.15 wt. % CAPB, where SLE1S (Fig. 4.1a) is an abbreviation for commercial sodium lauryl ether sulfate with one ethoxyl group (EO) on average (but with a distribution of the number of EOs ranging from 0 to 10); and CAPB (cocamidopropyl betaine, Fig. 4.1b) is a zwitterionic co-surfactant. The 11 wt. % BW-3EO solutions is similar to that of BW-1EO except that the former contains SLE3S, which has three EOs on average, and the ratio of surfactants is different: SLE3S (6.95 wt. %), SLS (i.e., SLE<sub>n</sub>S with n=0, 2.90 wt. %), CAPB (1.15 wt. %). SLE1S and SLE3S are commercially available from Stepan (Northfield, Ill) as 26% actives in H<sub>2</sub>O (pH ~11). The pH is adjusted to around 7 in the formulations. They both have an approximate chain length distribution of 65-68% C12, 25-27% C14 and 5-7% C16. The distribution of the ethoxylation was explicitly represented in the mixtures of molecules used in DPD to represent the respective

surfactants. A 1 wt. % “ACCORD” perfume mixture (which consists of six small organic perfume molecules as listed in Table 4.1) is also added to both BW-1EO and BW-3EO solutions to make the mixture more representative of commercial formulations. The” ACCORD” was a mixture that was created to span a range of octanol-H<sub>2</sub>O partitioning coefficients from hydrophilic (~ 1) to mildly hydrophobic (~ 4) (see Table 4.1). Linalool was obtained from Renessenz LLC; heliotropin was from Ungerer; undecavertol and ambroxan were from Givaudan; beta-ionone was from Aldrich and allyl amyl glycolate was from O’Laughlin Industries Inc. All PRMs were used as received. Note that the CAPB ingredient adds about 0.2 wt % of salt to the formulations. The experimental work in this paper reports the *added* salt, not including the amount carried by the CAPB. In the DPD simulation work the salt concentration reported (in Fig. 4.9 for example) represents the *total* salt in the formulation.

Table 4.1 Composition of ACCORD. For each component, the CAS number, IUPAC name, common name, chemical structure, octanol/water partition coefficient, molecular weight, and its weight percentage in the mixture, are given.

CAS Number	IUPAC name	Common Name	Chemical Structure	Octanol/Water Partition Coefficient LogPow	Molecular Weight	Weight %
120-57-0	1,3-Benzodioxole-5-carbaldehyde	Heliotropin		1.43	150.13	15.4
78-70-6	3,7-dimethylocta-1,6-dien-3-ol	Linalool		2.44	154.25	23.3
67634-00-8	prop-2-enyl 2-(3-methylbutoxy)acetate	Allyl amyl glycolate		2.81	186.25	13.5
81782-77-6	4-methyl-3-decen-5-ol	Undecavertol		3.06	170.29	25.6
14901-07-6	(3E)-4-(2,6,6-Trimethylcyclohex-1-en-1-yl)but-3-en-2-one	beta-Ionone		4.02	192.3	11.5
6790-58-5	Naphtho[2,1-b]furan,dodecahydro-3a,6,6,9a-tetramethyl-,	synambrian		4.58	236.4	10.7

In addition to ACCORD, four additional PRMs (Fig. 4.1c-f, details below) were also added one at a time to the BW-1EO and BW-3EO formulations (each of which already contains the ACCORD). Molar concentration is used to specify the addition of each PRM to study their

individual effects on viscoelastic properties of body washes. These additional PRMs were added to the pre-existing mixture including ACCORD because screening experiments suggest that the impact of a single perfume compound may not translate in a simple linear and additive fashion to mixtures of additives. Nevertheless, we also present data in *Appendix C*, Fig. C.1, for surfactant mixtures containing only a single PRM (i.e., no ACCORD), and find that the effects on the zero-shear viscosity of the single PRM added to the surfactant-only mixture are qualitatively similar to the effects of adding it to the mixture that also contains ACCORD. The PRMs chosen for one-at-a-time addition are: *A.* dipropylene glycol, abbreviated as DPG {a mixture of four isomers: 1) 1,1'-oxybis-2-propanol (CAS number 110-98-5); 2) 2,2'-oxybis-1-propanol (CAS number 108-61-2); 3) 2-(2-hydroxypropoxy)-1-propanol (CAS number 106-62-7); 4) 3,3'-oxybis-1-propanol (CAS number 2396-61-4).}; *B.* isopropylbenzene, common name cumene (CAS number: 98-82-8); *C.* 3,7-dimethylocta-1,6-dien-3-ol, common name linalool (CAS number: 78-70-6); *D.* propan-2-yl-tetradecanoate, common name isopropyl myristate, abbreviated as IPM (CAS number: 110-27-0). Components were added in the following order: concentrated surfactant paste, ACCORD, water, additional PRM (if added), and salts. Samples were well mixed and centrifuged at least an hour for degassing prior to measurements.

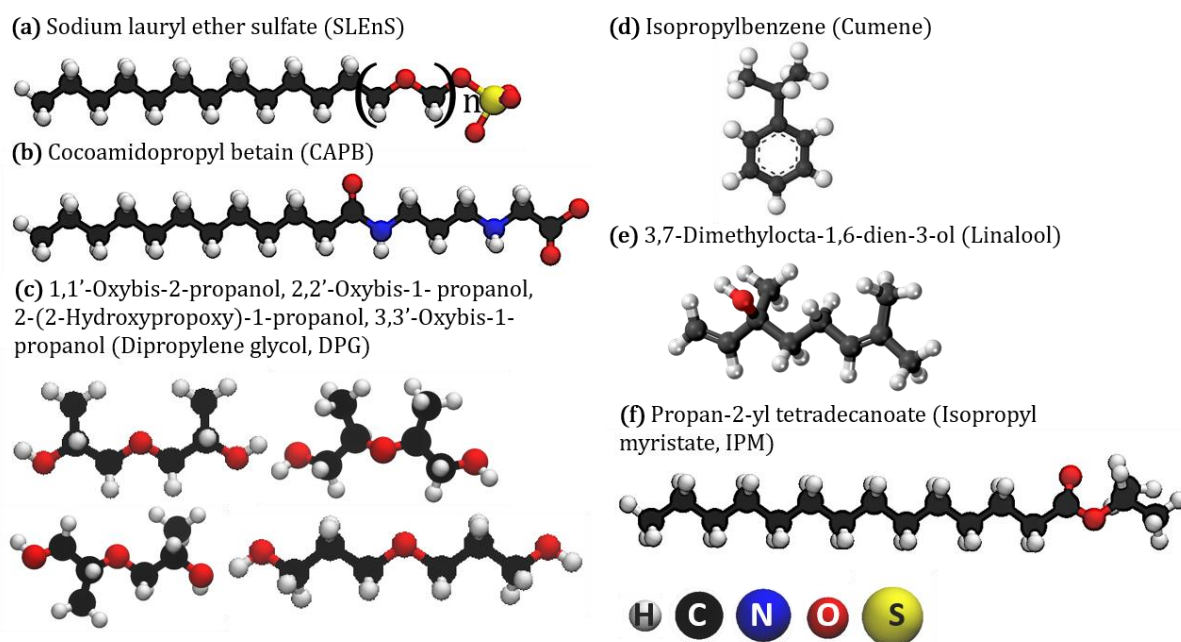


Figure 4.1 Structures of surfactants and perfume raw materials (PRMs) used in this study: (a) sodium lauryl ether sulfate (SLEnS) with number of EOs varying from 0 to 10; (b) cocamidopropyl betaine (CAPB); (c) dipropylene glycol modeled as a mixture of 1,1'-oxybis-2-propanol, 2,2'-oxybis-1-propanol, 2-(2-hydroxypropoxy)-1-propanol, and 3,3'-oxybis-1-propanol, and abbreviated as DPG; (d)

isopropylbenzene with common name cumene; (e) 3,7-dimethylocta-1,6-dien-3ol with common name linalool; f) propan-2-yl-tetradecanoate with common name isopropyl myristate and abbreviated as IPM.

## 2. Rheological experiments.

An AR-G2 rotational rheometer with an acrylic cone and plate (to minimize inertial effects) was used to measure the zero shear viscosity at constant shear rate, and rheological moduli at constant shear stress but varying frequency. We sampled 25 data points per decade at high frequency and 10 data points per decade at low frequency to obtain enough information for model fitting in a reasonable time. Samples were freshly loaded each time and a solvent trap was used to prevent sample evaporation near the edge. All the rheological measurements were performed within the linear viscoelastic regime at room temperature of close to 25°C unless otherwise specified. Randomly selected samples were re-measured and the standard deviation of rheological measurements was found to be less than 3%. Diffusing wave spectroscopy (DWS) [Oelschlaeger *et al.* (2003); Galvan-Miyoshi *et al.* (2008)] is also applied to get the high-frequency behavior ( $10\text{--}10^6$  rad/s). The wavelength of light and the diameter of beads used in DWS are 532 and 630 nm, respectively. The beads are made of IDC polystyrene latex from Life Technologies (cat# S37495) with hydrophobic surface, which are stabilized with a low level of sulfate charges and surfactant free. The WLM solution samples for DWS measurement were mixed with 0.5 wt. % beads before adding salt to ensure good mixing prior to thickening with salt. After 12 h equilibration, samples were measured in 5mm glass cells on an LS Instruments RheoLab II system. The transport mean free path  $l^*$  ( $\approx 580$   $\mu\text{m}$ ) was determined from the control sample with the same-size beads in water.

## 3. DPD simulation set up

Initially straight periodic cylindrical micelles were oriented along the  $z$  direction of the simulation box, packed with surfactants with heads on the surface, enclosing the tails. All surfactants, ACCORD, and additional PRM if added, were packed randomly into the periodic micelle close to a common axis at the beginning of the simulations, followed by solvation with water and salts. The tail beads of the micelle were first constrained in an NVT ensemble briefly to equilibrate the surfactants with water followed by simulations at NPT with semi-isotropic pressure coupling.



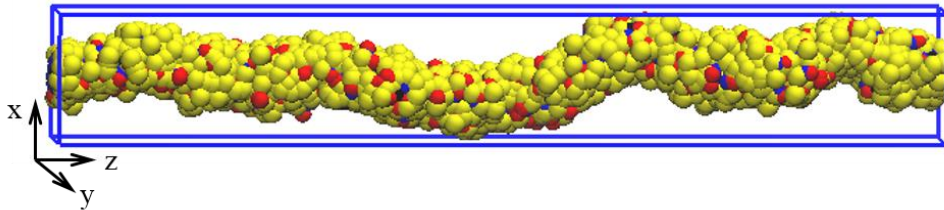


Figure 4.2 Snapshot of an equilibrated periodic wormlike micelle in a DPD simulation. Salt and water are omitted for clarity. Shown are sulfate (yellow) and other head groups including ethylene oxide, amide, tetramethyl ammonium, and acetate (red), ACCORD (black), and alkyl carbon tail beads (blue). ACCORD and tail beads are nearly covered over by head beads.

The radial density profiles of equilibrated periodic wormlike micelles were then analyzed by slicing the simulation box with planes perpendicular to the  $z$  axis with 1 nm spacing. For each slice, the center of mass (COM) of surfactants, excluding counter-ions, were computed for each slice. The bead number counts in each slice were calculated within a narrow circular shell of thickness  $0.1 \text{ \AA}$  centered at a given radial distance with respect to the COM of the micelle in that slice and was then averaged over time and over all slices. Normalizing the bead number counts by the shell volume gives the bead number densities. The “spine length” of the micelle is computed as the sum of the lengths of the segments connecting the micelle COMs of neighboring slices. For comparison between simulations, the radial distribution of the bead number count per frame and per average contour length is calculated. The “packing distance” (not to be confused with the dimensionless packing parameter in Section II.3) is then defined as the ratio of average micelle spine length to the number of surfactant molecules within the micelle. While we cannot at this point specify a quantitative relationship between “packing length” and the Israelachvili “packing parameter,” we expect the two to be inversely related to each other qualitatively. The simulations of DPD last for 700,000 time steps and the last 500,000 time steps are used for the analysis.

## IV. Effect of Salt

### 1. Rheological features

#### A. Salt curve.

Plots of the zero shear viscosity vs. the weight fraction of sodium chloride (NaCl), referred as “salt curves,” are shown in Fig. 4.3 for 11 wt. % solutions of two formulations (BW-

1EO and BW-3EO) with/without 1 wt. % ACCORD. The salt curve for 9.5 wt. % BW-3EO solution containing 1 wt. % ACCORD is also shown. As shown by Fig 4.3, when ACCORD is present in the solution (solid lines with filled symbols), the zero shear viscosity (simply called “viscosity” in the following) increases with salt concentration and reaches a maximum, followed by a decrease at high salt concentration. For solutions without ACCORD (dashed lines with hollow symbols), viscosity maxima are also expected if the salt concentration is increased further. Note that for all the solutions shown in Fig 4.3, the concentration of SLEnS on its own is already higher than its 2nd CMC, at which the majority of the micelles change from spheres to polydisperse elongated rods. [Kodama et al. (1972); Ma *et al.* (1998); Mazer *et al.* (1976)] Therefore, even in the absence of salts, the micelles in body washes are already expected to be cylindrical, although the viscosities are still low. Based on Fig. 4.3, by adding ACCORD to the solution, the salt curve is shifted to lower salt concentration with a lower viscosity maximum, which implies easier formation of long micelles and micellar branches (The viscosity maximum is attributed to formation of micellar branches.).

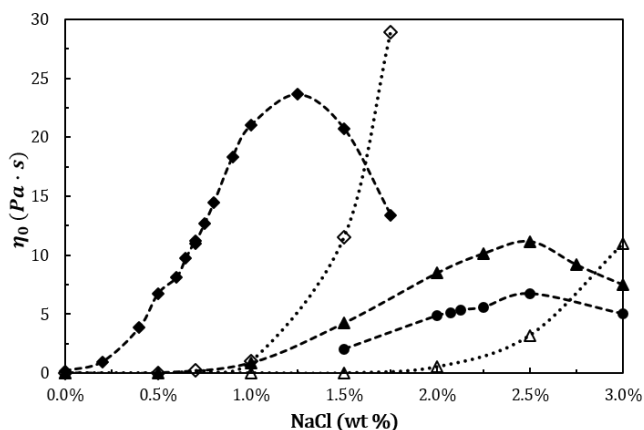


Figure 4.3 Salt curves for 11 wt. % and 9.5 wt. % formulations with 1 wt. % ACCORD (solid symbols) and without ACCORD (open symbols): diamonds – 11 wt. % BW-1EO, triangles – 11 wt. % BW-3EO, and circles – 9.5 wt. % BW-3EO.

From the above figure, both BW-1EO and BW-3EO solutions containing ACCORD (dashed lines with filled symbols) show initially nearly exponential increases in viscosity at low salt concentration, then a linear dependence, and finally a concave-downward shape near the maximum. The salt curve for the ACCORD-containing BW-3EO solution shows a slower increase of viscosity with increasing salt, as well as a lower viscosity maximum and a broader regime of linear viscosity increase than for the ACCORD-containing BW-1EO with shorter EO

groups. In addition, decreasing the total concentration of surfactants in BW-3EO (from 11 wt. % to 9.5 wt. %) results in a reduction in the viscosity without shifting of the viscosity maximum. Since actual body washes have rheological properties similar to those of 11 wt. % BW-1EO and BW-3EO formulations containing ACCORD, we will discuss these solutions in detail. Note that in what follows, unless otherwise stated, we use the terms “BW-1EO” and “BW-3EO” to refer to the 11 wt. % solutions containing 1 wt. % ACCORD.

### B. Storage and loss moduli

Storage ( $G'$ ) and loss moduli ( $G''$ ) are shown in Fig. 4.4 for BW-1EO at various salt concentrations (Data for BW-3EO are qualitatively similar and are therefore not shown.). As the salt concentration increases, at low frequencies both  $G'$  and  $G''$  shift leftward monotonically up to the maximum in the salt curve (i.e., the second highest salt concentration). This is accompanied by an increase of terminal relaxation time  $\tau$  (which is approximated by the inverse of the crossover frequency of  $G'$  and  $G''$ ) as shown by the inserted figure in Fig. 4.4b, which, as discussed below, indicates that micelles lengthen until reaching the salt peak. Once the concentration of salt passes the viscosity maximum (at 1.25 wt. % and 2.5 wt. % for BW-1EO and BW-3EO, respectively), branched micelles presumably proliferate, and a rightward shift of the  $G'$  and  $G''$  curves occurs over most of the frequency range.

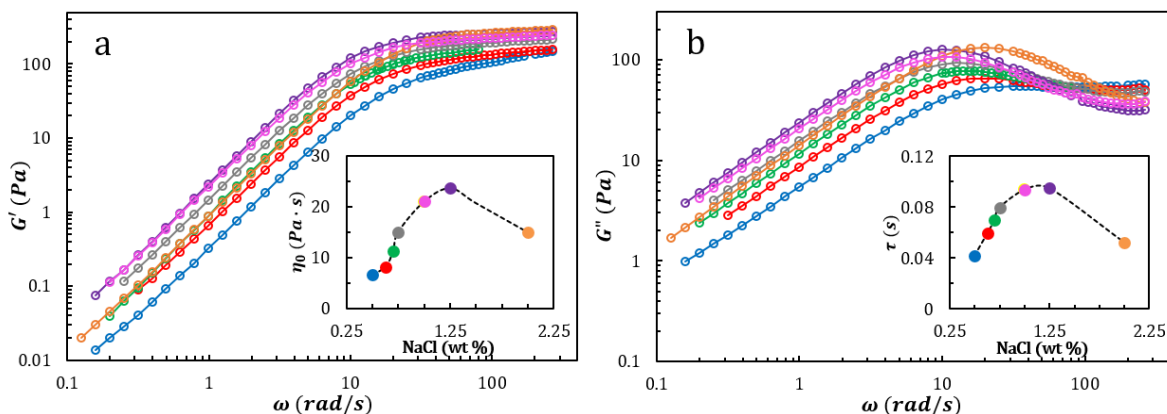


Figure 4.4 (a) Storage and (b) loss moduli for BW-1EO at different salt weight fractions, each coded by a color also used in the inserted figures giving (a) zero-shear viscosities and (b) terminal relaxation time as functions of salt concentration.

According to Fig. 4.4b, the loss moduli  $G''$  also shift downward monotonically at high frequencies, and this can be shown clearly in a “Cole-Cole” plot in which  $G''$  is plotted against

$G'$ . The normalized Cole-Cole plots (with  $G'$  and  $G''$  divided by the loss modulus maximum,  $G''_{max}$ ) for BW-1EO and BW-3EO are shown in Fig. 4.5, where the local minimum in  $G''$  ( $G''_{min}$ ) decreases as the salt concentration increases until the peak in the salt curve is passed. The deviations from perfect semi-circles (i.e., single-relaxation-time Maxwell model, denoted by dashed lines in Fig. 4.5) at low salt concentration are greatest on the right side of the plot, corresponding to the highest frequencies, where up-turns of  $G''$  can also be observed. BW-3EO (Fig. 4.5b), with longer EO groups, shows less sensitivity to salt concentration with smaller changes in the rheological curves than does BW-1EO (Fig. 4.5a).

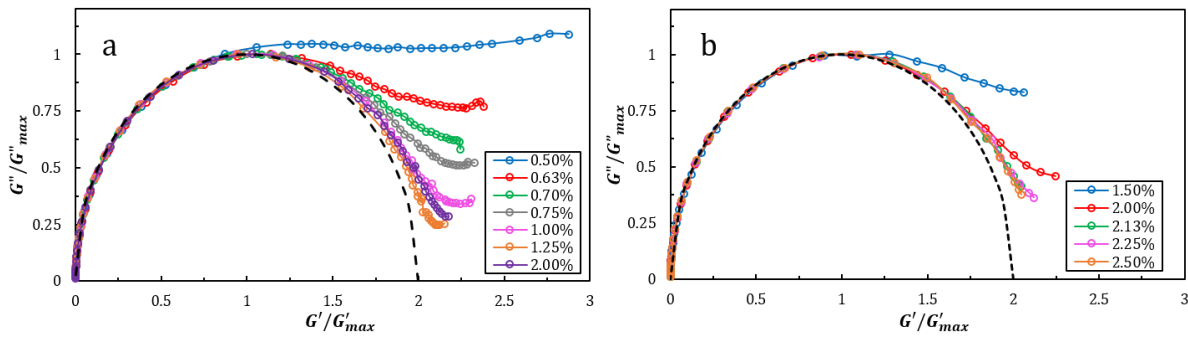


Figure 4.5 Normalized Cole-Cole plots for (a) BW-1EO and (b) BW-3EO. The percentages in the legends are the salt concentrations.

Time-temperature superposition (TTS) is performed for BW-1EO at each salt concentration. By shifting  $G'$  and  $G''$  curves with shift factor  $\alpha_T \equiv \eta_T/\eta_{T_0}$  for temperatures ranging from 20.0 to 25.0 °C, where  $\eta_T$  and  $\eta_{T_0}$  are the viscosity of the solution at temperature  $T$  and  $T_0 = 25$  °C, the storage moduli ( $G'$ ) overlap over the entire frequency domain (See Fig. 4.6a and b). TTS fails for loss moduli ( $G''$ ), however, at the highest frequencies before the salt peak is reached as shown by the small deviations among the  $G''$  curves at high frequency in Figure 6a. Interestingly, after passing the salt peak at which branched micelles begin to predominate, the superposition for  $G''$  again works perfectly (See Fig. 4.6b), which suggests that relaxation mechanisms of micelle branches are not temperature sensitive. We also note that the rheological properties of these highly complex mixtures of surfactants and perfumes are remarkable similar, qualitatively, to those of simple single-component surfactant solutions. [Zana and Kaler (2007); Candau *et al.* (1989); Cappelaere *et al.* (1994); Cates and Candau (1990); Croce *et al.* (2003); Imae *et al.* (1985); Imae *et al.* (1987); Kern *et al.* (1991); Khatory *et al.* (1993)] This indicates

that theories for thread-like micelles composed of simple surfactants should be equally applicable to complex commercial surfactant mixtures such as those studied here.

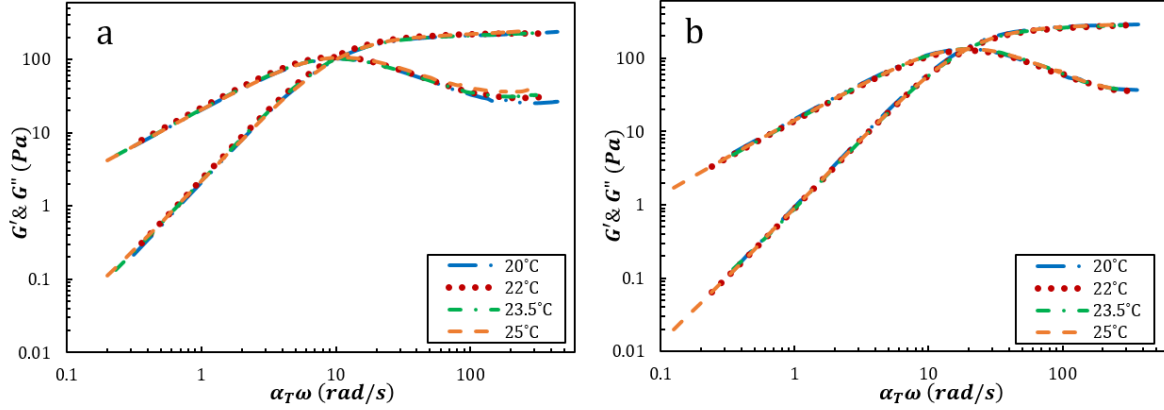


Figure 4.6 Master curves of frequency-dependent moduli obtained by time-temperature superposition (TTS), shifted to 25 °C at salt concentrations of (a) 1.0 wt. %, and (b) 2.0 wt. % NaCl for BW-1EO. The values of the shift factors  $\alpha_T$  are 1.1, 1.4 and 2.0 at 1.0 wt. % NaCl and 1.1, 1.2, and 1.4 at 2.0 wt. % NaCl at 23.5 °C, 22.0 °C and 20.0 °C, respectively.

## 2. Effect of salt on micellar properties from micellar-scale model

According to the Pointer Algorithm used here, [Zou and Larson (2014); Zou *et al.* (2015)] the rheological behaviors of entangled wormlike micelle solutions can be expressed by the following functional form:

$$G^*(\omega) = G_N F(\omega, G_N, \zeta, \langle L \rangle, \alpha_e, d) \quad (4.9)$$

where  $G^*(\omega)$  is the complex modulus, whose real and imaginary parts are  $G'(\omega)$  and  $G''(\omega)$ , respectively. In the above equation, the micelle diameter ( $d$ ) needs to be supplied from non-rheological measurements (due to the inability of rheology to determine its value as discussed in Zou *et al.* (2015)), which we fix at a value of 4 nm based on small angle neutron scattering (SANS) data (not shown). Therefore, four micellar parameters can be directly extracted from  $G'$  and  $G''$  data, i.e.: the plateau modulus ( $G_N$ ), the dimensionless breakage rate ( $\zeta$ ), the average micelle length ( $\langle L \rangle$ ), and the semi-flexibility coefficient ( $\alpha_e$ ). The dimensionless breakage rate  $\zeta$ , and the semi-flexibility coefficient  $\alpha_e$  are defined as

$$\zeta \equiv \frac{\bar{\tau}_{br}}{\bar{\tau}_{rep}}, \quad \alpha_e \equiv \frac{l_e}{l_p} \quad (4.10)$$

Here  $\bar{\tau}_{br}$ , called the average breakage time, is the lifetime a micelle of average length survives before breakage, while  $\bar{\tau}_{rep}$  is the characteristic time for reptation.  $l_e$  is the micelle entanglement

length, i.e., the average length of micelle between two entanglements; and  $l_p$  is the micelle persistence length. Given the five micellar parameters listed in Eq. (4.9), other micellar characteristic lengths ( $l_e$  and  $l_p$ ) and times ( $\bar{\tau}_{br}$  and  $\bar{\tau}_{rep}$ ) can also be obtained through theoretical derivations given elsewhere. [Zou and Larson (2014); Zou *et al.* (2015)]

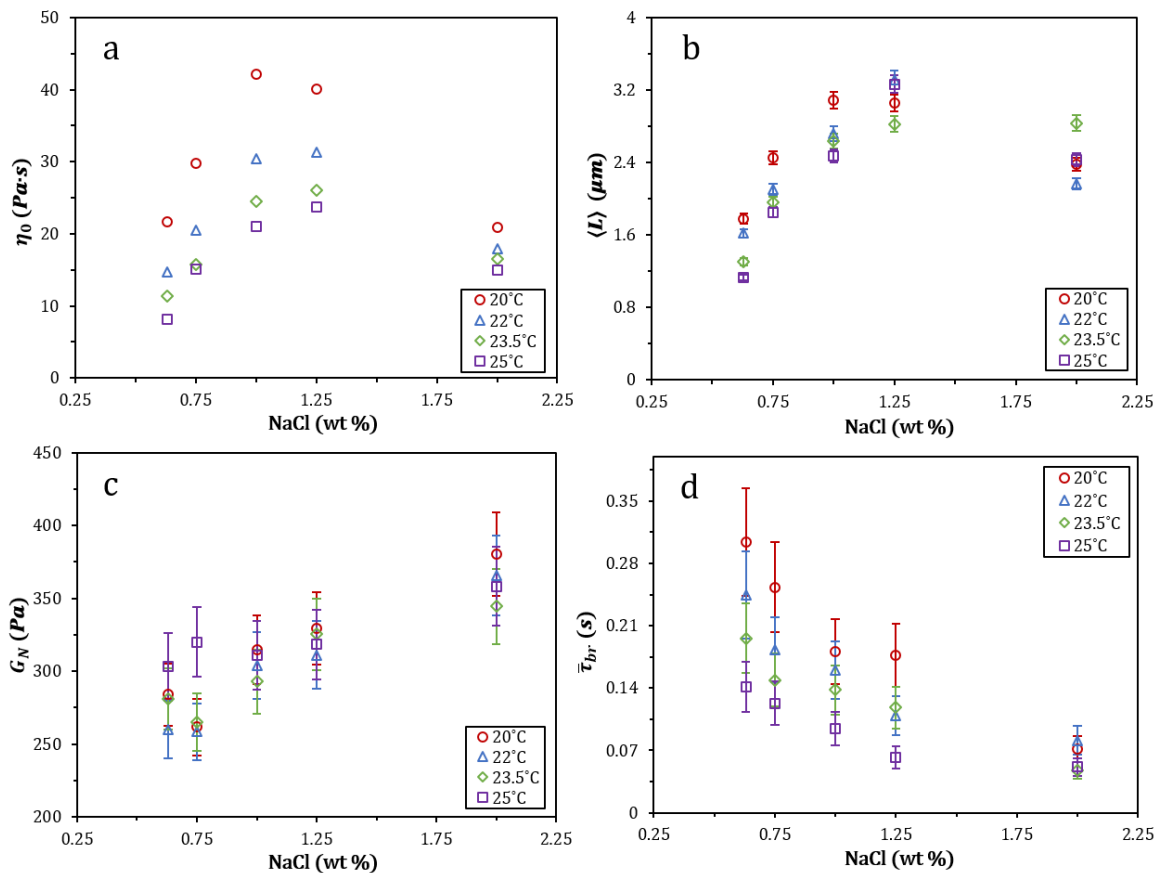


Figure 4.7 (a) Zero shear viscosity  $\eta_0$ , (b) average micelle length  $\langle L \rangle$ , (c) plateau modulus  $G_N$ , and (d) breakage time  $\bar{\tau}_{br}$  for various salt weight fractions for BW-1EO at 20.0, 22.0, 23.5, and 25.0 °C. The results in (a) are taken directly from the experiments with error bars much smaller than the size of the symbols, while the other results are obtained by fittings of the Pointer Algorithm whose error bars are estimated by the uncertainties when extracting parameters at different salt concentration. The procedure to determine the uncertainties (or so-called insensitivity) can be found in reference. [Zou *et al.* (2015)]

Using the data fitting procedure described in Zou *et al.* (2015), we extract micellar properties from the experimental  $G'$  and  $G''$  data for BW-1EO for various salt weight fractions at temperatures varying from 20.0 to 25.0 °C as shown in Fig. 4.7. Due to the limited upper range of frequency in  $G'$  and  $G''$  curves measured from mechanical rheometry, and the uncertainty that this introduces into the value of the persistence length  $l_p$  (which is especially difficult to extract

accurately in the absence of high frequency data), DWS was performed for solutions with 0.70 wt. % and 1.25 wt. % salt at 25.0 °C to provide high frequency data up to  $10^5$  rad/s. By combining these high frequency DWS data with the corresponding mechanical data, best-fits to the above model are obtained with predicted  $l_p$  in the range of 60-80 nm. Because we do not expect large changes in persistence length with small changes in temperature and because of the observed insensitivity of persistence length to salt concentration, the value, 70nm, is therefore used for all solutions to constrain the uncertainty in  $l_p$  when DWS data is not available. An example of the combined mechanical and DWS data and the corresponding fitting curves are shown in Fig. C.4 in *Appendix C*.

Figure 4.7a shows the salt dependence of zero shear viscosity ( $\eta_0$ ) for different temperatures, where the maximum of  $\eta_0$  occurs at around 1.25 wt. % NaCl for 25.0 °C, but shifts to a lower salt weight fraction (1.00 wt. %) at 20.0 °C. In contrast to the non-monotonic dependencies of zero shear viscosity (Fig. 4.7a) and apparent micelle length  $\langle L \rangle$  (Fig. 4.7b) on salt concentration, both the plateau modulus  $G_N$  (Fig. 4.7c) and the breakage time  $\bar{\tau}_{br}$  (Fig. 4.7d) show more nearly monotonic dependences ( $G_N$  increasing and  $\bar{\tau}_{br}$  decreasing) with salt concentration. Both  $\eta_0$  and  $\bar{\tau}_{br}$  decrease rapidly with increasing temperature, [Cates and Candau (1990); Helgeson *et al.* (2010)] while  $\langle L \rangle$  and  $G_N$  show weaker sensitivities to temperature.

Since the Pointer Algorithm does not distinguish branched from linear micelles, [Zou and Larson (2014); Zou *et al.* (2015)] the predicted  $\langle L \rangle$  at high salt concentration is more closely related to the length between branches, rather than the true micelle length. [Lequeux (1992)] Therefore, the non-monotonic dependence of  $\eta_0$  on salt concentration can be explained by the growth of micelles at low salt concentration and the increase of branching at high salt concentration, as observed by cryo-TEM. [Zana and Kaler (2007); Helgeson *et al.* (2010)] The relaxation of branched micelles is controlled by sliding of micellar material through the branch points, and the speed of this process increases with increasing branching even if the branched micelles become larger. [Lequeux (1992)] Thus, on the right side of the salt curve, as micelle branching increases with salt concentration, the “apparent micelle length,” which reflects that length between adjacent branch points, decreases, resulting in a sharp drop in viscosity.

By applying Eq. (4.2), the scission free energy  $E_s$  can be calculated from  $\langle L \rangle$ , which consists of contributions from both enthalpy ( $\Delta H_s$ ) and entropy ( $\Delta S_s$ ) as shown in Fig. C.5 in *Appendix C*. Here we only compute the scission free energy for salt concentrations up to the

maximum in the salt curve (i.e., 1.25 wt. %), to avoid results dominated by branch formation. The apparent scission free energy  $E_s$  in Fig. 4.8a is  $23\sim 27 k_B T$  near room temperature, which is equivalent to 55-65 kJ/mol with uncertainty of our method of extracting scission energy. As shown in Fig 4.8a,  $E_s$  decreases with temperature whereas it increases with salt concentration. In addition, the rapid decrease in breakage time  $\bar{\tau}_{br}$  with added salt, as shown in Fig. 4.7c, is presumably at least partly a consequence of the increasing micellar length, since longer micelles have more locations at which breakage can occur.

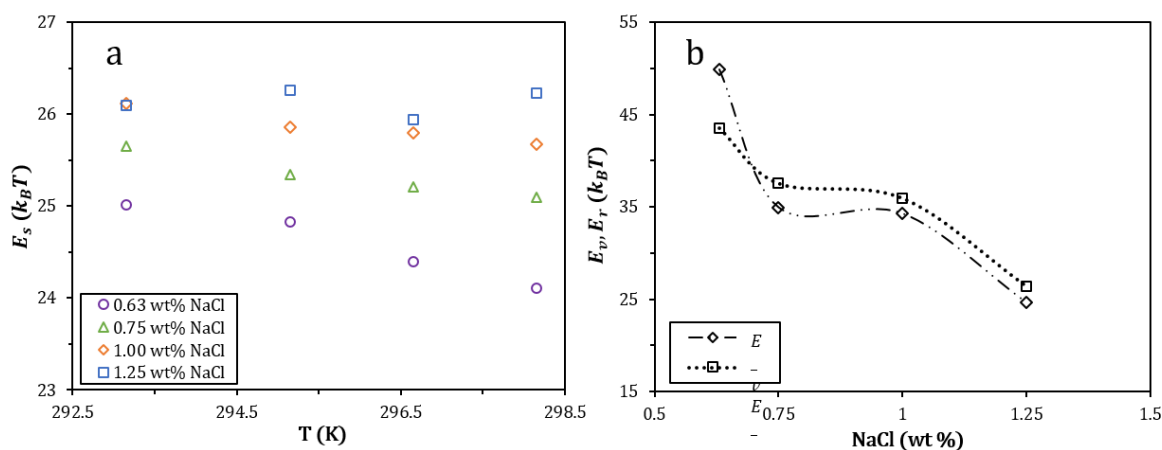


Figure 4.8 (a) Scission free energy  $E_s$  vs.  $T$  at various salt concentrations for BW-1EO. (b) Viscosity activation energy  $E_v$ , and terminal relaxation time activation energy  $E_r$ . The lines connecting the symbols are guides to the eye.

The more rapid dynamics with increased salt concentration is reflected in decreased activation energies for viscosity ( $E_v$ , Eq. (4.3)) and terminal relaxation time ( $E_r$ , Eq. (4.3)), also shown in Figure 8b. Not surprisingly, the activation energies for viscosity and relaxation time are nearly equal to each other over the whole range of salt concentration, since the modulus, which is roughly the ratio of viscosity to relaxation time, is relatively insensitive to salt. The decrease in activation energies with increased salt presumably reflect the reduced electrostatic energy barrier to micelle fusion and breakage at increased salt, and hence their faster dynamics. For CTAC/NaSal micelles, Kern *et al.* (1991) reported a value of around 37 kcal/mol =  $63 k_B T$  for both  $E_v$  and  $E_r$  and 27 kcal/mol =  $45 k_B T$  for  $E_s$ . These values are significantly higher than we find for BW-1EO. We note here that without our Pointer Algorithm, which gives us the length of the micelles as a function of temperature, the value of  $E_s$  would need to be obtained by neutron



scattering [Vogtt *et al.* (2017)] or from a combination of temperature-jump experiments and temperature-dependent rheological data. [Kern *et al.* (1991)]

### 3. Effect of salt on micellar structure from DPD simulations

Surfactant packing at the molecular scale determines the micellar-scale properties, and, through this, the rheological properties at the macroscopic scale. Here we investigate surfactant packing through DPD simulations of preassembled periodic wormlike micelles at various concentrations of surfactant and salt. A snapshot of one periodic cylindrical micelle at equilibrium is shown in Fig. 4.2. Figures 4.9a-c compare the bead number density distributions of surfactant tail, head and water as functions of radial distance from the micelle radial COM (the center of mass) for BW-1EO and BW-3EO with different surfactant concentrations and added NaCl. (The method of determining the COM at each axial position along the micelle was described in Section III.3.) Figure 4.9d shows the corresponding surfactant packing distances, defined in Section III as the micelle “spine length” per surfactant molecule.

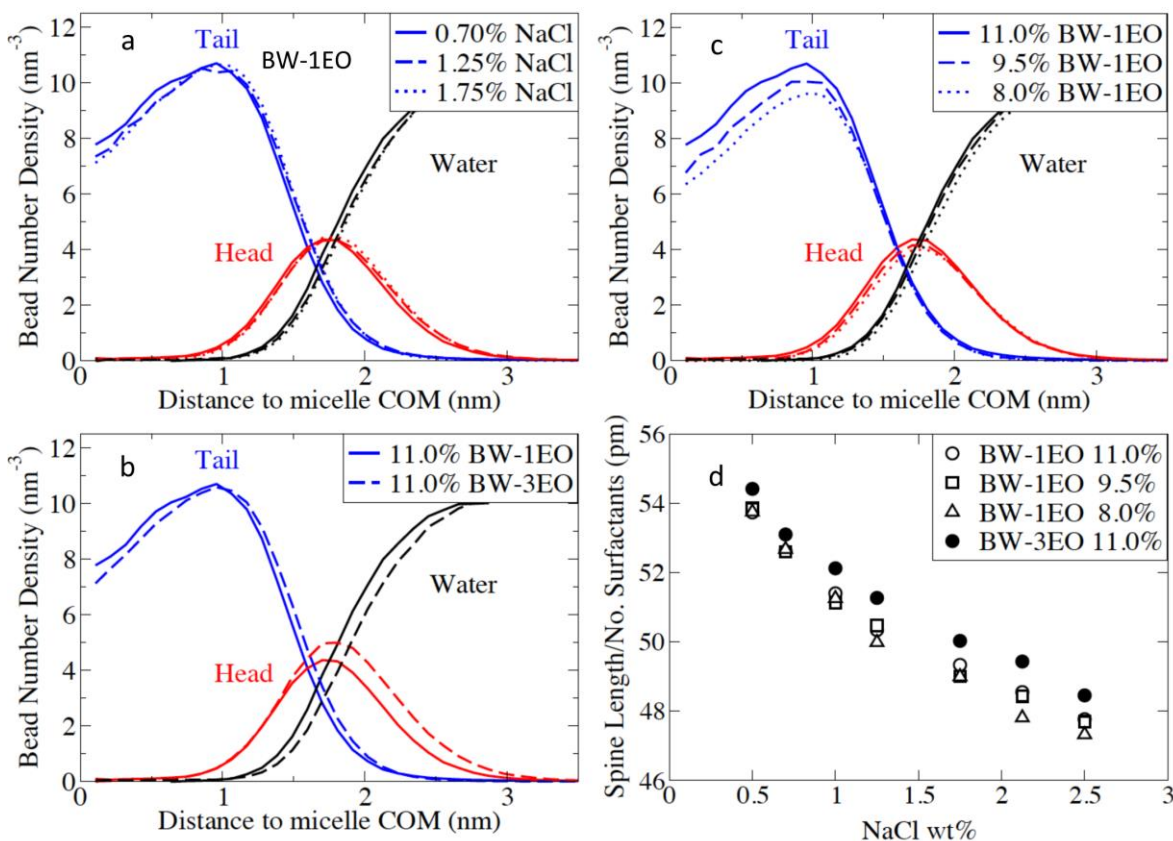


Figure 4.9 Normalized DPD bead number density radial distributions of head, tail, and water as functions of radial distance from COM; (a) for 11.0 wt. % BW-1EO at salt concentrations spanning the peak of the salt curve; (b) for 11.0 wt. % BW-1EO at 0.70 wt. % NaCl and 11.0 wt. % BW-3EO at 2.13 wt. % NaCl, which have the same experimental viscosity of 11.0 Pa · s; and (c) for BW-1EO solutions of three different surfactant concentrations at 0.7 wt. % NaCl. (d) Surfactant packing distance defined as the ratio of the micelle spine length (defined in Section III.3) to the number of surfactants in the micelle in all of the above systems. The bead number density is calculated by dividing the DPD bead number count by the shell volume.

In the packing parameter model, the impact of salt addition to linear micelles can be explained by shielding the Coulomb repulsion between neighboring head groups. By reducing the area per surfactant  $a_0$ , while keeping  $l_c$  and  $V$  constant, the packing parameter  $p$  (Eq. (4.7)) is increased, favoring areas of lower curvature. This implies making end-caps less favorable, increasing the scission energies and leading to longer micelles and higher viscosity.

In analyzing the packing of surfactants in cylindrical micelles using the packing distance, we can assess two different changes: a decrease in the proximity of the surfactants through screening and a change in the radius of the cylinder which is also reflected in the number of surfactants per unit length of the cylindrical micelle. The addition of salt induces a lower packing distance (Fig. 4.9d), while the cross-sectional structure of the micelle is affected by only a slight radial expansion at the higher salt concentration of 1.75% (Fig. 4.10a). Hence, the addition of salt makes a smaller area per head group more favorable at the same effective length and volume of the tail group corresponding to a higher packing parameter in the Israelachvili model.

As shown in Fig. 4.9b, BW-3EO, which has surfactants with longer EOs, has a thicker head layer than does BW-1EO. The thicker EO layer (which is electrostatically neutral) is less sensitive to the addition of salts and leads to smaller changes in viscoelasticity on addition of salt. The longer EO group in BW-3EO also decreases  $p$  because of its larger area per head group, which leads to a greater packing distance as shown in Fig. 4.9d, and thereby shortens the micelle relative to BW-1EO. The shift in the radial density profiles in Fig. 4.9b is only about 1 Angstrom, however. The even smaller increase in packing distance in Fig. 4.9d would be difficult to quantify experimentally, even though it may be enough to produce differences in rheological properties. This illustrates the importance of supplementing experimental characterization of micellar solutions with simulation data.

## V. Effect of PRM Addition

### 1. Effect of PRM described through $\log P_{ow}$

To understand how different PRMs modify the packing of the wormlike micelles and result in changes of the rheological properties of surfactant solutions, 15 PRMs (whose names, values of  $\log P_{ow}$ , and detailed chemical structures are listed in Table C.2 in Supporting Information), with a broad distribution of  $\log P_{ow}$  varying from -0.6 to 7.4, were added individually to BW-1EO formulations with and without the ACCORD (perfume mixture, defined in Section III.1) as noted earlier. Note that PRMs with similar values of  $\log P_{ow}$  but different chemical structures are among the 15 considered. Figure 4.10 plots the zero shear viscosities  $\eta_0$  of BW-1EO with ACCORD upon addition of each of these additional PRMs at a concentration of 15 mM against  $\log P_{ow}$ .

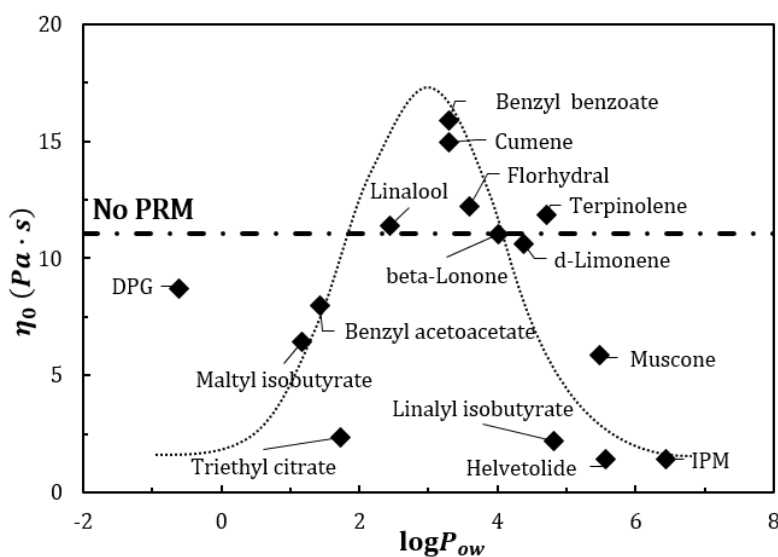


Figure 4.10 Zero shear viscosities  $\eta_0$  of BW-1EO in the presence of ACCORD and 0.7% NaCl on addition of each of 15 PRMs at 15 mM plotted against  $\log P_{ow}$ , of the added PRM. The dot-dashed line shows  $\eta_0$  of BW-1EO without any additional PRM beyond the six ACCORD components present in BW-1EO. Some data, if not available at 15 mM, are interpolated from the best linear or polynomial fit of  $\eta_0$  of BW-1EO vs. PRMs at different concentrations.

Compared to the viscosity without additional PRMs (i.e., the dashed line in Fig. 4.10),  $\eta_0$  is reduced significantly by adding PRMs with very low or very high values of  $\log P_{ow}$ . While for most PRMs with intermediate values of  $\log P_{ow}$ ,  $\eta_0$  is modified only slightly, an increase of  $\eta_0$  can be found for a few PRMs with intermediate  $\log P_{ow}$ , leading to a local maximum in the

vicinity of  $\log P_{OW}$  around 2-4. A maximum in this range is also seen in Fig. C.1 in *Appendix C*, for surfactant solutions with each of 25 individual PRMs added, i.e., without the presence of the ACCORD mixture of PRMs. The compounds in Fig. 4.10 that cause the largest increase in viscosity are benzyl benzoate and cumene.

These overall trends are consistent with findings by Fischer *et al.* (2008), who plotted the hydrodynamic radius  $R_H$  of the micelle (taken from the diffusion coefficient using the Stokes-Einstein equation) against  $\log P_{OW}$  for 22 PRMs and thereby also showed a maximum at  $\log P_{OW}$  around 2-4. Since  $R_H$  should increase monotonically with micelle length, and hence with  $\eta_0$ , the overall trends should be comparable.

The overall overlap of compounds between the data sets by Fischer and the data shown in this paper is small; the commonality is that compounds with a  $\log P_{OW}$  of 2-4 have the best potential to boost viscosity. It is remarkable however that the detailed trends do not match up as well. The data by Fischer *et al.* (2009) suggest that alcohols and aldehydes with a  $\log P_{OW}$  2-4 show the largest viscosity increases. In our data set the alcohol linalool only increases viscosity slightly, and the apolar cumene molecular increases viscosity more significantly.

The  $\log P_{OW}$  model is very crude in predicting the location of the probe molecule in the micelle. Consider the molecules cumene ( $\log P_{OW} = 3.7$ ) and linalool ( $\log P_{OW} = 3.3$ ) with very similar  $\log P_{OW}$  values. Based on their chemical structure, one would expect for the hydrophobic cumene to sit in the core of a micelle, while the alcoholic group of linalool would take a more water-exposed position at the surface of the micelle.

Also, the three esters methyl isobutyrate, benzyl acetoacetate, and triethyl citrate, (detailed structures listed in Table C.2 in *Appendix C*) have values of  $\log P_{OW}$  between 1 and 2. However, triethyl citrate has the least compact structure and reduces the viscosity the most, while the other two PRMs in this range of  $\log P_{OW}$  have relatively more compact structures and fewer branches and reduce the viscosity only moderately.

The COSMOmic [Ingram *et al.* (2013)] model can provide predictions of the location of small solutes in micelles and bilayers under the assumption of infinite dilution of the solute and can provide a more differentiated analysis. Molecular simulations can provide not only a picture of where the solute partitions in to the micelle but also provide information on how the micelle structure is altered upon addition of the solute. In the following, we will compare micellar and molecular scale models for a limited set of compounds.

## 2. Effect of PRM on micellar properties from the micellar-scale model

To study the relationship between rheological behavior and micellar structure, we choose four PRMs among the 15 for a detailed analysis of their effect on BW-1EO. The four PRMs, shown in Fig. 4.1c-f, span a broad range of  $\log P_{OW}$  from -0.7 (for DPG) to 7.4 (for IPM). Zero shear viscosities  $\eta_0$  as functions of concentration of each of these four PRMs added to BW-1EO are shown in Fig. 4.1a. Addition of DPG, with the lowest value of  $\log P_{OW}$ , decreases  $\eta_0$  roughly linearly; linalool with a moderately low value of  $\log P_{OW} = 3.3$  reduces  $\eta_0$  only marginally; cumene with a higher value of  $\log P_{OW} = 3.7$  increases  $\eta_0$  modestly; and IPM, with the highest value of  $\log P_{OW}$ , reduces  $\eta_0$  very significantly.

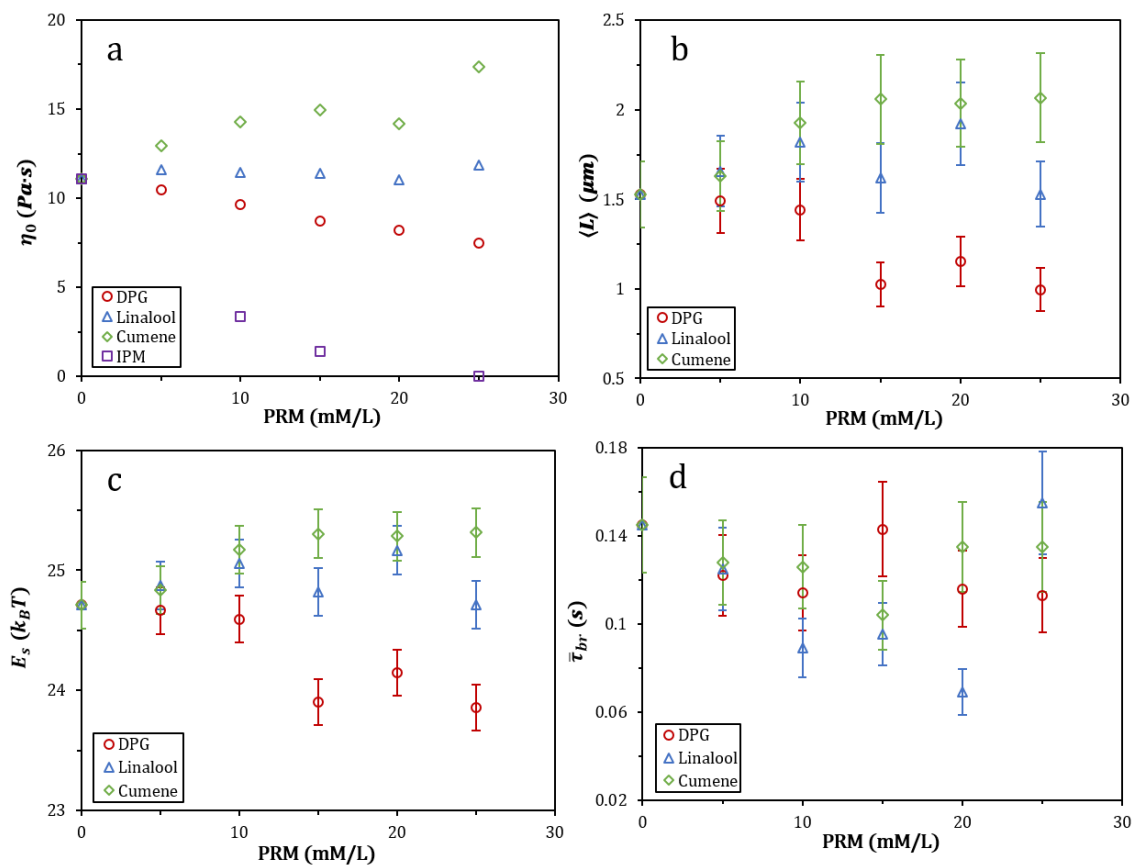


Figure 4.11 (a) Dependence of  $\eta_0$  on concentration of dipropylene glycol (DPG), cumene, linalool, and isopropyl myristate (IPM) in BW-1EO containing ACCORD and 0.7 wt. % NaCl. (b) Estimated average micelle length  $\langle L \rangle$ , (c) scission free energy  $E_s$ , and (d) average breakage time  $\bar{\tau}_{br}$ , inferred from the Pointer Algorithm, vs. PRM concentration. Note that  $\langle L \rangle$  of IPM is too short to be estimated by the Pointer Algorithm. Same as Fig. 4.7, the results in (a) are taken directly from the experiments with error bars much smaller than the size of the symbols, while the other results are obtained by fittings of the Pointer Algorithm whose error bars are estimated by the uncertainties when extracting parameters at

different salt concentration. The procedure to determine the uncertainties (or so-called insensitivity) can be found in reference. [Zou *et al.* (2015)]

We now follow the same procedure used in Section IV.2 to extract the average micelle length  $\langle L \rangle$  and the scission free energy  $E_s$  from the rheological data, giving the results shown in Fig. 4.11b and c: For DPG having an extremely low value of  $\log P_{OW}$ ,  $\langle L \rangle$  and  $E_s$  decrease slowly with added PRM, while for linalool and cumene with intermediate values of  $\log P_{OW}$ ,  $\langle L \rangle$  and  $E_s$  initially increases with added PRM with some oscillations that may reflect the uncertainty in obtaining these values from rheological data. Other micellar parameters, i.e., breakage time  $\bar{\tau}_{br}$  (See Fig. 4.11d) and plateau modulus  $G_N$  (data for  $G_N$  not shown here), remain nearly constant with the addition of PRM (within uncertainties), except for linalool whose  $\bar{\tau}_{br}$  decreases before an abrupt rise occurs at high concentration as shown by Fig. 4.11d. For constant  $G_N$ , the zero-shear viscosity  $\eta_0$  of a micelle solution is proportional to the terminal relaxation  $\tau$ , which is a function of both  $\langle L \rangle^3$  and  $\bar{\tau}_{br}$ . Therefore, a decrease of  $\langle L \rangle$  with a nearly constant  $\bar{\tau}_{br}$  leads to a decrease in  $\eta_0$ , as is the case for DPG according to Fig. 4.11. Note that the drop of  $\langle L \rangle$  and jump of  $\bar{\tau}_{br}$  at the highest concentration of linalool as shown in Fig. 4.11b and d is due, we believe, to a change of micelle structure from linear to branched. Changes in micellar properties upon addition of the above four different PRMs presumably result from different PRM partitioning within the micelles, which is related to molecular-scale surfactant packing, which is assessed using DPD simulations in next section.

In addition, we examine the effect of one of these four PRMs, linalool, on the rheology of BW-3EO, which when compared to the effects of linalool addition to BW-1EO, allows us to investigate the additional effect of average EO length on micellar properties. Linalool is chosen since its effects have been modeled before. [Fischer *et al.* (2009); Parker and Fieber (2013)] Adding the same amount of linalool to BW-1EO and BW-3EO results in very different changes in viscoelastic properties as shown in Figure 12. The addition of linalool modifies the rheology of BW-1EO only slightly, as shown by the near overlap of loss moduli  $G''$  at low frequency in Fig. 4.13a. This indicates a moderate change of  $\langle L \rangle$  as discussed earlier. On the other hand, addition of linalool to BW-3EO decreases  $\eta_0$  significantly (data not shown here) resulting in considerably larger shifts of both  $G'$  and  $G''$  (Fig. 4.12b) than for BW-1EO.

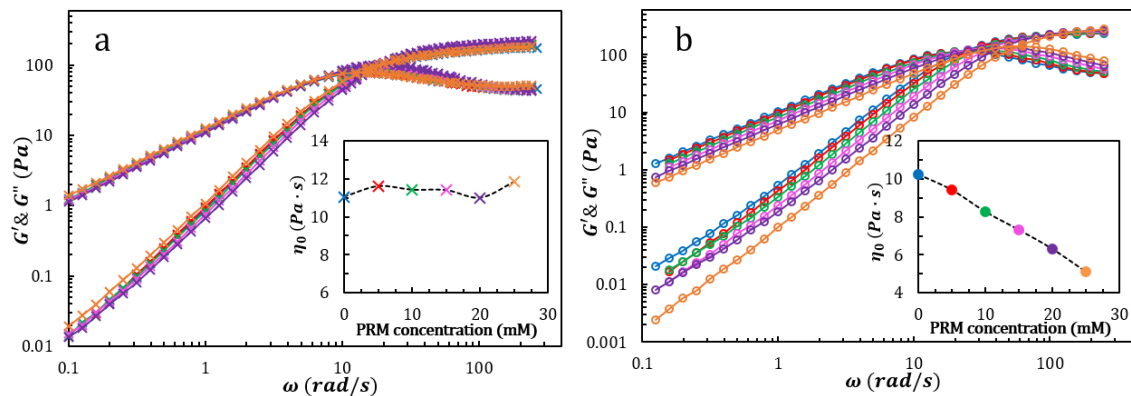


Figure 4.12 Storage  $G'$  and loss moduli  $G''$  vs. frequency for (a) BW-1EO and (b) BW-3EO, at various linalool concentrations, each coded by a color also used in the inserted figures giving zero-shear viscosities as functions of PRM concentration.

### 3. Effect of PRM on surfactant packing from DPD simulations

We carried out DPD simulations of 11 wt. % BW-1EO and 0.7 wt. % NaCl in the presence of each of the four additional PRMs (i.e., DPG, linalool, cumene, and IPM) to study the relationship between surfactant packing and micellar properties. Our analysis shows that the radial distribution of ACCORD (perfume mixture, defined in Section III.1) present in these formulations is not modified significantly upon addition of DPG, linalool, or cumene (Fig. C.3 in *Appendix C*). The following figure (Fig. 4.13) shows zero shear viscosities  $\eta_0$  (colored filled diamonds) and surfactant packing distances (colored open triangles) upon addition of 15 mM PRM to BW-1EO vs. their values of  $\log P_{OW}$ .

We would expect dipropylene glycol (DPG) with its extremely low value of  $\log P_{OW}$  -0.6 to partition mainly into water and to some extent into the surfactant head group region, as is in fact seen in the first cartoon at the lower left of Fig. 4.13. This is also consistent with the analysis of locations of the compound as shown in Fig. 4.14a: The near-perfect overlap of tail, head, and water distribution with those in the absence of DPG indicates that the partitioning of DPG does not modify the radial distribution of surfactants within the micelle, and maintains the micelle radius and surfactant tail length  $l_c$  constant. Although small in size, DPG molecules are branched (Fig. 4.1c), so that they take a relatively larger volume within the micelle when partitioning into it than do other PRMs. As expected, the packing distance increases significantly (as shown by the open cyan triangle in Fig. 4.13). This indicates that the partitioning of DPG into the head group region increases the surfactant head group surface area  $a_0$ , leading to a larger packing

distance. This corresponds to a decrease in the packing parameter  $p$  (Eq. (4.7)), and results in a shorter  $\langle L \rangle$ , smaller  $E_s$ , and lower  $\eta_0$  (as shown by the circles in Fig. 4.11a, b, and c).

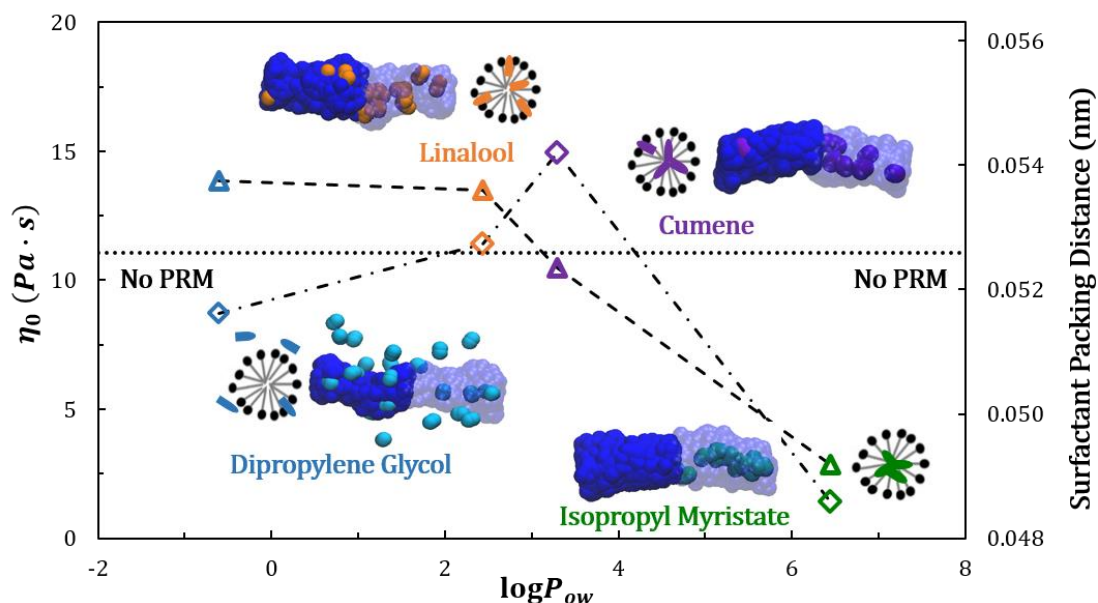


Figure 4.13 Plot of  $\eta_0$  (colored open diamonds connected by dash-dotted line, left axis) and surfactant packing distance (colored open triangles connected by dashed line, right axis) for BW-1EO upon addition of 15 mM dipropylene glycol (DPG), cumene, linalool, and isopropyl myristate (IPM) vs. their  $\log P_{OW}$  for 11 wt. % BW-1EO in 0.7 wt. % NaCl. The dotted line gives the viscosity and packing distance in the absence of the added PRM. Each of the four PRMs is given a color used consistently in symbols and text, as well as in the PRM molecules contained in snapshots of 15 nm-long sections of the periodic wormlike micelles. The snapshots show the tail beads in blue; for the right half of each micelle, the blue tail beads are rendered translucent to show the positioning of PRMs deep within the micelles. Head and water beads are omitted for clarity. The schematic cartoons at the right side of each micelle show the location of the PRMs (colored bullets) in the cross section of the wormlike micelles at the corresponding  $\log P_{OW}$  range.

Linalool, with a moderately low value of  $\log P_{OW}$ , partitions into both the tail region and into the interfacial region between the surfactant tail and the head groups as shown at the upper left of Fig. 4.13 by the second cartoon with orange beads representing linalool. Similar to DPG, partitioning of linalool does not much modify the radial distribution of surfactants within the micelle as shown in Fig. 4.14b. Thus, micelle radius and surfactant tail length  $l_c$  remain the same on addition of linalool. From Fig. 4.1e, linalool has two branches at or near the ends of the molecule. Because of its partitioning into both head and tail regions, it is expected to crowd both regions, and result in increases in both  $a_0$  and  $V$ . This is consistent with the increased packing distances as shown in Fig. 4.13. Interestingly,  $\langle L \rangle$  and  $E_s$  increase initially and then stay nearly constant upon addition of linalool (Fig. 4.11b and c) indicates a possible competition between



changes of  $a_0$  and  $V$  in determining the packing parameter  $p$ , leading to nearly constant  $\eta_0$  at macroscopic scale (Fig. 4.11a).

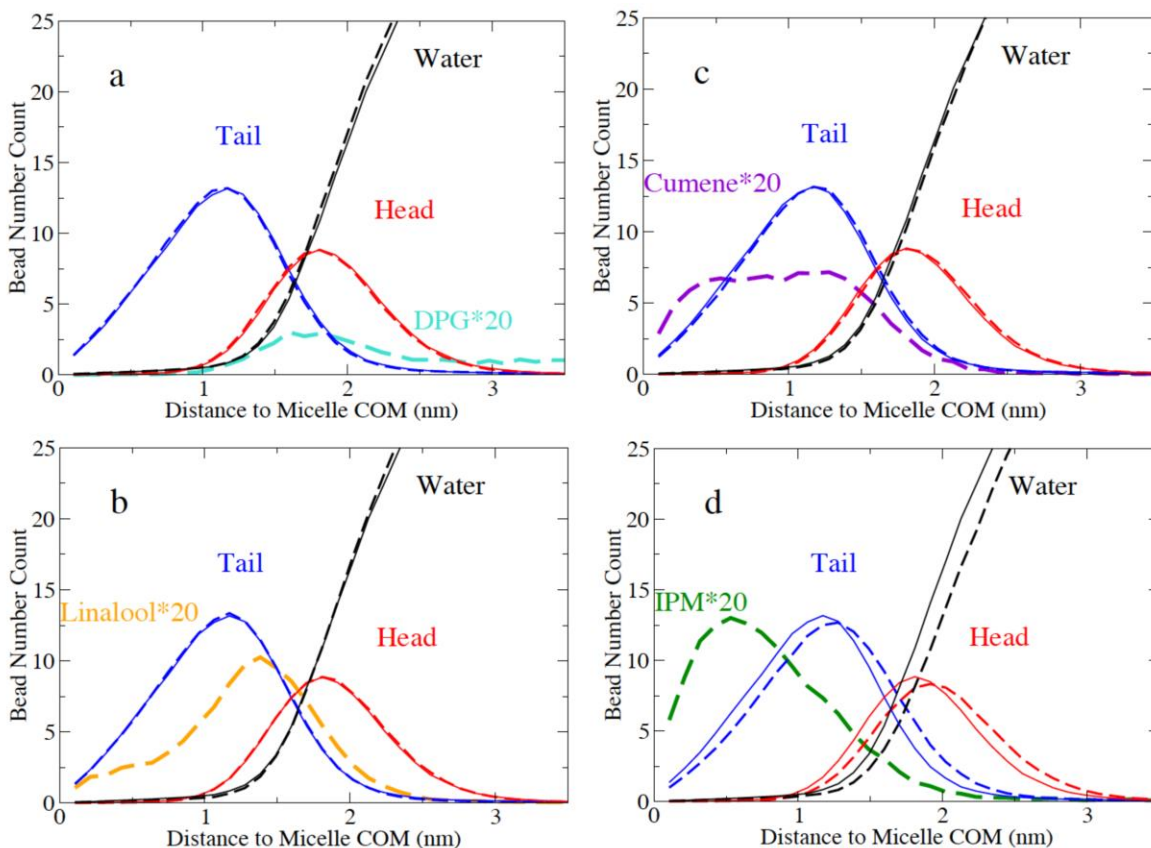


Figure 4.14 Bead number count within a shell of 0.1 nm width as a function of radial distance to the spine of the micelle of tail, head, water and an additional PRM, namely (a) DPG, (b) linalool, (c) cumene, and (d) IPM as functions of radial distance to the COM. The dashed lines represent the distributions in the presence of 15 mM of the added PRM and the solid lines correspond to the absence of the added PRM. In all solutions, with or without the single added PRM, ACCORD was present.

Cumene, with a moderately high  $\log P_{OW}$ , partitions mainly within the surfactant tail region in the micelle core, while only a small amount enters the interface between tail and head groups as shown in the third cartoon at the upper right of Fig. 4.13. This is consistent with the snapshots showing many fewer cumene purple dots protruding from the left half of the micelle in the third cartoon than orange linalool dots from the left half of the micelle in the second cartoon in Fig. 4.13. Similar to DPG and linalool, the nearly perfect overlap of the radial distributions of tail, head, and water with those in the absence of cumene, as shown in Fig. 4.14c, indicates a constant micelle radius and surfactant tail length  $l_c$  before and after the addition of cumene. The packing distance, instead of increasing as occurred on addition of DPG and linalool, decreases

slightly on addition of cumene. To fit cumene into the tightly packed surfactant tail region while keeping the micellar radius constant without increasing the packing distance, the packing of the surfactant tails has to be modified. Possibly the planar structure of cumene (Fig. 4.1d) both pushes tails away and condenses head groups so that the micelle radius has no significant net change. Thus, cumene mixes with the tails, increasing their effective volume  $V$  without increasing  $l_c$  and  $a_0$ , which should lead to an increase of packing parameter  $p$ , leading to longer  $\langle L \rangle$ , larger  $E_s$ , and higher  $\eta_0$ , as is observed in Fig. 4.11.

DPG is miscible with water. There is some enrichment at the micelle-water interface (Fig. 4.14, cartoon in Fig. 4.13). A tentative interpretation of the impact of DPG on the viscosity is that the micelle endcaps show a higher curvature and hence larger hydrophobic-hydrophilic interface. DPG partitioning to this interface will reduce the interfacial tension and end cap energy. In terms of the packing parameter framework, DPG can be conceptualized as a surfactant head group without the tail, decreasing the packing parameter. In addition to the interfacial mechanism described, DPG could also lower the dielectric constant at the micelle water interface, increasing the repulsion between head groups, favoring higher curvature and smaller micelles. This effect is not described in the simulation model and could further increase the packing distance. Simulations of the scission energy (manuscript in preparation) suggests that the impact of DPG on the interface is sufficient for explaining the decrease in viscosity.

IPM has a very high  $\log P_{OW}$ , and therefore partitions predominantly within the surfactant tail region as shown in the last cartoon at the lower right of Fig. 4.13. Although the molecule is large in size, it buries itself almost completely within the tail region. The presence of IPM causes the packing distance to decrease (as shown by the open green triangle in Fig. 4.13), implying greater crowding of micelle head groups. One might expect this to lead to a lengthening of the micelles. However, DPD simulations show that at a higher concentration of 100 mM, IPM the periodic wormlike micelles start to break into shorter rodlike micelles. Previous studies have shown that large oils that partition almost entirely within the tail region can swell the micelle radius and induce a transition towards spherical shape, [Afifi *et al.* (2012)] which is consistent with our rheological data showing that  $\eta_0$  is reduced significantly at high IPM concentration (Fig. 4.11a). This transition likely occurs because the PRM is too large to mix well with the surfactant tails, and so instead segregates into the center of the micelle, pushing tails outward and increasing micellar radius as shown in Fig. 4.14d. This acts to effectively increase the tail length

$l_c$  without increasing much the tail volume  $V$ , therefore decreasing the packing parameter  $p$ , shortening the micelle length, and inducing a transition towards a spherical surfactant-coated oil droplet at high PRM concentration. The above effect on the packing parameter  $p$  is opposite to that of smaller hydrophobic molecules, like cumene, which mix with the tails, increasing their effective volume  $V$  without increasing their length  $l_c$ . Thus, small hydrophobic molecules should increase the packing parameter  $p$ , causing micelles to increase in length, while large hydrophobic molecules are expected have the reverse effect.

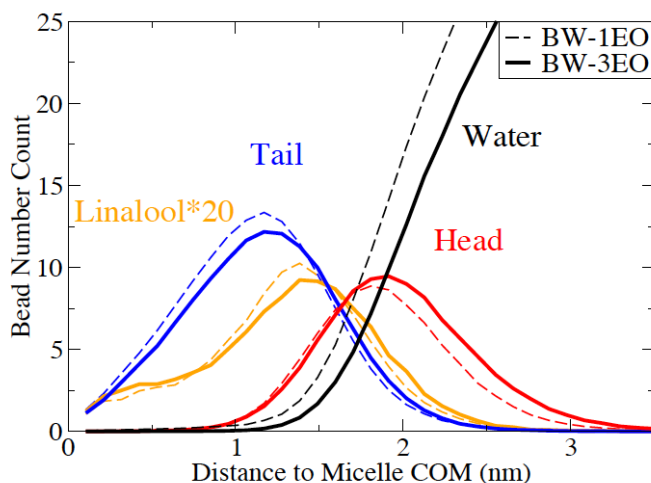


Figure 4.15 Normalized DPD bead number count of tail, head, and additional linalool within a shell of 0.1 nm width as a function of radial distance to the COM of the wormlike micelles. The dashed lines represent the distributions in BW-1EO and the solid lines in BW-3EO. In all solutions, ACCORD was present.

Finally, we study the effect of average EO length upon the addition of linalool, on micellar structure by carrying out DPD simulations on BW-3EO. As with BW-1EO, the distributions of head, tail and water upon linalool addition to BW-3EO remain constant (data not shown here), resulting in the same radius of the wormlike micelles. The packing distance increases due to the branched structure of linalool. However, the distributions of linalool within the two formulations are different as shown in Fig. 4.15: there is more partitioning of linalool into the head region of BW-3EO than of BW-1EO due to longer averaged EOs in BW-3EO. Therefore,  $\alpha_0$  increases more upon linalool addition to BW-3EO than it does on addition of linalool to BW-1EO, leading to a decrease of packing parameter  $p$ , shorter micelles, and lower  $\eta_0$  in BW-3EO, in contrast to its more negligible effect on BW-1EO.

To sum up this section, we find that, except at intermediate values of  $\log P_{OW}$  in the range 2-4, the PRMs shorten micelles, either because they partition to the head group region (at low  $\log P_{OW}$ ), leading to a decreased packing parameter, or they segregate into the center of the micelle (at high  $\log P_{OW}$ ), acting to increase micelle radius, leading to micelle breakup and eventually spherical droplets at high concentrations of PRM.

## VI. Conclusions

We have combined linear rheology and multi-scale modeling to connect macroscopic viscoelastic properties to surfactant packing structures at the molecular scale. Specifically, we studied the rheological property changes in two body wash formulations, namely BW-1EO and BW-3EO, upon addition of NaCl salt and perfume raw materials (PRMs) at various concentrations and temperatures. We fit the linear rheology to predictions of a micelle-level model, the “Pointer Algorithm,” which is an advanced implementation of the Cates model. We thereby obtained micelle-level properties such as micelle length, breakage time, and scission free energy. To complement this information, we determined the surfactant packing structure at the molecular scale within the micelle using dissipative particle dynamics (DPD) simulations and traditional surfactant packing arguments.

Although the qualitative effect of salt on the viscosity of a micelle solution is well understood, our DPD simulations confirm and quantify the effect of salt on head group packing, through use of a “packing distance” defined as the length of wormlike micelle per surfactant molecule, which decreases as salt concentration increases in the two body wash formulations we studied here. If the radius of the wormlike micelle remains constant, this should result in a higher Israelachvili packing parameter  $p$ . This, in turn, should produce longer micelles, larger scission free energy, and shorter micellar breakage time, all of which agrees with our quantitative estimates of these parameters from application of the micellar-scale model to our linear viscoelastic data. Thus, while our analysis of the effects of salt on micelle properties is consistent with current understanding, we have been able to quantify this connection more thoroughly than before, through use of the Pointer Algorithm to extract quantitative measures of micelle properties from rheology and the use of DPD molecular simulations to connect this to the detailed surfactant packing within the micelle. In fact, the changes in surfactant packing quantified by our simulations are often too subtle to be obtained from experimental probes, such

as neutron scattering, and yet these small changes have significant effects on rheological properties.

By measuring linear rheology over a 5 °C range of temperature, and using the Pointer Algorithm to infer the temperature dependence of the micellar length, we have also been able to estimate the micellar end cap free energy, which is found to be around 23~27  $k_B T$  for our solutions, which is significantly less than that reported earlier for CTAC/NaSal micelles (around 50  $k_B T$ ) while the activation energies for viscosity and relaxation time both drop from around 50  $k_B T$  to 25  $k_B T$  as salt concentration increases up to salt concentration that maximizes viscosity, with the larger value being similar to that in CTAC/NaSal micelles. By using the Pointer Algorithm, we also inferred that the micellar breakage time decreases with salt concentration almost monotonically from around 0.15 s to around 0.05 s, at 25 °C. PRMs modify the viscoelastic properties of body washes by partitioning within the micelles at different locations according to their values of  $\log P_{OW}$  and their chemical structures. We find through micellar-scale modeling and DPD simulations that PRMs having a very low or a very high  $\log P_{OW}$  reduce the average micelle length  $\langle L \rangle$ , scission free energy  $E_s$ , and zero shear viscosity  $\eta_0$  significantly. PRMs with low values of  $\log P_{OW}$  mainly partition within the head group region of the micelle, increase the head group surface area  $a_0$  at constant micellar radius, decrease the packing parameter  $p$  and result in shorter micelles and lower  $\eta_0$ . Large, hydrophobic, PRMs with very high  $\log P_{OW}$  mainly partition into the center of the micelle, and rather than mixing with the tails, and push them radially outwards, which increases the effective tail length  $l_c$  which favors shorter micelles. PRMs with moderately large  $\log P_{OW}$  values can induce some growth of micelle length  $\langle L \rangle$ , but does not change the viscosity  $\eta_0$  or the scission energy  $E_s$  of the solutions much or at most increases them slightly, relative to the viscosity in the absence of the added PRM. Partitioning of PRMs depends on the composition of the surfactant solution as well as on the PRM. The use of the packing distance in cylinders as a tool to describe the impact of the PRMs on the structure and viscosity is insufficient as it lacks a description of the packing of the surfactant in the endcaps. To even qualitatively describe the impact of molecules with different polarities, a parameter needs to capture the impact on both the cylindrical and the end caps needs to be captured.

In summary, multi-scale modeling and rheological measurements were used to determine the structure-property relationships of surfactant formulations. Consistent results were obtained

at different length scales, from molecular, to micellar, to bulk rheological. The development of molecular parameters for simulating more complex PRMs, for use in both DPD and atomistic molecular dynamics simulations are needed. Application of similar methods to determine the synergistic effects of two or more PRMs are also needed.

## Chapter 5: Mesoscopic Modeling on the Rheology of Partially Unentangled and Branched Micelle Solutions

### I. Introduction

Surfactant micelles, known for their versatile in self-assembled structure and flow behaviors, have extensively been served as carriers, [Crothers *et al.* (2005)] templates, [Kunieda *et al.* (2001)] solubilizer, [Huang *et al.* (2016)] extractants, [Gao *et al.* (2016)] and rheology modifiers, [Lin *et al.* (2001)] among industrial formulations either as mixtures or as individual components. Given the relative facileness in tuning the non-covalent interactions between surfactant molecules, a wide range of micellar morphologies, such as ellipsoids, worms, vesicles, lamellae, can be achieved through the addition of simple electrolytes, cosurfactants, or strongly binding counterions (so-called hydrotropes) into the solutions. [Kaler *et al.* (1989); Villeneuve *et al.* (1999); Wang *et al.* (2016)] Such mixed surfactant systems sometimes exhibit prominent gains in viscoelasticity indicating the existence of large surfactant aggregates, in particular, the transient network of entangled wormlike micelles (WLMs), which have commonly been practiced in the realm of detergent-related industries. [Adamy (2016); Oelschlaeger and Willenbacher (2012); Zhao *et al.* (2015)] The formation of these long WLMs is attributed to the favor of a specific molecular packing, also known as the spontaneous curvature of the micelles. [Adamy (2016); Lonetti *et al.* (2011)] Because of the various ways the additives can tailor the micellar curvature, for instance, through electrostatic screening, hydrophobic binding, etc.; [Dai *et al.* (2016); da Silva *et al.* (2011); Padalkar *et al.* (2009); Padalkar *et al.* (2012)] there exist great opportunities in the synthesis of new functional materials: recent years have witnessed a growing attention on stimuli-responsive WLMs. [Hideki *et al.* (2005); Lu *et al.* (2016)]

However, the interplay between structural energy and system entropy brings two types of topological defects to the cylindrical body: end-caps and junctions, resulting in micelles with finite length and formation of branched structures, respectively. [Dan and Safran (2006)] The latter is thought to enable percolation and phase separation with the emergence of an interconnected network when temperature is increased. [Zilman *et al.* (2004); Zilman and Safran

(2002)] Since the local packing geometry is subject to physicochemical subtleties of the system, the dimension, topology, and flexibility of the micellar aggregates can thereof be manipulated progressively to achieve the transition between linear and branched micelles. [Danino *et al.* (2000); Angelescu *et al.* (2003); Chellamuthu and Rothstein (2008); Ouchi *et al.* (2006)] Such transitions have been shown to dramatically impact the thermodynamic and viscoelastic behaviors of the surfactants as studied extensively by various approaches. [Zhang and Wei (2013); Helgeson *et al.* (2010); Decruppe and Ponton (2003); Fischer *et al.* (1997); Danino *et al.* (2000)]

Besides the fundamental interest on molecular interactions among surfactants, intense efforts have been made for WLM solutions over decades to better understand the coupling between their complex rheological properties and the microstructure as well as their topology at mesoscale level. As directly visualized by cryo-TEM, [Clausen *et al.* (1992); Lin (1996)] these WLMs have a diameter of 3-5 nm whilst their contour length can reach a few micrometers in the semi-dilute regime giving rise to the occurrence of entanglements and eventually an enhanced viscoelasticity. [Padalkar *et al.* (2012); Yusof *et al.* (2012)] In this regard, WLMs are much similar to polymers except that they are subjected to constantly breaking and reforming in thermal equilibrium with their surfactant “monomers”, [Kalur *et al.* (2005); Feng and Han (2016)] which prevents them from mechanical degradation and hence being a desirable candidate as heat-transfer fluids and fracturing liquids. [Barhoum *et al.* (2012)] However, when the applied flow rate is high enough to disturb the equilibrium WLM structures, which in turn modify the flow itself, a rich variety of nonlinear rheological features would appear including localization of stress, heterogeneous shear bands, and flow induced phase separation etc. [Gallot *et al.* (2013); Cardiel *et al.* (2014)]

Although they exhibit distinct flow properties and phase behaviors, the quantitative differentiation of branched structures from linear ones turns out to be a conundrum over decades. Part of this difficulty is associated with the hierarchical length and time scales for micelles under equilibrium, over which comprehensive characterizations through scattering or visualization techniques can hardly be fulfilled due to their limited accessible range. [Helgeson *et al.* (2010); Danino *et al.* (2000)] A rich variety of theories and models are therefore proposed to enhance the understanding of micellar branching, which generally falls into two categories: thermodynamic-topological or statistical-mechanical. The thermodynamic-topological models can well predict



the “inverted” micellar phase behavior on the basis of a complex balance between mixing entropy and enthalpic/curvature energy, where a coarse-grained local packing parameter, called spontaneous curvature, is introduced to explain the temperature induced evolution of micelle morphology. [Dan and Safran (2006); Tlusty and Safran (2000)] While for statistical-mechanical models, the main concept relies on the analogy between cylindrical micelles and polymer chains with behaviors of topological defects, i.e., chain-ends and junctions, reminiscent of binary fluid in the sense that their competition corresponds to a shift of micellar connectivity. [Zilman and Safran (2002); Drye and Cates (1992)]

Thus, to unveil the basic property-structure relationships behind different flow behaviors of WLMs, methods that allows for monitoring the dynamics of micelles are in need. Nourished by the continuing development of instrument science and technology, micelle characterization sustains its prosperity which involves an increasing number of advanced techniques from conventional flow birefringence, light and neutron scattering to more recent ultrasonic velocimetry, [Gallot *et al.* (2013)] and micro-cantilevers. [Youssry *et al.* (2012)] However, quantitative estimates and comparisons of the determined micellar characteristic lengths from those methods still remain challenging. The difficulties, to a large extent, rest on the gaps between individual methods in probing the structure beyond specific length scales or concentrations, which can hardly be overcome by a simple combination of several aforementioned characterization measurements. Since the rheology of WLM solutions appears to be rather sensitive to subtle changes in either length scales or lifetime of the microstructure, once coupled with an appropriate model, it can offer an indispensable route in micelle characterization. For entangled WLM solutions, as confirmed by Cates in his well-recognized theory, micellar properties such as micelle length and micellar breakage and reformation time can be withdraw from the linear rheological responses, namely, the storage ( $G'$ ) and the loss ( $G''$ ) modulus. [Cates (1987); Turner and Cates (1991); Khatory *et al.* (1993)]

Nevertheless, it was found that the Cates model failed to account for the sensitivity of scaling exponents to the electrostatic and synergistic effects of salts, and  $\langle L \rangle$  tend to be considerably underestimated [Angelescu *et al.* (2003); Keohler *et al.* (2000); Raghavan *et al.* (2015); Larson (2012); Zou and Larson (2014); Zou *et al.* (2015)] Moreover, different approximations applied on the model further complicates the rigorous interpretation of the micellar structure. For instance, in the absence of well-defined local features in  $G''$ , the Cates

model is known to be inapplicable on capturing the rheological behaviors for solutions with low surfactant concentration, where micelles can be too short to form entanglements, therefore carry extra freedom resulting in a much faster relaxation. While on the experimental side, two most notable techniques, namely cryo-TEM and extensional flow measurements, both of which claim to offer unambiguous identification for micellar branches, are very much likely to be plagued by specimen preparation related artifacts and nonlinear flow induced structure formation, respectively. [Danino *et al.* (2000); Chellamuthu and Rothstein (2008); Sachsenheimer *et al.* (2014); Fischer *et al.* (1997); Ouchi *et al.* (2006)] Consequently, lacking quantitative connections between microstructural mechanisms and large scale micellar properties, some basic questions on behaviors of micelle solutions still remain elusive. Such generic structure-property relationship is of great importance in tailoring micelle solutions with desired viscoelasticity and had been partially explored in a series of work by Zou, Larson and coworkers [Larson (2012); Zou and Larson (2014); Zou *et al.* (2015); Xueming *et al.* (2016)], where a computer simulation aided mesoscopic model was established for entangled micelles. The model has been currently applied to commercial surfactant systems and yields semi-quantitative estimations on micelle length as well as reasonable explanations on the effect of salts and additives. [Xueming *et al.* (2016)] Unlike the Cates model, the evolution of the portions between unrelaxed tube ends, representing the relaxation of micelles, is introduced in a coarse-grained mean-field fashion as a set of “pointers”, named pointer algorithm. In this way, it is possible to consider relaxation mechanisms of micellar chains under different length scales. [Zou and Larson (2014); Zou *et al.* (2015)] Since it is computationally less prohibitive to track those pointers instead of to include a delicate disentanglement kinetics, the model manifest itself with notable advantage when handling branched structure as well as unentangled micelles.

In what follows, the original simulation model is briefly reviewed with the detailed consideration when applying it to both branched and partially unentangled WLM solutions. Since macro-rheology by itself is insufficient to indicate the local structure, diffusing wave spectroscopy (DWS) is thereby employed in order to fully characterize WLMs over six decades of oscillation frequency. A number of important physics for WLMs including the effects of entanglements and branch associated kinetics on rheology, as well as the possibility of micellar self-recombination were also elaborated in this work.

## II. Experimental Section

### 1. Materials

Two types of surfactants, “SLE1S” and “CAPB”, with a simple salt (sodium chloride, NaCl), were used. SLE1S (Fig. 5.1a) is an abbreviation for commercial SLES (sodium lauryl ethylene glycol sulfate, industrial grade) with one ethoxyl group (EO) on average; (but with a distribution of the number of Eos ranging from 0 to 10) and CAPB (Fig. 5.1b, cocoamidopropyl betaine, industrial grade) is a zwitterionic co-surfactant. The weight ratio of SLE1S/CAPB in the solution is fixed at 8.57. The activity of the SLE1S paste was verified using the potentiometric anionic surfactant titration ASTM D4251 procedure. (99-96%, analytical grade, from Cambridge Isotope Laboratories, Inc.) D2O was used as the solvent of WLM solutions to facilitate the comparison of characterized micellar properties from rheology and from SANS. Sulfate latex particles (8.2 wt. %, analytical grade, from life technology) with a bead size of 600 nm were added in the solutions as molecular probes for DWS measurements. Because of the complexity of these materials, weight percentage (wt. %) instead of molar concentration, is generally chosen to represent the composition. Samples were prepared by mixing the above individual components with the following orders: concentrated surfactant pastes, D2O, beads solution, and salt solution (20 wt. % in D2O, analytical grade). All the samples were then well mixed and waited overnight for degassing prior to measurements.

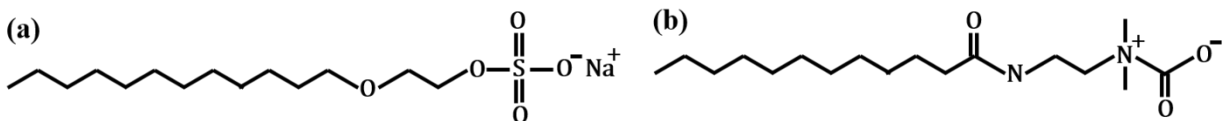


Figure 5.1 The chemical structure for (a) SLE1S (b) CAPB.

### 2. Macro-rheology

MCR-702 TwinDrive rheometer (Anton Paar) with a 50mm steel, 0.5° cone and plate was used to measure the zero shear viscosity at constant shear rate, and rheological moduli at constant shear stress but varying frequency. The counter-rotation mode is applied to minimize inertial effects at high frequencies. The geometry was inertially corrected prior to measurement, and the air bearing was mapped and coded in precision mode as prescribed in the RheoCompass software. The frequency spectrum was collected from 0.1 to 600 rad/s with strain amplitude varying logarithmically from 13% to 0.05%, but only data where the ratio of torque to lower

drive electric torque  $> 2\%$  was included. For the samples we measured, the above criteria usually limited the frequency spectrum to 10–100 rad/s, and data points with abrupt changes in moduli would also be rejected. We sampled 10 data points per decade of frequency to obtain enough information in a reasonable time. Samples were freshly loaded each time and a solvent trap was used to prevent sample evaporation near the edge. All rheological measurements were performed within the linear viscoelastic regime at 25 °C, unless otherwise specified. Each sample were remeasured and the standard deviation of rheological measurements was found to be less than 5%.

### 3. DWS

An optical micro-rheology approach, diffusing wave spectroscopy (DWS) was also applied to observe the high-frequency behavior (10–105 rad/s) of WLM solutions. Details about DWS can be found in references. [Buchanan *et al.* (2005); Oelschlaeger *et al.* (2009)] The wavelength of light and the diameter of the beads used in DWS are 532 and 600 nm, respectively. The beads, made of IDC polystyrene latex with a hydrophobic surface, are stabilized with a low level of sulfate charges, and are surfactant free. The samples for DWS measurement were mixed with 0.5 wt % beads before adding salt to ensure good mixing prior to thickening with salt. After 12 h of equilibration, samples were measured in 5 mm glass cells on an LS Instruments RheoLab 7.1.0 system. The transport mean free path  $l^*$  ( $=437 \mu\text{m}$ ) was determined from the control sample with the same-size beads in water.

## III. Modeling and Simulation

For the linear rheology of entangled WLMs, Cates theory turns out to be a notable success in explaining the single Maxwellian relaxation behavior through the context of tube and the associated dynamics. As refined later by many coworkers, this theory assumes the successive breakage and reformation events are uncorrelated as well as blind to local length scales. Lack of descriptions on micelle rigidity, unentangled micelles, as well as a complete spectrum of relaxation mechanisms, drawbacks and limitations are found when applying the theory to a rich variety of surfactant systems with different composites, temperature, salt level, and additives. [Oelschlaeger and Willenbacher (2012); Lonetti *et al.* (2011), Feng and Han (2016); Cardiel *et al.* (2014); Youssry *et al.* (2012); Shikata *et al.* (1988); Messenger *et al.* (1988)] However, when compared to other models and simulations in this area, [Padalkar *et al.* (2012); 4.38-4.41] the

concept underlying the Cates model maintains its attractiveness and by supplemented with an adequate amount of physics, we believe, a sophisticated model can be established for quantitative estimation of micellar properties from rheology which can hardly be obtained otherwise. Such model shall be able to accommodate the relaxation mechanisms over all relevant length scales with the living feature of WLMs. Therefore, a novel fast “pointer” simulation model was developed for entangled WLMs, where “pointers” are used to track the unrelaxed portions of WLMs from not only their original tube ends but also the internal breakage points. [Zou and Larson (2014); Zou *et al.* (2015)] A modified “Genetic computer algorithm,” which mimics biological evolution of optimized structures was also incorporated into the model to make the transformation of simulation results from time to frequency domain, thereby allowing direct comparison to experimental  $G'$  and  $G''$  data. [Zou and Larson (2014)] A recent application of this model to commercial surfactant solutions [Xueming *et al.* (2017)] yields predictions regarding average micelle length  $\langle L \rangle$ : 1~3  $\mu\text{m}$ ; mesh size  $\xi$ : 80~100 nm; persistence length  $l_p$ : 60~70 nm; as well as intermicellar reaction time  $\bar{\tau}_{rc}$ : 0.05~0.15 s, and these estimated values have shown to be in good accordance with those reported in literatures; i.e.,  $\sim 1 \mu\text{m}$  for  $\langle L \rangle$ , [Barhoum *et al.* (2012)] 50~100 nm for  $\xi$ , [Sarmiento-Gomez *et al.* (2010)] 30~125 nm for  $l_p$ , [Oelschlaeger and Willenbacher (2012)] 0.01~0.1 s for  $\bar{\tau}_{rc}$ . [Waton and Zana (2007)]

To extend the above success in modeling unbranched but well-entangled WLMs for the whole range of surfactant and salt concentrations, additional relaxation dynamics, besides those have already included in the original model, [Zou and Larson (2014)] are required to account for the effects of unentangled micelle rods and micelle branches. The former effect usually takes place at low surfactant concentration, where aggregates with large curvature are energetically favored, giving way to a low end-cap energy and short rods. Different from the entangled long WLMs, the diffusion of these unentangled micelle rods is not restricted within the tube so that the stress imposed on them can be relaxed in a much faster way by rotation. This rotary relaxation mechanism, as shown in Eq. (5.1), [Larson (1999)] is now incorporated to enable both the characterization of WLM solutions at low surfactant concentration and the comparison with micellar parameters from SANS as discussed later.

$$G'(\omega) = \sum_i G_i \frac{(\omega/D_{r,i})^2}{1 + (\omega/D_{r,i})^2}, \quad G''(\omega) = \sum_i G_i \frac{(\omega/D_{r,i})}{1 + (\omega/D_{r,i})^2} \quad (5.1a)$$

$$D_{r,i} = \frac{3k_B T}{\pi\eta_s L_i^3} [\ln(L_i/d) - 0.8], \quad G_i = \nu(L_i)k_B T \quad (5.1b)$$

In the above equation,  $G_i$  and  $D_{r,i}$  are the modulus and the rotary diffusivity for WLM with length of  $L_i$ , respectively.  $k_B$  is the Boltzmann constant,  $T$  is the temperature,  $\eta_s$  is the solvent viscosity, and  $d$  is the micelle diameter.  $\nu(L_i)$  is the number of micelles with length of  $L_i$  per unit volume. Note that Eq. (5.1) is only applicable to micelles with length smaller than the entanglement length  $l_e$ .

Because of the polydispersity in micelle length distribution, it is reasonable to believe there always exist a certain amount of micelles which remain unentangled ( $L_i < l_e$ ) with their contributions to the viscoelasticity only being noticeable as the solution becomes sufficiently dilute. Depending on the ratio of  $\langle L \rangle$  to  $l_e$ , i.e., the average entanglement number ( $\bar{Z}$ ), the percentage of entangled vs unentangled WLMs varies, and the micelle within these two subpopulations would experience distinct relaxation mechanisms as illustrated in Table 5.1.

Table 5.1 A comparative list of relaxation mechanisms and the associated characteristic times between entangled and unentangled micelles

Length scales	Unentangled		Entangled
	$L_i < l_p$	$l_p < L_i < l_e$	
$d \sim l_p$	Bending motion with $\tau_{p,i}(L_i)$	Bending motion with $\tau_p(l_p)$	Bending motion with $\tau_p(l_p)$
$l_p \sim l_e$		Rouse motion with $\tau_{R,i}(L_i)/p^2, p = 1, \dots, N_{K,i}$	Local Rouse motion with $\tau_{R,i}(L_i)/p^2, p = Z_i, \dots, N_{K,i}$
$l_e \sim L_i$	Rotation with $D_{r,i}(L_i)$	Rotation with $D_{r,i}(L_i)$	Reptation, contour length fluctuation, constraint release

Note that  $\tau_p$  and  $\tau_R$  are the characteristic times for bending and Rouse motions.  $Z$  and  $N_K$  are the number of entanglements and Kuhn steps, respectively. The subscript  $i$  represents the micelles of length  $L_i$ . The detailed expression for the above relaxation dynamics can be found either in the supplementary material or our previous work. [Zou and Larson (2014); Zou *et al.* (2015)]

Reminiscent of the modeling on high frequency Rouse and bending modes, the dynamics of unentangled micelles are incorporated separately, therefore only indicated as relaxed ones (i.e., without any pointers on them) during the intermicellar reaction, in contrast to those entangled micelles where loss of tube segments would cause pointers to move along their backbone as the relaxation process continues. A flowchart with detailed information about the above simulation procedure can be found in the supplementary material.

In the absence of closed rings and intra-loops, architectures for any branched micelles are built up by linear strands jointed through branch junctions and terminated with free end-caps.

Because in a branched micelle the surfactant molecules can diffuse rapidly through cross-linking junctions causing individual branch to grow, and shrink, the presence of these intermicellar connections provide extra paths allowing micelles to slide quickly from their entanglements, thus reduce viscosity. [Berret *et al.* (1993); Khatory *et al.* (1993)] Albeit indirectly surmised, it is widely accepted that branch junctions can be formed or destroyed via specific mechanisms. [Turner and Cates (1992); Drye and Cates (1992); Tlusty *et al.* (2000); Yamamoto and Hyodo (2005)] Mostly appeared as “Y” shape under cryo-TEM, [Danino *et al.* (1995); Dan and Safran (2006)] the detailed geometry, thermodynamics, and stability of these junctions are well studied, and we shall not be concerned with them here. [Andreev and Victorov (2006); May *et al.* (1997); Tang and Carter (2013)] Thus, to account for the above branching-associated kinetics on the micellar relaxation behaviors, a “constrained” diffusion model as well as a mechanism to create new branches are developed, and then these mechanisms are incorporated into the evolution of “pointers”. Originated from the work of Lequeux (1992), the “constrained” diffusion model draw heavily on the idea that micellar materials in each strands undergo a reptation-like slipping motion with constraint forces imposed at branch junctions to balance the flux. The resulting displacement of certain strand is written as a Langevin equation:

$$\Delta x_{ij} = \sqrt{\frac{2k_B T \Delta t}{\zeta_{ij}}} n_{ij} + \frac{F_i - F_j}{\zeta_{ij}} \Delta t \quad (5.2)$$

In the above equation,  $\Delta x_{ij}$  is the displacement of strand  $ij$  from terminus  $i$  towards  $j$ ,  $\Delta t$  is the time step. The first term on the right of Eq. (5.2) is the 1D diffusion term due to Brownian motion, where  $\zeta_{ij}$  is the drag coefficient of strand  $ij$  and  $n_{ij}$  is a uniformly distributed random number between -1 and 1. While  $F_i$  and  $F_j$  are “constraint forces” imposed to allow satisfaction of the mass conservation for all the displacement at each junctions.

In virtue of thermal fluctuation on local curvature, a Y junction can be generated by sprouting a tiny branch, so-called a “bud,” along the micelle randomly as implied by experiments and simulations. [Dan and Safran (2006); Jain and Bates (2003); Tang and Carter (2013)] Such sprouting process resembles the nucleation step during crystallization in which buds act similarly as excitation sites: Once formed, they enable full-fledged branches to grow through either end-cap fusion or “constrained” diffusion otherwise disappear in a very short time. Doubtless both the size and the time scale at which the buds are introduced control the branching level of the system, the linear to branch transition in micelle morphology is thereof explained by an increase

of bud size or sprouting rate as temperature or salt concentration varies. More detailed information on the above mechanisms can be found in the supplementary material. Due to the complexities in these mechanisms, the linear rheological response of a micellar solution can therefore be expressed schematically by the mathematical formula given below:

$$G^*(\omega) = G^U(\omega) + \mathcal{F}[G_N \mu^\alpha(t, \langle M \rangle, \alpha_e, \zeta, \beta)] + G^H(\omega) \quad (5.3)$$

Here,  $G^*(\omega)$  is the complex modulus whose real and imaginary part are storage and loss moduli, i.e.,  $G'$  and  $G''$ , respectively.  $\mathcal{F}[\cdot]$  stands for the time-frequency transformation.  $G_N$  is the elastic modulus as a result of transit network formed by entanglements. The exponent  $\alpha$  accounts for the effect of constraint release. By assuming the topological entanglement as a binary event,  $\alpha$  is set to be 2, known as double reptation. According to the tube theory, the time-dependent stress relaxation  $\mu(\cdot)$  is a function of the length and the diameter of tube, whereas for micellar systems the above two parameters are replaced by average micelle size  $\langle M \rangle$  (which is the sum of total strand length in a micelle, the ensemble average  $\langle \cdot \rangle$  is needed here due to the polydispersity of micelle size distribution) and flexibility  $\alpha_e$  (i.e., the ratio of micelle entanglement length  $l_e$  to persistence length  $l_p$ ). However, unlike the conventional tube theory,  $\mu(\cdot)$  contains two additional parameters,  $\zeta$  and  $\beta$ , which signifies the living feature and the branching level of the micelles, respectively:  $\zeta$  is the time scale ratio of the breakage/reformation to the reptation relaxation, i.e.,  $\zeta = \bar{\tau}_{br}/\bar{\tau}_{rep}$ , while  $\beta$  is defined as the average number of branched junctions per micron of micellar material. Thus, with  $\zeta \gg 1$  the model recovers the behavior of unbreakable polymer solution strikingly in contrast to the single-mode Maxwellian relaxation at  $\zeta \ll 1$ . [Berret *et al.* (1993); Koshy *et al.* (2011)]  $G^U(\omega)$  and  $G^H(\omega)$  represents all the fast relaxation dynamics, the superscript  $U$  and  $H$  denote the contributions from unentangled micellar subpopulation and high frequency Rouse and bending motions, respectively. Since these dynamics take place on the length scale smaller than tube diameter, their contributions are thought to be independent of  $\mu(\cdot)$ , therefore added analytically at high frequencies.

Before moving onto the next section, it is noteworthy that in our simulations both the intermicellar reaction and the entanglements are depicted in a mean-field (MF) manner in the sense that the reaction and the entanglement details are merely important for the overall relaxation behavior of WLMs. However, there are always some concerns revolving the MF treatment on intermicellar reactions: the intermediate states (three-/four-arm branched structure) [Turner and Cates (1992)] and non-uniform breakage (shedding/end evaporation). [Waton and



Zana (2007); Cates (1988)] Their existence, as inferred from theories and simulations, can alter the concentration dependencies of micellar properties, however, for linear rheology the effects remain marginal unless the system undergoes the morphology change or phase transition.

[Waton and Zana (2007); Turner and Cates (1992)]

#### IV. Result and Analysis

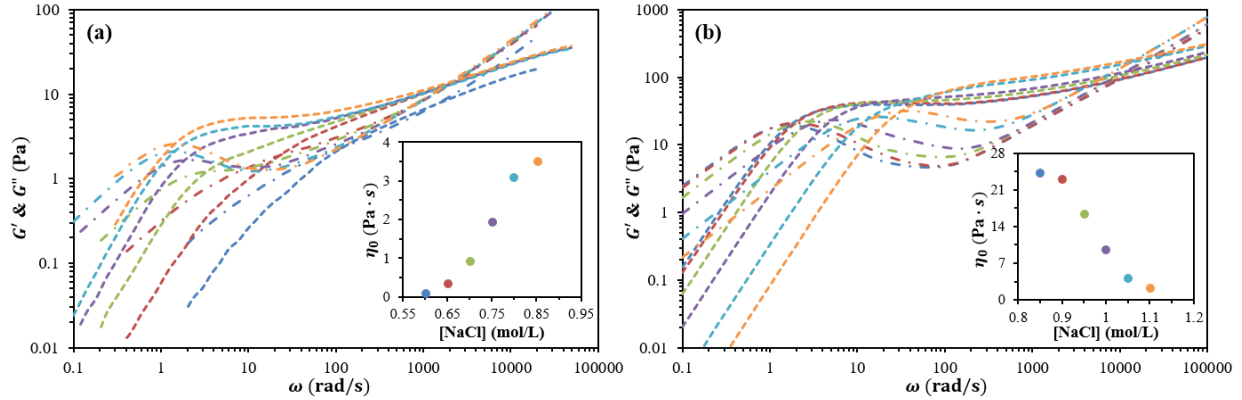


Figure 5.2 The combined rheological response (from mechanical rheometry at low frequencies and DWS at high frequencies) for WLM solutions with constant surfactant (SLE1S+CAPB) concentrations: (a) 1.5 wt. %, (b) 4.0 wt. % , and various salt concentrations at 25 C, each coded by a color also used in the inserted figures give zero shear viscosities.

Since our aim is to understand both the slow and fast dynamic-microstructure relationships for WLM solutions through a combination of macro- and micro-rheology, two surfactant concentrations, i.e., 1.5 wt. % and 4.0 wt. %, were chosen for the rheological investigation of partially unentangled and branched systems respectively. Overcoming the mechanical limitations, micro-rheology, including diffusing wave spectroscopy (DWS), video and laser particle tracking techniques, has the capability to access much higher frequencies ( $10 \sim 10^5$  rad/s) with the upper limit corresponds to the Brownian motion of the probe particles. The rheological modulus are calculated based on the use of fluctuation-dissipation theorem, where the thermal motion of probe particles is monitored and directly related to the viscoelasticity of the medium. [Cardiel *et al.* (2014); Youssry *et al.* (2012); Oelschlaeger *et al.* (2009)] Thus, by combining with macro-rheological data at low frequencies ( $0.1 \sim 500$  rad/s), an over six decade frequency range can be attained as a prerequisite for a complete description on micelle characteristic lengths through our simulation model. However, precautions are needed when handling the above two sets of data, since discrepancies are always observed possibly due

to the inertia of the rheometer and the probe-micelle interaction. [Cardiel *et al.* (2014); Rafati and Safatian (2008)] Therefore a data merging procedure is developed here, (details can be found in the supplementary material) the resulting combined rheological data for WLM solutions with different salt concentrations are given in Fig. 5.2.

According to Fig. 5.2a, prior to the maximum viscosity, by increasing the salt concentration, the terminal regime, where  $G'$  and  $G''$  have power laws of -2 and -1 respectively, shift to lower frequencies while the difference between  $G'$  and  $G''$  at intermediate frequencies becomes more prominent. These behaviors come along with an S-shaped upswing of zero shear viscosity  $\eta_0$  with the addition of salt (See the inserted plot of Fig. 5.2a) indicating different mechanisms for micellar growth at low and high salt concentrations. However, an exactly opposite trend can be observed in Fig. 5.2b, where branched micelles are thought to predominate as the solutions reach the right side of the salt curve. From both Fig. 5.2a and b, in the high frequency limit, another asymptotic crossover between  $G'$  and  $G''$  can be found, whose values are nearly independent of salt level. Such high frequency crossover  $\omega_{2c}$ , signaling a change from elastic response dominated by collective dynamics among entangled micelles to a viscous-dominant short-range intramicellar bending motion, [Morse (1998); Gittes and MacKintosh (1998)] is known to reflect the rigidity of WLMs and can only be captured by DWS. Since  $\omega_{2c}$  is free from the ambiguities related to the data merging process, this specific frequency can therefore be used to estimate the value of  $l_p$  as inspired by our previous sensitivity studies. [Zou *et al.* (2015)]

Quantitatively, the study of salt effects on micellar structures from experiment alone is a challenge, since there is no independent control of each characteristic lengths or times as varying the salt level. The addition of salt would, in general, cause micelle to grow as a result of a higher energy penalty for creating end-caps, but it may as well affect the intermicellar reaction time  $\bar{\tau}_{br}$  or cause micelle to form branches. Therefore, it is difficult to determine whether a decrease of viscosity is due to a smaller  $\langle L \rangle$ , the consequence of faster breakage and reformation or the formation of the branched structure. The above complications are embodied by the nontrivial changes in the predicted  $G'$  and  $G''$  curves (See Fig. 5.3 and 5.6) when using the micellar parameters as input for the simulation approach described previously. Since our interest here is to understand how the different length and time scales are manifested in the linear rheology of partially unentangled and branched WLM solutions, the parameters are either fixed at their

typical standard values (See Table 5.2 and 5.3) or allowed to vary within a range exemplified such system.

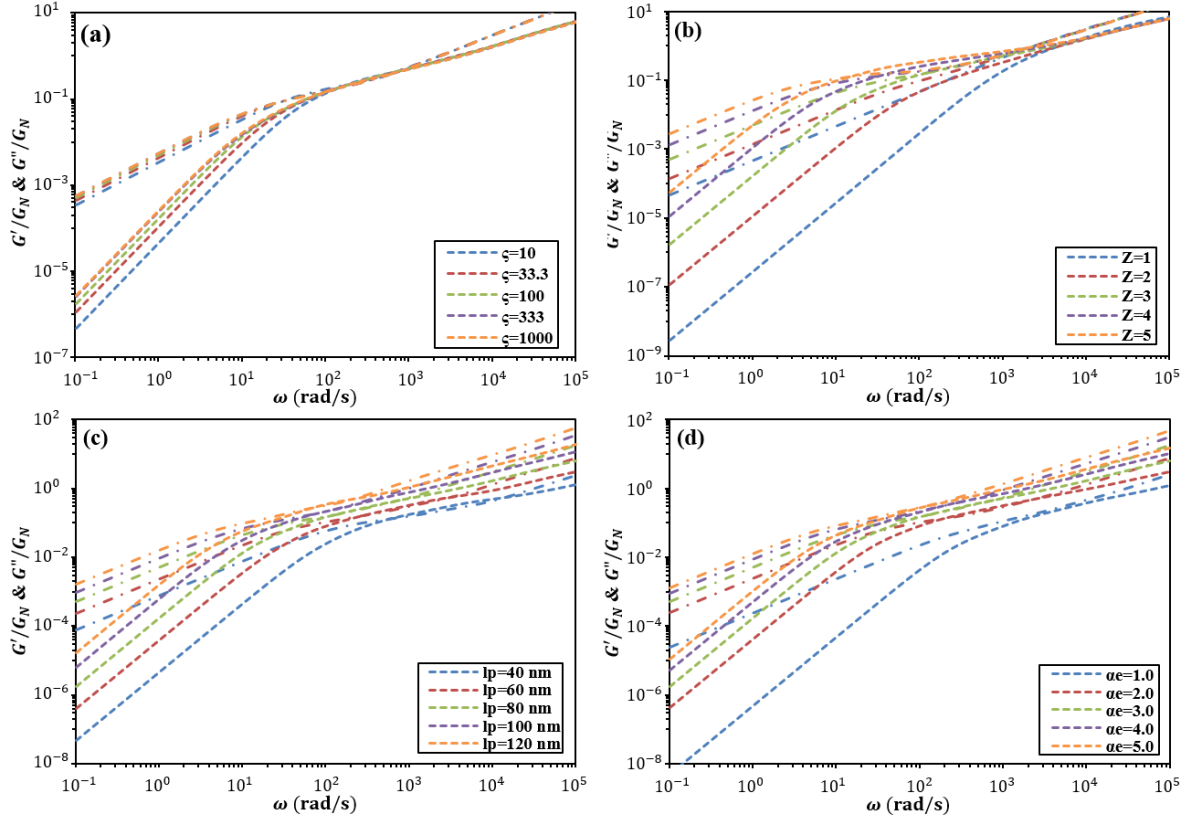


Figure 5.3 Effect of micellar parameters on normalized storage and loss modulus for partially unentangled micelles: (a)  $\zeta_{rc}$ , (b)  $\bar{Z}$ , (c)  $l_p$ , (d)  $\alpha_e$

Table 5.2 Standard values of micellar parameters for simulation predictions in Fig. 5.3

Micellar parameters					Solution conditions		
$\zeta_{rc}$	$\bar{Z}$	$\alpha_e$	$l_p$ (nm)	$d$ (nm)	$T$ (K)	$\phi$	$\eta_s$ (mPa.s)
100	3	3	80	4	300	2 %	0.89

As shown in Fig. 5.3, the rheology of partially unentangled micelle systems are strongly affected by the following parameters:  $\zeta$ , associated with the relatively slow intermicellar reaction, has its greatest influence on behaviors at the terminal regime: a larger  $\zeta$  would cause the terminal regime shift to lower frequencies. For  $\bar{Z}$ , since its value governs the transition between entangled and unentangled systems, at a small value of  $\bar{Z}$ , micelles are barely entangled, the predicted rheological response is similar as that for dilute solution of rigid rods; [Roitman and Zimm (1984); Carriere *et al.* (1985); Amis *et al.* (1985)] However, by increasing  $\bar{Z}$  (with  $\alpha_e$  and

$l_p$  fixed), the terminal regime of  $G'$  and  $G''$  evolves to lower frequencies giving rise to a wider frequency window where elastic response is dominant, which clearly indicates the emergence of transient networks formed by entangled WLMs. While in order to understand the complicated effects of  $\alpha_e$  and  $l_p$ , one would need to think of a micelle as a thread of ‘blobs’, [de Gennes (1979)] whose size is govern by  $\alpha_e \cdot l_p$ , and inside the blob, a micelle don’t “feel” the existence of entanglements so that the solution is effectively dilute. Thus, for micelles containing a certain number of blobs (i.e.,  $\bar{Z}$  is fixed), the consequences of a larger blob size are two-fold: increase the micelle length on one hand, tend to excite high frequency dynamics including Rouse and bending motions (manifested by a scaling law of 0.5 and 0.75 at high frequencies) at larger length scale therefore later times on the other hand. A combination of the above two effects can thus be identified by shifts in both magnitudes and frequencies for  $G'$  and  $G''$  curves.

Prior to detailed discussions on the effects of branching, it is noteworthy that although the abundance of branch junctions is of thermodynamic origin, the model here is purely topological, i.e. no delicate balance between entropic and enthalpic contributions nor possible singularities of the thermodynamic functions are involved. As outlined by a spontaneous budding process, where branch junctions are formed irrespective of strand orientation, therefore under equilibrium, the strand length would obey the Poisson distribution. In fact, this simplified treatment on junction properties remains adequate as long as strong interactions (exclude volume, electrostatic and hydrodynamic interactions) among micelles are effectively screened out and the structure of branched clusters is far away from saturation where the strand length has the order of the entanglement length. Thus, without any kinetic or thermodynamic subtleties on branching, our model offers a generic pathway to understand the viscoelasticity of branched “living” chain systems on the basis of polymer physics, which shall allow for predictions in a wide range of rheological behaviors among different self-assembled aggregates [Dan and Safran (2006); Zilman *et al.* (2004); Zilman and Safran (2002)] through appropriate reinterpretation of obtained parameters while extending the model to depict other amphiphile systems. [Jain and Bates (2003)] However, unfortunately, at this moment, the questions concerning whether the gelation (i.e., the transition from disconnected, branched clusters to a macroscopic, connected network) is a structure transition or a thermodynamic one [Zilman and Safran (2002)] as well as whether the micellar branches are truly equilibrium structures or metastable intermediates resulting from intermicellar reactions (for example, ghost-like crossing) [Koshy *et al.* (2011); May *et al.* (1991)]

cannot be answered solely from our model unless sophisticated description on thermo-statistics of micelle structure is available.

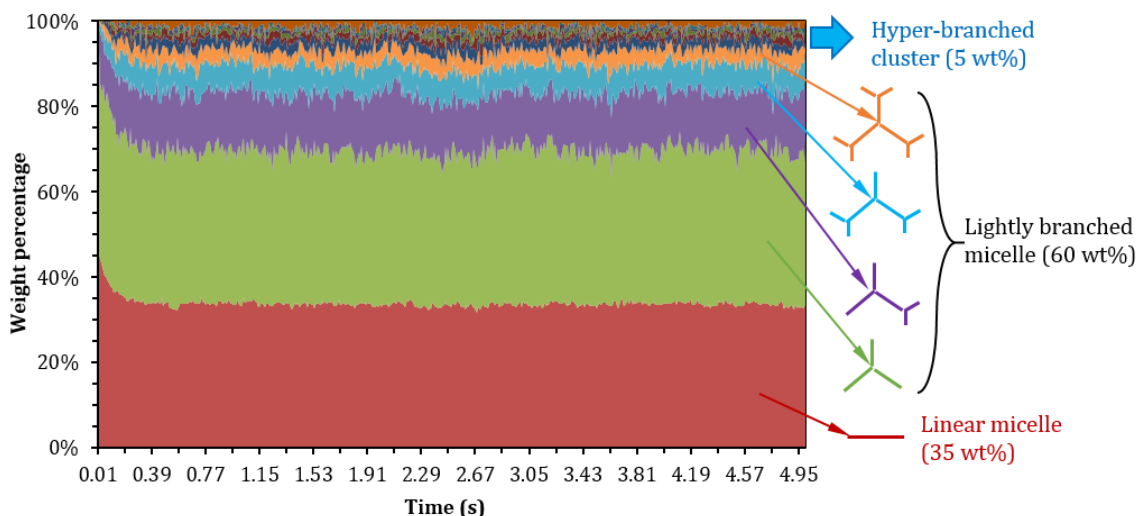


Figure 5.4 The evolution of micelle ensemble showing the equilibrate composition with average strand length  $\langle L_{st} \rangle = 2.2 \mu\text{m}$  and branching level  $\beta = 0.09$  per  $\mu\text{m}$  by the end of the simulation. Note that the simulation starts with 2500 linear micelles with micellar parameters given in Table 5.3.

Table 5.3 Values of micellar parameters for simulation predictions in Fig. 5.4

Micellar parameters					Solution conditions		
$\zeta$	$\langle M \rangle (\mu\text{m})$	$\alpha_e$	$l_p(\text{nm})$	$d (\text{nm})$	$T (\text{K})$	$\phi$	$\eta_s (\text{mPa.s})$
0.03	4	2	50	4	300	10 %	0.89

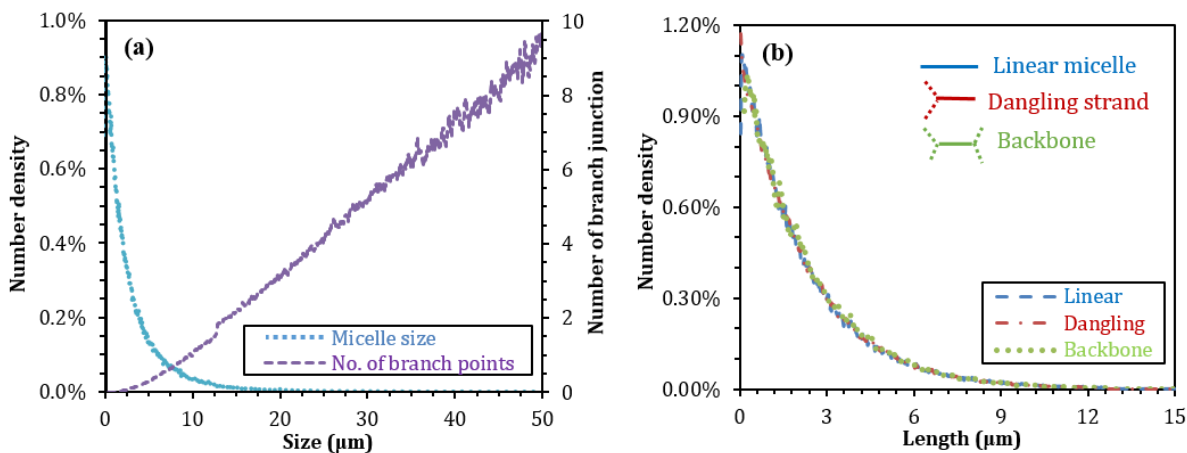


Figure 5.5 (a) The micelle size distribution and number of branched junctions contained in micelles with different sizes, (b) strand length distributions for equilibrated ensemble shown in Fig. 5.4.

As shown by Fig. 5.4, through the aforementioned constraint diffusion and budding process, a branched micelle system can be generated from a linear ensemble with micellar parameters given in Table 5.3. Such system would eventually evolve into a mixed micelle ensemble containing linear micelles, lightly branched structures (i.e., micelles contains no more than 4 branched junctions) as well as few giant micelle clusters indicated by both the long tail of micelle size distribution and the large number of branched junctions they contain (See Fig. 5.5a). However, according to Fig. 5.5b, under equilibrium the length distributions for three different types of micelle strands: linear micelles, dangling strand, and backbone, (whose definitions are based on whether termini are free end-caps or branched junctions) overlap and obey a single exponential function with the averaged strand length  $\langle L_{st} \rangle = 2.2 \mu m$ . This is the consequence of the randomness when branched junctions are introduced by the budding process. Since the level of the branching  $\beta$  can be tuned by the dimensionless budding time  $\zeta_{bud}$ : a smaller budding time would result in a highly branched micelle system, the effect of branching on the rheology of micellar solutions is illustrated by Fig. 5.6.

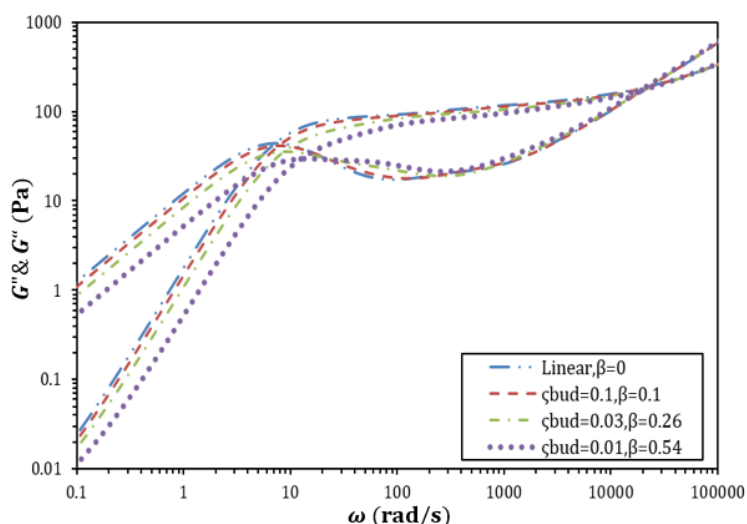


Figure 5.6 The predicted rheological behaviors for micelle systems with same micellar parameters except for branching levels. A rightward shift of both  $G'$  and  $G''$  implies a noticeable decrease of zero shear viscosity as the system becomes highly branched.

In Fig. 5.6, both  $G'$  and  $G''$  shift to higher frequencies and the difference between the two modulus decreases as more branches has been added to the system, which is consistent with the observed trend for micelle solutions upon the addition of salt. (See Fig. 5.2b) Since both the

average micelle size  $\langle M \rangle$  and the dimensionless intermicellar reaction time  $\zeta$  are hold constant, the above change in linear rheology can only be explained by the sliding motion of the branched arms, which induce extra freedom to the individual micelle therefore accelerate the relaxation. While for the fixed average micelle size  $\langle M \rangle$ , an increase in branching level would inevitably result in a shorter strand length, therefore a decrease in the number of entanglements that correspond to a less difference between  $G'$  and  $G''$ .

## V. Discussion

As mentioned previously in this paper, the use of a single parameter, i.e.,  $\bar{\tau}_{br}$ , to describe the intermicellar reaction is restricted by the validity of a MF picture, which becomes susceptible as the solution falls under the partially unentangled regime. Since the transport of one micelle to fuse with another surely depends on the statistics and dynamics of WLMs, the fundamental question must be answered as to which of the following two situations: reaction controlled and diffusion controlled (DC), actually governs the rheological properties of the given system.<sup>56</sup> In well-entangled WLM solutions, the current understanding for intermicellar reaction relies on the “universality” of blobs (same as the tube diameter or the mesh size), which is the screening length for hydrodynamic interactions and excluded volume repulsion. Thus, for sufficiently long WLMs in a “melt” of blob chains, the dependence on the local kinetics disappears altogether, and  $\bar{\tau}_{br}$  would be an only function of micelle length. In other words, MF theory is obeyed for well-entangled WLM solutions. In the dilute solution, on the contrary, a generalized MF treatment could be inadequate, one might expect the intermicellar reactions are DC, as whenever diffusion brings a pair of micellar coils to overlap the fusion is inevitable via a quick collision between two end-caps. Under this circumstance, a newly-created chain end is more likely to recombine with its original partner from the preceding breakage than with its surrounding neighbors. Such phenomenon is the so-called “self-recombination” which reflects the finite memory of WLM chains: the initial chain length can only be forgotten on a time-scale much greater than the diffusion time of that length after several sequences of breakage and reformation events. As a result, a typical WLM would be contaminated with fragments of relaxed tube at locations, where fresh tube ends were firstly created by breakage, then relaxed by fluctuation, and finally annihilated by self-recombination, leading to the anomalous short-time behavior and fat-tailed late time relaxation. [O’Shaughnessy (1993); O’Shaughnessy and Yu (1995)]

However, the above logic is presumably based on a constant  $\bar{\tau}_{br}$ , which is exactly opposite for WLM solutions as evidenced by a decrease of  $\bar{\tau}_{br}$  with salt concentration, [Tang *et al.* (2017)] owing to a lower potential barrier for breakage/reformation. Given this depression of tendency in reaction, it becomes less obvious and intuitive to find out the extent to which a partially unentangled WLM solution is MF or DC. Since at present, there is no rigid theory available for reaction kinetics in WLM solutions, “first principle” scaling arguments are thereby postulated in what follows.

The essence of DC kinetics is embodied by a much longer diffusion time between adjacent micelles than that required by reaction. According to Shaughnessy and Yu (1995), this can be represented by a dimensionless time ratio  $\zeta_{DC} \equiv \bar{\tau}_D/\bar{\tau}_{br}$  with  $\zeta_{DC} \gg 1$ . Here  $\bar{\tau}_D$  is the diffusion time for a micelle of average length  $\langle L \rangle$ , i.e.,

$$\bar{\tau}_D \equiv \frac{\langle h \rangle^2}{D}, \quad \langle h \rangle \equiv \sqrt[3]{\frac{\langle L \rangle \pi d^2}{4\phi}} \quad (5.4)$$

where  $D \sim 1/\langle L \rangle$  is the diffusivity, and  $\langle h \rangle$  is the average distance between any two micelles, which depends on the volume fraction  $\phi$  of the solution. Given  $\zeta \equiv \bar{\tau}_{br}/\bar{\tau}_{rep}$  and  $\bar{\tau}_{rep} \equiv \langle L_t \rangle^2/D$ , ( $\langle L_t \rangle \sim \langle L \rangle$  is the average micellar tube length, the detailed relationship between  $\langle L \rangle$  and  $\langle L_t \rangle$  can be found in our previous work. [Zou and Larson (2014)])  $\zeta_{DC}$  can therefore be expressed as

$$\zeta_{DC} = \frac{\langle h \rangle^2}{\langle L_t \rangle^2} \cdot \zeta^{-1} \quad (5.5)$$

By assuming  $\bar{\tau}_{rc} \sim \langle L \rangle^\alpha$ , ( $\alpha < 0$  due to the decrease of  $\bar{\tau}_{rc}$  with the growth of  $\langle L \rangle$ , and according to Cates theory, [Cates (1987)]  $\alpha = -1$ ) and  $\langle L \rangle \sim \phi^\nu$ , ( $\nu = 0.6$  predicted by Cates (1987) for nonionic surfactant solutions with a constant  $E_{sc}$ , which seems to be much smaller than those reported from other literatures, possibly arising from the dependence of  $E_{sc}$  on  $\phi$ . [Cates (1988)]) it yields the following scaling law of  $\zeta_{DC}$  vs  $\phi$ :

$$\zeta_{DC} \sim \langle L \rangle^{\frac{4}{3}-\alpha} \sim \phi^{\nu(\frac{4}{3}-\alpha)} \quad (5.6)$$

As demonstrated by Eq. (5.6) (with  $\alpha < 0$  and  $\nu > 0$ ), the validity of MF shall pertain even if a solution is further diluted since the decrease in concentration drives the system towards MF behavior. Hence one never truly reaches the DC regime before the onset of entanglements, in another word, the WLM solution is a “weakly reactive” system, which at first appears to be



counter-intuitive but actually consist with the trend predicted by Shaughnessy and Yu (1995) for dilute polymers in good solvent.

## VI. Conclusion

A recently developed simulation method for characterization of unbranched but well-entangled WLMs has been extended to provide a practical pathway to study the effects of both micelle branches and unentangled micelle rods in micellar solutions. Since in a branched micelle the surfactant molecules can diffuse rapidly through branch points causing micelle branch to grow, and shrink, the presence of these branches provide extra paths allowing micelles to slide quickly from their entanglements, however, few studies are available to explain these dynamics in detail. To account for the branching-associated kinetics on the micellar relaxation behaviors, a “constrained” diffusion model as well as a mechanism to create new branches are developed, where constraint forces are imposed to balance the flux of micellar materials at each branch junctions and a branch junction can be generated by sprouting a tiny branch, so-called a “bud,” along the micelle randomly. Thus, the linear to branch transition in micelle morphology can be represented by an increase of bud size or sprouting rate as temperature or salt concentration varies. By generating micelle systems with different level of branching, this extended simulation method is capable to predict a decrease in viscosity as more branches are introduced into the solutions, which consist with the well-known phenomenon for surfactant solutions at high salt concentration. On the contrary, for the unentangled micelle rods, their effects on the viscosity of solutions are only significant when surfactant concentration is low. Unlike those entangled long micelles, micelle rods are free to rotate therefore resulting in a much faster relaxation of the stress imposed on them and a lower viscosity. This additional rotary mechanism is now included in the model to enable characterization of micelle solutions at low surfactant concentration. By investigating the transition between entangled and unentangled micelle systems, the evolution of micellar structure can be predicted with the above extended simulation method. “First principle” scaling arguments are also postulated to conclude that WLM solutions is a “weakly reactive” system, i.e., the solution never truly reaches the diffusion controlled regime before the onset of entanglements, whose trend is similar as that for dilute polymers in good solvent. The accomplishments of the above progress allow, for the first time, modeling of the flow behaviors

of micelle solutions across the whole range of salt concentrations that is typically used in most WLM-related applications.

## Chapter 6: A Hybrid Brownian Dynamics/constitutive Model for Yielding, Aging, and Rejuvenation in Deforming Polymeric Glasses

### I. Introduction

Lacking long-range order, a glass is an amorphous solid conventionally formed by supercooling a liquid to the point of arresting molecular motion without crystallization, resulting in a non-equilibrium jammed state. [Debenedetti and Stillinger (2001)] On the macroscopic scale, the transformation of the liquid to the glass appears within a narrow range of temperatures approximated by what is referred to as the glass transition temperature  $T_g$ . The non-equilibrium, amorphous, structure of the glass is crucial to controlling the common characteristics of this type of material: hardness, brittleness, transparency, low conductivity, and soft magnetism. [Debenedetti and Stillinger (2001); Osborne and Lacks (2004); Greer (1995)] Applications of glasses can be found in a variety of fields: pharmaceuticals, food preservation, metallurgy, optics, and other applications going back as far as ancient Egypt in 12,000 B.C. [Dyre (2006)] Although the ability to form a glass is not restricted to a specific class of atoms or molecules, a fast cooling rate is required for many liquids. Polymers, however, with a great diversity of local length scales and a broad range of characteristic times, can be easily cooled to form glasses with impact resistance and toughness [Lee *et al.* (2009)] that are significantly higher than that of colloidal or metallic glasses.

Under deformation, polymeric glasses show a linear elastic response at small strain followed by yielding at larger strains where the energetic barriers to plastic flow are overcome. [Boyce *et al.* (1988); Hoy (2011)] After yielding, strain-softening, and a drop in stress with an increase of strain, may also occur, signaling inhomogeneous deformation and strain localization (crazing, necking, and shear banding etc.). [Fielding *et al.* (2012) and (2013)] The degree of softening and the magnitude of the yield stress are known to depend on the thermomechanical history of polymeric glasses. [Klompfen *et al.* (2005); Wendlandt *et al.* (2005)] In many respects polymeric glasses are similar to other glasses: they show a slow evolution towards equilibrium known as physical ageing, and many show non-Arrhenius temperature dependence of relaxation

called dynamic fragility, an every greater bifurcation of slower “alpha” from faster “beta” modes of relaxation as well as the decoupling of translational and rotational diffusion as the material is cooled deeply into the glass, indicating increasing local heterogeneity. [Schweizer and Saltzmann (2004); Chen *et al.* (2009)] However, it has been generally accepted that the long-chain feature of polymer molecular structure greatly alters the mechanical responses of polymeric glasses relative to non-polymer ones. [Wendlandt *et al.* (2005); Hoy and O’Hern (2010)] At very large strains, the polymeric glass enters the hardening regime, a phenomenon unique to polymeric glasses where strain localization is greatly suppressed. [Hoy and Robbins (2008)]

Understanding the above behaviors is of great importance in the manufacturing of polymeric glass to achieve designed mechanical properties. [Arruda *et al.* (1993)] Through techniques such as neutron and x-ray scattering, [Hansen and McDonald (1986)] nuclear magnetic resonance (NMR), [Loo *et al.* (2000)] birefringence, [Arruda *et al.* (1993)] and optical photo-bleaching, [Lee *et al.* (2009)] it has been learned that stress can enhance local mobility in the glass by either deforming the potential energy landscape or by introducing mechanical disorder. [Debenedetti and Stillinger (2001); Chen and Schweizer (2010)] The resulting decrease in structural (or segmental) relaxation time is known as mechanical rejuvenation. [Lee *et al.* (2009)] However, when strain hardening begins, the local mobility of the polymeric glass decreases [Lee *et al.* (2009)] and the material becomes highly anisotropic due to the orientation of polymers under large deformation. [Wendlandt *et al.* (2005); Arruda *et al.* (1993)] A sophisticated approach is required to characterize the above complex, and non-monotonic behavior of deforming polymeric glasses. Such an approach should be able to account for intramolecular cooperativity, including chain connectivity, stiffness, and finite extensibility. In what follows, after a brief review of existing models for polymeric glasses, we present our hybrid model, which allows Brownian dynamics (BD) simulations to be applied to polymeric glasses. The simulation results for mechanical behaviors, including strain hardening, strain recovery, and orientation of chain segments in either uniaxial extension or steady shear, are discussed in detail. Conclusions are given at the end of this Chapter.

## II. Model Review

Most models of polymeric glasses fall into one of two generic categories, i.e., kinetic or thermodynamic. [Chen and Schweizer (2007)] For thermodynamic models (Adams-Gibbs model, [Adam and Gibbs (1965)] random first order transition model, [Garrahan and Chandler (2003)] lattice cluster entropy model, [Lubchenko and Wolynes (2004)] etc.), configurational entropy is the major concern: it drives local structure rearrangements within a cooperative region, known as an “entropic droplet” in some of these models. Although it is hard to give a clear definition of the configurational entropy and the mapping between the “droplet” and the molecules, [Chen *et al.* (2009)] some of these models predict the observed decoupling of translational and rotational motion as well as the range of dynamic fragilities for different types of glasses. Kinetic models show much greater diversity: Some relate molecular rearrangement to plastic deformation through excited small clusters of “defects” or of “free volume” whose concentration is controlled by the competition between ageing and rejuvenation. Examples include Eyring’s model, [Eyring (1936); Halsey *et al.* (1945)] dislocation-based metallurgical models, [Escaig (1984)] percolated free volume models, [Merabia *et al.* (2004)] elastic “shoving” models, [Greer (1995)] and shear-transformation zone models. [Langer (2008)] Others introduce a state variable carrying structural information or “memory” which determines the structural relaxation of material functions. Examples include the Eindhoven glassy model, [Klompen *et al.* (2005)] the stress-clock model, [Bernstein and Shokooh (1980)] and the Boyce, Park, and Argon (BPA) model. [Boyce *et al.* (1988)] In these models, a polymeric glass is assumed to be a continuously deformed material with the time evolution of the state variable controlled by ageing and rejuvenation.

Many other sophisticated approaches have also been applied to describe various dynamics of polymeric glasses: phenomenological models, [Sollich *et al.* (1997)] density functional theories, [Xia and Wolynes (2000)] mode coupling theories, [Chong and Fuchs (2002)] nonlinear Langevin equations, [Schweizer and Saltzmann (2004)] molecular dynamics (MD) simulations, [Riggleman *et al.* (2007)] and the potential energy landscape (PEL) paradigm. [Debenedetti and Stillinger (2001)] However, most of the models are greatly challenged by the non-monotonic, complex dependence of the segmental (alpha) relaxation time on the deformation of the polymeric glass, especially during strain hardening and strain reversal, as revealed by recent studies. [Lee *et al.* (2009); Hoy and O’Hern (2010)] Given the blurred

boundaries between melts and glasses at the molecular level, the generic fluid point of view (i.e., that any liquid exhibits solid-like behavior on time scales much shorter than the material relaxation time) is favored for the characterization of ageing and rejuvenation: the polymeric glass becomes more solid-like through ageing, but fluidizes upon rejuvenation. Using this concept, a so-called “fluidity” equation [Moorcroft *et al.* (2011)] (Eq. (6.1e)) was used by Fielding, Cates and Larson [Fielding *et al.* (2012) and (2013)] to account for the time-evolution of the segmental relaxation time for polymeric glasses under deformation. In this “toy” model of Fielding *et al.*, the dynamics follow a “two-time-scale” scenario: [Berthier *et al.* (2000)] the macroscopic behavior is controlled by both a local segmental mode (Eq. (6.1b)) and a separate larger-scale, slower, polymeric mode (Eq. (6.1a)). A mathematical description of the model is given by Eq. (6.1) below:

$$\dot{\boldsymbol{\sigma}}^p + \mathbf{v} \cdot \nabla \boldsymbol{\sigma}^p = \boldsymbol{\sigma}^p \cdot \nabla \mathbf{v} + (\nabla \mathbf{v})^T \cdot \boldsymbol{\sigma}^p - (\boldsymbol{\sigma}^p - \mathbf{I})/\tau^p \quad (6.1a)$$

$$\dot{\boldsymbol{\sigma}}^s + \mathbf{v} \cdot \nabla \boldsymbol{\sigma}^s = \boldsymbol{\sigma}^s \cdot \nabla \mathbf{v} + (\nabla \mathbf{v})^T \cdot \boldsymbol{\sigma}^s - (\boldsymbol{\sigma}^s - \mathbf{I})/\tau^s \quad (6.1b)$$

$$\boldsymbol{\Sigma} = \boldsymbol{\Sigma}^p + \boldsymbol{\Sigma}^s = G^p(\boldsymbol{\sigma}^p - \mathbf{I}) + G^s(\boldsymbol{\sigma}^s - \mathbf{I}) \quad (6.1c)$$

$$\tau^p/\tau^s = \alpha \quad (6.1d)$$

$$\dot{\tau}^s = 1 - \lambda(\tau^s - \tau_0^s), \quad \lambda = \mu\sqrt{2\text{tr}(\mathbf{D} \cdot \mathbf{D})}, \quad \mathbf{D} = [\nabla \mathbf{v} + (\nabla \mathbf{v})^T]/2 \quad (6.1e)$$

In the above equations, polymeric and segmental modes are each described by an upper-convected Maxwell model with dimensionless configuration tensors and relaxation times denoted as  $\boldsymbol{\sigma}^{p,s}$  and  $\tau^{p,s}$ , respectively, where the superscript “*p*” or “*s*” represents “polymeric” or “segmental” mode, respectively. Although these two modes contribute additively to the overall stress  $\boldsymbol{\Sigma}$  through their moduli  $G^p$  and  $G^s$ , their relaxation times are coupled by a proportionality relationship, with coefficient  $\alpha$ . Since ageing and rejuvenation reflect local dynamics, and weakly depend on the type of glass, [Klumpen *et al.* (2005); Chen *et al.* (2009); Thureau and Ediger (2002)] the effects of the segmental relaxation time  $\tau^s$  (shown by Eq. (6.1e)) are accounted for in an isotropic and additive fashion with a constant ageing (or solidification) rate, which is consistent with observations that at temperatures sufficient below  $T_g$  the ageing rate approaches unity. [Chen *et al.* (2009)] We also include a deformation-controlled rate of rejuvenation (or fluidization) as inferred from recent findings. [Hoy and O’Hern (2010); Chen and Schweizer (2010)] Although such choices are highly over-simplified, the focus of the present work is on the contributions of the polymeric mode to nonlinear deformations of glassy polymers, and keeping the segmental mode highly schematic allows us to maintain this focus

without introducing the added complexities of a realistic treatment of the segmental mode. In future work, improvement of the description of the segmental mode, to include for example multiple relaxation times and more realistic aging and rejuvenation expressions, would be highly desirable. In Eq. (6.1e),  $\tau_0^s$  is the fully rejuvenated relaxation time,  $\mu$  is the rejuvenation coefficient,  $\mathbf{D}$  is the deformation rate tensor, and  $\nabla\mathbf{v}$  is the velocity gradient. According to Eq. (6.1e), the non-monotonic dependence of  $\tau^s$  on deformation under creep (constant stress) conditions is explained by the competition between ageing and rejuvenation: in the post-yield regime, strain-induced rejuvenation dominates, causing  $\tau^s$  to decline and the stress carried by the polymeric part ( $\Sigma^p$ ) to grow. However, as massive deformation builds up under constant stress,  $\Sigma^p$  saturates with the onset of strain hardening, and rejuvenation is suppressed by the small deformation rate that results under creep. As a result,  $\tau^s$  undergoes a rapid rise indicating the “victory” of ageing, even under a fixed load.

To achieve even qualitative predictions from this simple two-mode model for the uniaxial creep experiment reported by Lee and coworkers, [Lee *et al.* (2009)] the value of  $G^p$  is required to be an order of magnitude larger than the experimentally determined rubbery modulus. During elastic recoil, this high value needs to be reduced back closer to the rubbery modulus by arbitrarily introducing a so-called “crinkle factor” which is the degree of reduction of  $G^p$  required to capture the recoil behavior. Nonlinear elasticity [Wendlandt *et al.* (2005); Hoy and Robbins (2008); Larson (1990)] and the formation of “kinks” (i.e., the multiple-folded nearly fully stretched subsection of chains) [Fielding *et al.* (2012) and (2013); Larson (1990)] are thought to cause the above consequences, since such folded states occur in fast flows of dilute polymer solutions. [Larson (1990)] Since the upper-convected Maxwell model, which represents the polymer as a simple two-bead dumbbell, does not naturally describe the effect of these folded polymer states, the ad hoc “crinkle factor” is introduced to represent their effects artificially. An appropriate treatment that avoids both the artificially high polymer modulus and the “crinkle factor” requires a more realistic polymer model for local chain relaxation. As one of the most widely used models for polymers, the “bead-spring” model with multiple springs is a coarse-grained approximation of a freely-jointed chain whose equilibrium conformation is a random walk. In this model, the beads represent drag centers, and the springs represent the coarse-grained elasticity of sub-chains. Individual beads are therefore connected into chains by springs that each exert a spring force onto beads to account for chain connectivity and finite

extensibility. The movement of beads is controlled by an over-damped stochastic Langevin equation given by Eq. (6.2). Detailed discussion of the “bead-springs” model can be found in references. [Doi and Edwards (1986); Larson (1988); Bird et al. (1987)]

$$\zeta_b \dot{\mathbf{r}} = \zeta_b (\nabla \mathbf{v})^T \cdot \mathbf{r} - \frac{\partial U(\mathbf{r})}{\partial \mathbf{r}} + \mathbf{F}^R, \quad \mathbf{F}^R = \sqrt{\frac{6k_B T \zeta_b}{\Delta t}} \mathbf{n} \quad (6.2)$$

Here,  $\mathbf{r}$  is the position vector of the bead,  $\zeta_b$  is the viscous bead drag coefficient,  $U(\mathbf{r})$  is the intra-molecular potential, whose derivative with respect to  $\mathbf{r}$  is the spring force, and  $\mathbf{F}^R$  is the Brownian force representing the effect of thermal noise. An explicit expression for  $\mathbf{F}^R$  is also given in Eq. (6.2), which is obtained by averaging thermal forces over a short time interval  $\Delta t$ . [Larson (2005)]  $k_B$  is the Boltzmann constant,  $\mathbf{n}$  is a random vector with the magnitude of each component uniformly distributed between -1 and 1. Thus, for a large ensemble of chains containing multiple beads, the above Langevin equations need to be solved by Brownian dynamics (BD) simulations as discussed in what follows.

We note that our model for the polymeric mode ignores the effects of entanglements, and any interactions of polymers other than those mediated through the segmental mode. In that sense, the model is analogous to the Rouse model for molten polymers, which also neglects entanglement effects, and accounts for interactions with other polymer chains only through the drag coefficient representing local viscous friction exerted on the polymer beads. Thus, our model may be most appropriate for low molecular weight, unentangled, glassy polymers, but since in glassy polymers the longest polymer relaxation times are not accessed on experimental relaxation time scales, the molecular weight of the polymer chains, and perhaps even their entanglements, may play a smaller role in the nonlinear rheology of glassy polymers than it does in melts. We will see in what follows that chain length plays only a secondary role in the predictions of our model. Inclusion of entanglement effects is left to future work.

### III. Brownian Dynamic Simulations

To achieve a realistic description of the dynamics of a polymeric glass, we combine the fast segmental relaxation borrowed from the work of Fielding *et al.* (2012) and (2013) (Eqs. (6.1b) and (6.1e)), with BD simulations of a “bead-spring” model of a polymer whose relaxation is controlled by the segmental relaxation through the drag coefficient of beads ( $\zeta_b$  in Eq. (6.2)) as if the beads were suspended in a glassy “solvent.” The corresponding polymeric stress and



conformation are thereby determined from an ensemble of finitely extensible bead-spring chains under deformation. Hence, this “hybrid” BD simulation model can be expressed as the following three sets of equations:

1. Polymeric part: [Larson (2005)]

$$\begin{cases} \zeta_b \mathbf{r}_i = \zeta_b (\nabla \mathbf{v})^T \cdot \mathbf{r}_i + \mathbf{F}_i^{sp,t} + \mathbf{F}_i^R \\ \boldsymbol{\Sigma}^p = \nu \langle \sum_j^{N_{sp}} \mathbf{R}_j \mathbf{F}_j^{sp} \rangle, \quad \mathbf{R}_j = \mathbf{r}_j - \mathbf{r}_{j-1} \end{cases} \quad (6.3a)$$

In the above equation set,  $\mathbf{F}_i^{sp,t}$  is the total spring force (which is the sum of two spring forces for interior beads and only one for end beads) exerted on bead  $i$ ,  $\nu$  is the number of polymer molecules per unit volume,  $\mathbf{R}_j$  is the connector vector of spring  $j$  between two neighboring beads  $j$  and  $j - 1$ ,  $N_{sp}$  is the total number of springs in a bead-spring chain, and  $\mathbf{F}_j^{sp}$  is the spring force on spring  $j$ ,  $\mathbf{F}^R$  is the Brownian force defined in Eq. (6.2). Here, we use FENE (finitely extensible nonlinear elastic) springs to account for the finite extensibility of chains, which yields: [Larson (1988)]

$$\mathbf{F}_j^{sp} = \frac{H_{FENE} \cdot \mathbf{R}_j}{1 - (|\mathbf{R}_j|/R_0)^2}, \quad H_{FENE} = \frac{3k_B T}{N_{K,sp} b_K^2}, \quad R_0 = N_{K,sp} b_K, \quad N_{K,sp} = \frac{N_K}{N_{sp}} \quad (6.3b)$$

$H_{FENE}$  is the spring constant,  $N_K$  and  $b_K$  are the number and length of Kuhn steps in a polymer,  $N_{K,sp}$  is the number of Kuhn steps per spring, and  $R_0$  is the fully extended length of a single spring. Therefore, the polymeric stress tensor  $\boldsymbol{\Sigma}^p$  in Eq. (6.3a) can be determined from an ensemble average (denoted as  $\langle \cdot \rangle$  in Eq. (6.3a)) over the contributions from all the springs in each chain. The above two equations yield a coarse-grained description of polymers with certain number of Kuhn steps represented by a spring. If the level of coarse-graining ( $N_{K,sp}$ ) is well above the length scale for detailed interchain mechanisms as well as finite size effects, the segmental dynamics can thereof be sufficiently depicted in a mean field manner as the novel glassy “solvent.”

Substituting the formulas for both  $\mathbf{F}_i^R$  and  $\mathbf{F}_j^{sp}$  into Eq. (6.3a) (See *Appendix E*), we rewrite Eq. (6.3a) into a dimensionless and discretized form, i.e.,

$$\begin{cases} \Delta \tilde{\mathbf{R}}_j = (\nabla \mathbf{v})^T \cdot \tilde{\mathbf{R}}_j \Delta t + \frac{3\Delta t}{\tau_{sp}} \left[ \frac{\tilde{\mathbf{R}}_{j+1}}{f(\tilde{\mathbf{R}}_{j+1})} + \frac{\tilde{\mathbf{R}}_{j-1}}{f(\tilde{\mathbf{R}}_{j-1})} - \frac{2\tilde{\mathbf{R}}_j}{f(\tilde{\mathbf{R}}_j)} \right] + \sqrt{\frac{6\Delta t}{\tau_{sp}}} (\mathbf{n}_j - \mathbf{n}_{j-1}) \\ \boldsymbol{\Sigma}^p = G^p \left\{ \frac{\langle \Sigma_j^{N_{sp}} [\tilde{\mathbf{R}}_j \tilde{\mathbf{R}}_j / f(\tilde{\mathbf{R}}_j)] \rangle}{\langle \Sigma_j^{N_{sp}} [\tilde{\mathbf{R}}_j \tilde{\mathbf{R}}_j / f(\tilde{\mathbf{R}}_j)] \rangle_{eq}} - \mathbf{I} \right\}, \quad f(\tilde{\mathbf{R}}_j) = 1 - (|\tilde{\mathbf{R}}_j|/\tilde{R}_0)^2 \end{cases} \quad (6.4a)$$

Here,  $\tilde{\mathbf{R}}_j$  and  $\tilde{R}_0$  are the dimensionless connector vector of spring  $j$  and the fully extended length,  $\Delta t$  is the simulation time step,  $\tau_{sp}$  is the relaxation time associated with a single spring,  $\mathbf{I}$  is the unit tensor, and  $\langle \cdot \rangle_{eq}$  is the equilibrium ensemble average. Detailed expressions for  $\tilde{\mathbf{R}}_j$ ,  $\tilde{R}_0$ ,  $\tau_{sp}$ , and  $G^p$  are given below:

$$\tilde{\mathbf{R}}_j = \frac{\mathbf{R}_i}{\sqrt{N_{K,sp}} b_K}, \quad \tilde{R}_0 = \sqrt{N_{K,sp}}, \quad \tau_{sp} = \frac{N_{K,sp} b_K^2}{k_B T / \zeta_b}, \quad G^p = 3\nu k_B T \quad (6.4b)$$

The relationship between  $\tau^p$  and  $\tau_{sp}$  is given as: [Larson (1988)]

$$\tau^p = \frac{(N_{sp} + 1)^2 N_{K,sp} b_K^2}{6\pi^2 k_B T / \zeta_b} = \frac{(N_{sp} + 1)^2}{6\pi^2} \tau_{sp} \quad (6.4c)$$

2. Segmental part:

$$\begin{cases} \dot{\boldsymbol{\sigma}}^s + \mathbf{v} \cdot \nabla \boldsymbol{\sigma}^s = \boldsymbol{\sigma}^s \cdot \nabla \mathbf{v} + (\nabla \mathbf{v})^T \cdot \boldsymbol{\sigma}^s - (\boldsymbol{\sigma}^s - \mathbf{I}) / \tau^s \\ \dot{\tau}^s = 1 - \lambda(\tau^s - \tau_0^s), \quad \lambda = \mu \sqrt{2 \text{tr}(\mathbf{D} \cdot \mathbf{D})} \\ \boldsymbol{\Sigma}^s = G^s(\boldsymbol{\sigma}^s - \mathbf{I}), \quad \tau^s|_{t=0} = t_W \end{cases} \quad (6.5)$$

3. Coupling relationships:

$$\begin{cases} \boldsymbol{\Sigma}^{ext} = \boldsymbol{\Sigma}^p + \boldsymbol{\Sigma}^s \\ \tau^p = \alpha \cdot \tau^s \end{cases} \quad (6.6)$$

Thus, from Eqs. (6.4c) and (6.6), the bead drag coefficient  $\zeta_b$  can be expressed as:

$$\zeta_b = \frac{\alpha \cdot 6\pi^2 k_B T}{(N_{sp} + 1)^2 N_{K,sp} b_K^2} \tau^s \quad (6.7)$$

which turns out to be proportional to the segmental relaxation time  $\tau^s$  and coefficient  $\alpha$ . For unentangled polymers, the coefficient  $\alpha$  is proportional to  $N_K^2 = (N_{sp} N_{K,sp})^2$ , and  $\zeta_b$  would be proportional to  $N_{K,sp}$  (where the difference between  $N_{sp}$  and  $N_{sp} + 1$  is neglected). This is reasonable, since the bead drag coefficient should be proportional to the number of Kuhn steps in a single spring, whose drag is represented by  $\zeta_b$ . For the lightly cross-linked polymer to which

we will apply our model, there is no particular reason to assume that  $\alpha$  is proportional to  $N_K^2$ , and in what follows we will take it to be an adjustable parameter.

To sum up, from Eqs. (6.4a), (6.5), and (6.6), the parameters needed for our simulation are the following: *A.*  $G^p$  and  $G^s$ , the moduli for polymeric and segmental modes. A high value of  $G^s$  is expected due to the significance of interchain forces with  $G^p < G^s$  as a result of the much larger number of local “glassy” modes than of entropic “polymeric,” or “rubbery” modes. [Fielding *et al.* (2012)] *B.*  $N_K$  and  $N_{sp}$ , the number of Kuhn steps per polymer and the number of springs per chain, respectively. The ratio of  $N_K$  to  $N_{sp}$ , i.e.,  $N_{K,sp}$  determines the level of coarse-graining, and according to Eq. (6.4b), this ratio also affects the finite extensibility of the sub-chains. *C.*  $\tau_0^s$ , the segmental relaxation time for the fully rejuvenated state, which would hypothetically be attained under fast enough strain rates to render the glassy mode as a viscous Newtonian liquid, and sets a lower bound on the segmental relaxation time. [Coussot *et al.* (2002)] Here, we use the same value of  $\tau_0^s$  ( $= 6$  s) as in the work of Fielding *et al.* (2012) and (2013) *D.*  $\mu$ , the rejuvenation-associated coefficient. With a constant deformation rate  $\mathbf{D}$ , a larger  $\mu$  implies faster rejuvenation. *E.*  $t_w$ , the “waiting time” which sets the initial value of segmental relaxation time in our simulations, and is controlled by how long the sample has been aged since the last deformation. *F.*  $\Sigma^{ext}$ , the external stress imposed on the material, which is set by the experiment. *G.*  $\alpha$ , the ratio of polymeric to segmental relaxation time. In principle,  $\alpha$  should be sensitive to polymer molecular weight, but our comparisons will be with a lightly cross-linked PMMA, and, as discussed below, changes in this parameter can be offset by changes in other parameters in our model. Here we treat  $\alpha$  as a fitting parameter and discuss its value and that of other parameters in what follows.

Thus, starting with an equilibrated ensemble containing 500 chains, the simulations are carried out by solving the corresponding three sets of equations numerically, using a semi-implicit method developed by Somasi *et al.* (2002) to track the deformation of the polymer and a standard finite difference method to solve for the segmental stress and to update the strain or overall stress. The time step  $\Delta t$  is chosen to be  $\delta t = \min[10^{-3}\tau^s, 10^{-3}/(\mu|\dot{\epsilon}|), 10^{-2}]$  s, which ensures both the convergence and the efficiency of the simulations during rapid and slow deformation, respectively (See Fig. E.2b in *Appendix E*). To complete a simulation capturing 5 hours’ of material behavior, it takes a day of computation for a single Intel® Core™ i5 CPU with 2.27 GHz clock speed. These simulations represent the first time that BD simulations have been

applied to the dynamics of polymers in the glassy regime, where the effects of strong intermolecular interactions and local rearrangements are accounted for by a separate “glassy” segmental mode. The relaxation of this glassy mode is phenomenologically depicted as a “solvent”, which sets the elementary time scale for BD simulation via the drag coefficient  $\zeta_b$ . In so doing, we are taking  $\zeta_b$  to be a Stokes-Einstein drag coefficient for a polymer bead in a viscous liquid assumed to be homogeneous, isotropic, and Newtonian. While this assumption is not valid at small length scales for a polymeric glass, we believe that with a relatively slow polymeric relaxation (i.e.,  $\alpha \gg 1$ ), the glassy solvent can still be viewed as Newtonian liquid on time scales much longer than the segmental relaxation time, and that the level of coarse-graining in our model is large enough (i.e.,  $N_{K,sp} \gg 1$ ) for the dynamic heterogeneity to be averaged out. We also note here that it is well known that not only does the polymeric mode need to be described by a multi-mode model (here the bead-spring model), but that on shorter time scales the segmental relaxation itself is also governed by detailed microscopic physics with a distribution of relaxation times, often represented phenomenologically by the Kohrausch-Williams-Watts (KWW) relaxation function. [Dyre (2006); Lee *et al.* (2009); Chen *et al.* (2008)] For this paper, however, we will be content to replace only the single-mode dumbbell of the Fielding *et al.* model (Eq. (6.1a)) with a multi-mode bead-spring chain, leaving refinement of the solvent mode to future work.

## IV. Results and Discussion

### 1. Uniaxial creep

Our simulation model is first tested by fitting data of Lee *et al.* (2009) for lightly cross-linked PMMA undergoing uniaxial creep, where in our model the specimen is assumed to deform homogeneously. A detailed procedure (See *Appendix E*) is therefore needed to convert the general equations of the model into a discretized form for numerical computation for a given type of deformation. For uniaxial creep under the experimentally imposed stress of  $\Sigma_z^{ext} = 16$  MPa (with the sample deformed along  $z$  direction) and  $\tau_0^S = 6$  s (the same value in Fielding *et al.* (2012) and (2013)), simulation results as well as the corresponding values of model parameters are given in Fig. 6.1a and Table 6.1, respectively. From Fig. 6.1a, it is striking that important features of the experimental data, i.e., the initial drop and subsequent non-monotonic

change of  $\tau^s$ , yielding, strain-hardening, and incomplete strain recovery after removal of load are all well captured by our simulation model, without use of the ad hoc “crinkle factor” that was needed when the polymer was described as a dumbbell. As shown in Table 6.1, the value we obtained for  $G^p$  ( $\cong 0.12$  MPa) is close to the rubbery modulus (0.1 ~ 0.3 MPa) of PMMA above  $T_g$ . The values of  $G^s$  and  $t_w$  from our simulations are 500 MPa and  $9.5 \times 10^4$  s, respectively, as compared with those from experiments 1 GPa and  $10^4$  s for typical polymeric glasses near  $T_g$ . [Chen and Schweizer (2009); Ngai and Plazek (1995)] The effect of some model parameters on the predicted evolution of strain and  $\tau^s$  can be found in Figs. 6.1b-d. As will be discussed later, similar fits can be obtained for different sets of parameter values. Hence the fit shown in Fig. 6.1a is not unique to a particular parameter set. Although this redundancy might be broken by obtaining some of the parameters from experimental conditions, (for example the “waiting time,”  $t_w$ ), as discussed in more detail below, neither the experimental conditions nor the model are sufficiently well defined to make such an exercise meaningful at this point. The agreement shown in Fig. 6.1a is not, however, a mere exercise in data fitting; the dumbbell model for the polymer mode used in the model of Fielding *et al.* (2012) and (2013) contains a similar number of parameters, and yet is completely unable for any set of parameters to predict the small strain recovery seen experimentally without the introduction of the arbitrary “crinkle factor.” Thus, while further experimental and theoretical work will be required to obtain a model that can predict experimental results using parameters derived from experiment, the work presented here represents real progress towards a more realistic molecular model of the rheology of polymer glasses.

Table 6.1 Values of model parameters for simulation predictions in Fig. 6.1a.

Parameters	$G^p$ (MPa)	$G^s$ (MPa)	$t_w$ (s)	$\mu$	$\alpha$	$N_K$	$N_{sp}$
	0.117	500	$9.5 \times 10^4$	143	$5 \times 10^4$	400	10

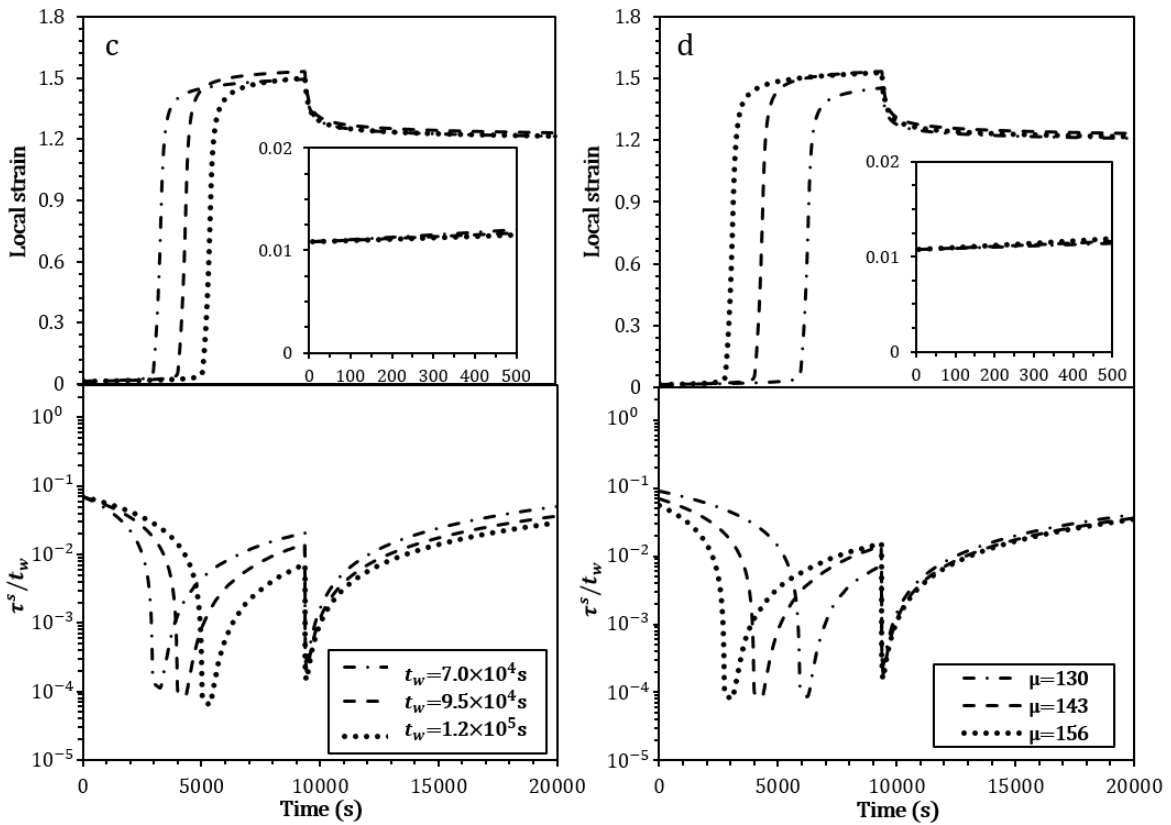
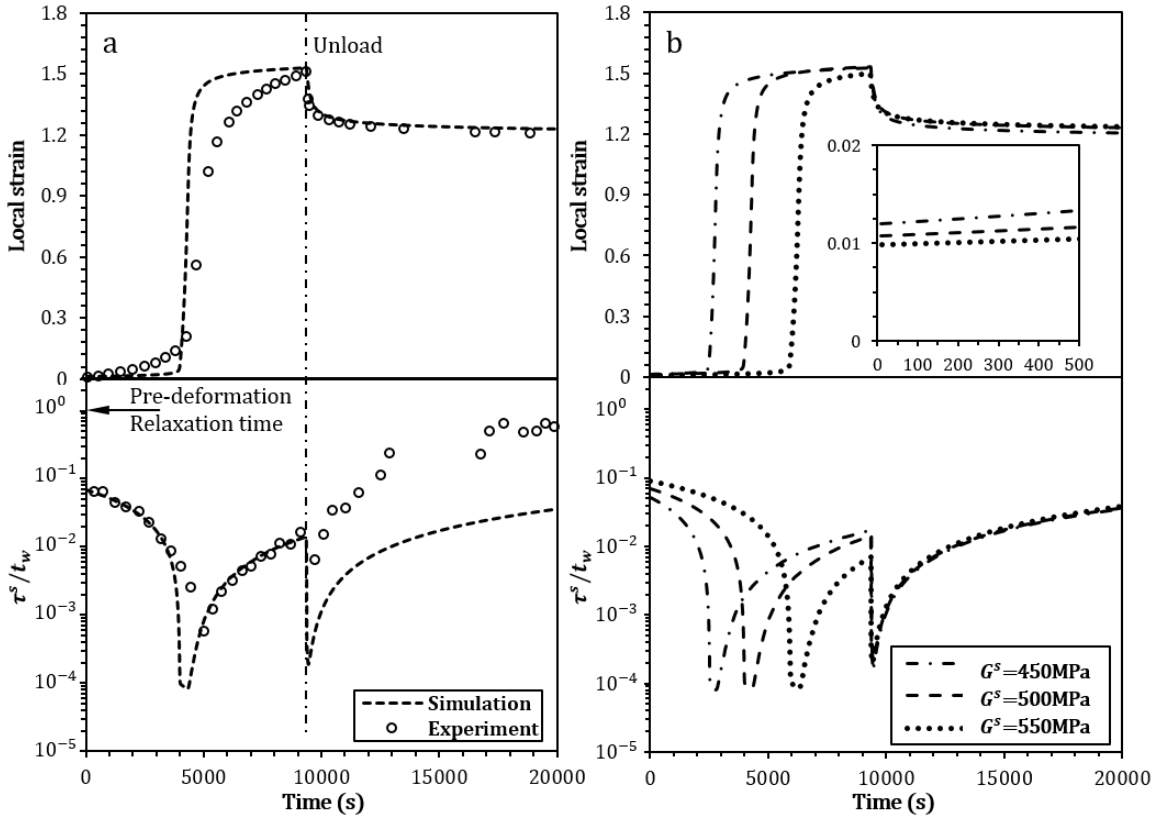


Figure 6.1 Simulation fits to experimental data from Lee *et al.* (2009) (a) and the effects of  $G^S$  (b),  $t_W$  (c), and  $\mu$  (d) on the evolution of strain and segmental relaxation time  $\tau^S$  for uniaxial extension with constant load ( $\Sigma_z^{ext} = 16$  MPa), which is removed at time  $t = 9375$  s. The inset shows an enlarged view of strain at early times. Note that in the experiments, the strain measured was in a local region of the sample, to avoid artifacts due to inhomogeneous global strain. In the simulations, the strain is taken to be uniform and defined as  $\exp(\epsilon) - 1$ .

Since most of the stress is carried by the segmental mode (Eq. (6.5)) before the onset of flow, the yielding behavior of the material depends on the value of  $G^S$  as illustrated by Fig. 6.1b: A smaller  $G^S$  leads to a larger jump/drop of initial strain/ $\tau^S$  and an earlier occurrence of plastic flow. As we mentioned before,  $t_W$  is the pre-deformation segmental relaxation time, and is controlled experimentally by the length of the aging time experienced by the sample. In the experiments of Lee *et al.* (2009), the sample was cooled into the glass over a period of 30 minutes and then aged for a further period of 30 minutes. Given the gradual cooling, the sample is presumably much better aged than would be case had the sample been aged at low temperature for only one hour or 3600 s, but our chosen aging time in Table 6.1 is obviously no better than a guess. However, according to Fig. 6.1c and d, both  $t_W$  and  $\mu$  affect how fast the material approaches a highly rejuvenated state, where  $\tau^S$  has a sharp minimum, and so an erroneous value of  $t_W$  can be offset by the choice of the parameter  $\mu$ . The magnitude of the strain necessary to induce yielding (Eq. (6.5)) is roughly  $1/\mu$ ; the value given here ( $\mu = 143$ ) implies that yielding occurs at a strain of around 0.01 for the aging time chosen. It can also be seen from Fig. 6.1d that by decreasing  $\mu$ , both the dip and the initial drop of  $\tau^S$  decrease. Since moderate changes in the above parameters ( $G^S$ ,  $t_W$ , and  $\mu$ ) have some effects on the hardening-associated strain plateau and the incomplete strain recovery, further analyses are required to understand these behaviors, which is of practical importance in polymer cold processing. It would also be of considerable value to have experimental data (including segmental relaxation times) on additional polymer samples, with different molecular weights, different polymer types, and different temperatures and ageing times, to determine how our best-fit parameters depend on material and experimental parameters.

Note in Fig. 6.1a that the predicted strain history in regions near the beginning and the end of the rapid flow yielding region shows more abrupt changes than observed in the experiment. This is likely due to the use of a minimal segmental relaxation dynamics in our model. As shown by Chen *et al.* (2008) to include detailed segmental-level physics could be of

importance for a comprehensive understanding of pre-yielding and recovery behaviors, which would likely lead to much better agreement with experimental data in these zones. In addition, use of a multi-mode segmental relaxation model, consistent with KWW relaxation as a result of dynamic heterogeneity, may also lead to better prediction of the recovery of the segmental relaxation time. Inclusion of those is left to future work, however.

## 2. Sub-chain orientation and stretch in uniaxial creep

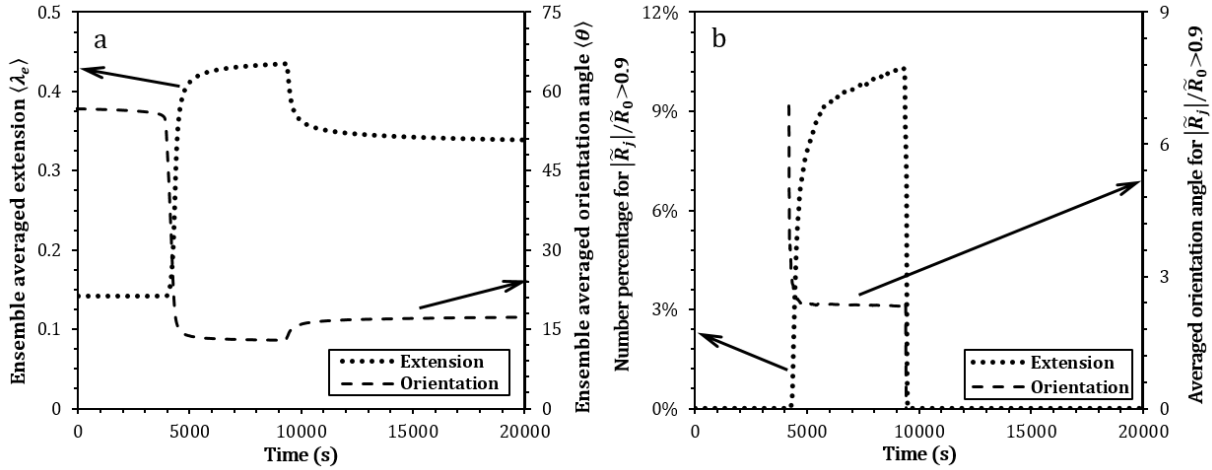


Figure 6.2 Plots of the ensemble averaged extension  $\langle \lambda_e \rangle$  (a, left axis) and orientation angle  $\langle \theta \rangle$  (a, right axis) of chain segments, represented by individual springs of the bead-spring model, as well as the number percentage (b, left axis) and the corresponding averaged orientation angle (b, right axis) of nearly fully extended springs for the simulation results shown in Fig. 6.1a.

Due to the uniqueness of strain-hardening for polymeric glass, classical theories attribute this rapid rise of resistance to deformation to an increase of the entropic elasticity of rubber networks, quantified by a so-called hardening modulus  $G_R$ . The value of  $G_R$  required to fit the strain hardening, however, is orders of magnitude higher than the rubbery modulus of typical polymer melts, while no significant change in entanglement or crosslink density is detected during the glass transition. [Wendlandt *et al.* (2005); Hoy and Robbins (2008); Chen and Schweizer (2009)] Based on recent findings from both experiments and simulations, it is now widely accepted that strain hardening does not arise primarily from linear elastic networks, [Wendlandt *et al.* (2005); Chen and Schweizer (2009); Hoy and Robbins (2009)] and instead has been attributed to finite extensibility, chain orientation, microscopic sub-affine deformation, as well as segmental scale intermolecular dynamics. [Chen *et al.* (2009); Hoy and Robbins (2008); Arruda *et al.* (1993); Chen and Schweizer (2009); Hoy and Robbins (2009)] For strain recovery,



a general understanding is derived from the entropic network model, where a chain-conformation dependent stress, known as “back stress” is thought to drive the strain reversal. [Boyce *et al.* (1988); Boyce and Arruda (1990)] Although entanglements and entropic chain orientation might be responsible for the incomplete strain recovery as suggested by MD simulations,<sup>16</sup> the sudden loss of stress with only modest strain reversal can also result from the rapid disappearance of nonlinear contributions to stress during the unloading. Specifically, Fielding *et al.* (2012) and (2013) suggested that the rapid loss of stress during recoil results from highly stretched, and quickly relaxing, short polymer segments produced by the formation of folded configurations during extensional flow. The effect of these folded conformations was accounted for by the inclusion of ad hoc “crinkle factor” in a previous dumbbell model for glassy polymers. [Fielding *et al.* (2012) and (2013); Larson (1990)]

The more detailed bead-spring description of the polymer chain introduced here, for the first time in a mesoscopic model of a glassy polymer, explicitly accounts for the folded states that arise in strong extensional flows of polymers. We investigate both the extension and the orientation of chain segments (represented by the springs in our BD simulations) in Fig. 6.2. Figure 6.2a shows the averaged fractional extension  $\langle \lambda_e \rangle (= \langle |\tilde{\mathbf{R}}_j| / \tilde{R}_0 \rangle)$  over the entire ensemble, where a sharp rise of  $\langle \lambda_e \rangle$  appears followed by a plateau ( $\langle \lambda_e \rangle \cong 0.4$ ), which coincides with the emergence of strain hardening, before a sudden drop when the material is unloaded. A similar, but opposite, trend is also observed in Fig. 6.2a for the orientation angle of chain segments  $\langle \theta \rangle$  (defined as the ensemble-averaged angle between the extension axis and the spring orientation). A detailed analysis of the hardening response also shows that during the hardening a significant fraction of chain segments ( $\cong 10\%$ ) are in a state of nearly full extension ( $|\tilde{\mathbf{R}}_j| / \tilde{R}_0 > 0.9$ ) and highly oriented ( $\langle \theta \rangle < 3^\circ$ ) along the extension direction ( $z$  axis) as illustrated by Fig. 6.2b. However, the above nearly fully extended spring states are only retained over the strain-hardening regime, and they quickly disappear upon removal of the load. It is important to note that this high stretch and orientation of individual springs is produced by a modest macroscopic strain, around 1.5 Hencky units, which is far too small to stretch and orient the entire polymer chain. We believe that these backfolds are the most likely explanation of the arrest of yielding in Fig. 6.1, as well as the strain hardening observed in glassy polymers, since such hardening is absent in non-polymeric glasses, and hardening (or arrest of yielding) occurs at strains much lower than needed to stretch the entire polymer molecule.

The above simulation results are thus explained by the coupling between nonlinear polymeric stress and segmental relaxation. The polymer segments are stretched in startup of flow much faster than they can relax by Brownian forces. This stretching continues until further deformation is impeded by the rapid rise of resistance due to the spring force nonlinearity as the polymer segment approaches nearly full extension. The resulting high resistance leads to strain hardening, which transfers ever more of the imposed constant stress from the segmental mode to the polymer mode. Because the time scale of polymeric relaxation is much larger than that of deformation, the stress carried by these tightly pulled chain segments can hardly relax until the removal of the load. When the load is removed, the stress accumulated in the material triggers a sudden reverse straining, which quickly reduces  $\tau^s$  (similar to drop of  $\tau^s$  when the material is loaded initially as shown in Fig. 6.1a) leading to relaxation of glassy segmental stress. However, this unloading also quickly and drastically reduces the huge nonlinear stresses in the tightly pulled polymer segments. This loss of the polymeric elastic driving force causes a slowdown in recoil, allowing the glassy segmental mode to age and re-vitrify. This prevents further relaxation of the strain, therefore leading to incomplete strain recovery. We note that the effects of sample temperature on strain hardening might be roughly explained within our model by varying the dynamic coupling parameter  $\alpha$ : Cooling a polymeric glass to lower temperatures would enlarge the time scale gap between the polymeric and segmental relaxation modes, which should lead to an increase of  $\alpha$ . As discussed later, with the same extensional stress a larger  $\alpha$  would result in a lower strain “plateau” before removal of the stress, implying a greater hardening modulus. However, an alternative explanation of hardening and recoil based on segmental level physics can be found in references. [Chen and Schweizer (2009) and (2010); Chen *et al.* (2008)]

Based on the above explanations, as shown in Fig. 6.3a, a larger extensional stress ( $\Sigma_z^{ext}$ ) results in an earlier yielding response and a larger strain due to the higher deformation rate. A lower stiffness of chain segments, which is quantified by a smaller value of  $G^p$  (Eqs. (6.4)) in our model, allows easier extension leading to a higher strain plateau as illustrated by Fig. 6.3b. By increasing  $\alpha$ , defined as the ratio of  $\tau^p$  to  $\tau^s$ , polymers become more reluctant to relax, therefore resisting deformation more strongly, and therefore show a lower strain-plateau and less strain recovery in Fig. 6.3c. However, if the degree of stress nonlinearity is reduced by increasing  $\tilde{R}_0$  (Eq. (6.4b)), chain segments will be stretched more before they achieve strain hardening and must recover more strain before they lose most of their stress. This leads to a

higher strain-plateau and a larger recovery (See Fig. 6.3d), which explains both the uncommonly large value of  $G_R$  obtained from the entropic models and the necessity of introducing a “crinkle factor” for the incomplete strain recovery in Fielding *et al.* (2012) and (2013). As  $\tilde{R}_0 \rightarrow \infty$ , a much greater stiffness ( $G^p$ ) is required for a finite increase of the strain, and during strain recovery its value needs to be reduced again (through multiplication by a “crinkle factor”) to account for the rapid loss of nonlinear stress during the strain reversal. Since  $\tilde{R}_0$  is roughly the ratio of the fully extended length of a spring to its equilibrium length, it follows that  $\ln \tilde{R}_0$  is roughly the strain at which strain hardening occurs.

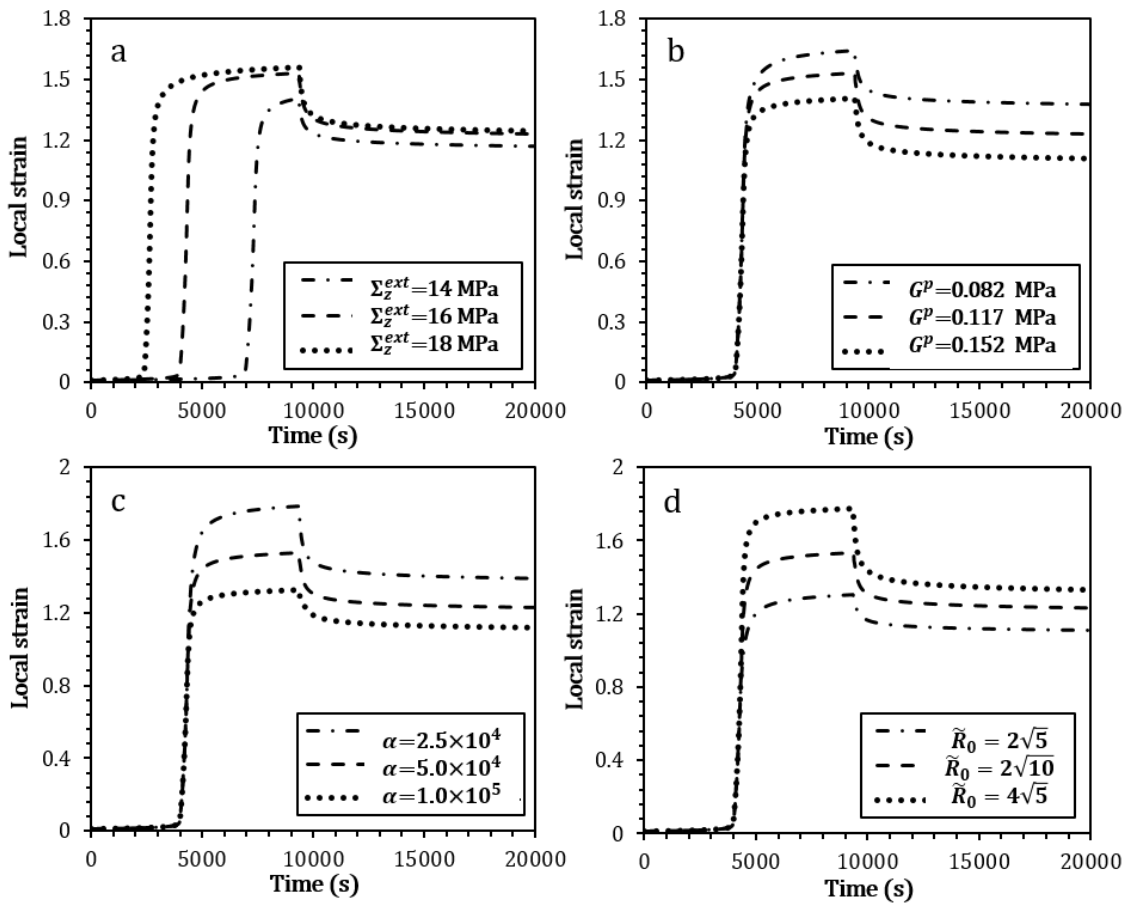


Figure 6.3 Effects of  $\Sigma_z^{ext}$  (a),  $G^p$  (b),  $\alpha$  (c), and  $\tilde{R}_0$  (d) on the hardening associated strain-plateau and incomplete strain recovery. Note that the definition of local strain is the same as Fig. 6.1.

### 3. Sensitivity to parameters

As mentioned in Section IV. A,  $G^s$  controls the yielding of the material. By varying  $G^s$ , both the initial strain and the evolution of  $\tau^s$  change as shown by Fig. 6.1b. The latter effect can

be compensated by adjusting  $\mu$  and  $t_w$ . (See Figs. 6.1c and d). Therefore, if the evolution of  $\tau^s$  and the yield strain are specified, the values of  $G^s$ ,  $\mu$ , and  $t_w$  needed to match the experiments are unique. However, the amount of recovered strain is affected by both  $\alpha$  and  $\tilde{R}_0$ . From Figs. 6.3c and d, a larger  $\tilde{R}_0$  leads to a greater recovery as well as a higher hardening associated strain plateau, both of which can be reduced by enlarging  $\alpha$  and adjusting  $G^p$  slightly. Since  $\tilde{R}_0$  is defined via  $N_K$  and  $N_{sp}$ , by setting  $N_K$  and  $N_{sp}$ , respectively, to values other than those in Table 6.1, the slight sensitivities of our simulation results to the values of  $N_K$  and  $N_{sp}$  are shown by Fig. 6.4 with the corresponding values of parameters given in Table 6.2. According to Fig. 6.4a, the effect of using the same number of springs to represent a longer chain on the simulation result can be offset if the value of  $G^p$  is adjusted slightly and  $\alpha$  is allowed to increase linearly with  $N_K$ , while, according to Fig. 6.4b, if the same degree of coarse-graining is used for larger  $N_K$  (i.e., the value of  $N_{K,sp}$  is fixed), to maintain both the strain plateau and the recovery requires a larger  $\alpha$  but the same polymeric modulus ( $G^p = 0.117$  MPa). Based on these results, our simulation model has some redundancy in the number of parameters, and so the exact values of  $N_K$  and  $\alpha$  cannot be obtained solely by fitting to the experimental data unless a correlation between  $N_K$  and  $\alpha$  is known. Of course, in principal  $N_K$  and  $\alpha$  should be set by the polymer molecular weight, and not be free parameters. However, since the data of Lee *et al.* (2009) are for weakly cross-linked PMMA, there is no value of  $N_K$  that matches the experimental conditions. The value of  $\alpha$ , which is the ratio of the longest polymer relaxation time to the segmental time, should be proportional to molecular weight to a power between 2 and 3.4 (depending on whether the polymers are entangled or not), and thus its value is also indeterminate for the data of Lee *et al.* (2009) Even for un-cross-linked polymers,  $\alpha$  would be hard to determine a priori, because our model uses a single segmental relaxation time, which is not realistic, and so the ratio of polymer relaxation time to segmental time is uncertain, except for its scaling with molecular weight. These issues would be clarified through experimental studies of polymeric glasses with different molecular weights. In addition, the use of a more refined model for the glassy modes that contains a spectrum of relaxation times should allow the parameter  $\alpha$  to be pinned down by fitting the linear viscoelasticity of the real polymer by the distribution of polymer and glassy relaxation times of the model. We note that the number of springs  $N_{sp}$  used to represent the chain is not a physical parameter, but reflects the degree of

coarse-graining in the model. Increasing  $N_{sp}$  in principle increases the resolution of the model; however, the FENE model (Eq. (6.3b)) begins to fail as the number of Kuhn steps per spring  $N_{K,sp}$  gets small. Refinements that bring  $N_{sp}$  near  $N_K$  would presumably require inclusion of torsional and bending potentials into the polymer model, and these begin to overlap with glassy modes, thus violating the separation of glassy and polymer modes needed for our basic approach to hold. Thus, the parameters of our model likely cannot be obtained entirely from fundamental molecular physics, but will remain phenomenological to some degree even after refinement of the model for the segmental stress.

Table 6.2 Values of model parameters for simulation predictions in Fig. 6.4.

Parameters	$G^p$ (MPa)	$G^s$ (MPa)	$t_w$ (s)	$\mu$	$\alpha$	$N_{K,sp}$	$N_K$	$N_{sp}$
Standard	0.117	500	$9.5 \times 10^4$	143	$5 \times 10^4$	40	400	10
$N_K=200$	0.146	500	$9.5 \times 10^4$	143	$2 \times 10^4$	20	200	10
$N_K=800$	0.13	500	$9.5 \times 10^4$	143	$1.4 \times 10^5$	80	800	10
$N_K=800, N_{sp}=20$	0.117	500	$9.5 \times 10^4$	143	$1.8 \times 10^5$	40	800	20
$N_K=1200, N_{sp}=30$	0.117	500	$9.5 \times 10^4$	143	$3.7 \times 10^5$	40	1200	30

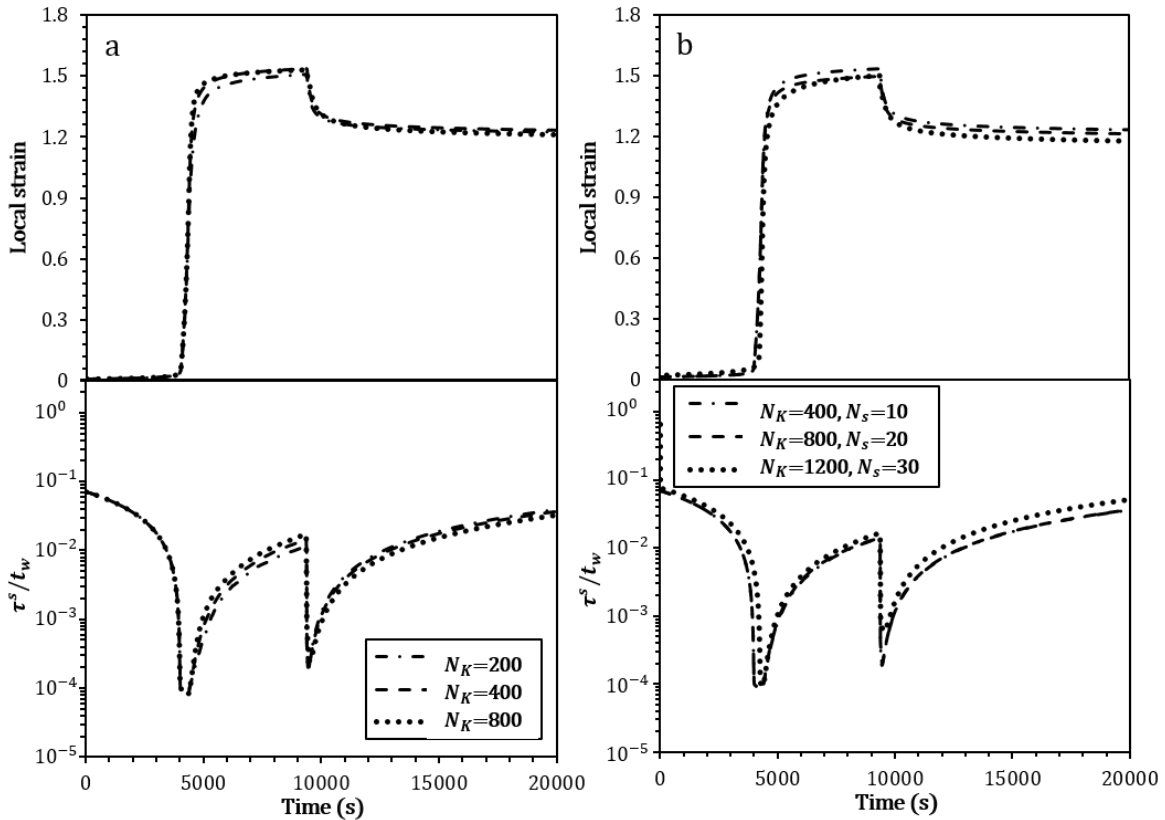


Figure 6.4 Sensitivities of simulation results to  $N_K$  with  $N_{sp}$  fixed and  $G^p$  and  $\alpha$  adjusted to keep the predictions nearly the same (a), and  $N_{sp}$  with  $N_{K,sp}$  fixed and  $\alpha$  adjusted to keep the predictions nearly the same (b). The dashed lines are the results for the standard parameter values listed in Table 6.1. In each figure, the parameters not given in the legend are the standard values in the first row of Table 6.2. Notice the same definition of local strain is used here as in Fig. 6.1.

#### 4. Startup of uniaxial extension

So far, all of our analyses and discussions have dealt with uniaxial creep, with a constant stress imposed on the material. However, our model can predict the mechanical behavior for polymeric glasses under other types of deformations. Here, we only consider two additional cases: uniaxial extension with a constant strain rate, and simple shear deformation with a constant shear stress. The same values of parameters listed in Table 6.1 are used in the simulations. A detailed procedure to account for the above two types of deformations can be found in Supplementary Information. For the uniaxial extension with a constant rate, both the stress and  $\tau^S$  are plotted against the Hencky strain ( $\epsilon$ ) in Fig. 6.5.

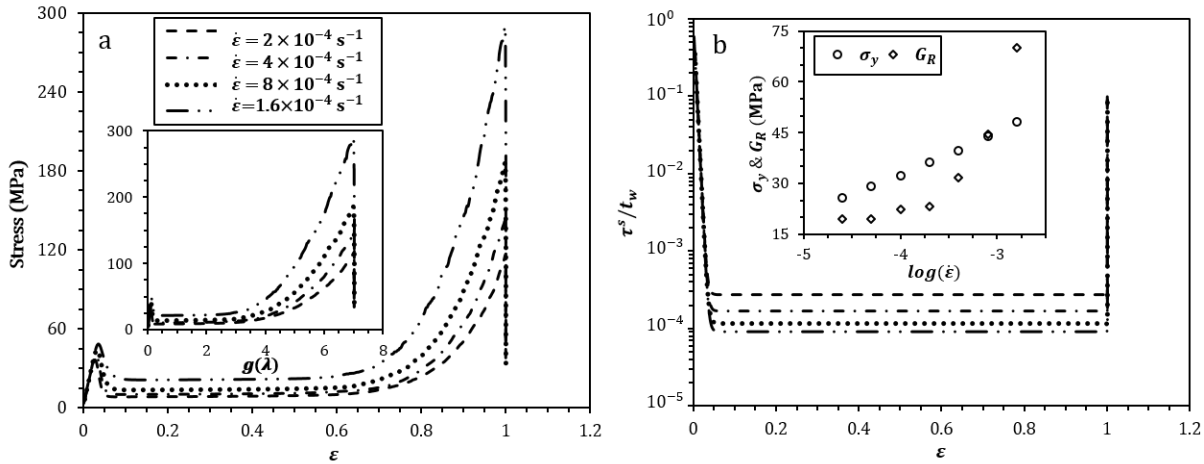


Figure 6.5 Mechanical response of polymeric glass under uniaxial extension with constant strain rates ( $\dot{\epsilon}$ ): Stress (a) and  $\tau^S/t_w$  (b). The stress at the same strain rates is replotted against  $g(\lambda)$  (defined in the main text) in the inset of Fig. 6.5a, and the dependences of stress overshoot ( $\sigma_y$ ) and hardening modulus ( $G_R$ ) on logarithm of strain rates are shown in the inset of Fig. 6.5b.

Figure 6.5a shows the entire range of mechanical response predicted by our simulation model, which successfully captures a rate-dependent stress overshoot at small strain, a plastic flow region with a nearly constant stress at intermediate strain, a hardening response at large strain, and a rapid loss of stress as the deformation ceases. The evolution of  $\tau^S$  in Fig. 6.5b under a constant rate differs from that in uniaxial extension under a constant stress (see Fig. 6.1a).

Instead of an initial abrupt change in strain/stress or a local minimum,  $\tau^s$  decreases to a specific value which depends on the strain rate, and remains constant until the end of the deformation. When the material starts to deform at a constant rate, the stress initially builds up quickly because of the large initial value of  $\tau^s$ . However, deformation-associated rejuvenation causes  $\tau^s$  to decline, and, under constant strain rate, the accumulated total stress can partially relax, which is not possible under a constant imposed stress. As a result, there is a local stress maximum  $\sigma_y$  (i.e., the overshoot in Fig. 6.5a) which depends logarithmically on strain rate (see inset of Fig. 6.5b), in agreement with experiments. This yielding behavior arises from the segmental fluidity model (Eq. (6.1e)) employed here. Since the physics underlying Eq. (6.1e) implies the segmental relaxation is affected by the competition between ageing (with a constant rate) and the deformation-rate-dependent rejuvenation, as long as the strain rate remains unchanged, the balance between ageing and rejuvenation would result in a constant  $\tau^s$  (see Fig. 6.5b). This prediction seems to be supported by recent experimental work from Bending and Ediger (2014); however, the relatively large error bars associated with their data do not eliminate other possibilities, for example the slight increase of segmental relaxation time predicted by Chen and Schweizer (2009). Hence more precise experimental measurements are still in need to elucidate this matter. As the polymer segments are stretched to nearly full extension at strains approaching unity, the polymeric stress continues to accumulate and becomes nonlinear (see Fig. 6.5a). The stress, when plotted against the ideal rubber elasticity factor, i.e.,  $g(\lambda) = \lambda^2 - \lambda^{-1}$  (here  $\lambda$  is the stretch ratio, i.e.,  $\exp(\epsilon)$ ), grows nearly linearly with  $g(\lambda)$  in the hardening regime (see the inset of Fig. 6.5a for  $g(\lambda) \gg 1$ ) with slope corresponding to the hardening modulus  $G_R$ , which is of the same order as the stress overshoot (20~60 MPa) and increases with strain rate as shown by the inset of Fig. 6.5b. Experimentally,  $G_R$  is also known to increase during cooling; however, a better model for the segmental dynamics is needed in our model before we could address the effect of temperature, which is therefore left to future work.

## 5. Simple shear deformation

Results for simple shear creep with a constant stress (see Figs. 6.6a and b) are similar in many respects to the results shown in Fig. 6.1a for uniaxial creep. For example, both show similar yielding responses (i.e., the jump/drop of strain/ $\tau^s$ ), leading to accelerated deformation. However, unlike extension, in shear there is no strain-hardening, or re-vitrification under

constant load. (After the rapid increase in strain during yielding, the bending over of the curves at larger times in Fig. 6.6 is a result of the semi-log plot.) Instead, if the added shear stress  $\Sigma_{xz}^{ext}$  is higher than a critical value (i.e.,  $\Sigma_{xz,c}^{ext} = 7.6$  MPa), the glass melts into a “liquid” (with a value of  $\tau^S \cong \tau_0^S$ ) and flows relatively rapidly before the stress is removed (see dashed and dash-dotted lines in Fig. 6.6b). From Fig. 6.6b, the higher  $\Sigma_{xz}^{ext}$  is, the earlier melting occurs, the less strain recovers during the unloading. As commonly been seen among yield stress fluids and soft glasses, the unbounded yielding in shear is caused by the flow-induced breakdown of the microstructure of the material. [Coussot *et al.* (2002)] Under shear polymer molecules rarely align along the flow direction, and when they do, they quickly tumble through the flow direction and recoil rather than stretch as they would in an extension. They cannot therefore induce a large polymer stress nonlinearity at large strain. As a result, in shear, unlike extension, there is not enough polymer stress to take sufficient load from the segmental mode to allow re-vitrification, and the deformation never slows down once the rejuvenation wins. Therefore, with a shear stress (8 and 9 MPa as shown in Fig. 6.6b) even smaller than that of extension (16 MPa), polymeric glass can maintain a nearly fully rejuvenated state with a small  $\tau^S$ , which leads to a fast relaxation of non-polymeric stress without any strain reversal.

## 6. Steady uniaxial extension in pre-oriented samples

As we mentioned in Section III, our simulations start with an equilibrated polymer ensemble, which, however, could be unrealistic if the as-received polymeric glass is anisotropic after processes like rolling, forging, and stamping, etc. [Arruda *et al.* (1993)] Also, we assume that the segmental mode is initially aged, but not at equilibrium, which in our fluidity model is never attained. Hence, it is inconsistent to assume that the slower polymer mode has somehow attained equilibration when the segmental mode can never do so. Furthermore, it is well known that an anisotropic material exhibits work hardening (i.e., an increase of flow strength) along the pre-deformation direction and Bauschinger effect (i.e., a decrease of flow strength and an increase of extensibility) along the corresponding perpendicular direction. [Arruda *et al.* (1993); Boyce and Arruda (1990)] Although it requires enough pre-strain to exploit the above effects, such methods are widely applied in solid phase polymer processing to achieve a material with desired mechanical properties. To analyze the behavior of an anisotropic polymeric glass under deformation, we generate an anisotropic “pre-deformed” polymer ensemble through a uniaxial



extension at a constant rate ( $= 10^{-4} \text{ s}^{-1}$ ), up to a Hencky strain of 0.5, and then relaxation for a time period same as  $t_w = 9.5 \times 10^4 \text{ s}$  before the final simulations are carried out. With the same extensional strain rate as in the pre-deformation ( $= 10^{-4} \text{ s}^{-1}$ ), and assuming that the strain rates in the directions perpendicular to the extension are equal to negative one half of the strain rate in the direction of the extension, the simulation results are shown in Fig. 6.7.

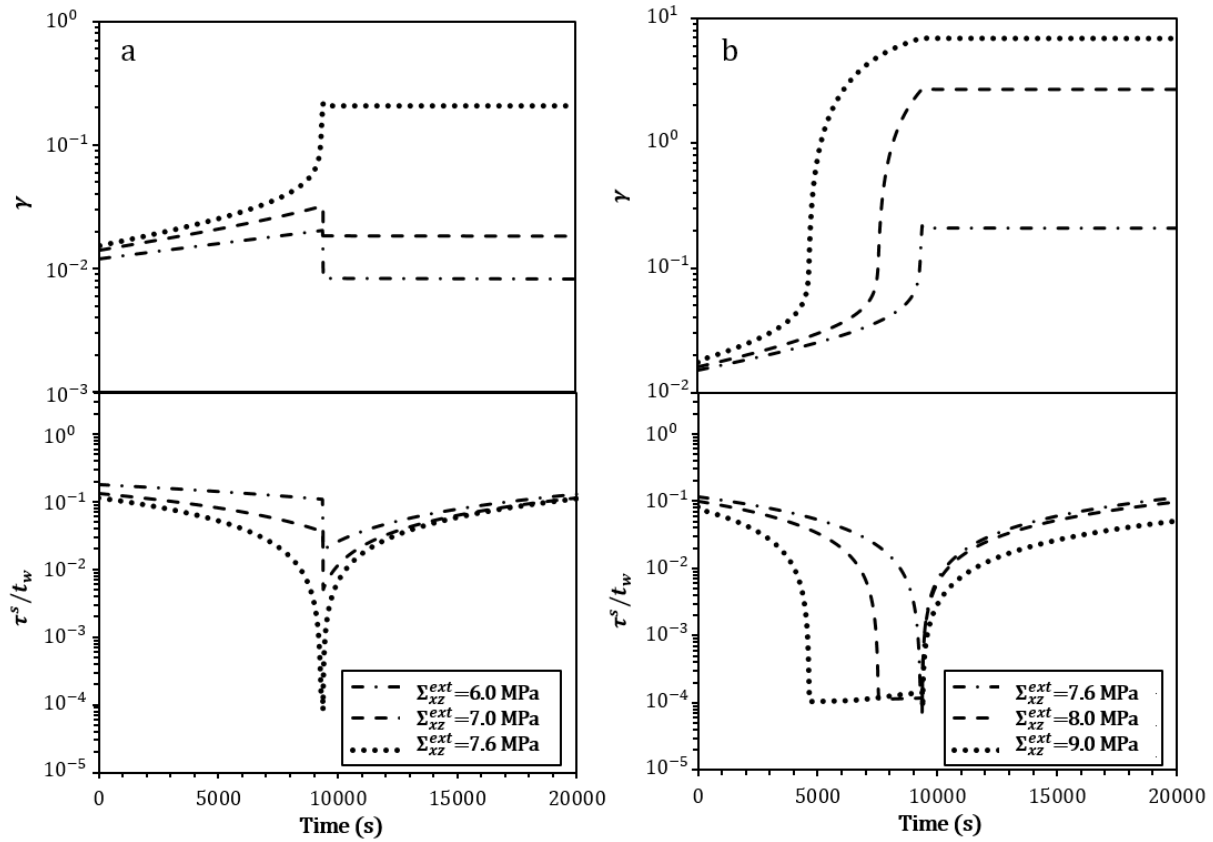


Figure 6.6 Mechanical response of polymeric glass under simple shear with constant shear stress ( $\Sigma_{xz}^{ext}$ ) with stress removed at time  $t = 9375 \text{ s}$ :  $\Sigma_{xz}^{ext} \leq \Sigma_{xz,c}^{ext}$  (a) and  $\Sigma_{xz}^{ext} \geq \Sigma_{xz,c}^{ext}$  (b).

Figure 6.7a shows a pre-deformation of the polymeric glass up to a strain of 0.5, and a relaxation period after which the stress relaxes, and then the glass is deformed again along either its pre-deformation direction, or an orthogonal direction. Note that the stress grows more rapidly if the deformation is in same direction as the first deformation period, rather than orthogonal to it. Hence in the former case a greater suppression of the plastic flow is observed in the second deformation, as the material more quickly approaches the strain-hardening regime than it does in the first deformation. This results from the significant number of chain segments aligned along

the deformation axis during the pre-deformation. However, as seen in Fig. 6.7a, if the deformation axis is perpendicular to the direction of pre-strain, a greater period of plastic flow is needed to reorient the chain segments along the new deformation axis before the onset of hardening response. This leads to an increase of macroscopic extensibility and weak flow strength in that direction. The above predictions are consistent with the experiments and simulations in this field. [Arruda et al. (1993); Boyce and Arruda (1990); Rottler and Robbins (2003)]

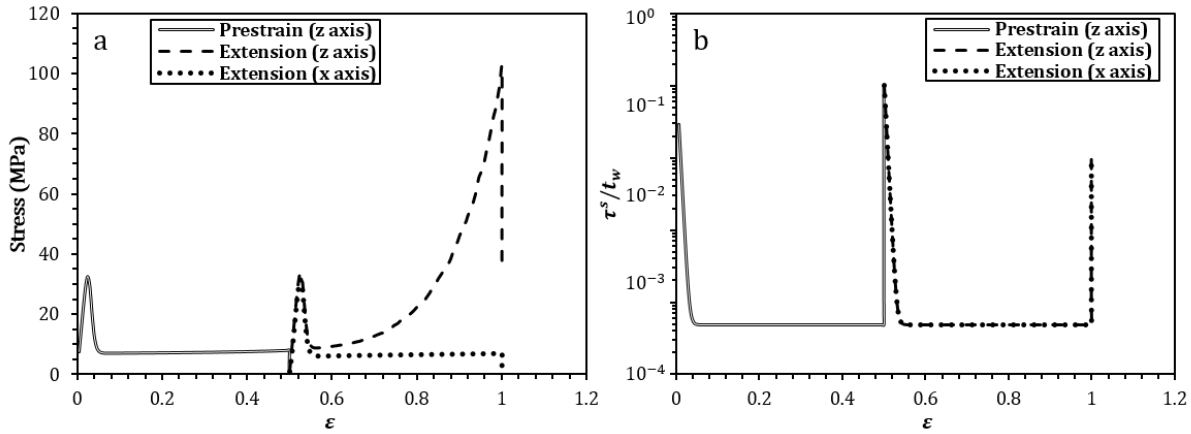


Figure 6.7 Mechanical response of polymeric glass under two successive uniaxial extensions, both at a constant rate ( $= 10^{-4} \text{ s}^{-1}$ ). In the initial period shown above, the sample is pre-stretched to a Hencky strain of 0.5, and then relaxed for  $9 \times 10^4 \text{ s}$  to create an anisotropic material. Then it is stretched further at the same constant strain rate but along either the same (z) axis or along an orthogonal (x) axis: Stress (a) and  $\tau^s/t_w$  (b). Note that the stress in Fig. 6.7a is defined as  $\Sigma_{zz} - \Sigma_{xx}$  and  $\Sigma_{xx} - \Sigma_{zz}$  for uniaxial extension in z and x direction, respectively. Following the second stretching period, the sample is allowed to relax, as shown by the drop in stress at the end of the deformation.

The results and discussions in this section show that our simulation model is successful in capturing and explaining numerous behaviors of polymeric glass under various types of deformations even without an explicit treatment of entanglements or crosslinks, which would lead to additional stress nonlinearities as chain segments between two entangled/crosslinked points are pulled tightly. The existence of entanglements/crosslinks could be critical in constraining the movement of chain segments causing strain hardening, but are not included in our model. In addition, the effect of local polymeric molecular structure such as side groups and chain stiffness, detailed segmental relaxation mechanisms, dynamic heterogeneity, and other monomer-level phenomena [Escaig (1984); Riggleman *et al.* (2007); Thureau and Ediger (2002)] are not addressed accurately by the minimal model (Eq. (6.5)) for segmental relaxation, although

some of these effects might be captured phenomenologically if Eq. (6.5) is replaced by a multi-mode segmental relaxation model.

The novel predictions above for the behavior of the glassy polymer in start-up of steady extension and shear and extension of pre-oriented samples could and should be compared with experimental data to determine if our model is basically correct. The success of such comparisons might justify further refinement of the model, as well as comparisons with experiments in which polymer molecular weight, aging time, and other experimental parameters are varied. Refinement of the model might be aided by taking advantage of other existing work in this field, referenced above.

## V. Conclusions

We have modeled a polymeric glass as an ensemble of bead-spring chains, which represent slow “polymer” relaxation modes, suspended in a glassy “solvent,” representing faster segmental dynamics, whose ageing and rejuvenation are modeled using a simple one-mode fluidity model. Our model extends the earlier work of Fielding and coworkers [Fielding *et al.* (2012) and (2013)] by replacing their simple one-mode dumbbell model for the polymeric mode with an ensemble of multi-mode bead-spring chains whose dynamics are solved by Brownian dynamics simulations. This new model yields good fits to experimental strain and segmental relaxation times of glassy PMMA under creep, [Lee *et al.* (2009)] and describes well the observed yielding, plastic flow, strain-hardening, and incomplete strain recovery, with an appropriate value of rubbery modulus for the polymeric mode. The new model is able to eliminate the artificial “crinkle factor” needed to fit the earlier polymer dumbbell model of Fielding *et al.* (2012) to the creep and recovery data, and to confirm that the small elastic recovery observed in experiments is due to the large nonlinear stress resulting from highly stretched, folded, polymer segments produced by extensional flow. A detailed analysis of the extension and orientation of the polymer springs shows that strain hardening sets in at strains near unity, which are much lower than that needed to fully extend the polymer, because even modest strains are able to fully extend a subset of relatively short strands that are trapped between folds. This also explains the small recoil; the stress disappears as soon as these highly stretched sub-chains recoil slightly. We predict that the increase in the segmental relaxation time after yielding that is seen in extensional creep is absent both in steady extensional straining and

in shear creep. In steady extension, there is no chance for re-vitrification of the segmental mode due to slow-down in straining that occurs in creep when most of the stress is transferred to the polymer mode. In shear, on the other hand, highly extended sub-chains do not appear because of tumbling. We also show that extensional deformation imposed on pre-oriented glassy polymer produces stress growth that is sensitive to the orientation of the pre-stressed polymer. These predictions remain to be tested in detail but appear to be consistent with observations reported in the literature. Future experimental work would be needed to relate some of the model's parameters to material properties and experimental conditions.

## Chapter 7: Conclusion

In this dissertation, a fast “pointer” simulation method that extends the model of Cates and coworkers for the rheology of entangled WLMs is presented, which I believe allows more accurate rheological predictions than before. This new method includes not only reptation, breakage and rejoining, contour length fluctuations, and Rouse modes, which had been previously considered, but also constraint release by double reptation, bending modes, and the cross-over between loose and tight entanglement regime, which are beyond those of Cates model. This method also contains correlations in micelle length across multiple breakage and rejoining cycles, not accounted for via previous approaches. Since the method uses “pointers” that track the ends of unrelaxed regions along each micelle, thereby allowing efficient simulations of relaxation dynamics for ensembles containing thousands of micelles, it is capable to obtain accurate results without preaveraging or neglecting correlations. A modified genetic algorithm is applied to transform the simulation data from the time to the frequency domain. Based on the aforementioned most up-to-date theories of polymer dynamics and innovations in modeling, this simulation method can span several regimes of behavior depending on the relative rates of reptation, contour length fluctuations, breakage/rejoining, and high frequency modes and is suitable for predicting the rheological behavior of experimental solutions for wormlike micelles.

Thus, fits to rheological data using the above method allow multiple micelle parameters to be estimated, and more accurate estimates to be obtained than was possible from the earlier approaches using Cates model. The advantages of this simulation method are illustrated by obtaining micelle parameters from fits to storage and loss modulus, i.e.,  $G'$  and  $G''$  data by Oelschlaeger *et al.* (2010) over six decades of frequency with an average deviation of only 6%. However, significant differences are found between the micelle parameters derived from the new method and those obtained by the traditional approach of Cates and coworkers (estimates are made on the basis of “local” frequency dependencies predicted by Cates model), especially in average micelle length and breakage time, which are an order of magnitude different from

previous. These differences are due to more complete physics included in the method and the fitting of rheological data across the entire frequency range. The method can also give forward predictions thereby provide quantitative relationships between these micellar parameters and rheological behaviors that improve on previous simple scaling results.

Generally, a comprehensive characterization of micelle properties require combinations of different experimental methods such as light and neutron scattering, electron microscopy, etc. While based on the improved empirical relationships and an associated data-fitting procedure, the above new method allow quantitative estimation of micellar characteristic lengths and time constants: i.e., average micelle length, breakage and reptation time, and entanglement and persistence lengths, to be extracted from linear rheological measurements include both mechanical rheometry and diffusing wave spectroscopy, the latter providing the high-frequency data needed to determine micelle persistence length accurately. A comparison of fitted micellar parameters was made between DWS data and mechanical rheometric data for WLM solution, and this indicates the importance of low-frequency data in estimating the plateau modulus, the breakage time, and the semiflexibility. The accuracy of the simulation method was demonstrated by sensitivity studies i.e., analyses on the sensitivity of estimated parameters to error or noise. For different micellar breakage mechanisms (reversible scission, end-interchange, and bond-interchange), their effects on the stress relaxation of WLM solutions for fixed surfactant concentration are found to be rather modest. By applying this method on commercial surfactant solutions, one containing sodium lauryl ether sulfate (SLE1S), and the other containing both SLE1S and cocoamidopropyl betaine to examine effects of added salt concentration, the method is shown to be of practical use in predicting monotonic and nonmonotonic dependences of different micellar parameters on salt concentration, which are difficult to obtain from other theoretical or experimental methods.

Combined with molecular simulations, the multiscale modeling of WLM solutions is achieved by using the aforementioned micellar-scale simulation method to connect macroscopic viscoelastic properties to surfactant packing structures at the molecular scale. Specifically, the changes of linear rheology in two body-wash formulations upon addition of NaCl salt and perfume raw materials (PRMs) are investigated at various concentrations and temperatures. Micelle-level properties, such as micelle length, breakage time, and scission free energy are thereby obtained with the surfactant packing structure determined through dissipative particle

dynamics (DPD) simulations and traditional surfactant packing arguments. Thus, the structure–property relationships of surfactant formulations can be explored with consistent results obtained at different length scales, from molecular, to micellar, to bulk rheological.

While much is known about the effect of salt on the viscosity of a micelle solution, the molecular-level DPD simulations confirm and quantify this effect on head group packing, through use of a “packing distance” defined as the length of WLM per surfactant molecule, which decreases as salt concentration increases in the two body-wash formulations. If the radius of the WLM remains constant, this should result in a higher Israelachvili packing parameter. This, in turn, should produce longer micelles, a larger scission free energy, and shorter micellar breakage time, all of which agrees with the quantitative estimates of these parameters from application of the micellar-scale simulation method to the linear viscoelastic data. Thus, consistent with current understanding on the effect of salt, the above findings make the connection between micelle properties extracted from rheology and the detailed surfactant packing inferred from DPD molecular simulations more thorough than before. In fact, the changes in surfactant packing quantified by our simulations are often too subtle to be obtained from experimental probes, such as neutron scattering, and yet, these small changes have significant effects on rheological properties.

By measuring linear rheology over a small range of temperature, and using the micellar-scale simulation method to infer the temperature dependence of the micellar length, the micellar end-cap free energy can also be estimated, which is significantly less than values reported earlier for CTAC/NaSal micelles. Further, both the activation energies for viscosity and relaxation time drop as salt concentration increases up to the salt concentration that maximizes viscosity, similar to that for CTAC/NaSal micelles. Using the above simulation method, the obtained micellar breakage time is found to decrease with salt concentration almost monotonically at constant temperature. PRMs modify the viscoelastic properties of body washes by partitioning within the micelles at different locations according to their hydrophobicity and their chemical structures. Through the multiscale modeling, we found that PRMs with a very low or a very high hydrophobicity reduce the average micelle length, scission free energy, and zero shear viscosity significantly. PRMs with low hydrophobicity mainly partition within the head group region of the micelle, increase the head group surface area at constant micellar radius, decrease the packing parameter therefore resulting in shorter micelles and lower viscosity. While for large,

highly hydrophobic PRMs, they mainly partition into the center of the micelle, and rather than mixing with the tails, push them radially outward, which favors shorter micelles. PRMs with moderately hydrophobicity can induce some growth in micelle length, but this does not change the viscosity or the scission energy of the solutions much, or at most increases them slightly, relative to the viscosity in the absence of the added PRM. Partitioning of PRMs depends on the composition of the surfactant solution, as well as on the PRM. The use of the packing distance in cylindrical part of micelle as a tool to describe the impact of the PRMs on structure and viscosity is insufficient as it lacks a description of the packing of the surfactant in the endcaps. To even qualitatively describe the impact of molecules with different polarities, such a parameter needs to capture the impact on both the cylindrical part and the end caps of the micelle.

Since this new simulation method manifest itself with notable advantage when handling unbranched but well-entangled WLMs, it provides a practical pathway to study the effects of both micelle branches and unentangled micelle rods in micellar solutions. Because in a branched micelle the surfactant molecules can diffuse rapidly through branch points causing micelle branch to grow, and shrink, the presence of these branches provide extra paths allowing micelles to slide quickly from their entanglements, however, few studies are available to explain these dynamics in detail. To account for the branching-associated kinetics on the micellar relaxation behaviors, a “constrained” diffusion model as well as a mechanism to create new branches are developed, where constraint forces are imposed to balance the flux of micellar materials at each branch junctions and a branch junction can be generated by sprouting a tiny branch, so-called a “bud,” along the micelle randomly. Thus, the linear to branch transition in micelle morphology can be represented by an increase of bud size or sprouting rate as temperature or salt concentration varies. By generating micelle systems with different level of branching, this extended simulation method is capable to predict a decrease in viscosity as more branches are introduced into the solutions, which consist with the well-known phenomenon for surfactant solutions at high salt concentration. On the contrary, for the unentangled micelle rods, their effects on the viscosity of solutions are only significant when surfactant concentration is low. Unlike those entangled long micelles, micelle rods are free to rotate therefore resulting in a much faster relaxation of the stress imposed on them and a lower viscosity. This additional rotary mechanism is now included in the model to enable characterization of micelle solutions at low surfactant concentration. By investigating the transition between entangled and unentangled



micelle systems, the evolution of micellar structure can be predicted with the above extended simulation method. “First principle” scaling arguments are also postulated to conclude that WLM solutions is a “weakly reactive” system, i.e., the solution never truly reaches the diffusion controlled regime before the onset of entanglements, whose trend is similar as that for dilute polymers in good solvent.

For the last part of this dissertation, polymeric glasses are modeled as an ensemble of bead-spring chains, which represent slow “polymer” relaxation modes, suspended in a glassy “solvent,” representing faster segmental dynamics, whose ageing and rejuvenation are modeled using a simple one-mode fluidity model. This new model extends the earlier work of Fielding and coworkers [Fielding *et al.* (2012) and (2013)] by replacing their simple one-mode dumbbell model for the polymeric mode with an ensemble of multi-mode bead-spring chains whose dynamics are solved by Brownian dynamics simulations. The model yields good fits to experimental strain and segmental relaxation times of glassy PMMA under creep, [Lee *et al.* (2009)] and describes well the observed yielding, plastic flow, strain-hardening, and incomplete strain recovery, with an appropriate value of rubbery modulus for the polymeric mode. The new model is able to eliminate the artificial “crinkle factor” needed to fit the earlier polymer dumbbell model of Fielding *et al.* (2012) to the creep and recovery data, and to confirm that the small elastic recovery observed in experiments is due to the large nonlinear stress resulting from highly stretched, folded, polymer segments produced by extensional flow. A detailed analysis of the extension and orientation of the polymer springs shows that strain hardening sets in at strains near unity, which are much lower than that needed to fully extend the polymer, because even modest strains are able to fully extend a subset of relatively short strands that are trapped between folds. This also explains the small recoil; the stress disappears as soon as these highly stretched sub-chains recoil slightly. While the model also predicts that the increase in the segmental relaxation time after yielding that is seen in extensional creep is absent both in steady extensional straining and in shear creep. In steady extension, there is no chance for re-vitrification of the segmental mode due to slow-down in straining that occurs in creep when most of the stress is transferred to the polymer mode. In shear, on the other hand, highly extended sub-chains do not appear because of tumbling. It is found that extensional deformation imposed on pre-oriented glassy polymer produces stress growth that is sensitive to the orientation of the pre-stressed polymer.

Further improvements of this new model would still be in need to clarify some of the issues including the degree of coarse-graining for polymers with different molecular weights as well as a broad spectrum of glassy relaxation times. These improvements, for example, should include the use of a more refined description for both the polymer chains and the glassy dynamics, and should allow some of parameters in the model to be pinned down physically as reflected by the properties of real polymers. Thus, in its current state, the parameters of this model remain phenomenological to some degree, but we believe, once combined with molecular level simulations, this model would provide a practical path for the multi-scale modelling of polymeric glass under deformation.

## **Appendices**

## Appendix A: Genetic Algorithm and Simulation Details

### I. Pre-factor for Modulus in Loose-entanglement Regimes

For wormlike micelles in water, the plateau modulus ( $G_N$ ) has been given by Milner (2005), which is valid for polymer chains in a good solvent:

$$G_N \cong \frac{216k_B T}{n^2 p_{Mil}^3} \phi^{\frac{9}{4}} \quad (A.1)$$

where  $\phi$  is the volume fraction of polymer;  $n$  is a constant determined empirically with a value of around 22.4; and  $p_{Mil}$  is the “packing length” as defined by Milner for polymer melts as:

$$p_{Mil} = \frac{6v_b}{b_K^2}, \text{ with } v_b = \frac{\pi}{4} d^2 b_K \quad (A.2)$$

Here  $v_b$  is the volume of a single Kuhn step for a micelle, and  $d$  is the micelle diameter. Note there is another definition of packing length, given by Fetters *et al.* (1999), which we do not use here but differs from that of Milner by a factor of 6.

Combining Eq. (A.1) and Eq. (A.2), yields:

$$G_N \cong \frac{512l_p^3}{\pi^3 n^2 d^6} k_B T \phi^{\frac{9}{4}} \quad (A.3)$$

The tube diameter ( $a$ ) is related to the packing length ( $p_{Mil}$ ) [Milner (2005)] for flexible polymers in the melt by:

$$a = \frac{np_{Mil}}{6} = \frac{n\pi d^2}{8 l_p} \quad (A.4)$$

In a solution with a good solvent, Eq. (A.4) must be modified to:

$$a = \frac{n\pi d^2}{8 l_p} \phi^{-3/4} \quad (A.5)$$

For loose entanglements in good solvents, the formula for  $d$  is therefore:

$$d^2 = 2^{2/5} \frac{8}{n\pi} l_e^{3/5} l_p^{7/5} \phi^{3/4} \quad (A.6)$$

Combining the above equation with Eq. (A.3) gives:

$$G_N \cong 9.75 \frac{k_B T}{(l_p^{0.4} l_e^{0.6})^3} = 9.75 \frac{k_B T}{\xi^3} \quad (A.7)$$

which yields the value of pre-factor  $A = 9.75$  used in the main text of Chapter 2.

## II. Genetic Algorithm for Converting to Frequency Domain

The Genetic Algorithm (GA) belongs to the family of evolutionary algorithms that provide useful solutions to multi-variable optimization and searching problems [Melanie (1996)]. By mimicking the phenomenon of evolution in nature, a genetic algorithm evolves an ensemble of solutions gradually toward better ones. A standard genetic algorithm involves “selection”, “inheritance”, “crossover”, and “mutation” steps. During each generation, every individual solution (which in our case is an independent set of fitting parameters) will pass through the above steps with a possibility of thereby forming a better solution. Meanwhile, some solutions will be eliminated from the ensemble because of their weak fitness (large fitting error). A detailed description of genetic algorithm applied to our problem is detailed in what follows.

### 1. Problem set up

We first express the stress relaxation function ( $\mu$ ) as a summation of finite exponential functions with time constants ( $\tau_i$ ) and weights ( $\mu_i$ ):

$$\mu(t) = \sum_{i=1}^{20} \mu_i \exp(-t/\tau_i), \quad \mu_i > 0 \quad (A.8)$$

Here, 20 terms are used as a compromise between computational cost and accuracy. Equation (A.8) can be transformed into the frequency domain analytically as:

$$G'(\omega) = G_N \sum_{i=1}^{20} \mu_i \frac{\omega^2 \tau_i^2}{1 + \omega^2 \tau_i^2}, \quad G''(\omega) = G_N \sum_{i=1}^{20} \mu_i \frac{\omega \tau_i}{1 + \omega^2 \tau_i^2} \quad (A.9)$$

Thus, the transformation problem has been converted into a nonlinear fitting problem with multiple (40) variables, and the genetic algorithm yields an optimized solution for the set of constants ( $\mu_i, \tau_i$ ), whose detailed procedure is shown below:

### 2. Initialization

In a genetic algorithm, the initial guess is generated by randomly choosing parameter values within established ranges. For our problem, the frequency typically spans  $0.01 \sim 10^6$  rad/s, and  $\mu(t)$  is no greater than 1, which yields ranges for the parameters of:

$$\mu_i: 10^{-5} \sim 10^0, \tau_i: 10^{-8} \sim 10^3 \quad (A.10)$$

An outline of the initialization for our genetic algorithm is presented in Fig. A.1, where  $N = 20$  is the number of exponential terms (Eq. (A.8)) and  $M$  is the size of the solution ensemble.

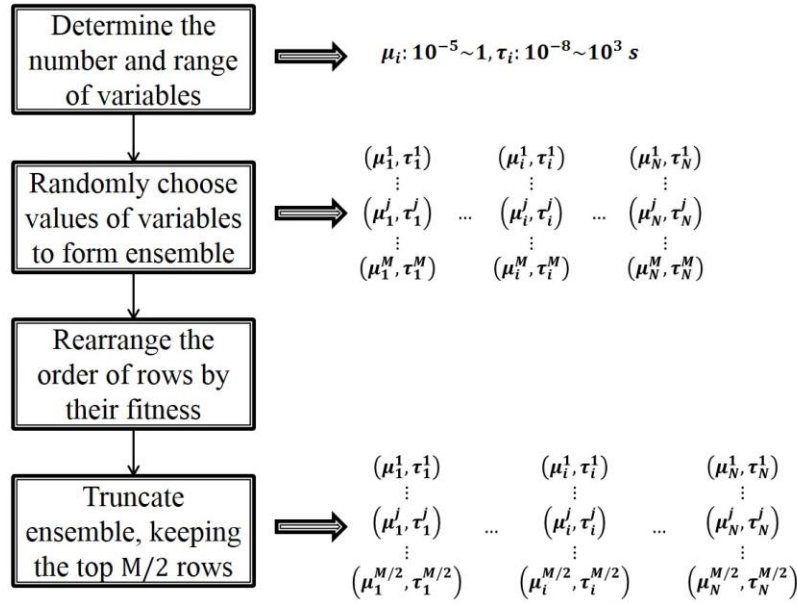


Figure A.1 The initialization of genetic algorithm.

According to the above routine, the genetic algorithm is initiated by an ensemble consisting of: an  $M \times N$  matrix with  $M$  rows of  $N$  pairs of entries  $(\mu_i, \tau_i)$ . Each row is an independent parameter set ordered so that the larger  $\tau_i$  is placed at the left side of the matrix, while each row is ordered by the fitness  $\varepsilon$  (fitting error) calculated by Eq. (A.11), with smaller errors towards the top:

$$\varepsilon = \frac{\sum_{j=1}^n |\mu(t_j) - \sum_{i=1}^N \mu_i \exp(-t_j/\tau_i)|}{\sum_{j=1}^n \mu(t_j)} \quad (\text{A.11})$$

where,  $n$  is the total number of simulation data points in time domain.

After initialization, the ensemble will be truncated to half of its original size ( $M/2$ ) for further manipulation. The truncated ensemble is called “father” generation.

### 3. Evolution

As illustrated in Fig. A.2, after two important steps (crossover and mutation), the “father” generation will evolve to a “son” generation: a better ensemble with size ( $M$ ) at the end of evolutionary step  $k$ . As a starting ensemble for next iteration, the “son” generation contains the

top  $M/4$  rows of the “father” generation with the least fitting error, and  $M/2$  rows resulting from crossover and mutation (described below). The remaining  $M/4$  rows are generated from the same random process used to create the initial sets of parameters. A more detailed description for crossover and mutation is given below.

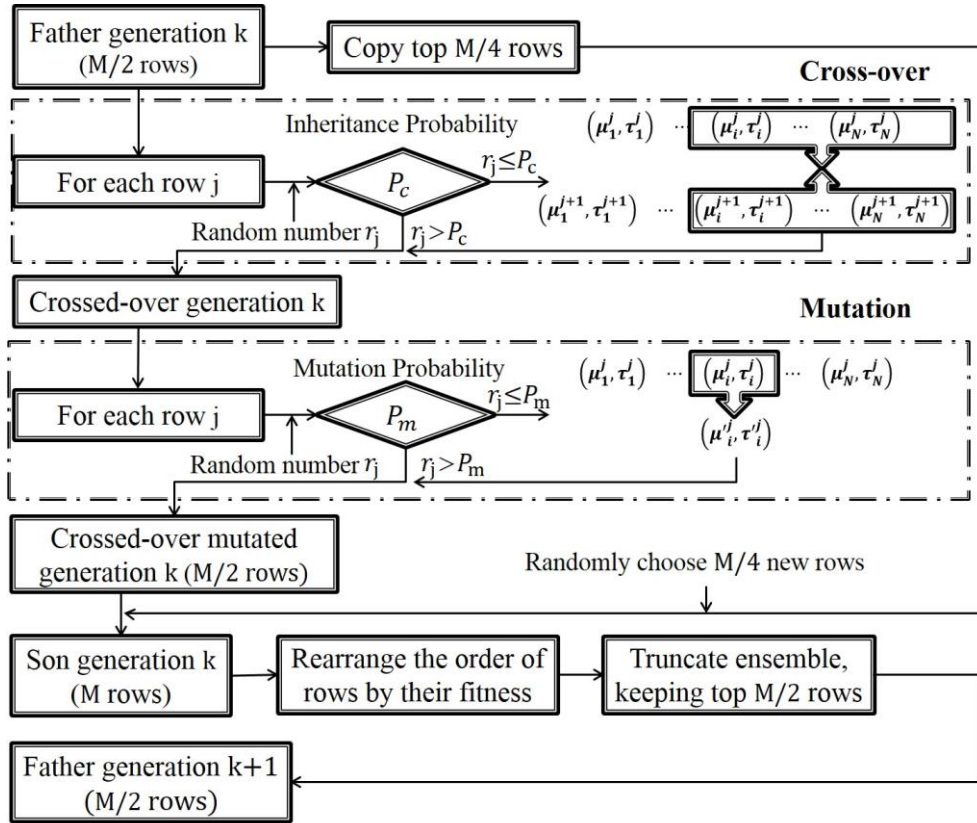


Figure A.2 Flowchart of genetic algorithm.

a) *Crossover*

Comparisons are made between computer-generated random numbers and an “inheritance probability” ( $P_c$ ), whose value is the probability that “crossover” occurs. In our case, a one-point crossover technique is used: all parameter pairs beyond a randomly selected pair are switched with the corresponding values of the neighboring row. This allows for parameters with high “fitness” in one row to be transmitted to another row, with the possibility that a superior overall fitness might arise.

b) *Mutation*

Similarly to crossover, we set a mutation probability ( $P_m$ ), but this time for replacing a single randomly chosen parameter pair with random numbers generated from the range given by Eq. (A.10). Note that crossover acts on a portion of a row, while mutation acts on a single parameter pair.

The algorithm is continued for enough generations to find a parameter set with acceptable fitting error, which we take to be an average error of 1% per point. The transformed results are shown in Fig. A.3. Based on simulation performance, we find that the optimal choices for  $M$ ,  $P_c$  and  $P_m$  are 40, 0.5 and 0.05 respectively. The CPU time of a single processor (on Intel<sup>®</sup> Core<sup>™</sup> i5 CPU with 2.27GHz) for fitting 500 rheological data points is around 0.5 hours for 15000 generations, which is the number of generations typically needed for convergence.

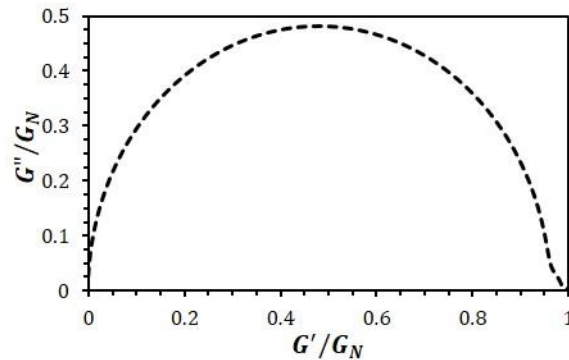


Figure A.3 Normalized Cole-Cole plot for standard values of parameters obtained from genetic algorithm-aided Fourier transform.

#### 4. Constraint method

However, as  $\zeta$  increases, and the distribution of relaxation times becomes broader, even small fitting deviations for  $\mu(t)$  at early times cause obvious “wiggles” at high frequencies in the normalized Cole-Cole plot (Fig. A.4). We find that this high sensitivity to early-time fitting results from very unevenly distributed  $\tau_i$  and magnitudes of  $\mu_i$  that can change by one or two orders with increasing mode number  $i$ , where  $i$  is numbered sequentially from slowest to fastest mode. Thus, modifications are needed to achieve better high-frequency behavior.

We fix the above problem using an artificial constraint that confines the ratios of neighboring  $\mu_i$  values to the range 0.01 to 100. Although this method slightly increases the computational time, the “fitness” (See Eq. (A.9)) is still minimized within this constraint. Since



spacing values of  $\tau_i$  logarithmically only works well for a wide distribution of relaxation times (large  $\zeta$ ), a more general approach is to make each  $\tau_i$  movable within an interval satisfying:

$$I_{min} + \frac{I_{max} - I_{min}}{N} (i - 1) < \log(\tau_i) < I_{min} + \frac{I_{max} - I_{min}}{N} i \quad (A.12)$$

where  $I_{max}$  and  $I_{min}$  are the maximum and minimum values for  $\log(\tau_i)$ , respectively.  $N = 20$  is the total number of modes. For our case ( $\tau_i: 10^{-8} - 10^3$ s, see Eq. (A.8)), we have  $I_{max} = 3, I_{min} = -8$ .

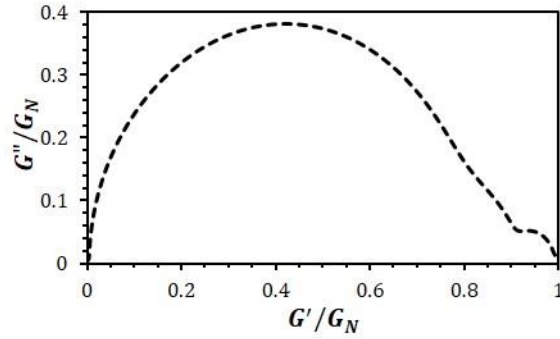


Figure A.4 The same as Fig. A.3, except with  $\zeta = 0.05$ .

The advantage of setting boundaries for each  $\tau_i$  is that for different values of  $\zeta$  each  $\tau_i$  can slide within its interval to obtain the best fit for the stress relaxation function  $\mu(t)$ . Using standard values of parameters except for  $\zeta = 0.05$ , transformation results with the constraint method are given in Fig. A.5.

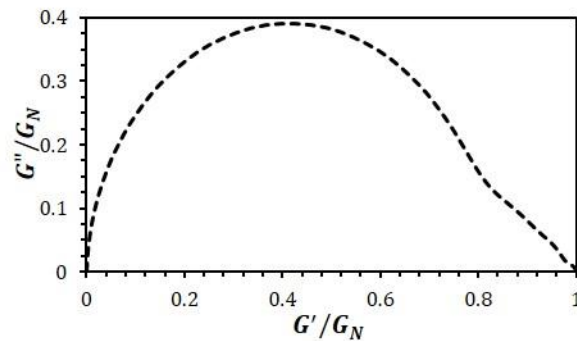


Figure A.5 The same as Fig. A.4, except that a constraint method is used.

### III. Simulation Testing Details

#### 1. Equilibrium distribution

The random breakage/rejoining within the pointer algorithm produces a simulated micelle length distribution that matches the theoretical equilibrium one (Eq. (2.15)) after fluctuations are averaged out ( $R^2 = 0.97$ ) over a simulation time of duration ten times the terminal relaxation,  $10\bar{\tau} \sim 10\bar{\tau}_{rep}\zeta^{0.62}$  (See Table IV for the scaling of relaxation time with  $\zeta$ ), which in computer time is typically half a day for a single Intel<sup>®</sup> Core<sup>™</sup> i5 CPU with 2.27GHz. Checks using different run lengths established the adequacy of this run duration.

#### 2. Pure reptation

To test that the simulation correctly accounts for reptation, we turn off all the other mechanisms, and simulate a set of chains with the same length. The results of simulation compare favorably ( $R^2 = 0.98$ ) with the theoretical ones from the Doi-Edwards theory (Eq. (2.13)), indicating that our simulation method captures reptation properly.

#### 3. Reptation and contour length fluctuations (CLFs)

Next, we add contour length fluctuations to pure reptation, again simulating with a monodisperse ensemble of chains. We find that our simulation results are close to ( $R^2 = 0.96$ ) the theoretical prediction for a single-mode relaxation, whose reptation time is corrected by CLFs, according to Eq. (2.21) from Likhtman and McLeish (2002). As shown in Fig. A.6, the rather small deviations are concentrated at early times, where the single-mode description of CLFs given by Eq. (2.21) is not expected to work perfectly, and relaxation is somewhat faster than predicted by Eq. (2.21). Thus, since CLFs introduce additional fast modes, the deviation between this theory and the simulations seen at early times is expected and does not necessarily reflect inaccuracy in the simulations. In addition, at very long times where the un-relaxed fraction  $\mu$  falls below 0.1%, our treatment on CLFs (Eq. (2.40)) overestimates the rate of relaxation. Thus, when relaxation is nearly complete and  $\mu$  reaches 0.1%, we simply switch off CLFs, which is reasonable since its effect is negligible at such late times.

#### 4. Convergence

To obtain convergence with time step, we need to modify the simulation time step from that given in Eq. (2.38), to:

$$\Delta t = \min \left[ \frac{\bar{\tau}_{br}}{2 \cdot num}, \Delta t_L \right], \quad \Delta t_L \sim O \left( \frac{\bar{\tau}_{rep}}{\langle L \rangle^3} \right) \quad (A.13)$$

where  $\Delta t_L$  is a time constant with units of seconds. The reason for preventing the time step from becoming larger than  $\Delta t_L$  lies in the convergence requirement when other mechanisms (reptation, CLFs) become important, as  $\zeta$  (and thus  $\bar{\tau}_{br}$ ) becomes larger. We find empirically that  $\Delta t_L = 10^{-6}s$  fits most of our convergence requirements. This criterion no doubt depends on our simulation of aqueous systems, and is likely set by the shortest relaxation time of micelles in the ensemble.

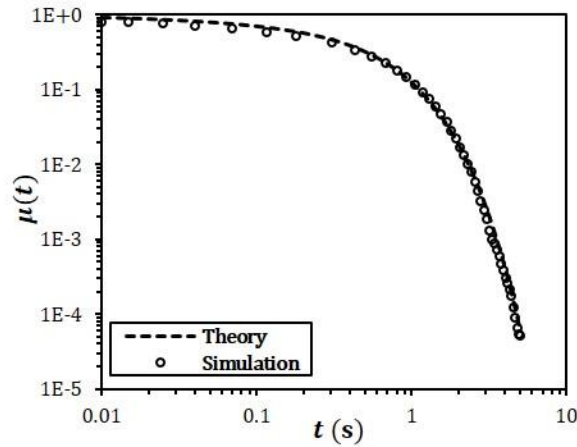


Figure A.6 Relaxation function with CLFs and reptation for monodisperse ensemble for  $Z = 33.5$ ,  $\tau_{rep} = 1s$ ,  $\alpha_e = 2$ ,  $l_p = 30nm$  and  $d = 3nm$ . The “Theory” here is the single-mode relaxation expression given by Eq. (2.21).

In addition, we compare results obtained from averaging over three different run durations ( $C\bar{\tau}_{rep}\zeta^{0.62}$ ,  $5C\bar{\tau}_{rep}\zeta^{0.62}$  and  $10C\bar{\tau}_{rep}\zeta^{0.62}$ , which are, respectively, roughly equal to  $C$ ,  $5C$  and  $10C$  times the terminal relaxation time  $\bar{\tau} \sim \bar{\tau}_{rep}\zeta^{0.62}$ ; where this formula is given in Table 2.4,  $C$  is system dependent constant). We find that simulations are insensitive to fluctuations in length distribution for the ensemble size we have chosen (10,000 micelles), and only the shortest of these durations,  $C\bar{\tau}_{rep}\zeta^{0.62}$  (1~3 hours on a single processor of Intel® Core™ i5 CPU with 2.27GHz), is needed to obtain reproducible rheological properties. Thus, our pointer algorithm simulation successfully captures the “living” feature of wormlike micelles with convergence with respect to time step, run duration, and size of ensemble.

#### IV. Cole-Cole Plots for a Wide Range of $\zeta$ and $\bar{Z}_t$

As described in the text, we obtain normalized Cole-Cole plots for a range of  $\zeta$  and  $\bar{Z}_t$ , which are presented below, in Figs. A.7 and A.8. These plots were used to obtain the correlations discussed in the text.

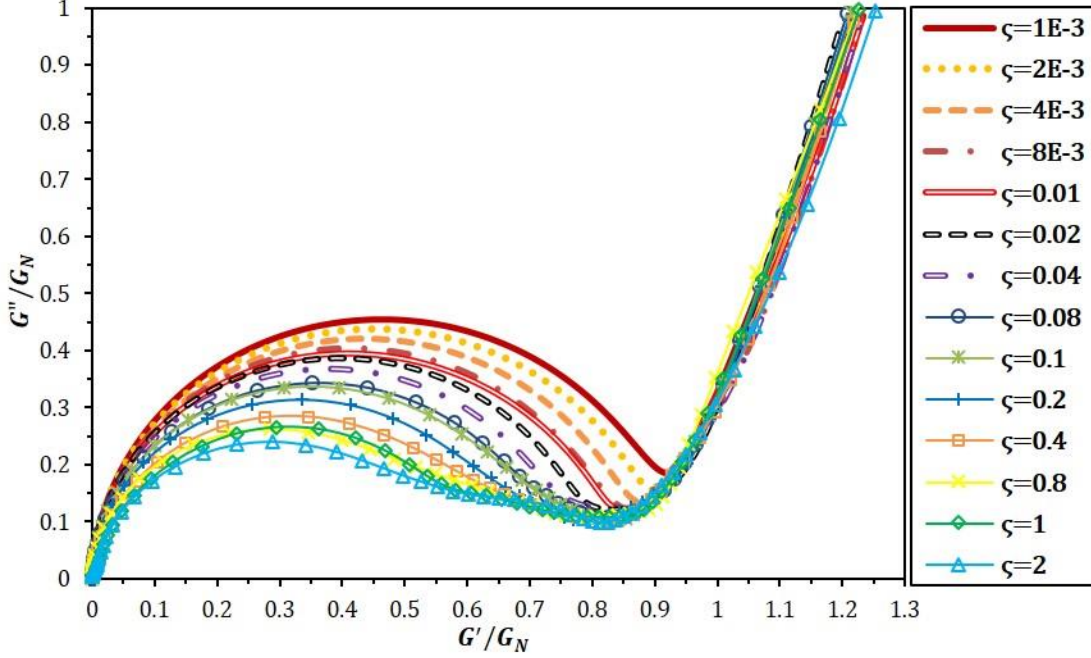


Figure A.7 Family of normalized Cole-Cole plots for different values of  $\zeta$  with standard values of other parameters.

#### V. Functional Forms for Micelle Parameters

The detailed functional forms for Eq. (2.44b) are:

For the average number of entanglements per tube, by combining Eqs. (2.2), (2.9) and (2.28), we obtain

$$\bar{Z}_t = \frac{\langle L \rangle}{\alpha_e l_p \cdot \max[\sqrt{0.5\alpha_e}, 1]} \quad (\text{A.14})$$

To obtain  $\bar{\tau}_{rep}$ , combining Eqs. (2.4), (2.12) and (2.28), gives:

$$\bar{\tau}_{rep} = \frac{2}{\pi} \frac{\eta_s}{k_B T \ln(\alpha_e^{0.6} l_p / d)} \frac{\langle L \rangle^3}{\{\max[\sqrt{0.5\alpha_e}, 1]\}^2} \quad (\text{A.15})$$

For  $G_N$ , we use Eq. (2.32):

$$G_N = \frac{\alpha_e^3}{\alpha_e^3 + 3} \cdot 9.75 \frac{k_B T}{\alpha_e^{9/5} l_p^3} + \frac{3}{\alpha_e^3 + 3} \cdot \frac{28}{5\pi} \frac{\phi k_B T}{d^2 \alpha_e l_p} \quad (\text{A.16})$$

Finally, according to Eqs. (2.33) and (2.34), a detailed expression for Eq. (2.44c) is also given here

$$G^H(\omega) = \frac{4(2i)^{3/4}}{15\pi} (k_B T)^{1/4} \phi \left[ \frac{4\pi\eta_s}{\ln(0.6\alpha_e^{0.6}l_p/d)} \right]^{3/4} \cdot \frac{l_p^{5/4}\omega^{3/4}}{d^2} + i\omega\eta_s \quad (A.17)$$

The definitions of all above parameters are the same as in the main text of Chapter 2.

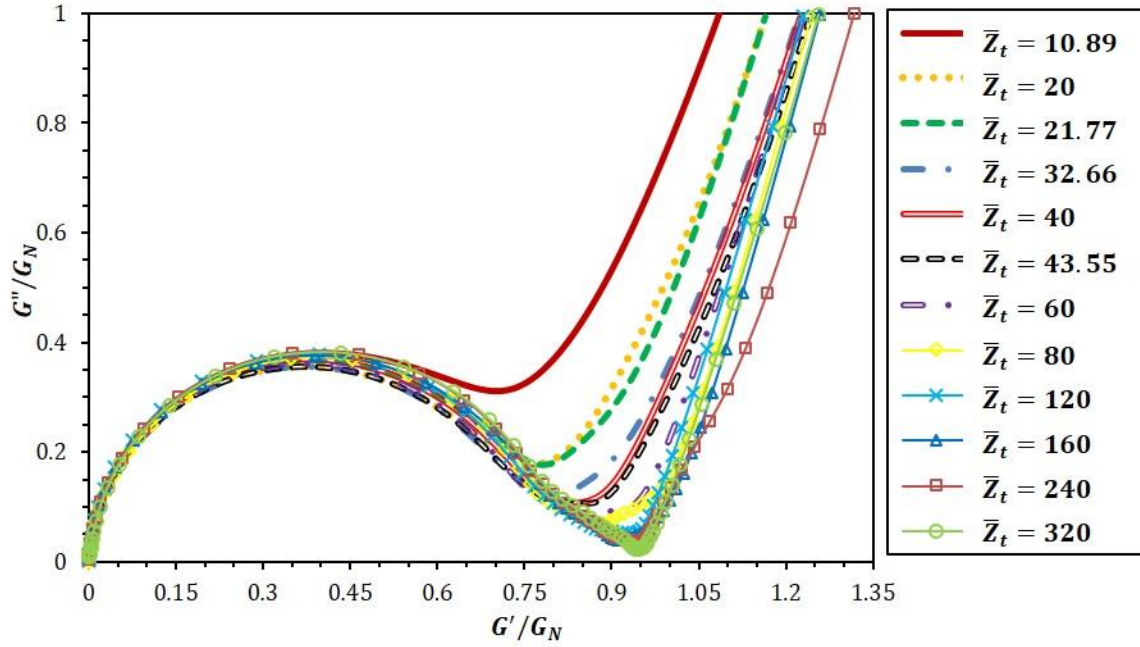


Figure A.8 Family of normalized Cole-Cole plots for different values of  $\bar{Z}_t$  with standard values of other parameters.

## Appendix B: Data Fitting Procedure and Sensitivity Study

### I. Detailed Data Fitting Procedure

The data fitting flowchart (Fig. B.1) as well as equations used to update the parameters ( $G_N, \varsigma, \bar{\tau}_{rep}, \bar{Z}, l_p$ ) from one iteration to the next are given in this Appendix.

#### 1. $l_p$

According to Eq. (3.10),  $l_p$  relates to the high-frequency rheological behavior of WLM solutions through its scaling effect on both the magnitudes of  $G'(\omega)$  &  $G''(\omega)$  and the ‘‘upturn’’ frequency ( $\omega_{min}$ ), i.e.:  $G'(\omega) \& G''(\omega) \sim l_p^{1.25}$  and  $\omega_{min} \sim \tau_p^{-1} \sim l_p^{-3}$ . The former scaling implies that if the fitted high-frequency modulus is higher than the experimental one (which means that the average deviation for region 3 and 4 in Eq. (3.15) is positive), then one needs to reduce  $l_p$ . The latter scaling implies that if the fitted upturn frequency is higher than the experimental value, one needs to increase  $l_p$ . From these scaling rules given above, we specify the following two ways, one ‘‘regional’’ (i.e., tuning specific micellar parameters based on the average deviations over a particular frequency region in Fig. 3.7) and the other ‘‘local,’’ (i.e., tuning micellar parameters based on the difference between experimental and simulation results for specific frequencies in Fig. 3.3) to update  $l_p$  at iteration  $k$ :

$$l_p^{k+1} = l_p^k \exp(-0.8\varepsilon_{avg}^k), \quad \begin{cases} \text{If } N_4 \neq 0, & \varepsilon_{avg}^k = (\varepsilon_3^k + \varepsilon_4^k)/2 \\ \text{Otherwise,} & \varepsilon_{avg}^k = \varepsilon_3^k \end{cases} \quad (B.1)$$

$$l_p^{k+1} = l_p^k \sqrt[3]{\omega_{min}^{k,fit} / \omega_{min}^{exp}} \quad (B.2)$$

As depicted in Fig. B.1, Eq. (B.1) is used in odd-numbered iteration steps, and Eq. (B.2) in even-numbered steps.

#### 2. $G_N$ and $\alpha_e$

Since  $G_N$  can be treated as the scaling factor for the low frequency behavior, as shown in Eq. (3.14c), it can therefore be updated by comparing the simulated value of  $G_{max}^{k,fit}$  with the experimental one,  $G_{max}^{exp}$ :



$$\begin{aligned}
& \text{If } \alpha_e^{k+1} > 1.5 \text{ and } \bar{Z}^{k+1} \leq \bar{Z}_c(\zeta^{k+1}), \quad \bar{Z}^{k+1} = \bar{Z}^k \frac{G_{\min}^{k,fit} G_N^{k+1}}{G_{\min}^{exp} G_N^k} \\
& \text{If } \alpha_e^{k+1} > 1.5 \text{ and } \bar{Z}^{k+1} > \bar{Z}_c(\zeta^{k+1}), \quad \bar{Z}^{k+1} = \bar{Z}^k \left( \frac{G_{\min}^{k,fit} G_N^{k+1}}{G_{\min}^{exp} G_N^k} \right)^{4/3} \\
& \text{If } \alpha_e^{k+1} < 1.5, \quad \bar{Z}^{k+1} = \bar{Z}^k \left( \frac{G_{\min}^{k,fit} G_N^{k+1}}{G_{\min}^{exp} G_N^k} \right)^5
\end{aligned} \tag{B.4}$$

Instead of using the ratio of simulated to experimental modulus at the specific frequency where  $G''$  is minimum, the overall fit in the transition 1 region (See Fig. 3.7) can also be used to modify  $\bar{Z}$ . To do this, we simply replace  $G_{\min}^{k,fit}/G_{\min}^{exp}$  with  $\exp(\varepsilon_2^k)$  in the above equation, which yields:

$$\begin{aligned}
& \text{If } \alpha_e^{k+1} > 1.5 \text{ and } \bar{Z}^{k+1} \leq \bar{Z}_c(\zeta^{k+1}), \quad \bar{Z}^{k+1} = \bar{Z}^k \exp(\varepsilon_2^k) \frac{G_N^{k+1}}{G_N^k} \\
& \text{If } \alpha_e^{k+1} > 1.5 \text{ and } \bar{Z}^{k+1} > \bar{Z}_c(\zeta^{k+1}), \quad \bar{Z}^{k+1} = \bar{Z}^k \exp\left(\frac{4}{3} \varepsilon_2^k\right) \left( \frac{G_N^{k+1}}{G_N^k} \right)^{4/3} \\
& \text{If } \alpha_e^{k+1} < 1.5, \quad \bar{Z}^{k+1} = \bar{Z}^k \exp\left(\frac{4}{3} \varepsilon_2^k\right) \left( \frac{G_N^{k+1}}{G_N^k} \right)^5
\end{aligned} \tag{B.5}$$

Equation (B.4) and (B.5) is used in even- and odd- numbered iteration steps, respectively, according to Fig. B.1. According to Fig. 3.8, with known  $l_p, \alpha_e$  and  $d, \bar{\tau}_{rep}$  is related to  $\bar{Z}$  through  $\langle L \rangle$  and  $\langle L_t \rangle$ . Thus, once  $\bar{Z}$  is updated,  $\langle L \rangle^{k+1}, \langle L_t \rangle^{k+1}, \bar{\tau}_{rep}^{k+1}$  can be calculated from Eqs. (3.2), (3.7), (3.8), (3.11).

#### 4. $\zeta$

According to Eq. (3.14a), corrections of  $\zeta$  can be made by  $\varepsilon_1^k$  or  $\omega_{\max}^{k,fit}/\omega_{\max}^{exp}$  with known  $\alpha_e^{k+1}$  and  $\bar{\tau}_{rep}^{k+1}$ :

$$\zeta^{k+1} = \zeta^k \left[ \frac{\omega_{\max}^{k,fit} \bar{\tau}_{rep}^k}{\omega_{\max}^{exp} \bar{\tau}_{rep}^{k+1}} \left( \frac{\alpha_e^{k+1}}{\alpha_e^k} \right)^3 \right]^{3/2} \tag{B.6}$$

Again, if we wish to update  $\zeta$  using fitting deviation over a range of frequencies, we can replace  $\omega_{\max}^{k,fit}/\omega_{\max}^{exp}$  with  $\exp(2/3\varepsilon_1^k)$ , giving:

$$\zeta^{k+1} = \zeta^k \exp(\varepsilon_1^k) \left[ \frac{\bar{\tau}_{rep}^k}{\bar{\tau}_{rep}^{k+1}} \left( \frac{\alpha_e^{k+1}}{\alpha_e^k} \right)^3 \right]^{3/2} \tag{B.7}$$

Equation (B.6) is used in even-numbered iterations and (B.7) in odd-numbered ones.



## 5. Limits of parameter modification

To avoid instability during the iteration, we limit the extent to which parameters ( $l_p, \bar{\tau}_{rep}, \zeta$ ) can change in a single iteration. The upper and lower bound for modifications are given in Eq. (B.8). As an example, the evolution of the allowed modification range for  $l_p$  is illustrated below:

$$l_p^{k,up} = l_p^k \exp(0.8|\varepsilon_{avg}^k|), \quad l_p^{k,low} = l_p^k \exp(-0.8|\varepsilon_{avg}^k|) \quad (B.8a)$$

$$\bar{\tau}_{rep}^{k,up} = \bar{\tau}_{rep}^k \exp\left(\frac{2}{3}|\varepsilon_1^k|\right), \quad \bar{\tau}_{rep}^{k,low} = \bar{\tau}_{rep}^k \exp\left(-\frac{2}{3}|\varepsilon_1^k|\right) \quad (B.8b)$$

$$\begin{aligned} \text{If } \omega_{max}^{k,fit} > \omega_{max}^{exp}, \quad \zeta^{k,up} &= \zeta^k \left(\frac{\omega_{max}^{k,fit}}{\omega_{max}^{exp}}\right)^{3/2}, \quad \zeta^{k,low} = \zeta^k \left(\frac{\omega_{max}^{k,fit}}{\omega_{max}^{exp}}\right)^{-3/2} \\ \text{Otherwise, } \zeta^{k,up} &= \zeta^k \left(\frac{\omega_{max}^{exp}}{\omega_{max}^{k,fit}}\right)^{3/2}, \quad \zeta^{k,low} = \zeta^k \left(\frac{\omega_{max}^{exp}}{\omega_{max}^{k,fit}}\right)^{-3/2} \end{aligned} \quad (B.8c)$$

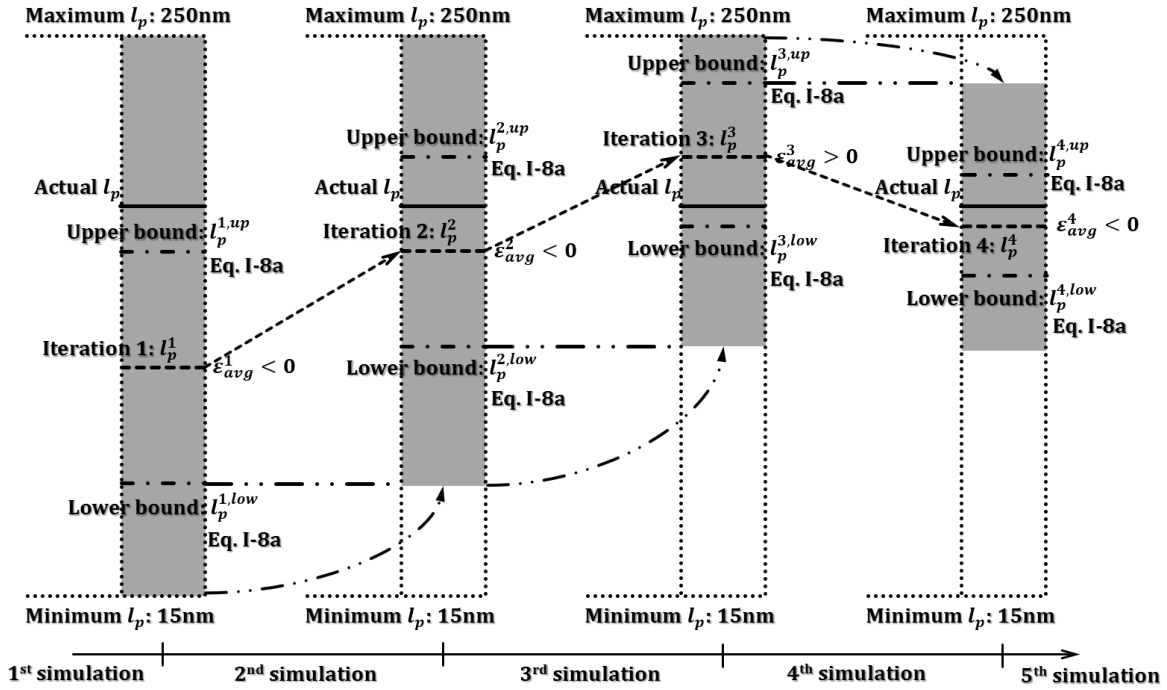


Figure B.2 Evolution of the allowed modification range for  $l_p$  represented by gray regions.

## II. Sensitivity Studies for Micelle Parameters

The estimates of parameters and associated fitting curves for sensitivity studies to parameters  $d, G_N, \zeta, \langle L \rangle, \alpha_e, l_e$  are shown in Tables B.1 to B.6 and Figs. B.3 to B.8 below:

Table B.1 Estimated parameters from best fits in Fig. B.3 with different imposed values of  $d$ .

Parameters	$d = 3 \text{ nm}$	$d = 3.5 \text{ nm}$	$d = 4 \text{ nm}$	$d = 4.5 \text{ nm}$
$G_N$ (Pa)	108	104	115	108
$\zeta$	0.65	0.63	1.82	1.8
$\langle L \rangle$ ( $\mu\text{m}$ )	2.2	2.03	1.59	1.36
$\alpha_e$	2.162	1.682	1.363	1.182
$l_e$ (nm)	147	164	153	156
$l_p$ (nm)	68	98	112	132

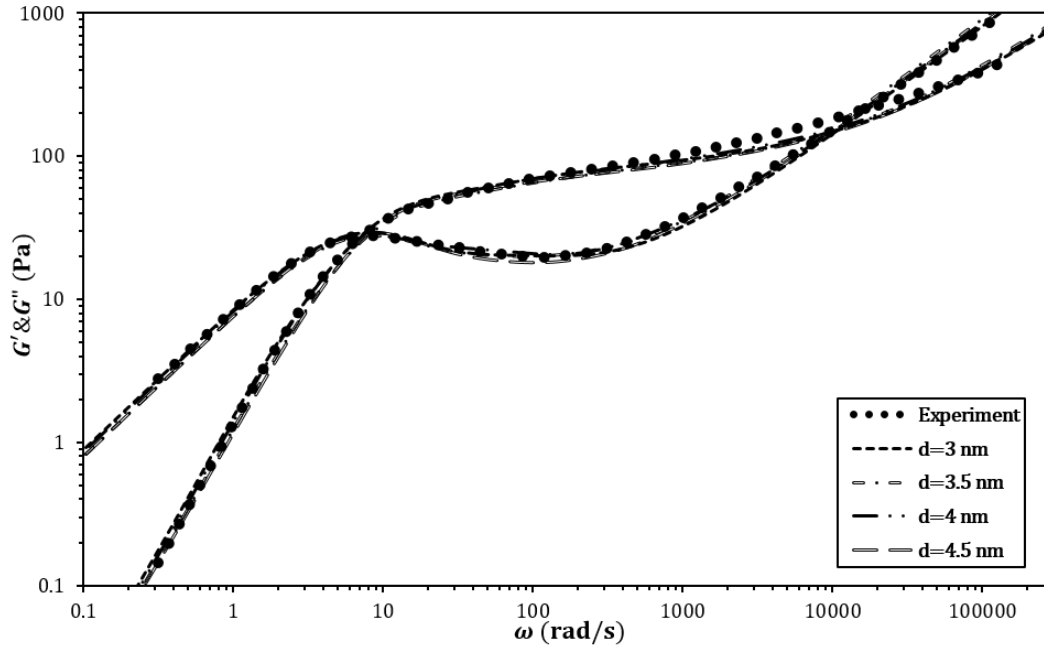


Figure B.3 Best fits for WLM solution (6.67 wt% SLE1S, 3.10 wt% NaCl with solvent viscosity  $\eta_s=0.9$  cP at 25°C) with different imposed values of  $d$  showing the inability of rheology to determine micelle diameter.

Table B.2 Parameter values obtained by best fitting rheological data, for imposed values of  $G_N$ .

Parameters	80% $G_N$	85% $G_N$	90% $G_N$	95% $G_N$	Best-fit $G_N$	105% $G_N$	110% $G_N$	115% $G_N$	120% $G_N$
$G_N$ (Pa)	92	97.75	103.5	109.25	115	120.75	126.5	132.25	138
$\zeta$	1.74	1.71	1.99	2.18	1.82	1.71	1.23	1.70	1.48
$\langle L \rangle$ ( $\mu\text{m}$ )	1.64	1.64	1.59	1.54	1.59	1.59	1.72	1.61	1.60
$\alpha_e$	1.421	1.375	1.387	1.371	1.363	1.361	1.333	1.347	1.365
$l_e$ (nm)	179	176	165	159	153	147	144	136	131
$l_p$ (nm)	126	128	119	116	112	108	108	101	96
$\epsilon_{max}$	19.1%	13%	9.4%	5.8%	4.1%	4.5%	9.6%	11.8%	16.8%

Note that by varying  $G_N$  from its unconstrained best-fit value, the maximum average fitting error ( $\epsilon_{max}$ , defined in the notes of Table 3.2) occurs in transition 1 region (See Fig. 3.7), as shown by Fig. B.4.

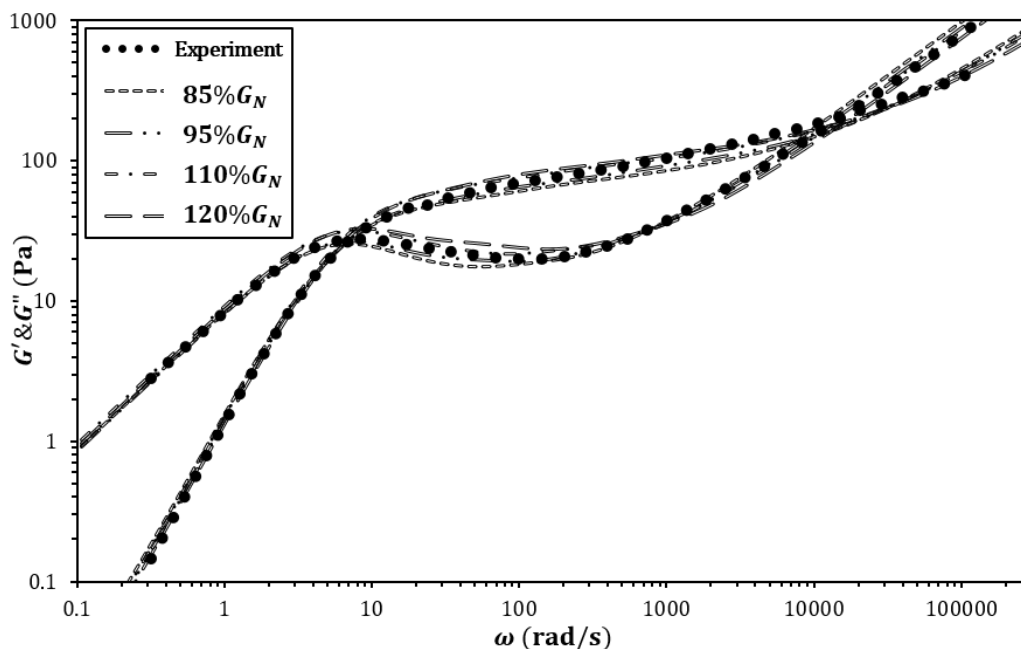


Figure B.4 Fitting results showing sensitivity of best fits to imposed values of  $G_N$  with  $d = 4 \text{ nm}$  for WLM solution (6.67 wt% SLE1S, 3.10 wt% NaCl with solvent viscosity  $\eta_s=0.9 \text{ cP}$  at  $25^\circ\text{C}$ ).

Table B.3 The same as Table B.2, except for imposed values of  $\zeta$ .

Parameters	20% $\zeta$	40% $\zeta$	60% $\zeta$	80% $\zeta$	Best-fit $\zeta$	120% $\zeta$	140% $\zeta$	160% $\zeta$	180% $\zeta$
$G_N$ (Pa)	86.8	91.4	97.1	112.8	115	117	119.4	118	122.1
$\zeta$	0.36	0.73	1.1	1.46	1.82	2.18	2.55	2.91	3.28
$\langle L \rangle$ ( $\mu\text{m}$ )	1.33	1.39	1.42	1.63	1.59	1.53	1.59	1.59	1.62
$\alpha_e$	1.418	1.372	1.372	1.375	1.363	1.404	1.37	1.38	1.352
$l_e$ (nm)	190	188	177	154	153	146	148	149	149
$l_p$ (nm)	134	137	129	112	112	104	108	108	108
$\varepsilon_{max}$	>100%	90%	58%	4.9%	4.1%	8.6%	25%	29.3%	36.6%

Note that for imposed values of  $\zeta$ ,  $\varepsilon_{max}$  occurs in the low frequency region, as shown by Fig. B.5.

Table B.4 The same as Table B.2, except for imposed values of  $\langle L \rangle$ .

Parameters	40% $\langle L \rangle$	55% $\langle L \rangle$	70% $\langle L \rangle$	85% $\langle L \rangle$	Best-fit $\langle L \rangle$	115% $\langle L \rangle$	130% $\langle L \rangle$	145% $\langle L \rangle$	160% $\langle L \rangle$
$G_N$ (Pa)	80	111.5	116	112	115	108	104.5	100	95.5
$\zeta$	13.03	9.42	5.95	3.17	1.82	1.04	0.60	0.43	0.28
$\langle L \rangle$ ( $\mu\text{m}$ )	0.636	0.875	1.11	1.35	1.59	1.83	2.07	2.31	2.54
$\alpha_e$	1.626	1.396	1.413	1.391	1.363	1.402	1.378	1.39	1.391
$l_e$ (nm)	174	155	147	153	153	157	164	171	178
$l_p$ (nm)	107	111	104	110	112	112	119	123	128
$\varepsilon_{max}$	32.6%	26.3%	9.8%	6.7%	4.1%	6.4%	7.8%	11.4%	15.8%

Note that for imposed values of  $\langle L \rangle$ ,  $\varepsilon_{max}$  occurs in low frequency and transition 1 region, as shown by Fig. B.6.

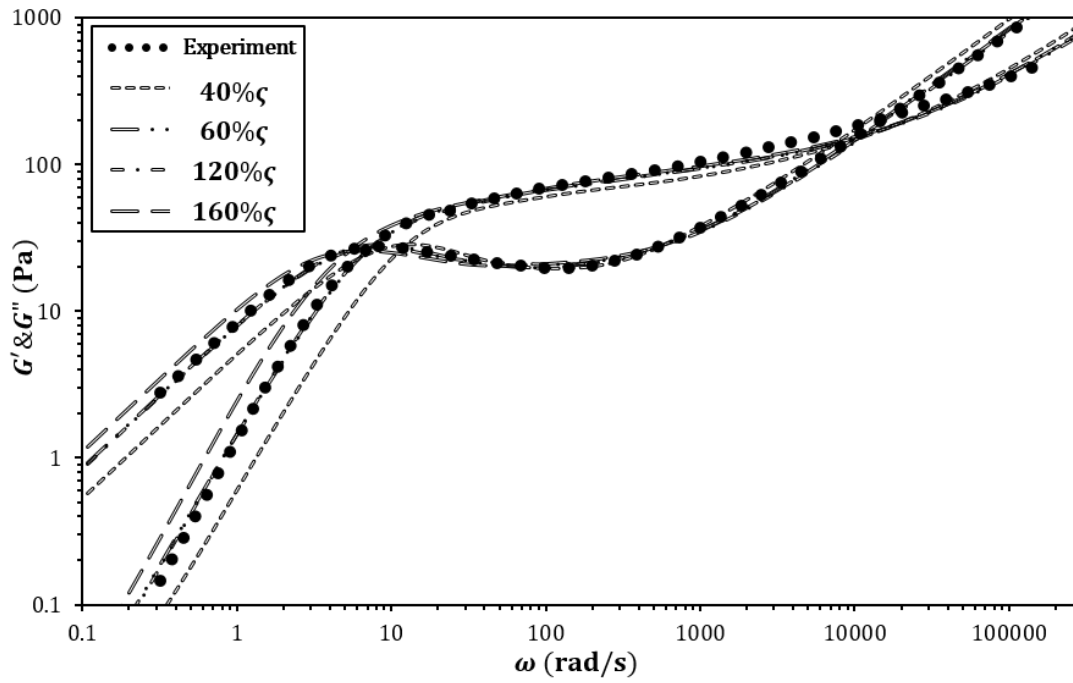


Figure B.5 The same as Fig. B.4, except that variation is made in  $\zeta$ .

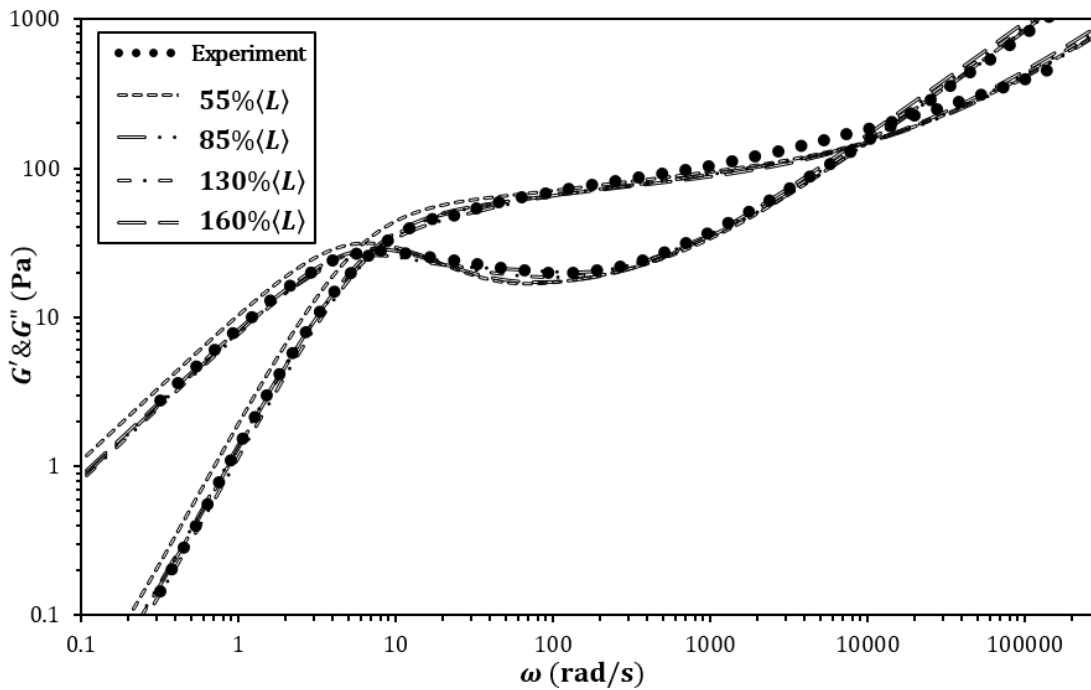


Figure B.6 The same as Fig. B.4, except that variation is made in  $\langle L \rangle$ .

Table B.5 The same as Table B.2, except for imposed values of  $\alpha_e$ .

Parameters	90% $\alpha_e$	92.5% $\alpha_e$	95% $\alpha_e$	97.5% $\alpha_e$	Best-fit $\alpha_e$	102.5% $\alpha_e$	105% $\alpha_e$	107.5% $\alpha_e$	110% $\alpha_e$
$G_N$ (Pa)	163.5	145	135	127	115	115.5	110.5	106.5	102
$\zeta$	1.11	2.47	2.49	1.24	1.82	1.94	1.9	2.08	2.24
$\langle L \rangle$ ( $\mu\text{m}$ )	1.75	1.57	1.62	1.7	1.59	1.58	1.59	1.58	1.57
$\alpha_e$	1.227	1.261	1.295	1.329	1.363	1.397	1.431	1.465	1.499
$l_e$ (nm)	123	130	140	144	153	149	150	152	154
$l_p$ (nm)	100	103	108	108	112	107	105	104	103
$\varepsilon_{max}$	43.9%	40.7%	38.4%	9.8%	4.1%	7.3%	9.7%	12.1%	15%

Note that for imposed values of  $\alpha_e$ , there is no specific frequency region where  $\varepsilon_{max}$  always occurs, as shown by Fig. B.7.

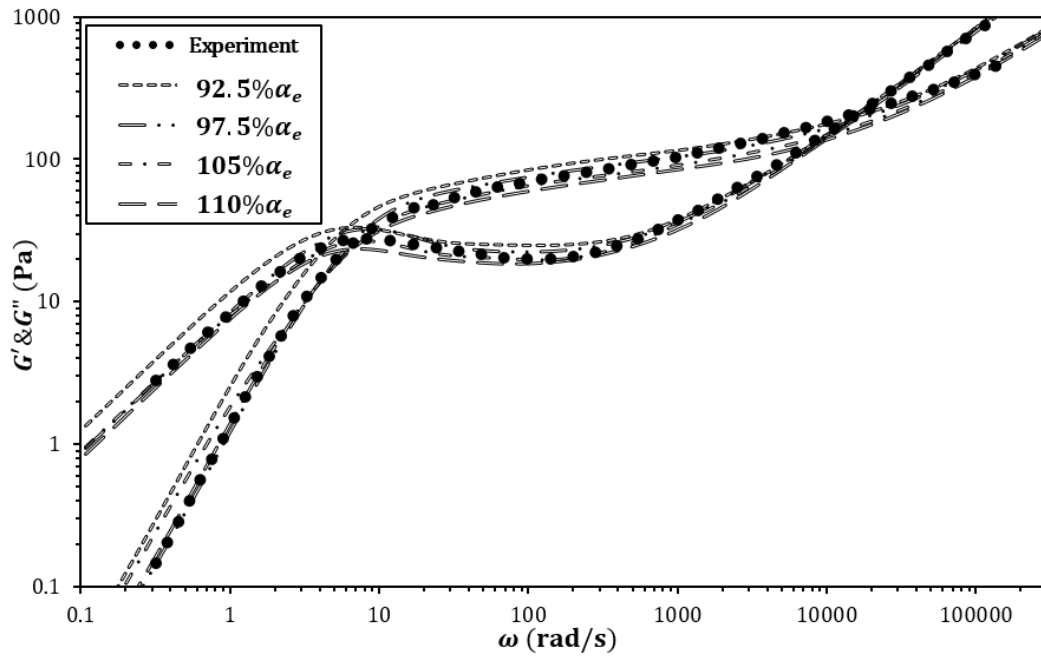


Figure B.7 The same as Fig. B.4, except that variation is made in  $\alpha_e$ .

Table B.6 The same as Table B.2, except for imposed values of  $l_e$ .

Parameters	70% $l_e$	80% $l_e$	90% $l_e$	Best-fit $l_e$	110% $l_e$	120% $l_e$	130% $l_e$	140% $l_e$	150% $l_e$
$G_N$ (Pa)	180	150	132	115	107.5	98.5	90	82	75.5
$\zeta$	0.63	2.09	1.51	1.82	2.11	1.86	2.16	2.1	2.04
$\langle L \rangle$ ( $\mu\text{m}$ )	2	1.81	1.64	1.59	1.45	1.49	1.4	1.27	1.17
$\alpha_e$	1.342	1.36	1.343	1.363	1.325	1.319	1.32	1.331	1.349
$l_e$ (nm)	106	122	137	153	167	182	198	213	228
$l_p$ (nm)	79	90	102	112	126	138	150	160	169
$\varepsilon_{max}$	48.1%	23.6%	12.1%	4.1%	6.4%	9.9%	15.1%	18.2%	21%

Note that for imposed values of  $l_e$ , there is no specific frequency region where  $\varepsilon_{max}$  always occurs, as shown by Fig. B.8.

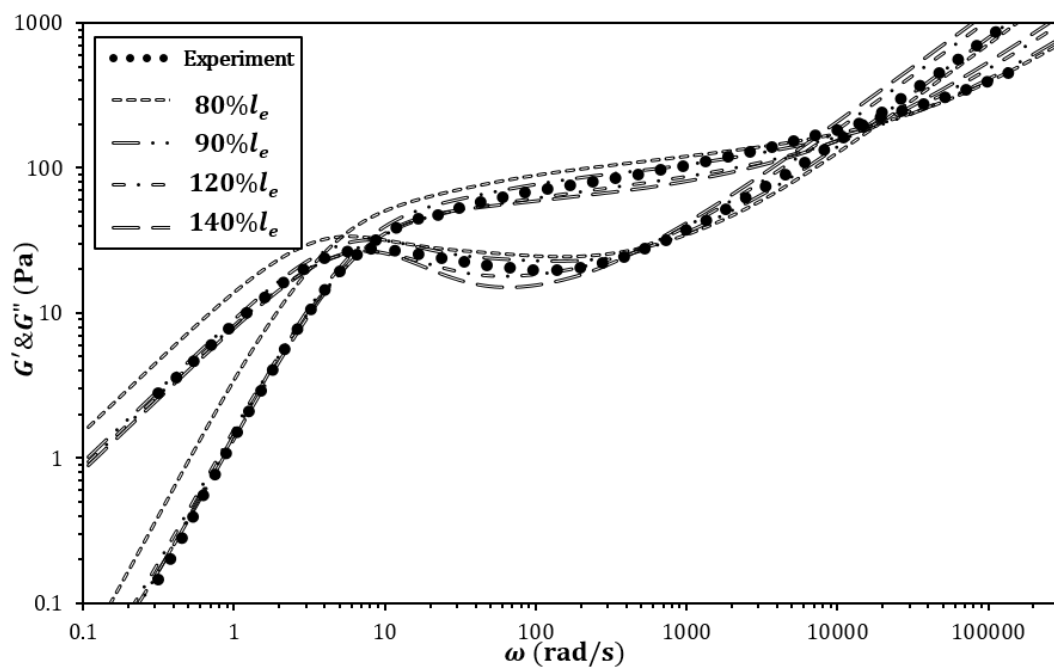


Figure B.8 The same as Fig. B.4, except that variation is made in  $l_e$ .

## Appendix C: DPD parameters, Effect of Individual PRMs, Scission Enthalpy and Entropy

### I. DPD Forcefield Parameters and Molecular Mapping

Parameters were derived using the revised Groot and Warren-equation of state (rGW-EO) [Español and Warren (1995); Groot and Warren (1997); Liyana-arachchi *et al.* (2015)] and listed in the Ph.D. thesis of Tang (2015). The revised equation of state for a single-bead DPD fluid is as:

$$P_{rGW}(\rho, T) = \rho k_B T + [f_{B_2}(\rho)B_2(a_{ii}) + f_a(\rho)a_{ii}]\rho^2 \quad (C.1)$$

where  $P$  is the pressure measured in Monte Carlo simulations, parameter  $a_{ii}$  is a positive number (in units of energy) that governs the strength of the repulsive interaction between DPD particles, and  $\rho$  is the particle number density given as the number of DPD particles in a unit volume ( $r_{cut}^3$ ).  $r_{cut} = \sqrt[3]{v_{ref}\rho_{ref}} = 7.66\text{\AA}$  at reference molecular volume  $v_{ref} = 90.0\text{\AA}^3$  (which is the volume of three water molecules at ambient conditions), and reference number density  $\rho_{ref} = 5$ .  $T$  is the absolute temperature,  $k_B$  is Boltzmann's constant, and  $k_B T$  is set to unity in dimensionless DPD units.  $B_2(a_{ii})$  is a fifth-order polynomial for  $a_{ii}$ , namely  $B_2(a_{ii}) = 1.705 \times 10^{-8}a_{ii}^5 - 2.585 \times 10^{-8}a_{ii}^4 + 1.566 \times 10^{-4}a_{ii}^3 - 4.912 \times 10^{-3}a_{ii}^2 + 9.755 \times 10^{-2}a_{ii}$ . The two density-dependent ‘‘switching’’ functions,  $f_{B_2}(\rho)$  and  $f_a(\rho)$  are solved using two empirical fittings as shown below:

$$f_{B_2}(\rho) = \frac{1}{1 + \rho^3}, \quad f_a(\rho) = \frac{c_1 \rho^2}{1 + c_2 \rho^3} \quad (C.2)$$


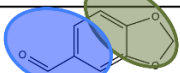

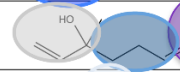

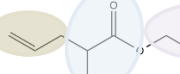
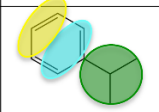
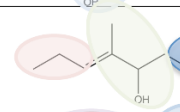

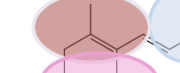
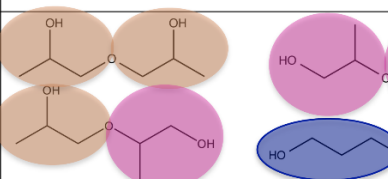
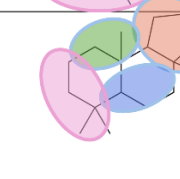
Here  $c_1 = 0.0802$ , and  $c_2 = 0.7787$ . Thus, from the Monte Carlo simulations that give the pressure, the pure-component values of  $a_{ii}$  are obtained.

The cross-component terms  $a_{ij}$  are obtained from the interaction parameters  $\chi$ , which can be expressed as

$$\chi = \frac{v_{ref}}{2RT} \left( \frac{\Delta G_{i,j}(T)}{v_i} + \frac{\Delta G_{j,i}(T)}{v_j} \right) \quad (C.3)$$

where  $\Delta G_{i,j}$  is the transfer free energy change for transferring an  $i$ -type bead from its pure phase into a pure phase of  $j$ -type bead at absolute temperature  $T$ .  $v_i$  is the molecular volume of the  $i$ -type bead. By inputting these  $\chi$  values into Eqs. (4.19) and (4.20) from Liyana-Arachchi *et al.* (2015), the values of the  $a_{ij}$  can be obtained, as tabulated in the Ph.D. thesis of Tang (2015). The revised rGW-EO method improves the accuracy of the  $a_{ij}$  parameters for a larger range of densities than in the traditional GW-EO method.

Table C.1 Coarse-grained DPD molecular mapping of surfactants and PRMs.

Common Name	Chemical Structure	Common Name	Chemical Structure
Dodecyl Sulfate (C3T)(C3)(C3)(C3)(SO4)		Heliotropin (CDO)(O2rc)	
Lauryl Ether Sulfate (C3T)(C3)(C3)(C3) -(EO)n(SO4)		Linalool (BTNL)(CCD)(CDC1)	
Cocamidopropyl Betain (C3T)(C3)(C3)(C2P)(C3tg) -(NC2)(ACE)		Allyl Amyl Glycolate (PPT)(COSR)(iPT)	
Cumene (TLB)(TLA)(iPBb)		Undecavertol (DCCT)(PPL2)(C4T)	
Isopropyl Myristate (C3T)(C4)(C4)(iPBc)(iPBb)		beta-Ionone (CDMC)(C3DM)(P3O)	
Dipropylene Glycol (DPGA)(DPGB)(DPGC)		Synambran (CDMC)(CTMC) (CrDM)(OCCr)	

For the case of Gaussian charge clouds, it is possible to show that the general expression for the real-space Ewald contribution is:

$$U_{ij}^{Real} = \frac{q_i q_j}{4\pi\epsilon\epsilon_0 r_{ij}} \operatorname{erf} \left[ \frac{r_{ij}}{\sqrt{2(\sigma_i^2 + \sigma_j^2)}} \right] - \frac{q_i q_j}{4\pi\epsilon\epsilon_0 r_{ij}} \operatorname{erf} \left[ \frac{r_{ij}}{\sqrt{2}\sigma^{Ewald}} \right] \quad (C.4)$$

where  $\sigma_i$  represents the standard deviation for the Gaussian charge cloud  $i$  and  $\sigma^{Ewald}$  represents the standard deviation for the Ewald Gaussian smearing parameter and all other terms are as expected. As the standard deviations of the charge clouds approach zero, the common real-space Ewald term for point charges is recovered. In the restricted case where all charge clouds are



given the same standard deviation, it is possible to choose the Ewald smearing parameter such that the real-space term disappears:

$$\sigma_i = \sigma_j = \frac{\sigma^{Ewald}}{\sqrt{2}} \quad \Rightarrow \quad U_{ij}^{Real} = 0$$

In this case, it is possible to use standard Ewald solvers to calculate electrostatic energies and forces for Gaussian charge clouds. It is only necessary to tune the smearing parameter based on the common charge cloud standard deviation and only calculate the Fourier space contribution along with the common self-interaction corrections.

## II. Additional PRMs and Their Effects on Viscosity

Detailed information is listed in Table C.2 regarding the 15 added PRMs considered in Fig. 4.10 in the main text of Chapter 4. Figure 4.10 plots the zero-shear viscosity  $\eta_0$  of BW-1EO (containing ACCORD) vs.  $\log P_{OW}$  for these 15 added PRMS. In this Supporting Information we also present data for BW-1EO containing only one each of 25 single PRMs (i.e., with no ACCORD). The results for these 25 PRMs in Fig. C.1 are qualitatively similar to those in Figure 10, where ACCORD is present. Details regarding the 25 PRMs are given in Table C.3.

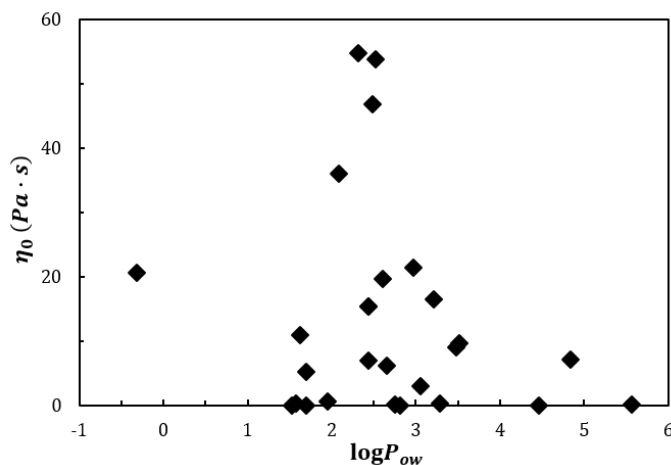


Figure C.1 Viscosities of 8.0 wt. % BW-1EO in the absence of ACCORD at 1.0 wt. % NaCl on addition of each of 25 PRMs (from Table C.3) at 15 mM plotted against  $\log P_{OW}$ , of the PRM.

Table C.2 15 PRMs added separately to BW-1EO at 15 mM, resulting in zero shear viscosities  $\eta_0$  plotted in Fig. 4.10 and tabulated in Table C.3. The corresponding values of  $\log P_{OW}$ , the molecular structures, and resulting  $\eta_0$  (in Pa·s) are tabulated. Some data, if not available at 15 mM, are computed from the best linear or polynomial fit of the viscosities of BW-1EO vs. PRMs at different concentrations.

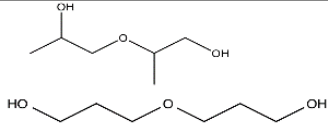
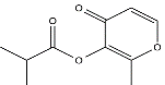
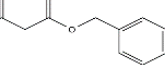
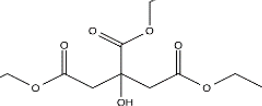
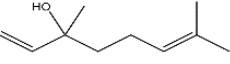
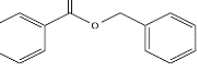
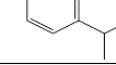
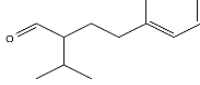
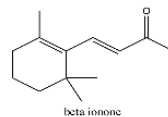
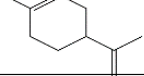
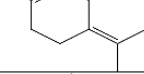
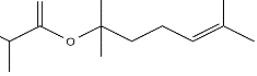
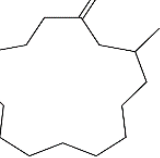
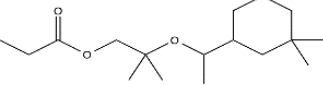
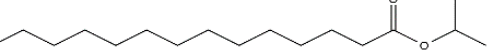
Name of PRMs	LogP <sub>ow</sub>	Structures	Viscosity
No PRM			11.06
Dipropylene Glycol	-0.61		8.72
Maltly isobutyrate	1.16		6.44
Benzyl acetoacetate	1.43		7.99
Triethyl citrate	1.73		2.33
Linalool	2.44		11.41
Benzyl benzoate	3.29		15.87
Cumene	3.30		14.95
Florhydral	3.59		12.20
beta-Ionone	4.02		11.04
d-Limonene	4.38		10.62
Terpinolene	4.71		11.84
Linalyl isobutyrate	4.82		2.22
Muscone	5.48		5.86
Helvetolide	5.56		1.43
Isopropyl myristate	6.44		1.41

Table C.3 Names of 25 PRMs, viscosities  $\eta_0$  (in Pa · s) upon addition of each of the 25 PRMs at 15 mM to BW-1EO in the absence of ACCORD at 1.0 wt. % NaCl, and the corresponding  $\log P_{ow}$ .

Common names of Fragrances	Viscosity	$\log P_{ow}$
Maltol	20.59	-0.31
p-Anisaldehyde	0.01	1.53
p-Hydroxy phenyl butanone	0.28	1.58
Acetophenone	10.88	1.63
Benzyl acetate	5.19	1.70
trans-Geraniol	0.56	1.95
Methyl salicylate	36.09	2.08
Fenchyl alcohol	54.72	2.32
Benzyl-tert-butanol	15.37	2.44
Linalool	6.93	2.44
Citronellol	46.78	2.49
p-Cresyl methyl ether	53.73	2.52
Ethyl methylphenylglycidate	19.68	2.60
Citronellyl nitrile	6.19	2.65
Caprylic aldehyde	0.12	2.75
Allyl amyl glycolate	0.01	2.81
Methyl beta-naphthyl ketone	21.34	2.97
Isopentyl butyrate	2.93	3.05
2-Methoxy-naphthalene	16.42	3.21
Hivernal	0.23	3.29
Alpha-terpinyl acetate	9.01	3.48
Pomarose	9.67	3.51
Alpha-pinene	0.04	4.46
Lauronitrile	7.11	4.84
Helvetolide	0.16	5.56

## Appendix D: Simulation Procedure for Unentangled Micelles and Branching-associated Kinetics

### I. Simulation Procedure.

As we discussed briefly in the main text of Chapter 5, the specific types of relaxation dynamics a micelle would go through are strongly affected by its length. According to Table 5.1, due to the exponential length distribution, micelles in a sufficiently large ensemble can be classified into three subpopulations, namely, unentangled micelle rods ( $L_i \leq l_p$ ), unentangled short WLMs ( $l_p < L_i < l_e$ ), and entangled long WLMs ( $L_i \geq l_e$ ). Since the former two groups of micelles relax quickly through rotary, Rouse, and bending motions, whose contributions are only significant at high frequencies, to simulate these dynamics require lengthy and costly computational process, which can hardly be scaled up to account for the fact that the overall relaxation behavior is dominated by the much slower reptation of those long entangled WLMs. Therefore, the dynamics of these relatively short micelles are treated in an analytic form (See Eq. (5.1), Eq. (D.1) and (D.2)) and added directly to the predicted  $G'$  and  $G''$  curves.

$$\begin{cases} G'(\omega) = \sum_i G_i \sum_{p=1}^{N_{K,i}} \frac{(\omega\tau_{R,i}/2p^2)^2}{1 + (\omega\tau_{R,i}/2p^2)^2} \\ G''(\omega) = \sum_i G_i \sum_{p=1}^{N_{K,i}} \frac{2(\omega\tau_{R,i}/2p^2)}{1 + (\omega\tau_{R,i}/2p^2)^2} \end{cases}, \quad \tau_{R,i} = \frac{4\eta_s L_i^2 l_p}{3\pi k_B T \ln(L_i/d)}, \quad \text{for } l_p < L_i < l_e \quad (D.1)$$

$$G^*(\omega) = \frac{\rho}{15} \frac{2^{3/4} k_B T}{l_p} (i\omega\tau_p)^{3/4} + i\omega\eta_s, \quad \rho = \frac{4\phi}{\pi d^2}, \quad \tau_p = \begin{cases} \frac{\zeta_{\perp} L_i^4}{k_B T l_p}, & \text{for } L_i < l_p \\ \frac{\zeta_{\perp} l_p^3}{k_B T}, & \text{for } L_i \geq l_p \end{cases} \quad (D.2)$$

In the above equations,  $\eta_s$  is the solvent viscosity,  $\rho$  is the micelle contour length per unit volume,  $\phi$  is the surfactant volume fraction, and  $\zeta_{\perp}$  is the perpendicular drag coefficient for bending motions. The definition of other parameters can be found in the main text of Chapter 5.

While for the partially unentangled WLM system, pointers are assigned to track the loss of tube segments accompanied with the intermicellar reactions so that the evolution of the pointers would be the same as that for well-entangled system. [Zou and Larson (2014); Zou *et al.*

(2015)] The only difference is that part of the ensemble containing unentangled short micelles always stays as relaxed from the beginning to the end of the simulation. No pointers are thereby associated with those micelles, and they only participate in the intermicellar reactions. Finally, the stress relaxation function  $\mu^2(t)$  (The square here takes into account for the effect of tube rearrangement.) can be calculated through summarizing unrelaxed tube segments between neighboring pointers, which is further transformed into  $G'$  and  $G''$  curves with low frequency behaviors dominated by entangled WLM subpopulations. [Zou and Larson (2014); Zou *et al.* (2015)] The above simulation scheme is illustrated in the following flow chart:

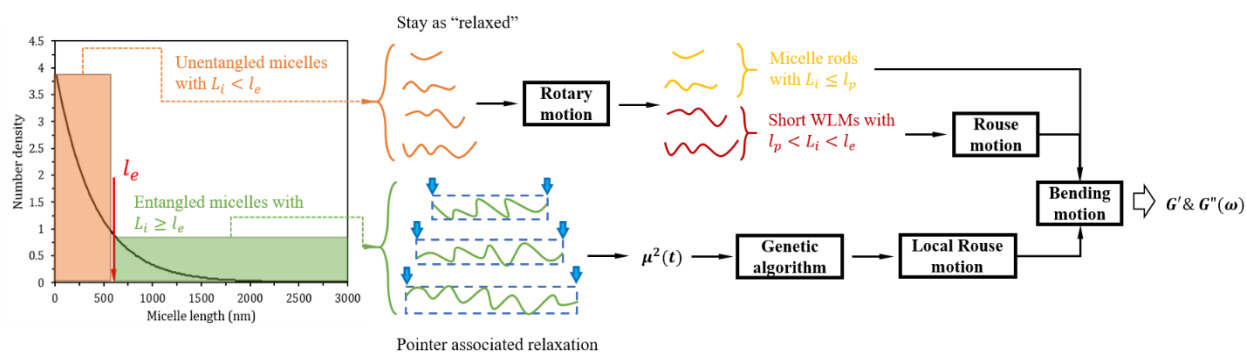


Figure D.1 The simulation flow chart for generating the linear rheological behaviors

## II. Data Merging

When combining the rheological measurements from DWS with that of mechanical rheometer, ideally, the two sets of  $G'$  and  $G''$  data are expected to overlap with at intermediate frequencies (10~100 rad/s). However, pronounced discrepancies are always found for WLM solutions with high surfactant or salt concentrations. [Zou *et al.* (2015)] It is now well-accepted that the micro-rheology would underestimate the elastic modulus due to the slip condition and compression effects on the probe particles as well as the formation of probe-micelle aggregation. [Cardiel *et al.* (2014); Rafati and Safatian (2008)] In consequence, to merge with the mechanical rheometric data at low frequencies the magnitudes of  $G'$  and  $G''$  from DWS are usually shifted by a factor whose value depends on the specific frequency range where the two data sets overlap. The following procedure is therefore used to obtain a combined  $G'$  and  $G''$  curve: As shown in Fig. D.2, mechanical rheometric data is firstly truncated giving rise to a frequency window of 0.5-100 rad/s beyond which the data is either subject to the effect of inertia or low signal-to-noise ratio. High frequency DWS data is then calibrated to allow for the best overlap with those

from mechanical rheometry at frequencies between 50 to 150 rad/s. However, if the solutions become sufficiently dilute, the above frequency range narrows and would finally disappear, which force us to rely on non-rheological methods, for example SANS, to determine local micellar length scales such as  $l_p$  while extracting the other micellar parameters from our simulation model.

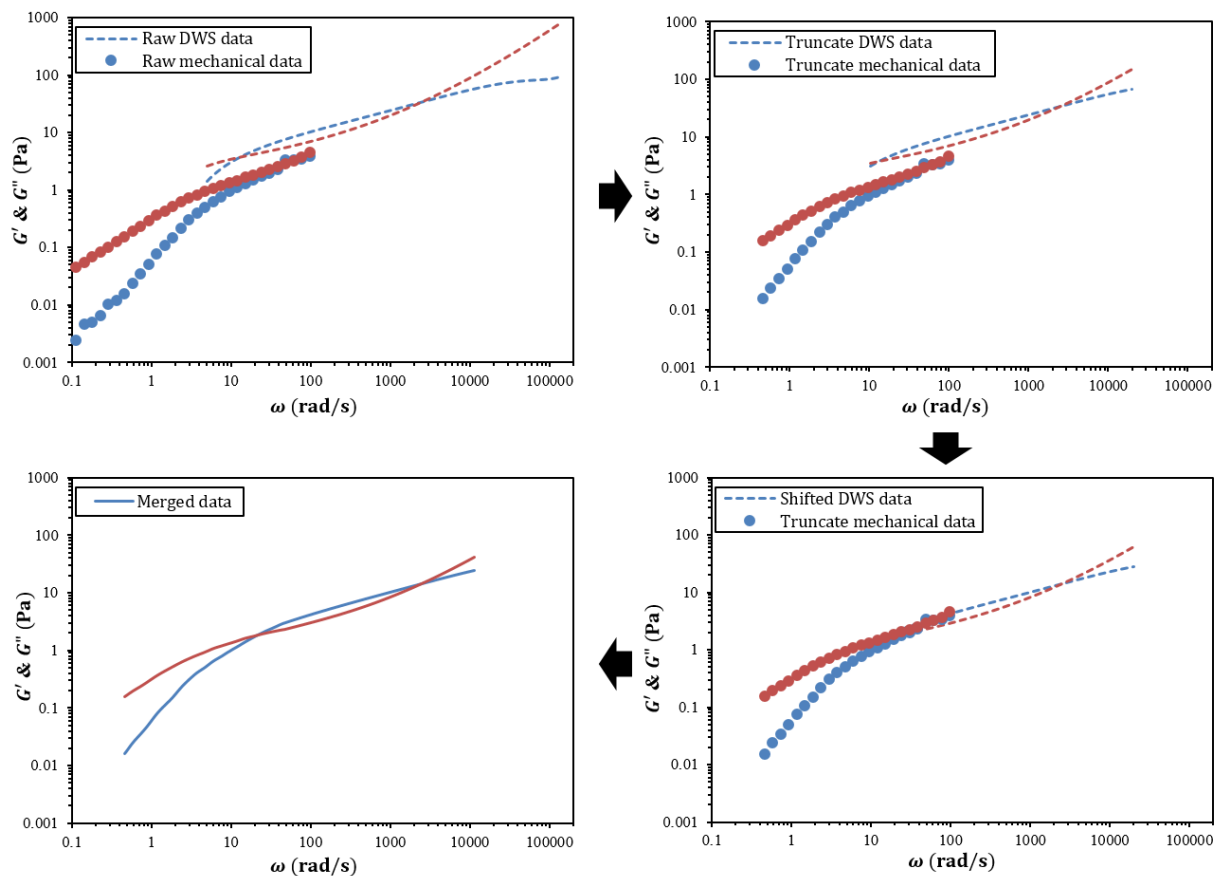


Figure D.2 A flow chart illustrating the procedure to merge the mechanical rheometrical data with those from DWS

### III. Branching-associated Kinetics

Here a thorough description on the practical pathway to unify branching-associated kinetics with living nature of micelles as well as advanced tube theories in the picture of pointer algorithm is shown. This is followed by presentation of some complementary materials mentioned in the main text of Chapter 5.

## 1. Constrained Diffusion and Micelle Architecture

Because of their self-assembling nature, branched micelles are not geometrically fixed, both the length and the number of the strands between termini (i.e., end-caps or junctions) are momentary. This structure lability for individual branched micelle can be depicted by the constrained Brownian dynamics (BD): The Brownian motion of each strand creates a current in a random direction equivalent to the reptation as strands are confined in their tubes. For the simplest 3-arm micelle stars, one needs to solve the following set of equations to determine the currents in each arm:

$$\begin{cases} \Delta x_i = \sqrt{\frac{2k_B T \Delta t}{\zeta_i}} n_i + \frac{F}{\zeta_i} \Delta t, & \zeta_i = \zeta_0 L_i \\ \sum_{i=1}^3 \Delta x_i = 0 \end{cases} \quad (D.3)$$

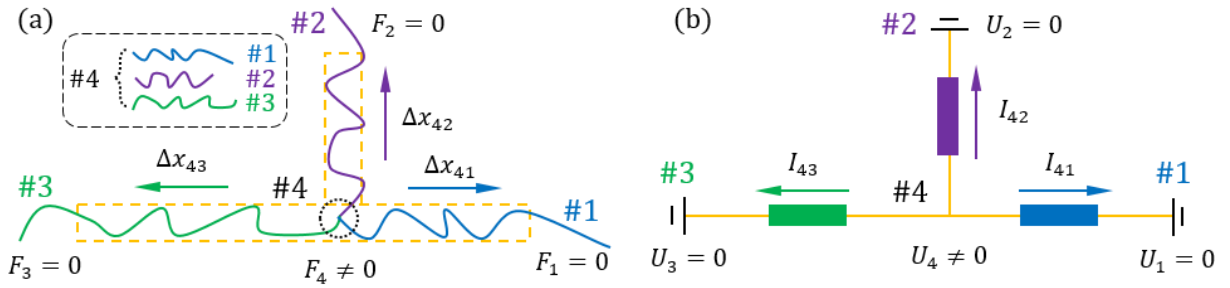


Figure D.3 (a) The 3-arm branched architecture of micelles and (b) the corresponding analogy to the Kirchhoff circuit system.

In the above, the subscript  $i$  stands for the  $i$ th arm,  $L_i$  is the length of arm  $i$ , and  $\zeta_0$  is the drag coefficient per unit length of strand. The role of non-zero constrained force  $F$  at the only junction for a 3-arm star can be understood simply as fluctuating “potential” arise from imbalances in currents of each strands if the forces were absent: When an inward current were to occur, a high potential is then produced which would be just large enough to push back against the inflow. Since the microscopic topology of termini has little effect on the overall relaxation behavior, it is sufficient to label each of them as point-like objects (with functionality  $z$ ) numerically in order ( $i = 1, 2, \dots$ ). Assuming there is no restriction on the angles with which the strands meet at a junction, any strands can be thereof denoted simply by the two labels of the termini it connected with, for example  $(i, j)$ . Such labelling results in a bidirectional linked list to represent all the connectivity relationships among individual strands contained in a micelle

cluster regardless of its complexity, named connectivity list, its use simplifies the mapping between the specific cluster configurations and the dynamic property of the above constrained diffusion. Thus, Eq. (D.3) can be rewritten in a matrix form corresponding to its labelled architecture (See Fig. D.3a) given as:

$$\begin{bmatrix} 1 & 0 & 0 & a_{41} & 0 & 0 & -a_{41} \\ 0 & 1 & 0 & 0 & a_{42} & 0 & -a_{42} \\ 0 & 0 & 1 & 0 & 0 & a_{43} & -a_{43} \\ 0 & 0 & 0 & 1 & 0 & 0 & 0 \\ 0 & 0 & 0 & 0 & 1 & 0 & 0 \\ 0 & 0 & 0 & 0 & 0 & 1 & 0 \\ -1 & -1 & -1 & 0 & 0 & 0 & 0 \end{bmatrix} \begin{bmatrix} \Delta x_{41} \\ \Delta x_{42} \\ \Delta x_{43} \\ F_1 \\ F_2 \\ F_3 \\ F_4 \end{bmatrix} = \begin{bmatrix} b_{41} \\ b_{42} \\ b_{43} \\ 0 \\ 0 \\ 0 \\ 0 \end{bmatrix} \quad (\text{D. 4})$$

where,

$$a_{ij} = \frac{\Delta t}{\zeta_{ij}}, \quad b_{ij} = \sqrt{\frac{2k_B T \Delta t}{\zeta_{ij}}} n_{ij}$$

Note that the forth to the sixth rows in the above matrices correspond to the constrained forces (i.e.,  $F_1, F_2$  and  $F_3 = 0$ ) at the free end-caps. From Eq. (D.4), the above constrained diffusion problem for a micelle cluster is very much similar to the Kirchhoff's circuit problem (See Fig. D.3b), both of which are linear systems and can be solved by the same numerical tools, for example, LU decomposition with the increase of system complexity.

## 2. Intermicellar reaction and sprouting process

However, the above constrained diffusion is not efficient to release the stress: the relaxation turns out to be rather slow since the strands located in the treelike cluster can disentangle only if one of its ends is free. Instead of waiting all branch junctions on one side of a strand to disappear, this process can be easily accelerated by intermicellar reactions, i.e., breakage and reformation of micelles, which are modelled to occur on a time scale of  $\bar{\tau}_{br}$  with equal probability per strand length for breakage and per micelle free ends for reformation. It is evident that these intermicellar reactions affect configurations of micelle clusters and hence their relaxation by constantly creating free ends, exchanging micelle pieces, and varying cluster connectivity as illustrated in Fig. D.4. Since “pointers” are used to track the boundaries between relaxed and unrelaxed portion of micelles, over time each strand in a micelle would be contaminated by pointers that are created during the breakage and reformations, and eventually all parts of all micelle clusters are relaxed.



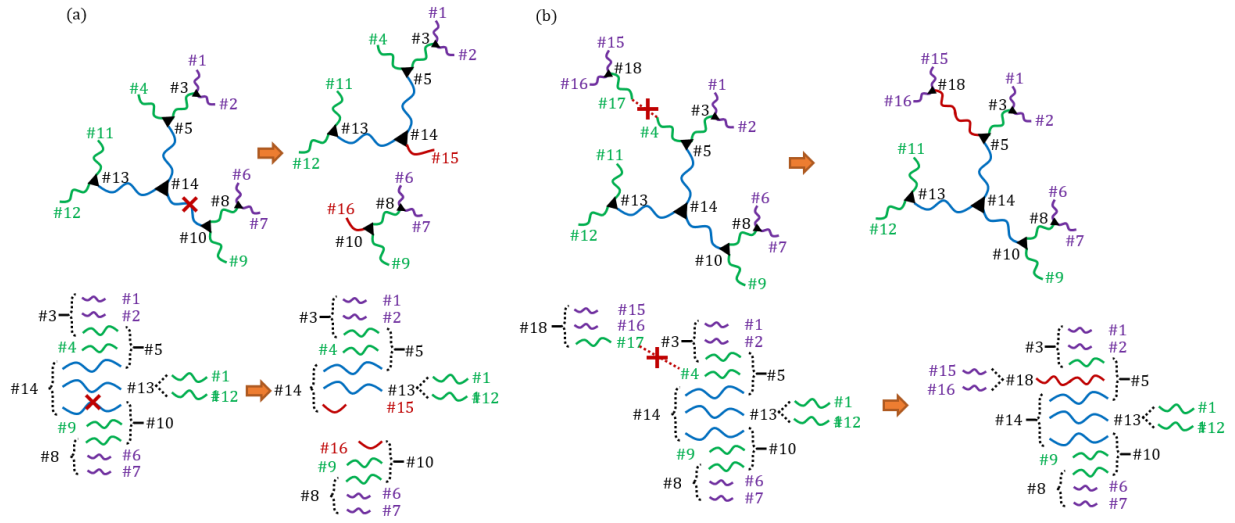


Figure D.4 The intermicellar reactions between branched clusters: (a) breakage (b) recombination.

To mimic local curvature perturbation triggered creation of new branch junctions, sprouting of a nearly infinitesimal bud (i.e.,  $l_b/l_s \approx r/l_p \ll 1$ , where  $l_s$  is the segmental length and  $r$  is the micelle radius) at an arbitrary location along a micelle strand is carried out with equal probability per strand length on the time scale  $\bar{\tau}_{bud}$ . Due to its perturbation nature, these buds survive no more than a single time step ( $\Delta t \sim 1 \mu s$ ) before smeared out by constrained diffusion. In fact, this sprouting process is the only mechanism for adding branch junctions to compensate their destruction in thermal equilibrium. Since a newly sprouted bud is free to fuse with any dangling arms through breakage and reformation, which makes us believe that such sprouting is practically indistinguishable from other branching mechanisms, and thus to include it with characteristic time  $\bar{\tau}_{bud}$  should be adequate for the investigation of relaxation behaviors among branched micelle systems.

### 3. Evolution of pointers and relaxation mechanisms

Given the involvement of all the above mechanisms, one can finally envisage the relaxation of branched micelles through the evolution of pointers. Because of the polydispersity in micelle size distribution, each stands are discretized into a sequence of basic units called “segments.” Physically, these segments do not occupy any real space, they have a length  $l_s \cong l_p$  and are interpreted as the minimal structure that attribute to the viscoelasticity of the micelle solution. Between neighboring segments in a strand, pointers are assumed to travel along the straight lines despite their microscopic details, whose effects can only be depicted by dynamics

at shorter time and length scales than tube theory where micelle topology and entanglements do not matter. As a result, these fast relaxation dynamics (i.e.,  $G^H(\omega)$  in Eq. (5.2) of the main text of Chapter 5), including Rouse and bending motions, are excluded from the simulation of pointers, but added later in an analytic form at high frequencies to avoid any unnecessary computational cost. Representing the unrelaxed tube ends, the strand portions bounded by a pair of neighboring pointers are used to calculate the stress relaxation function  $\mu(t)$  (See Eq. (5.2) in the main text of Chapter 5) for long time relaxation behaviors, given as

$$\mu(t) = \frac{1}{M} \sum_{i=1}^M \frac{1}{S_i} \left\{ \sum_{j=1}^{S_i} \sum_{k=1}^{N_j} [\xi_{k+1}(t) - \xi_k(t)] \right\} \quad (D.5)$$

where,  $N_j$ ,  $S_i$ , and  $M$  is the numbers of pointers, strands, and micelles contained in strand  $j$ , micelle  $i$ , and the simulation ensemble, respectively.  $\xi_k$  is the location of pointer  $k$  at tube coordinates, which varies according to different relaxation mechanisms. For the constrained diffusion, as illustrated in Fig. D.5, the shrinkage of a dangling arm results in a corresponding inward movement of pointers on that arm. Whereas the pointers on a growing arm or inner backbone (i.e., a strand terminated by branch junctions at both ends) are not allowed to move, since the unrelaxed portions between these pointers remain unrelaxed even if micellar material is flowing into or through the strand.

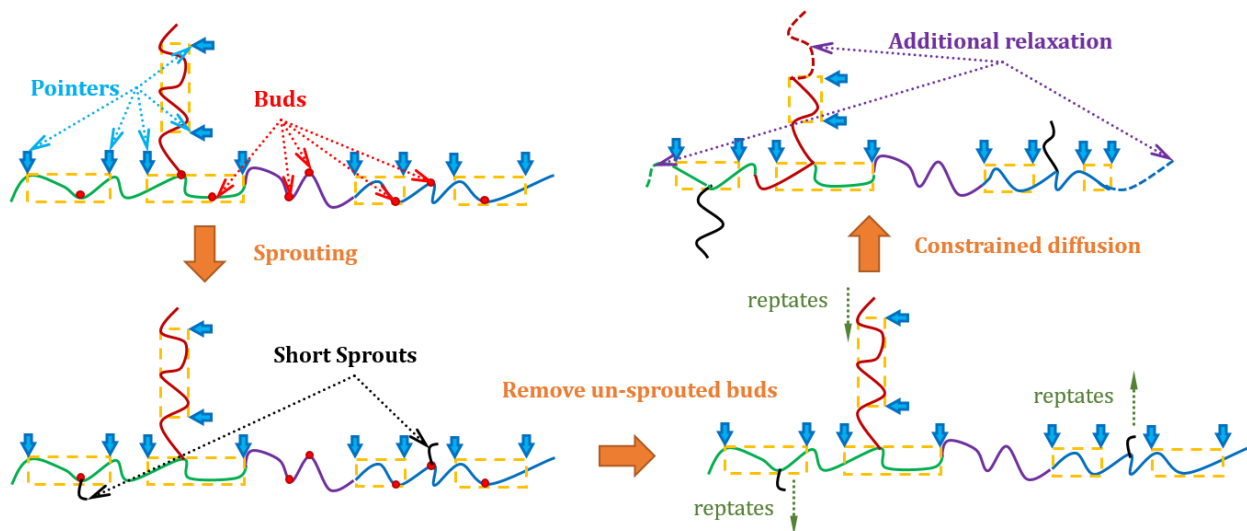


Figure D.5 The relaxation of branched micelles represented by the evolutions of pointers in the presence of sprouting and constrained diffusion.

Similar to a linear micelle, a dangling arm within a micelle cluster also undergoes end fluctuations, known as the contour length fluctuations (CLFs) in polymer physics. Thus, to account for its effects, only the nearest pointers to the free ends are moved inward. Since the new branches formed by sprouting process represent exploration of different configurations, and hence cannot increase the amount of unrelaxed segments, their further growth would actually induce relaxation due to the sacrifice made by other unrelaxed materials to feed the growth of those branches. (See Fig. D.5) In addition, each new dangling arms created by a breakage event can relax with both constrained diffusion and CLFs. Inner backbones can also be reformed by these arms, and when this occurs, the pointers on the arms are retained. Now these pointers are inside a backbone and remain stationary until the strand breaks again, which creates new free ends and makes the pointers mobile. Thus, a table is kept for each strand to record the above changes in number and positions of the pointers. Over time, the unrelaxed portions between neighboring pointers decrease. When the two pointers pass through each other, they will be removed from the table indicating the completeness of the relaxation for that portion.

## Appendix E: Brownian Dynamics Simulation for Bead-spring Chains

### I. Equations of Bead-spring Chain

In this Appendix, the dimensionless governing equation of bead motion, i.e., Eq. (6.4a) in the main text of Chapter 6, are derived in details as below:

The movement of beads  $j$  and  $j - 1$  of a bead-spring chain shown in Fig. E.1 are given by Eq. (6.3a):

$$\begin{cases} \zeta_b \dot{\mathbf{r}}_j = \zeta_b (\nabla \mathbf{v})^T \cdot \mathbf{r}_j + \mathbf{F}_j^{sp,t} + \mathbf{F}_j^R \\ \zeta_b \dot{\mathbf{r}}_{j-1} = \zeta_b (\nabla \mathbf{v})^T \cdot \mathbf{r}_{j-1} + \mathbf{F}_{j-1}^{sp,t} + \mathbf{F}_{j-1}^R \end{cases} \quad (E.1)$$

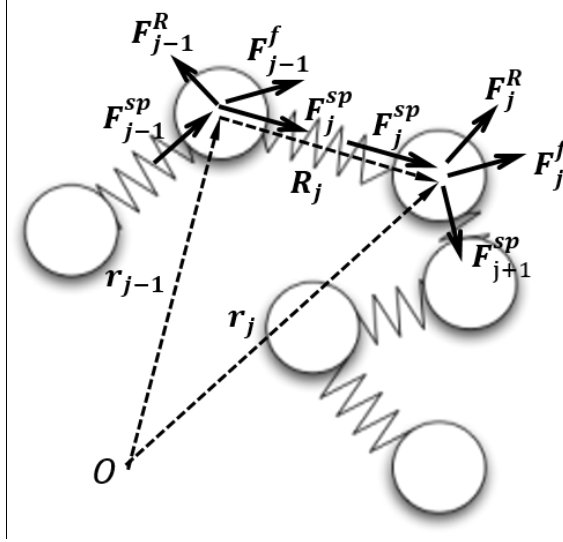


Figure E.1 Illustration of bead-spring chain and the forces exerted on beads  $j$  and  $j - 1$ . Note that  $\mathbf{F}_j^f$  is the friction force defined as  $\mathbf{F}_j^f = \zeta_b (\nabla \mathbf{v})^T \cdot \mathbf{r}_j$

From Fig. S1, we have  $\mathbf{R}_j = \mathbf{r}_j - \mathbf{r}_{j-1}$  and  $\mathbf{F}_j^{sp,t} = \mathbf{F}_{j+1}^{sp} - \mathbf{F}_j^{sp}$ ; thus

$$\begin{aligned} \zeta_b (\dot{\mathbf{r}}_j - \dot{\mathbf{r}}_{j-1}) &= \zeta_b (\nabla \mathbf{v})^T \cdot (\mathbf{r}_j - \mathbf{r}_{j-1}) + (\mathbf{F}_j^{sp,t} - \mathbf{F}_{j-1}^{sp,t}) + (\mathbf{F}_j^R - \mathbf{F}_{j-1}^R) \\ \zeta_b \dot{\mathbf{R}}_j &= \zeta_b (\nabla \mathbf{v})^T \cdot \mathbf{R}_j + (\mathbf{F}_{j+1}^{sp} + \mathbf{F}_{j-1}^{sp} - 2\mathbf{F}_j^{sp}) + (\mathbf{F}_j^R - \mathbf{F}_{j-1}^R) \end{aligned} \quad (E.2)$$

According to Eqs. (2) and (3b):

$$\mathbf{F}_j^{sp} = \frac{3k_B T}{N_{K,sp} b_K^2} \frac{\mathbf{R}_j}{1 - (|\mathbf{R}_j|/R_0)^2}, \quad R_0 = N_{K,sp} b_K, \quad N_{K,sp} = \frac{N_K}{N_{sp}}, \quad \mathbf{F}_j^R = \sqrt{\frac{6k_B T \zeta_b}{\Delta t}} \mathbf{n}_j$$

We substitute the above expressions into Eq. (E.2), yielding:

$$\zeta_b \frac{\Delta \mathbf{R}_j}{\Delta t} = \zeta_b (\nabla \mathbf{v})^T \cdot \mathbf{R}_j + \frac{3k_B T}{N_{K,sp} b_K^2} \left[ \frac{\mathbf{R}_{j+1}}{f(\mathbf{R}_{j+1})} + \frac{\mathbf{R}_{j-1}}{f(\mathbf{R}_{j-1})} - \frac{2\mathbf{R}_j}{f(\mathbf{R}_j)} \right] + \sqrt{\frac{6k_B T \zeta_b}{\Delta t}} (\mathbf{n}_j - \mathbf{n}_{j-1}) \quad (E.3)$$

where  $f(\mathbf{R}_j) = 1 - (|\mathbf{R}_j|/R_0)^2$ .

And for the polymeric stress,

$$\boldsymbol{\Sigma}^p = \nu \langle \Sigma_j^{N_{sp}} \mathbf{R}_j \mathbf{F}_j^s \rangle = \frac{3\nu k_B T}{N_{K,sp} b_K^2} \langle \Sigma_j^{N_{sp}} \mathbf{R}_j \mathbf{R}_j / f(\mathbf{R}_j) \rangle \quad (E.4)$$

Replacing  $\mathbf{R}_j$  with the corresponding dimensionless variable  $\tilde{\mathbf{R}}_j = \mathbf{R}_j / \sqrt{N_{K,sp}} b_K$ , Eqs. (E) and (E.4) can be rewritten as:

$$\begin{cases} \Delta \tilde{\mathbf{R}}_j = (\nabla \mathbf{v})^T \cdot \tilde{\mathbf{R}}_j \Delta t + \frac{3\Delta t}{\tau_{sp}} \left[ \frac{\tilde{\mathbf{R}}_{j+1}}{f(\tilde{\mathbf{R}}_{j+1})} + \frac{\tilde{\mathbf{R}}_{j-1}}{f(\tilde{\mathbf{R}}_{j-1})} - \frac{2\tilde{\mathbf{R}}_j}{f(\tilde{\mathbf{R}}_j)} \right] + \sqrt{\frac{6\Delta t}{\tau_{sp}}} (\mathbf{n}_j - \mathbf{n}_{j-1}) \\ \boldsymbol{\Sigma}^p = 3\nu k_B T \langle \Sigma_j^{N_{sp}} \tilde{\mathbf{R}}_j \tilde{\mathbf{R}}_j / f(\tilde{\mathbf{R}}_j) \rangle \end{cases} \quad (E.5)$$

where  $f(\tilde{\mathbf{R}}_j) = 1 - (|\tilde{\mathbf{R}}_j|/\tilde{R}_0)^2$ ,  $\tilde{R}_0 = \sqrt{N_{K,sp}}$ , and  $\tau_{sp} = \zeta_b N_{K,sp} b_K^2 / k_B T$ .

Since for chains in equilibrium,  $\boldsymbol{\Sigma}^p = \mathbf{0}$ , and otherwise  $\boldsymbol{\Sigma}^p = G^p (\boldsymbol{\sigma}^p - \mathbf{I})$ , we have

$$\boldsymbol{\Sigma}^p = G^p \left\{ \frac{\langle \Sigma_j^{N_s} [\tilde{\mathbf{R}}_j \tilde{\mathbf{R}}_j / f(\tilde{\mathbf{R}}_j)] \rangle}{\langle \Sigma_j^{N_s} [\tilde{\mathbf{R}}_j \tilde{\mathbf{R}}_j / f(\tilde{\mathbf{R}}_j)] \rangle_{eq}} - \mathbf{I} \right\}, \quad G^p = 3\nu k_B T \quad (E.6)$$

## II. Simulation Algorithm

Here we describe our procedure for combining our bead-spring Brownian dynamics simulation results into specific types of deformation, i.e., uniaxial extension and simple shear, in either steady deformation or creep.

Under homogeneous deformation,  $\nabla \cdot \boldsymbol{\sigma} = \mathbf{0}$ , the original upper-convective Maxwell equation for segmental dynamics (Eq. (6.5)) can be simplified as:

$$\begin{cases} \dot{\boldsymbol{\sigma}}^s = \boldsymbol{\sigma}^s \cdot \nabla \mathbf{v} + (\nabla \mathbf{v})^T \cdot \boldsymbol{\sigma}^s - (\boldsymbol{\sigma}^s - \mathbf{I}) / \tau^s \\ \dot{\tau}^s = 1 - \lambda(\tau^s - \tau_0^s), \quad \lambda = \mu \sqrt{2 \text{tr}(\mathbf{D} \cdot \mathbf{D})} \\ \boldsymbol{\Sigma}^s = G^s (\boldsymbol{\sigma}^s - \mathbf{I}), \quad \tau^s|_{t=0} = t_w \end{cases} \quad (E.7)$$

If we assume the external stress is applied along the z direction, then the detailed form of deformation rate tensor  $\mathbf{D}$  is given as: [Larson (1988)]

For uniaxial extension:

$$\mathbf{D} = \nabla \mathbf{v} = \begin{bmatrix} \dot{\varepsilon}_x & 0 & 0 \\ 0 & \dot{\varepsilon}_y & 0 \\ 0 & 0 & \dot{\varepsilon}_z \end{bmatrix} \quad (E.8a)$$

For simple shear:

$$\nabla \mathbf{v} = \begin{bmatrix} 0 & 0 & \dot{\gamma}_{xz} \\ 0 & 0 & 0 \\ 0 & 0 & 0 \end{bmatrix}, \quad \mathbf{D} = \begin{bmatrix} 0 & 0 & \dot{\gamma}_{xz}/2 \\ 0 & 0 & 0 \\ \dot{\gamma}_{xz}/2 & 0 & 0 \end{bmatrix} \quad (E.8b)$$

where  $\dot{\varepsilon}_x$ ,  $\dot{\varepsilon}_y$ , and  $\dot{\varepsilon}_z$  are the extension rates in  $x, y, z$  directions, and  $\dot{\gamma}_{xz}$  is the simple shear rate in  $xz$  plane.

The condition of incompressibility, i.e.,  $\text{tr}(\nabla \mathbf{v}) = 0$ , implies

For uniaxial extension:

$$\dot{\varepsilon}_x = \dot{\varepsilon}_y = -\dot{\varepsilon}_z/2 = \dot{\varepsilon} \quad (E.9a)$$

For simple shear:

$$\dot{\gamma}_{xz} = \dot{\gamma} \quad (E.9b)$$

Therefore, application of our simulation model to the above two types of deformations is accomplished by substituting the above expressions into Eqs. (6.4a) and (E.7). Since for both cases, the deformation in the  $y$  direction is the same as in the  $x$  direction, Eq. (E.7) can be rewritten in a scalar form with only  $x$  and  $z$  components, i.e.,

For uniaxial extension:

$$\begin{cases} \dot{\sigma}_{zz}^s = 2\dot{\varepsilon}\sigma_{zz}^s - (\sigma_{zz}^s - 1)/\tau^s \\ \dot{\sigma}_{xx}^s = -\dot{\varepsilon}\sigma_{xx}^s - (\sigma_{xx}^s - 1)/\tau^s \\ \dot{\tau}^s = 1 - \mu(\tau^s - \tau_0^s)\sqrt{3}|\dot{\varepsilon}| \end{cases} \quad (E.10a)$$

For simple shear:

$$\begin{cases} \dot{\sigma}_{xz}^s = \dot{\gamma}\sigma_{xz}^s - \sigma_{xz}^s/\tau^s \\ \dot{\sigma}_{xx}^s = -(\sigma_{xx}^s - 1)/\tau^s \\ \dot{\tau}^s = 1 - \mu(\tau^s - \tau_0^s)|\dot{\gamma}| \end{cases} \quad (E.10b)$$

Equations (S10) are now ready for numerical analysis if a constant deformation rate is imposed. For the imposition of a constant stress, a general force balance can be established as:

$$\nabla \cdot (\boldsymbol{\Sigma} + 2\eta\mathbf{D}) = \mathbf{0} \quad (E.11a)$$

For uniaxial extension:

$$\begin{aligned} \Sigma_z^{ext} &\equiv A/A_0(\Sigma_{zz} - \Sigma_{xx} + 3\eta\dot{\varepsilon}) \\ \Sigma_z^{ext} &\equiv e^{-\varepsilon}(\Sigma_{zz} - \Sigma_{xx} + 3\eta\dot{\varepsilon}) \end{aligned} \quad (E.11b)$$

For simple shear:

$$\begin{aligned}\nabla_{xz} \cdot (\boldsymbol{\Sigma} + 2\eta\mathbf{D}) &= 0 \\ \Sigma_{xz}^{ext} &\equiv \Sigma_{xz} + \eta\dot{\gamma}\end{aligned}\tag{E.11c}$$

where  $\eta$  is a small artificial viscosity ( $= 0.33\%G^p\tau_0^s$ ), which is added to ease numerical simulation, and results are insensitive to this small value as shown by Fig. E.2.  $\boldsymbol{\Sigma}$  is the overall stress with contributions from both polymeric (Eq. (E.6)) and segmental parts.

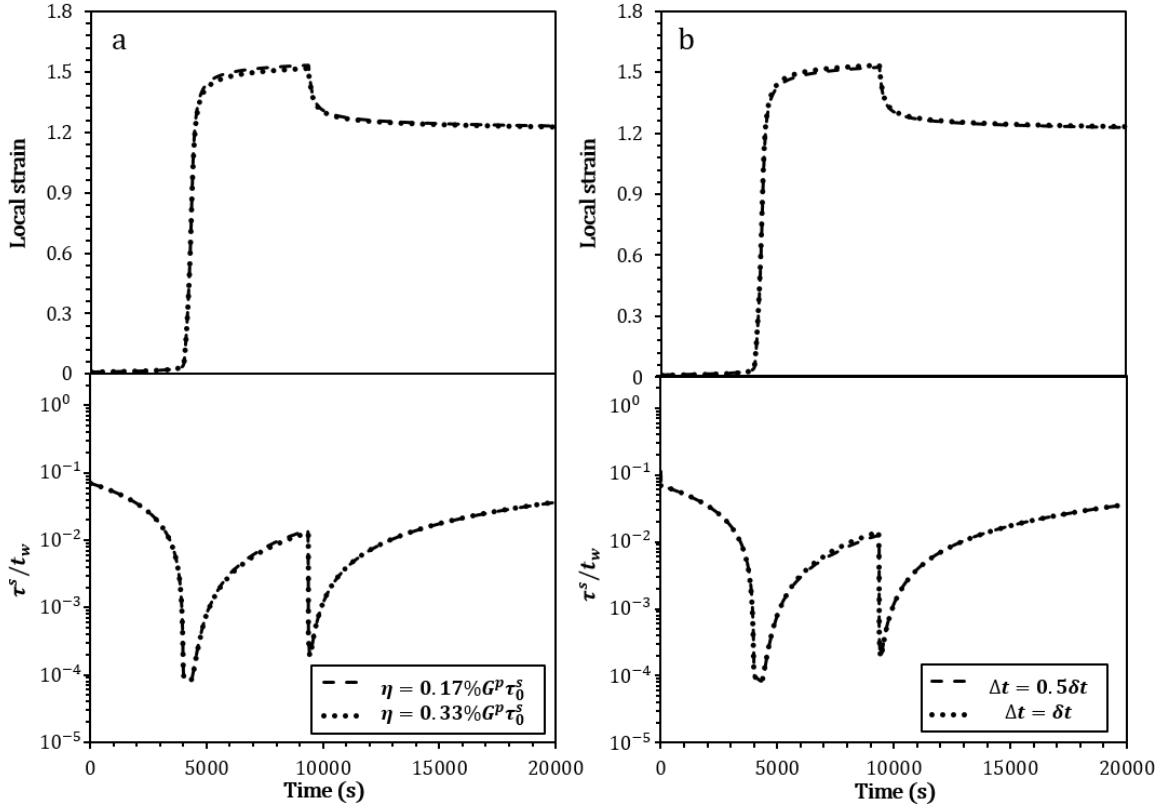


Figure E.2 Illustration of the insensitivity of simulation results to the value of  $\eta$  and simulation time step  $\Delta t$ . The parameters are the standard values listed in Table 6.1.

## Bibliography

- Acharya, D. P.; Sato, T.; Kaneko, M.; Singh, Y.; Kunieda, H. Effect of Added Poly(oxyethylene)dodecyl Ether on the Phase and Rheological Behavior of Wormlike Micelles in Aqueous SDS Solutions. *J. Phys. Chem. B* **2006**, *110*, 754–760.
- Adam, G. and Gibbs, J. H. On the Temperature Dependence of Cooperative Relaxation Properties in Glass-Forming Liquids. *J. Chem. Phys.*, 1965, **43**, 139-146.
- Adamy, S. T. Viscoelastic Behavior of Alkyl Ether Sulfate Systems Containing Sodium Carbonate. *J. Surfact. Deterg.* **2016**, *19*, 599–608.
- Afifi, H.; Karlsson, G.; Heenan, R. K.; Dreiss, C. Structural Transitions in Cholesterol-based Wormlike Micelles Induced by Encapsulating Alkyl Ester Oils with Varying Architecture. *J. Colloid Interface Sci.* **2012**, *378*, 125–134.
- Amis, E. J.; Carriere, C. J.; and Ferry, J. D.; and Veis, A. Effect of pH on Collagen Flexibility Determined From Dilute Solution Viscoelastic Measurements. *Int. J. Biol. Macromol.* **1985**, *7*, 130-134.
- Andreev, V. A. and Victorov, A. I. Molecular Thermodynamics for Micellar Branching in Solutions of Ionic Surfactants. *Langmuir* **2006**, *22*, 8298-8310.
- Angelescu, D.; Khan, A.; and Caldararu, H. Viscoelastic Properties of Sodium Dodecyl Sulfate with Aluminum Salt in Aqueous Solution. *Langmuir* **2003**, *19*, 9155-9161.
- Aniansson, E. A. G.; and Wall, S. N. On the Kinetics of Step-Wise Micelle Association. *J. Phys. Chem.* **1974**, *78*, 1024-1030.
- Appell, J. and Marignan, J. Structure of Giant Micelles – A Small-angle Neutron-scattering Study. *Journal de physique II* **1991**, *1*, 1447-1454.
- Appell, J.; and Porte, G.; Poggi, Y. Quantitative Estimate of the Orientational Persistence Length of Flexible Enlongated Micelles of Cetylpyridinium Bromide. *J. Colloid Interface Sci.* **1982**, *87*, 492-499.
- Arruda, E. M.; Boyce, M. C.; and Quintus-Bosz, H. Effects of Initial Anisotropy on the Finite Strain Deformation Behavior of Glassy Polymers. *Int. J. Plast.* **1993**, *9*, 783-811.
- Babintsev, I. A.; Adzhemyan, L. T.; and Shchekin, A. K. Kinetics of Micellisation and Relaxation of Cylindrical Micelles Described by the Difference Becker-Döring Equation. *Soft Matter* **2014**, *10*, 2619-2631.



- Baccile, N.; Babonneau, F.; Jestin, J.; Pehau-Arnaudet, G.; and Bogaert, I. V. Unusual, pH-induced, Self-assembly of Sophorolipid Biosurfactants. *ACS Nano* **2012**, *6*, 4763-4776.
- Barhoum, S.; Castillob, R.; and Yethiraja A. Characterization of Dynamics and Internal Structure of a Mixed-surfactant Wormlike Micellar System Using NMR and Rheometry. *Soft Matter* **2012**, *8*, 6950–6957.
- Batchelor, G. K. The Stress Generated in a Non-dilute Suspension of Elongated Particles by Pure Straining Motion. *J. Fluid Mech.* **1971**, *46*, 813-829.
- Beaumont, J.; Louvet, N.; Divoux, T.; Fardin, M-A.; Bodiguel, H.; Lerouge, S.; Manneville, S.; and Colin, A. Turbulent Flows in Highly Elastic Wormlike Micelles. *Soft Matter* **2013**, *9*, 735-749.
- Beck, J. S.; Vartuli, J. C.; Roth, W. J.; Leonowicz, M. E.; Kresge, C. T.; Schmitt, K. D.; Chu, C. T-W.; Olson, D. H.; Sheppard, E. W.; McCullen, S. B.; Higgins, J. B.; and Schlenker, J. L. A New Family of Mesoporous Molecular Sieves Prepared with Liquid Crystal Templates. *J. Am. Chem. Soc.* **1992**, *114*, 10834-10843.
- Bending, B.; Christison, K.; Ricci, J.; and Ediger, M. D. Measurement of Segmental Mobility During Constant Strain Rate Deformation of a Poly(methyl methacrylate) Glass. *Macromolecules* **2014**, *47*, 800-806.
- Bernheim-Groswasser, A.; Wachtel, E.; and Talmon, Y. Micellar Growth, Network Formation, and Criticality in Aqueous Solutions of the Nonionic Surfactant C<sub>12</sub>E<sub>5</sub>. *Langmuir* **2000**, *16*, 4131-4140.
- Bernstein, B. and Shokooh, A. The Stress Clock Function in Viscoelasticity. *J. Rheol.* **1980**, *24*, 189-211.
- Berret, J-F.; Appell, J.; Porte, G. Linear Rheology of Entangled Wormlike Micelles. *Langmuir* **1993**, *9*, 2851-2854.
- Berthier, L.; Barrat, J.-L.; and Kurchan. J. A Two-time-scale, Two-temperature Scenario for Nonlinear Rheology. *Phys. Rev. E* **2000**, *61*, 5464-5472.
- Bird, R. B.; Curtiss, C. R.; Armstrong, R. C.; and Hassager, O. Dynamics of Polymeric Liquids, 2<sup>nd</sup> Ed. Wiley, New York, 1987.
- Bradbury, R.; Penfold, J.; Thomas, R. K.; Tucker, I. M.; Petkov, J. T.; Jones, C.; Grillo, I. Impact of Model Perfume Molecules on the Self-assembly of Anionic Surfactant Sodium Dodecyl 6-benzene Sulfonate. *Langmuir* **2013**, *29*, 3234–45.
- Bradbury, R.; Penfold, J.; Thomas, R. K.; Tucker, I. M.; Petkov, J. T.; Jones, C. The Impact of Alkyl Sulfate Surfactant Geometry and Electrolyte on the Co-adsorption of Anionic Surfactants with Model Perfumes at the Air-solution Interface. *J. Colloid Interface Sci.* **2013**, *403*, 84–90.

- Boyce, M. C. and Arruda, E. M. An Experimental and Analytical Investigation of the Large Strain Compressive and Tensile Response of Glassy Polymers. *Polymer Engineering and Science* **1990**, *30*, 1288-1298.
- Boyce, M. C.; Parks, D. M.; and Argon, A. S. Large Inelastic Deformation of Glassy Polymers Part I: Rate Dependent Constitutive Model. *Mechanics of Materials* **1988**, *7*, 15-33.
- Brown, W.; Johansson, K.; and Almgren, M. Threadlike Micelles from Cetyltrimethylammonium Bromide in Aqueous Sodium Naphthalenesulfonate Solutions Studied by Static and Dynamic Light Scattering. *J. Phys. Chem.* **1989**, *93*, 5888-5894.
- Bruce, C. D.; Berkowitz, M. L.; Perera, L.; Forbes, M. D. Molecular Dynamics Simulation of Sodium Dodecyl Sulfate Micelle in Water. *J. Phys. Chem. B* **2002**, *106*, 3788 -3793.
- Buchanan, M.; Ataknorrani, M.; Paliarne, J. F.; and Schmidt, C. F. Comparing Macrorheology and One- and Two-point Microrheology in Wormlike Micelle Solutions. *Macromolecules* **2005**, *38*, 8840–8844.
- Candau, S. J.; Hirsch, E.; Zana, R.; Delsanti, M. Rheological Properties of Semidilute and Concentrated Aqueous Solutions of Cetyltrimethylammonium Bromide in the Presence of Potassium Bromide. *Langmuir* **1989**, *5*, 1225–1229.
- Candau, S. J.; Khatory, A.; Lequeux F.; and Kern, F. Rheological Behavior of Wormlike Micelles: Effect of Salt Content. *Journal de Physique IV* **1993**, *3*, 197-209.
- Cates, M. E. Dynamics of Living Polymers and Flexible Surfactant Micelles: Scaling Laws for Dilution. *J. Phys. France* **1988**, *49*, 1593-1600.
- Cates, M. E. Reptation of Living Polymers: Dynamics of Entangled Polymers in the Presence of Reversible Chain-Scission Reactions. *Macromolecules* **1987**, *20*, 2289–96.
- Cates, M. E.; Candau, S. J. Statics and Dynamics of Worm-like Surfactant Micelles. *J. Phys. Condens. Matter* **1990**, *2*, 6869–6892.
- Cates, M. E.; Fielding, S. M. Rheology of Giant Micelles. *Adv. Phys.* **2006**, *55*, 799–879.
- Cappelaere, E.; Cressely, R.; Makhloufi, R.; Decruppe, J. P. Temperature and Flow-Induced Viscosity Transitions for CTAB Surfactant Solutions. *Rheol. Acta* **1994**, *437*, 431–437.
- Cardiel, J. J.; Zhao, Y.; de La Iglesia, P.; Pozzoc, L. D.; and Shen, A. Q. Turning Up the Heat on Wormlike Micelles with a Hydrotopic Salt in Microfluidics. *Soft Matter* **2014**, *10*, 9300–9312.
- Carriere, C. J.; Amis, E. J.; Schrag, J. L.; and Ferry, J. D. Dilute-solution Dynamic Viscoelastic Properties of Schizophyllan Polysaccharide. *Macromolecules* **1985**, *18*, 2019-2023.
- Chen, K.; Saltzman, E. J.; and Schweizer, K. S. Segmental Dynamics in Polymers: from Cold Melts to Ageing and Stressed Glasses. *J. Phys.: Condens. Matter* **2009**, *21*, 503101.

Chen, K. and Schweizer, K. S. Theory of Relaxation and Elasticity in Polymer Glasses. *J. Chem. Phys.* **2007**, *126*, 014904.

Chen, K. and Schweizer, K. S. Suppressed Segmental Relaxation as the Origin of Strain Hardening in Polymer Glasses. *Phys. Rev. Lett.* **2009**, *102*, 038301.

Chen, K. and Schweizer, K. S. Theory of Aging, Rejuvenation, and the Nonequilibrium Steady State in Deformed Polymer Glasses. *Phys. Rev. E.* **2010**, *82*, 041804.

Chen, K.; Schweizer, K. S.; Stamm, R.; Lee, E.; and Caruthers, J. M. Theory of Nonlinear Creep in Polymer Glasses. *J. Chem. Phys.* **2008**, *129*, 184904.

Chen, W.; Butler, P. D.; and Magid, L. J. Incorporating Intermicellar Interactions in the Fitting of SANS Data from Cationic Wormlike Micelles. *Langmuir* **2006**, *22*, 6539-6548.

Chellamuthu, M. and Rothstein, J. P. Distinguishing Between Linear and Branched Wormlike Micelle Solutions Using Extensional Rheology Measurements. *J. Rheol.* **2008**, *52*, 865-884.

Chong, S.-H. and Fuchs, M. Mode-Coupling Theory for Structural and Conformational Dynamics of Polymer Melts. *Phys. Rev. Lett.* **2002**, *88*, 185702.

Christov, N. C.; Denkov, N. D.; Kralchevsky, P. A.; Ananthapadmanabhan, K. P.; Lips, A. Synergistic Sphere-to-Rod Micelle Transition in Mixed Solutions of Sodium Dodecyl Sulfate and Cocoamidopropyl Betaine. *Langmuir* **2004**, *20*, 565-571.

Clausen, T. M.; Vinson, P. K.; Minter, J. R.; Davis, H. T.; Talmon, Y.; Miller, W. G. Viscoelastic Micellar Solutions: Microscopy and Rheology. *J. Phys. Chem.* **1992**, *96*, 474-484.

Couillet, I.; Hughes, T.; Maitland, G.; Candau F.; and Candau, S. J. Growth and Scission Energy of Wormlike Micelles Formed by a Cationic Surfactant with Long Unsaturated Tails. *Langmuir* **2004**, *20*, 9514-9550.

Coussot, P.; Nguyen, Q. D.; Huynh, H. T.; and Bonn, D. Avalanche Behavior in Yield Stress Fluids. *Phys. Rev. Lett.* **2002**, *38*, 175501.

Croce, V.; and Cosgrove, T.; Maitland, G.; Hughes, T.; and Karlsson, G. Rheology, Cryogenic Transmission Electron Spectroscopy, and Small-angle Neutron Scattering of Highly Viscoelastic Wormlike Micellar Solutions. *Langmuir* **2003**, *19*, 8536-8541.

Crothers, M.; Zhou, Z. Y.; Ricardo, N. M. P. S.; Yang, Z.; Taboada, P., Chaibun-dit, C.; Attwood, D.; Booth, C. Solubilisation in Aqueous Micellar Solutions of Block Copoly(oxyalkylene)s. *Int. J. Pharm.* **2005**, *293*, 91-100.

da Silva, G. C.; Rossi, C. G. F. T.; Dantas Neto, A. A.; Dantas, T. N. C.; Fonseca, J. L. C. Characterization of Wormlike Micellar Systems Using DLS, Rheometry and Tensiometry. *Colloids and Surfaces A: Physicochem. Eng. Aspects* **2011**, *377*, 35-43.

- Dai, C.; Li, W.; Cui, Y.; Sun, Y.; Wu, W.; Xu, Z.; Liu, Y.; Yanga, Z.; Wu, X. The Effect of Functional Groups on the Sphere-to-wormlike Micellar Transition in Quaternary Ammonium Surfactant Solutions. *Colloids and Surfaces A: Physicochem. Eng. Aspects* **2016**, *500*, 32–39.
- Dan, N.; Safran, S. A. Junctions and End-caps in Self-assembled Non-ionic Cylindrical Micelles. *Adv. Colloid Interface Sci.* **2006**, *123-126*, 323-331.
- Danino, D.; Talmon, Y.; Levy, H.; Beinert, G.; and Zana, R. Branched Threadlike Micelles in an Aqueous Solution of a Trimeric Surfactant. *Science* **1995**, *269*, 1420-1421.
- Danino, D.; Talmon, Y.; Zana, R. Cryo-TEM of Thread-like Micelles: On-the-grid Microstructural Transformations Induced during Specimen Preparation. *Colloids and Surfaces A: Physicochem. Eng. Aspects* **2000**, *169*, 67–73.
- Danov, K. D.; Kralchevska, S. D.; Kralchevsky, P. A.; Ananthapadmanabhan, K. P.; Lips, A. Mixed Solutions of Anionic and Zwitterionic Surfactant (Betaine): Surface-Tension Isotherms, Adsorption, and Relaxation Kinetics. *Langmuir* **2004**, *20*, 5445–5453.
- de Gennes, P. G. *Scaling Concepts in Polymer Physics*. Cornell University Press, Ithaca, New York, **1979**.
- de Silva, M. A.; Weinzaepfel, E.; Afifi, H.; Eriksson, J.; Grillo, I.; Valero, M.; and Dreiss, C. A. Tuning the Viscoelasticity of Nonionic Wormlike Micelles with  $\beta$ -cyclodextrin Derivatives: A Highly Discriminative Process. *Langmuir* **2013**, *29*, 7697-7708.
- Dealy, J. M. and Larson, R. G. *Structure and Rheology of Molten Polymers: From Structure to Flow Behavior and Back Again*. Hanser Gardner Publications, Cincinnati, **2005**.
- Debenedetti, P. G. and Stillinger, F. H. Supercooled Liquids and the Glass Transition. *Nature*, **2001**, *410*, 259-267.
- Decruppe, J. P. F.; and Lerouge, S. A Comparison of Some Rheophysical Properties of Cetyltrimethylammonium Bromide/H<sub>2</sub>O and Cetyltrimethylammonium Bromide/D<sub>2</sub>O Solutions. *Colloid Polym. Sci.* **1999**, *227*, 891-894.
- Decruppe, J. P. F. and Ponton, A. Flow Birefringence, Stress Optical Rule and Rheology of Four Micellar Solutions with the Same Low Shear Viscosity. *Eur. Phys. J. E* **2003**, *10*, 201–207.
- des Cloizeaux, J. Double Reptation vs. Simple Reptation in Polymer Melts. *Europhys. Lett.* **1988**, *5*, 437-442.
- Doi, M. and Edwards, S. F. *The Theory of Polymer Dynamics*. Clarendon Press, Oxford, **1986**.
- Dyre, J. C. Colloquium: The glass transition and elastic models of glass-forming liquids. *Rev. Mod. Phys.* **2006**, *78*, 953-972.
- Drye, T. J. and Cates, M. E. Living networks: The Role of Crosslinks in Entangled Surfactant Solutions. *J. Chem. Phys.* **1992**, *96*, 1367-1375.

- Eguchi, K.; Kaneda, I.; Hiwatari, Y.; Masunaga, H.; Sakurai, K. Salt-concentration Dependence of the Structure and Form Factors for the Wormlike Micelle Made from a Dual Surfactant in Aqueous Solutions. *J. Appl. Crystallogr.* **2007**, *40*, S264–S268.
- Escaig, B. A Metallurgical Approach to the Pre-Yield and Yield Behavior of Glassy Polymers. *Polym. Eng. and Sci.* **1984**, *24*, 737-749.
- Español, P.; Warren, P. Statistical Mechanics of Dissipative Particle Dynamics. *Europhys. Lett.* **1995**, *30*, 191–196.
- Eyring, H. Viscosity, Plasticity, and Diffusion as Examples of Absolute Reaction Rates. *J. Chem. Phys.* **1936**, *4*, 283-291.
- Feng, Y.; Han Y. Effect of Counterion Size on Wormlike Micelles Formed by a C22-tailed Anionic Surfactant. *J. Mol. Liq.* **2016**, *218*, 508-514.
- Fetters, L. J.; Lohse, D. J.; Graessley, W. W. Chain Dimensions and Entanglement Spacings in Dense Macromolecular Systems. *J. Polym. Sci. B – Poly. Phys.* **1999**, *37*, 1023-1033.
- Fielding, S. M.; Larson, R. G.; and Cates, M. E. Simple Model for the Deformation-Induced Relaxation of Glassy Polymers. *Phys. Rev. Lett.* **2012**, *108*, 048301.
- Fielding, S. M.; Moorcroft, R. L.; Larson, R. G.; and Cates, M. E. Modeling the Relaxation of Polymer Glasses under Shear and Elongational Loads. *J. Chem. Phys.* **2013**, *138*, 12A504.
- Fischer, E.; Fieber, W.; Navarro, C.; Sommer, H.; Benczédi, D.; Velazco, M. I.; Schönhoff, M. Partitioning and Localization of Fragrances in Surfactant Mixed Micelles. *J. Surfactants Deterg.* **2009**, *12*, 73–84.
- Fischer, P.; Fuller, G. G.; Lin, Z. Branched Viscoelastic Surfactant Solutions and Their Response to Elongational Flow. *Rheol Acta* **1997**, *36*, 632-638.
- Friedman, B.; O’Shaughnessy, B. Kinetics of Intermolecular Reactions in Dilute Polymer Solutions and Unentangled Melts. *Macromolecules* **1993**, *26*, 5726-5739.
- Galvan-Miyoshi, J.; Delgado, J.; Castillo, R. Diffusing Wave Spectroscopy in Maxwellian Fluids. *Eur. Phys. J. E* **2008**, *26*, 369–77.
- Gallot, T.; Perge, C.; Grenard, V.; Fardin, M.-A.; Taberlet, N.; and Manneville, S. Ultrafast Ultrasonic Imaging Coupled to Rheometry: Principle and Illustration. *Rev. Sci. Instrum.* **2013**, *84*, 045107.
- Gamez-Corrales, R.; Berret, J. F.; Walker, L. M.; and Oberdisse, J. Shear-thickening Dilute Surfactant Solutions: Equilibrium Structure as Studied by Small-angle Neutron Scattering. *Langmuir* **1999**, *15*, 6755-6763.

- Gao, S.; Sun, T.; Chen, Q.; and Shen, X. Characterization of Reversed Micelles Formed in Solvent Extraction of Thorium(IV) by Bis(2-ethylhexyl) Phosphoric Acid. Transforming from Rodlike to Wormlike Morphology. *Radiochim. Acta* **2016**, *104*, 457–469.
- Garrahan, J. P. and Chandler, D. Coarse-grained Microscopic Model of Glass Formers. *PNAS*, **2003**, *100*, 9710-9714.
- Gittes, F.; and MacKintosh, F. C. Dynamic Shear Modulus of a Semiflexible Polymer Network. *Phys. Rev. E* **1998**, *58*, 1241–1244.
- Gomez, E. S.; Diaz, D. L.; and Castillo, R. Microrheology and Characteristic Lengths in Wormlike Micelles Made of a Zwitterionic Surfactant and SDS in Brine. *J. Phys. Chem. B* **2010**, *114*, 12193-12202.
- Granek, R. Dip in  $G''(\omega)$  of Polymer Melts and Semidilute Solutions. *Langmuir* **1994**, *10*, 1627-1629.
- Granek, R.; Cates, M. E. Stress Relaxation in Living Polymers: Results from a Poisson Renewal Model. *J. Chem. Phys.* **1992**, *96*, 4758–4767.
- Greer, A. L. Metallic Glasses. *Science* **1995**, *267*, 1947–1953.
- Grmela, M.; and Chinesta, F.; Ammar, A. Mesoscopic Tube Model of Fluids Composed of Worm-like Micelles. *Rheol. Acta* **2010**, *49*, 495-506.
- Groot, R. D. Electrostatic Interactions in Dissipative Particle Dynamics—Simulation of Polyelectrolytes and Anionic Surfactants. *J. Chem. Phys.* **2003**, *118*, 11265-11277.
- Groot, R. D.; Warren, P. B. Dissipative Particle Dynamics: Bridging the Gap Between Atomistic and Mesoscopic Simulation. *J. Chem. Phys.* **1997**, *107*, 4423–4435.
- Halsey, G.; White, H. J.; and Eyring, H. Mechanical Properties of Textiles, I. *Textile Research Journal* **1945**, *15*, 295-311.
- Hansen, J. P. and McDonald, I. R. *Theory of Simple Liquids*, 2<sup>nd</sup> Ed. Academic Press, New York, **1986**.
- Hassan, P. A.; Candau, S. J.; Kern F.; and Manohar, C. Rheology of Wormlike Micelles with Varying Hydrophobicity of the Counterion. *Langmuir* **1998**, *14*, 6025-6029.
- Helgeson, M. E.; Hodgdon, T. K.; Kaler, E. W.; Wagner, N. J. A Systematic Study of Equilibrium Structure, Thermodynamics, and Rheology of Aqueous CTAB/NaNO<sub>3</sub> Wormlike Micelles. *J. Colloid Interface Sci.* **2010**, *349*, 1–12.
- Helgeson, M. E.; Hodgdon, T. K.; Kaler, E. W.; Wagner, N. J.; Vethamuthu, M.; Ananthapadmanabhan, K. P. Formation and Rheology of Viscoelastic “Double Networks” in Wormlike Micelle-Nanoparticle Mixtures. *Langmuir* **2010**, *26*, 8049–8060.

- Heo, Y.; Larson, R. G. The Scaling of Zero-shear Viscosities of Semidilute Polymer Solutions with Concentration. *J. Rheol.* **2005**, *49*, 1117-1128.
- Hideki, S.; Yoichi, O.; Hideki, K.; Atsutoshi, M.; Takahiro, O.; Koji, T.; Masahiko, A. Photoinduced Reversible Change of Fluid Viscosity. *J. Am. Chem. Soc.* **2005**, *127*, 13454–13455.
- Hines, J. D.; Thomas, R. K.; Garrett, P. R.; Rennie, G. K.; Penfold, J. Investigation of Mixing in Binary Surfactant Solutions by Surface Tension and Neutron Reflection: Anionic/Nonionic and Zwitterionic/Nonionic Mixtures. *J. Phys. Chem. B* **1998**, *102*, 8834–46.
- Hoogerbrugge, P. J.; Koelman, J. M. V. Simulating Microscopic Hydrodynamic Phenomena with Dissipative Particle Dynamics. *Europhys. Lett.* **1992**, *19*, 155–160.
- Hoy, R. S. Why is Understanding Glassy Polymer Mechanics So Difficult? *J. Polym. Sci.: Part B: Polym. Phys.* **2011**, *49*, 979-984.
- Hoy, R. S. and O'Hern, C. S. Viscoplasticity and Large-scale Chain Relaxation in Glassy-polymeric Strain Hardening. *Phys. Rev. E* **2010**, *82*, 041803.
- Hoy, R. S. and Robbins, M. O. Strain Hardening of Polymer Glasses: Entanglements, Energetics, and Plasticity. *Phys. Rev. E.* **2008**, *77*, 031801.
- Hoy, R. S. and Robbins, M. O. Strain Hardening in Bidisperse Polymer Glasses: Separating the Roles of Chain Orientation and Interchain Entanglement. *J. Chem. Phys.* **2009**, *131*, 244901.
- Huang, J.; Zhang, S.; Feng, Y.; Li, J.; Yan, H.; He, F.; Wang, G.; Liu, Y.; Wang, L. Rheological Properties and Application of Wormlike Micelles Formed by Sodium Oleate/benzyltrimethyl Ammonium Bromide. *Colloids and Surfaces A: Physicochem. Eng. Aspects* **2016**, *500*, 222–229.
- Ilgenfritz, G.; Schneider, R.; Grell, E.; Lewitzki, E.; and Ruf, H. Thermodynamic and Kinetic Study of the Sphere-to-rod Transition in Nonionic Micelles: Aggregation and Stress Relaxation in C<sub>14</sub>E<sub>18</sub> and C<sub>16</sub>E<sub>8</sub>/H<sub>2</sub>O System. *Langmuir* **2004**, *20*, 1620-1630.
- Imae, T. Light Scattering of Spinnable, Viscoelastic Solutions of Hexadecyltrimethylammonium Salicylate. *J. Phys. Chem.* **1990**, *94*, 5953-5959.
- Imae, T. and Ikeda, S. Sphere-rod Transition of Micelles of Tetradecyltrimethylammonium Halides in Aqueous Sodium Halide Solutions and Flexibility and Entanglement of Long Rodlike. *J. Phys. Chem.* **1986**, *90*, 5216-5223.
- Imae, T.; Ikeda, S. Characteristics of Rodlike Micelles of Cetyltrimethylammonium Chloride in Aqueous NaCl Solutions : Their Flexibility and the Scaling Laws in Dilute and Semidilute Regimes. *Colloid and Polym. Sci.* **1987**, *265*, 1090–1098.
- Imae, T.; Kamiya, R.; Ikeda, S. Formation of Spherical and Rod-like Micelles of Cetyltrimethylammonium Bromide in Aqueous NaBr Solutions. *J. Colloid Interface Sci.* **1985**, *108*, 215–225.

- Ingram, T.; Storm, S.; Kloss, L.; Mehling, T.; Jakobtorweihen, S.; Smirnova, I. Prediction of Micelle/water and Liposome/water Partition Coefficients Based on Molecular Dynamics Simulations, COSMO-RS, and COSMOmic. *Langmuir* **2013**, *29*, 3527–3537.
- Israelachvili, J. N.; Mitchell, D. J.; Ninham, B. W. Theory of Self-Assembly of Hydrocarbon Amphiphiles into Micelles and Bilayers. *J. Chem. Soc. Faraday Trans. II* **1976**, *72*, 1525–1568.
- Jain, S. and Bates, F. S. On the Origins of Morphological Complexity in Block Copolymer Surfactants. *Science* **2003**, *300*, 460-464.
- James, G. K. and Walz, J. Y. Experimental Investigation of the Effects of Ionic Micelles on Colloidal Stability. *J. Colloid Interface Sci.* **2014**, *418*, 283-291.
- Jensen, G. V.; Lund, R.; Gummel, J.; Monkenbusch, M.; Narayanan, T.; and Pedersen, J. S. Direct Observation of the Formation of Surfactant Micelles under Nonisothermal Conditions by Synchrontron SAXS. *J. Am. Chem. Soc.* **2013**, *135*, 7214-7222.
- Jusufi, A.; Hynninen, A. P.; and Panagiotopoulos, A. Z. Implicit Solvent Models for Micellization of Ionic Surfactants. *J. Chem. Phys. B* **2008**, *112*, 13783-13792.
- Kaler, E. W.; Murthy, A. K.; Rodriguez, B. E.; Zasadzinski, J. A. N. Spontaneous Vesicle Formation in Aqueous Mixtures of Single-Tailed Surfactants. *Science* **1989**, *245*, 1371-1374.
- Kalur, G. C.; Frounfelker, B. D.; Cipriano, B. H.; Norman, A. I.; and Raghavan, S. R. Viscosity Increase with Temperature in Cationic Surfactant Solutions Due to the Growth of Wormlike Micelles. *Langmuir* **2005**, *21*, 10998-11004.
- Kekicheff, P. Phase Diagram of Sodium Dodecyl Sulfate-Water System: 2. Complementary Isolethal and Isothermal Phase Studies. *J. Colloid Interface Sci.* **1989**, *131*, 133–152.
- Kern, F.; Zana, R.; Candau, S. J. Rheological Properties of Semidilute and Concentrated Aqueous Solutions of Cetyltrimethylammonium Chloride in the Presence of Sodium Salicylate and Sodium Chloride. *Langmuir* **1991**, *7*, 1344–1351.
- Ketner, A. M.; Kumar, R.; Davies, T. S.; Elder, P. W.; and Raghavan, S. R. A Simple Class of Photorheological Fluids: Surfactant Solutions with Viscosity Tunable by Light. *J. Am. Chem. Soc.* **2007**, *129*, 1553-1559.
- Khatory, A.; Kern, F.; Lequeux, F.; Appell, J.; Porte, G.; Morie, N.; Ott, A.; and Urbach, W. Entangled versus Multiconnected Network of Wormlike Micelles. *Langmuir* **1993**, *9*, 933-939.
- Khatory, A.; Lequeux, F.; Kern, F.; Candau, S. J. Linear and Nonlinear Viscoelasticity of Semidilute Solutions of Wormlike Micelles at High Salt Content. *Langmuir* **1993**, *9*, 1456–64.
- Klamt, A. The COSMO and COSMO-RS Solvation Models. *Wiley Interdiscip. Rev. Comput. Mol. Sci.* **2011**, *1*, 699–709.



- Klamt, A.; Eckert, F.; Arlt, W. COSMO-RS: An Alternative to Simulation for Calculating Thermodynamic Properties of Liquid Mixtures. *Annu. Rev. Chem. Biomol. Eng.* **2010**, *1*, 101–22.
- Klompen, E. T. J.; Engels, T. A. P.; Govaert, L. E.; and Meijer, H. E. H. Modeling of the Postyield Response of Glassy Polymers: Influence of Thermomechanical History. *Macromolecules* **2005**, *38*, 6997-7008.
- Kodama, M.; Kubota, Y.; Miura, M. The Second CMC of the Aqueous Solution of Sodium Dodecyl Sulfate: 3. Light-scattering. *Bull. Chem. Soc. Jpn.* **1972**, *45*, 2953–2955.
- Koehler, R. D.; Raghavan, S. R.; and Kaler, E. W. Microstructure and Dynamics of Wormlike Micellar Solutions Formed by Mixing Cationic and Anionic Surfactants. *J. Phys. Chem. B* **2000**, *104*, 11035-11044.
- Koshy, P.; Aswal, V. K.; Venkatesh, M.; and Hassan, P. A. Unusual Scaling in the Rheology of Branched Wormlike Micelles Formed by Cetyltrimethylammonium Bromide and Sodium Oleate. *J. Phys. Chem. B* **2011**, *115*, 10817–10825.
- Kralova, I.; Sjoblom, J. Surfactants Used in Food Industry : A Review. *J. Disper. Sci. Technol.* **2009**, *30*, 1363–1383.
- Kunieda, H.; Horii, M.; Koyama, M.; Sakamoto, K. Solubilization of Polar Oils in Surfactant Self-organized Structures. *J. Colloid Interface Sci.* **2001**, *236*, 78–84.
- Kuperkar, K.; Abezgauz, L.; Danino, D.; Verma, G.; Hassan, P. A.; Aswal, V. K.; Varade, D.; and Bahadur, P. Viscoelastic Micellar Water/CTAB/NaNO<sub>3</sub> Solution: Rheology, SANS and Cryo-TEM Analysis. *J. Colloid Interface Sci.* **2008**, *323*, 403-409.
- Kusano, T.; Iwase, H.; Yoshimura, T.; and Shibayama, M. Structural and Rheological Studies on Growth of Salt-free Wormlike Micelles Formed by Star-type Trimeric Surfactants. *Langmuir* **2012**, *28*, 16798-16806.
- Langer, J. S. Shear-transformation-zone Theory of Plastic Deformation Near the Glass Transition. *Phys. Rev. E* **2008**, *77*, 021502.
- Larson, R. G. *Constitutive Equations for Polymer Melts and Solutions*. Butterworth Publishers, Stoneham, **1988**.
- Larson, R. G. The Unraveling of a Polymer Chain in a Strong Extensional Flow. *Rheol. Acta.* **1990**, *29*, 371-384.
- Larson, R. G. *The Structure and Rheology of Complex Fluids*. Oxford University Press: New York, USA, **1999**.
- Larson, R. G. The Rheology of Dilute Solutions of Flexible Polymers: Progress and Problems. *J. Rheol.* **2005**, *49*, 1-70.

- Larson, R. G. The Lengths of Thread-like Micelles Inferred from Rheology. *J. Rheol.* **2012**, *56*, 1363–1374.
- Larson, R. G.; Sridhar, T.; Leal, L. G.; McKinley, G. H.; Likhtman, A. E.; and McLeish, T. C. Definition of Entanglement Spacing and Time Constants in the Tube Model. *J. Rheol.* **2003**, *47*, 809-818.
- Lawrence, M. J. Surfactant Systems: Their Use in Drug Delivery. *Chem. Soc. Rev.* **1994**, *23*, 417-424.
- Lee, H.-N.; Paeng, K.; Swallen, S. F.; and Ediger, M. D. Direct Measurement of Molecular Mobility in Actively Deformed Polymer Glasses. *Science* **2009**, *323*, 231-234.
- Lee, H.-N.; Paeng, K.; Swallen, S. F.; Ediger, M. D.; Stamm, R. A.; Medvedev, G. A.; and Caruthers, J. M. Molecular Mobility of Poly(methyl methacrylate) Glass During Uniaxial Tensile Creep Deformation. *Journal of Polymer Science: Part B: Polymer Physics* **2009**, *47*, 1713-1727.
- Lequeux, F. Reptation of Connected Wormlike Micelles. *Europhys. Lett.* **1992**, *19*, 675–681.
- Lequeux, F. Structure and Rheology of Wormlike Micelles. *J. Colloid Interface Sci.* **1996**, *1*, 341-344.
- Lequeux, F. and Candau, S. J. Chapter 3. Dynamical Properties of Wormlike Micelles: Deviations from the "Classical" Picture. *Structure and Flow in Surfactant Solutions*. ACS Symposium Series, American Chemical Society: Washington, DC, **1994**.
- Likhtman, A. E. and McLeish, T. C. B. Quantitative Theory for Linear Dynamics of Linear Entangled Polymers. *Macromolecules* **2002**, *35*, 6332-6343.
- Lin, Z. Branched Worm-like Micelles and Their Networks. *Langmuir* **1996**, *12*, 1729-1737.
- Lin, Z. Q.; Zheng, J. L. Y.; Davis, H. T.; Scriven, L. E.; Talmon, Y. Comparison of the Effects of Dimethyl and Dichloro Benzoate Counterions on Drag Reduction, Rheological Behaviour, and Microstructures of a Cationic Surfactant. *J. Rheol.* **2001**, *45*, 963–981.
- Liyana-arachchi, T. P.; Jamadagni, S. N.; Eike, D.; Koenig, P. H.; Siepmann, J. I. Liquid – liquid Equilibria for Soft-repulsive Particles: Improved Equation of State and Methodology for Representing Molecules of Different Sizes and Chemistry in Dissipative Particle Dynamics. *J. Chem. Phys.* **2015**, *142*, 044902–1–13.
- Lonetti, B.; Tsigkri, A.; Lang, P. R.; Stellbrink, J.; Willner, L.; Kohlbrecher, J.; and Lettinga, M. P. Full Characterization of PB-PEO Wormlike Micelles at Varying Solvent Selectivity. *Macromolecules* **2011**, *44*, 3583–3593.
- Loo, L. S.; Cohen, R. E.; and Gleason, K. K. Chain Mobility in the Amorphous Region of Nylon 6 Observed Under Active Uniaxial Deformation. *Science* **2000**, *288*, 116-119.

- Lu, H.; Shi, Q.; Wang, B.; Huang, Z. Spherical-to-wormlike Micelle Transition in a Pseudogemini Surfactant System with Two Types of Effective pH-responsive Groups. *Colloids and Surfaces A: Physicochem. Eng. Aspects* **2016**, *494*, 74–80.
- Lu, H.; Yang, L.; Wang, B.; and Huang, Z. Switchable Spherical-wormlike Micelle Transition in Sodium Oleate/N-(3-(dimethylamino)propyl)-octanamide Aqueous System Induced by Carbon Dioxide Stimuli and pH Regulation. *J. Disper. Sci. Technol.* **2016**, *37*, 159-165.
- Lu, Y.; Zhou, T.; Fan, Q.; Dong, J.; and Li, X. Light-responsive Viscoelastic Fluids Based on Anionic Wormlike Micelles. *J. Colloid Interface Sci.* **2013**, *412*, 107-111.
- Lubchenko, V. and Wolynes, P. G. Theory of Aging in Structural Glasses. *J. Chem. Phys.* **2004**, *121*, 2852.
- Ma, C.; Li, G.; Xu, Y.; Wang, H.; Ye, X. Determination of the First and Second CMCs of Surfactants by Adsorptive Voltammetry. *Colloids Surf. A Physicochem. Eng. Asp.* **1998**, *143*, 89–94.
- Maitland, G. Oil and Gas Production. *Curr. Opin. Colloid Interface Sci.* **2000**, *5*, 301–311.
- Magid, L. J.; Han, Z.; and Lin, Z.; Butler, P. D. Tuning the Contour Lengths and Persistence Lengths of Cationic Micelles: The Role of Electrostatics and Specific Ion Binding. *J. Phys. Chem. B* **2000**, *104*, 6717-6727 (2000).
- Marignan, J.; Appell, J.; Bassereau, P.; Porte, G.; and May, R. P. Local Structures of the Surfactant Aggregates in Dilute-solutions Deduced from Small-angle Neutron-scattering Patterns. *Journal de physique* **1989**, *50*, 3553-3566.
- May, S.; Bohbot, Y.; and Ben-Shaul, A. Molecular Theory of Bending Elasticity and Branching of Cylindrical Micelles. *J. Phys. Chem. B* **1997**, *101*, 8648-8657.
- Mazer, N. A.; Benedek, G. B.; Carey, M. C. Investigation of the Micellar Phase of Sodium Dodecyl Sulfate in Aqueous Sodium Chloride Solutions Using Quasielastic Light Scattering Spectroscopy. *J. Phys. Chem.* **1976**, *80*, 1075–1085.
- Melanie, M. *An Introduction to Genetic Algorithms*. Cambridge, MIT Press, **1996**.
- Merabia, S.; Sotta, P.; and Long, D. Heterogeneous Nature of the Dynamics and Glass Transition in Thin Polymer Films. *Eur. Phys. J. E* **2004**, *15*, 189-210.
- Messenger, R.; Ott, A.; Chatenay, D.; Urbach, W.; and Langevin, D. Are Giant Micelles Living Polymers? *Phys. Rev. Lett.* **1988**, *60*, 1410-1413.
- Michels, B. and Waton, G. Effect of Pentanol and Salt on the Fusion-scission Kinetics for CTAB Micelles. *J. Phys. Chem. A* **2003**, *107*, 1133-1137.
- Milner, S. T. Predicting the Tube Diameter in Melts and Solutions. *Macromolecules* **2005**, *38*, 4929-4939.

Milner, S. T. and McLeish, T. C. B. Parameter-free Theory for Stress Relaxation in Star Polymer Melts. *Macromolecules* **1997**, *30*, 2159-2166.

Milner, S. T.; McLeish, T. C. Reptation and Contour-length Fluctuations in Melts of Linear Polymers. *Phys. Rev. Lett.* **1998**, *81*, 725-728.

Moorcroft, R. L.; Cates, M. E.; and Fielding, S. M. Age-Dependent Transient Shear Banding in Soft Glasses. *Phys. Rev. Lett.* **2011**, *106*, 055502.

Morse, D. C. Viscoelasticity of Concentrated Isotropic Solutions of Semiflexible Polymers: 1. Model and Stress Tensor. *Macromolecules* **1998**, *31*, 7030–7043.

Morse, D. C. Viscoelasticity of Concentrated Isotropic Solutions of Semiflexible Polymers: 2. Linear Response. *Macromolecules* **1998**, *31*, 7044–7067.

Nagarajan, R. Association of Nonionic Polymers with Micelles, Bilayers, and Microemulsions. *J. Chem. Phys.* **1989**, *90*, 1980-1994.

Nakamura, K. and Shikata, T. Threadlike Micelle Formation of Anionic Surfactants in Aqueous Solution. *Langmuir* **2006**, *22*, 9853-9859.

Naruse, K.; Eguchi, K.; Akiba, I.; Sakurai, K.; Masunaga, H.; Ogawa, H.; Fossey, J. S. Flexibility and Cross-sectional Structure of an Anionic Dual-surfactant Wormlike Micelle Explored with Small-angle X-ray Scattering Coupled with Contrast Variation Technique. *J. Phys. Chem. B* **2009**, *113*, 10222–10229.

Nemoto, N.; Kuwahara, M.; Yao, M.; and Osaki, K. Dynamic Light Scattering of CTAB/NaSal Threadlike Micelles in a Semidilute Regime. 3. Dynamical Coupling between Concentration Fluctuation and Stress. *Langmuir* **1995**, *11*, 30-36.

Nettesheim, F.; Wagner, N. J. Fast Dynamics of Wormlike Micellar Solutions. *Langmuir* **2007**, *23*, 5267–9.

Ngai, K. L. and Plazek, D. J. Identification of Different Modes of Molecular Motion in Polymers That Cause Thermorheological Complexity. *Rubber Chem. Technol.* **1995**, *68*, 376-434.

Oelschlaeger, C.; Schopferer, M.; Scheffold, F.; and Willenbacher, N. Linear-to-branched Micelles Transition: A Rheometry and Diffusing Wave Spectroscopy (DWS) Study. *Langmuir* **2009**, *25*, 716–723.

Oelschlaeger, C.; Suwita, P.; and Willenbacher, N. Effect of Counterion Binding Efficiency on Structure and Dynamics of Wormlike Micelles. *Langmuir* **2010**, *26*, 7045-7053.

Oelschlaeger, C.; Waton, G.; Candau, S. J. Rheological Behavior of Locally Cylindrical Micelles in Relation to Their Overall Morphology. *Langmuir* **2003**, *19*, 10495–10500.

- Oelschlaeger, C.; Willenbacher, N. Mixed Wormlike Micelles of Cationic Surfactants: Effect of the Cosurfactant Chain Length on the Bending Elasticity and Rheological Properties. *Colloids and Surfaces A: Physicochem. Eng. Aspects* **2012**, *406*, 31–37.
- Osborne, M. J. and Lacks, D. J. Inherent Structure Analysis of the Thermal History Dependence of Yielding in Glasses. *J. Phys. Chem. B* **2004**, *108*, 19619-19622.
- O’Shaughnessy, B. From Mean Field to Diffusion-Controlled Kinetics: Concentration-Induced Transition in Reacting Polymer Solutions. *Phys. Rev. Lett.* **1993**, *71*, 3331-3334.
- O’Shaughnessy, B.; Yu, J. Rheology of Wormlike Micelles: Two Universality Classes. *Phys. Rev. Lett.* **1995**, *74*, 4329-4332.
- Ouchi, M.; Takahashi, T.; and Shirakashi, M. Shear-induced Structure Change and Flow-instability in Start-up Couette Flow of Aqueous, Wormlike Micelle Solution. *J. Rheol.* **2006**, *50*, 341-352.
- Padalkar, K. V.; Gaikar, V. G.; Aswal V. K. Characterization of Mixed Micelles of Sodium Cumene Sulfonate with Sodium Dodecyl Sulfate and Cetyl Trimethylammonium Bromide by SANS, FTIR Spectroscopy and NMR Spectroscopy. *J. Mol. Liq.* **2009**, *114*, 40-49.
- Padalkar, K. V.; Pal, O. R.; Gaikar, V. G. Rheological Characterization of Mixtures of Cetyl Trimethylammonium Bromide and Sodium Butyl Benzene Sulfonate in Aqueous Solutions. *J. Mol. Liq.* **2012**, *173*, 18-28.
- Padding, J. T.; Briels, W. J.; Stukan, M. R.; and Boek, E. S. Review of Multi-scale Particulate Simulation of the Rheology of Wormlike Micellar Fluids. *Soft Matter* **2009**, *5*, 4367–4375.
- Padia, N. F.; Yaseen, M.; Gore, B.; Rogers, S.; Bell, G.; and Lu, J. R. Influence of Molecular Structure of Nonionic  $C_nE_m$  Surfactant Micelles. *J. Phys. Chem. B* **2014**, *118*, 179-188.
- Parker, A.; Fieber, W. Viscoelasticity of Anionic Wormlike Micelles: Effects of Ionic Strength and Small Hydrophobic Molecules. *Soft Matter* **2013**, *9*, 1203–13.
- Pasquali, M.; Shankar, V.; and Morse, D. C. Viscoelasticity of Dilute Solutions of Semi-flexible Polymers. *Phys. Rev. E* **2001**, *64*, 020802.
- Penfold, J.; Tucker, I.; Green, A.; Grainger, D.; Jones, C.; Ford, G.; Roberts, C.; Hubbard, J.; Petkov, J.; Thomas, R. K.; Grillo, I. Impact of Model Perfumes on Surfactant and Mixed Surfactant Self-assembly. *Langmuir* **2008**, *24*, 12209–12220.
- Pérez, S. V.; Olea, A. F.; and Gárate, M. P. Formation and Morphology of Reverse Micelles Formed by Nonionic Surfactants in “Dry” Organic Solvents. *Curr. Top. Med. Chem.* **2014**, *14*, 774-780.
- Porte, G.; Appell, J.; and Poggi, Y. Experimental Investigations on the Flexibility of Elongated Cetylpyridinium Bromide Micelles. *J. Phys. Chem.* **1980**, *84*, 3105-3110.

- Rafati, A. A.; Safatian, F. Thermodynamic Studies of Inclusion Complex between Cetyltrimethylammonium Bromide (CTAB) and  $\beta$ -cyclodextrin ( $\beta$ -CD) in Water/n-butanol Mixture, Using Potentiometric Technique. *Phys. Chem. Liq.* **2008**, *46*, 587–598.
- Raghavan, S. R.; Fritz, G.; and Kaler, E. W. Wormlike Micelles Formed by Synergistic Self-Assembly in Mixtures of Anionic and Cationic Surfactants. *Langmuir* **2002**, *18*, 3797–3803.
- Razak, N. A. and Khan, M. N. Determination of Flow Activation Energy at Viscosity Maximum for Spherical and Wormlike Micelles of Different Lengths and Flexibility. *Rheol. Acta* **2013**, *52*, 927–937.
- Rehage, H.; Hoffmann, H. Rheological Properties of Viscoelastic Surfactant Systems. *J. Phys. Chem.* **1988**, *92*, 4712–4719.
- Rhein, L. D.; Schlossman, M.; O’Lenick, A.; Somasundaran, P. *Surfactants in Personal Care Products and Decorative Cosmetics, third edition*. CRC Press: Boca Raton, FL, **2006**.
- Riggleman, R. A.; Lee, H.-N.; Ediger, M. D.; and de Pablo, J. J. Free Volume and Finite-Size Effects in a Polymer Glass under Stress. *Phys. Rev. Lett.* **2007**, *99*, 215501.
- Roitman, D. B.; and Zimm, B. H. An Elastic Hinge Model for Dynamics of Stiff Chains. I. Viscoelastic Properties. *J. Chem. Phys.* **1984**, *81*, 6333–6347.
- Romano, S. D. and Kurlat, D. H. Rheological Measurements in Titania Gels Synthesized from Reverse Micelles. *Chem. Phys. Lett.* **2000**, *323*, 93–97.
- Rosen, M. J. *Surfactants and Interfacial Phenomena 2<sup>nd</sup> edition*. Wiley, New York, **1989**.
- Rothstein, J. P. Transient Extensional Rheology of Wormlike Micelle Solutions. *J. Rheol.* **2003**, *47*, 1227–1247.
- Rottler, J. and Robbins, M. O. Shear Yielding of Amorphous Glassy Solids: Effect of Temperature and Strain Rate. *Phys. Rev. E* **2003**, *68*, 011507.
- Sachsenheimer, D.; Oelschlaeger, C.; Muller, S.; Jan Kustner, J.; Bindgen, S.; and Willenbacher, N. Elongational Deformation of Wormlike Micellar Solutions. *J. Rheol.* **2014**, *58*, 2017–2042.
- Saito, Y.; Hashizaki, K.; Taguchi, H.; Ogawa, N. Solubilization of (+)-limonene by Anionic/cationic Mixed Surfactant Systems. *Drug Dev. Ind. Pharm.* **2003**, *29*, 345–348.
- Sarmiento-Gomez, E.; Lopez-Diaz, D.; and Castillo, R. Microrheology and Characteristic Lengths in Wormlike Micelles made of a Zwitterionic Surfactant and SDS in Brine. *J. Phys. Chem. B* **2010**, *114*, 12193–12202.
- Scamehorn, J. F. An Overview of Phenomena Involving Surfactant Mixtures. *Phenomena in Mixed Surfactant Systems* **1986**, *311*, 1–27.

- Schubert, B. A.; Kaler, E. W.; and Wagner, N. J. The Microstructure and Rheology of Mixed Cationic/anionic Wormlike Micelles. *Langmuir* **2003**, *19*, 4079-4089.
- Schweizer, K. S.; and Saltzmann, E. J. Theory of Dynamic Barriers, Activated Hopping, and the Glass Transition in Polymer Melts. *J. Chem. Phys.* **2004**, *121*, 1984-2000.
- Shang, B. Z.; Wang, Z.; and Larson, R. G. Effect of Headgroup Size, Charge, and Solvent Structure on Polymer-micelle Interactions, Studied by Molecular Dynamics Simulation. *J. Phys. Chem. B* **2009**, *113*, 15170-15180.
- Shi, H.; Ge, W.; Wang, Y.; Fang, B.; Huggins, J. T.; Russell, T. A.; Talmon, Y.; Hart, D. J.; and Zakin, J. L. A Drag Reducing Surfactant Threadlike Micelle System with Unusual Rheological Responses to pH. *J. Colloid Interface Sci.* **2014**, *418*, 95-102.
- Shikata, T.; Dahman, S. J.; and Pearson, D. S. Rheo-Optical Behavior of Wormlike Micelles. *Langmuir* **1994**, *10*, 3470-3476.
- Siriwatwechakul, W.; LaFleur, T.; Prudhomme, R. K.; and Sullivan, P. Effects of Organic Solvents on the Scission Energy of Rodlike Micelles. *Langmuir* **2004**, *20*, 8970-8974.
- Sollich, P.; Lequeux, F.; Hébraud, P.; and Cates, M. E. Rheology of Soft Glassy Materials. *Phys. Rev. Lett.* **1997**, *78*, 2020-2023.
- Somasi, M.; Khomami, B.; Woo, N. J.; Hur, J. S.; and Shaqfeh, E. S. G. Brownian Dynamics Simulations of Bead-rod and Bead-spring Chains: Numerical Algorithms and Coarse-graining Issues. *J. Non-Newtonian Fluid Mech.* **2002**, *108*, 227-255.
- Sreejith, L.; Parathakkat, S.; Nair, S. M.; Kumar, S.; Varma, G.; Hassan, P. A.; and Talmon, Y. Octanol-triggered Self-assemblies of the CTAB/KBr System: A Microstructural Study. *J. Phys. Chem. B* **2011**, *115*, 464-470.
- Suratkar, V.; Mahapatra, S. Solubilization Site of Organic Perfume Molecules in Sodium Dodecyl Sulfate Micelles: New Insights from Proton NMR Studies. *J. Colloid Interface Sci.* **2000**, *225*, 32-38.
- Tang, M. and Carter, W. C. Branching Mechanisms in Surfactant Micellar Growth. *J. Phys. Chem. B* **2013**, *117*, 2898-2905.
- Tang, X.; Zou, W.; Koenig, P. H.; McConaughy, S. D.; Weaver, M. R.; Eike, D. M.; Schmidt, M. J.; and Larson, R. G. Multiscale Modeling of the Effects of Salt and Perfume Raw Materials on the Rheological Properties of Commercial Threadlike Micellar Solutions. *J. Phys. Chem. B* **2017**, *121*, 2468-2485.
- Terech, P.; Schaffhauser, V.; Maldivi, P.; and Guenet, J. M. Living Polymers in Organic Solvents. *Langmuir* **1992**, *8*, 2104-2106.
- Thureau, C. T.; and Ediger, M. D. Influence of Spatially Heterogeneous Dynamics on Physical Aging of Polystyrene. *J. Chem. Phys.* **2002**, *116*, 9089-9099.

- Trusty, T. and Safran, S. A. Defect-Induced Phase Separation in Dipolar Fluids. *Science* **2000**, *290*, 1328-1331.
- Trusty, T.; Safran, S. A.; Strey, R. Topology, Phase Instabilities, and Wetting of Microemulsion Networks. *Phys. Rev. Lett.* **2000**, *84*, 1244-1247.
- Tokuoka, Y.; Uchiyama, H.; Abe, M. Solubilization of Some Synthetic Perfumes by Anionic-Nonionic Mixed Surfactant Systems. *J. Phys. Chem.* **1994**, *98*, 6167–6171.
- Tsenoglou, C. Viscoelasticity of Binary Homopolymer Blends. *ACS Polymer Preprints* **1987**, *8*, 185-186.
- Tuminello, W. H. Molecular-weight Polydispersity Effects on the Viscoelasticity of Entangled Linear –polymers. *Polym. Eng. Sci.* **1986**, *26*, 1339-1347.
- Turner, M. S.; and Cates, M. E. Linear Viscoelasticity of Living Polymers: A Quantitative Probe of Chemical Relaxation Times. *Langmuir* **1991**, *7*, 1590-1594.
- Turner, M. S.; and Cates, M. E. Linear Viscoelasticity of Wormlike Micelles: A Comparison of Micellar Reaction Kinetics. *J. Phys.* **1992**, *2*, 503–519.
- van der Schoot, P.; Wittmer, J. P. Linear Aggregation Revisited: Rods, Rings and Worms. *Macromolecules, Theory Simulation* **1999**, *8*, 428-432.
- Villeneuve, M.; Kaneshina, S.; Imae T.; and Aratono, M. Vesicle-Micelle Equilibrium of Anionic and Cationic Surfactant Mixture Studied by Surface Tension. *Langmuir* **1999**, *15*, 2029–2036.
- Vogtt, K; Jiang, H.; Beaucage, G.; Weaver, M. Free Energy of Scission for Sodium Laureth-1-Sulfate Wormlike Micelles. *Langmuir* **2017**, submitted.
- Wang, Z.; Chen, X.; and Larson, R. G. Comparing Tube Models for Predicting the Linear Rheology of Branched Polymer Melts. *J. Rheol.* **2010**, *54*, 223-260.
- Wang, Z. and Larson, R. G. Molecular Dynamics Simulations of Threadlike Cetyltrimethyl-ammonium Chloride Micelles: Effects of Sodium Chloride and Sodium Salicylate Salts. *J. Phys. Chem. B* **2009**, *113*, 13697-13710.
- Wang, A.; Shi, W.; Huang, J.; and Yan, Y. Adaptive Soft Molecular Self-assemblies. *Soft Matter* **2016**, *12*, 337–357.
- Watson, G.; and Zana, R. Relaxation in Wormlike Micelle Solutions, in Giant Micelles; Properties and Application. *Surfactant Science Series*, Chap. 10, CRC Taylor & Francis group, Boca Raton, **2007**.
- Wendlandt, M.; Tervoort, T. A.; and Suter, U. W. Non-linear, Rate-dependent Strain-hardening Behavior of Polymer Glasses. *Polymer* **2005**, *46*, 11786-11797.



Wheeler, E. K.; Izu, P.; Fuller, G. G. Structure and Rheology of Wormlike Micelles. *Rheol. Acta* **1996**, *35*, 139–149.

Willenbacher, N.; Oelschlaeger, C.; and Schopferer, M.; Fischer, P.; Cardinaux, F.; and Scheffold, F. Broad Bandwidth Optical and Mechanical Rheometry of Wormlike Micelle Solutions. *Phys. Rev. Lett.* **2007**, *99*, 068302.

Wittmer, J. P.; Milchev, A. and Cates, M. E. Dynamics Monte Carlo Study of Equilibrium Polymers: Static Properties. *J. Chem. Phys.* **1998**, *109*, 834-844.

Xia, X.; and Wolynes, P. G. Fragilities of Liquids Predicted from the Random First Order Transition Theory of Glasses. *PNAS* **2000**, *97*, 2990-2994.

Yamamoto, S. and Hyodo, S. Mesoscopic Simulation of the Crossing Dynamics at an Entanglement Point of Surfactant Threadlike Micelles. *J. Chem. Phys.* **2005**, *122*, 204907.

Yan, Z.; Dai, C.; Zhao, M.; and Sun, Y. Rheological Characterizations and Molecular Dynamics Simulations of Self-assembly in an Anionic/cationic Surfactant Mixture. *Soft Matter* **2016**, *12*, 6058—6066.

Yasunaga, T.; Oguri, H.; Miura, M. Acoustic Study on the Kinetics for the Dissociation-recombination Reaction Between Micelle and Counterion in Sodium Dodecyl Sulfate Solution. *J. Colloid Interface Sci.* **1967**, *23*, 352–357.

Youssry, M.; Lemaire, E.; Caillard, B.; Colin, A.; and Dufour, I. On-chip Characterization of the Viscoelasticity of Complex Fluids Using Microcantilevers. *Meas. Sci. Technol.* **2012**, *23*, 125306.

Yu, Y.; Wang, M.; Zhang, D.; Wang, B.; Sant, G.; and Bauchy, M. Stretched Exponential Relaxation of Glasses at Low Temperature. *Phys. Rev. Lett.* **2015**, *115*, 165901.

Yusof, N. S. M.; Khan, M. N.; and Ashokkumar, M. Characterization of the Structural Transitions in CTAB Micelles Using Fluorescein Isothiocyanate. *J. Phys. Chem. C* **2012**, *116*, 15019–15027.

Yusof, N. S. M. and Khan, M. N. Quantitative Correlation of Counterion (X) Affinity to Ionic Micelles and X- and Temperature-induced Micellar Growth (Spherical—Wormlike Micelles—Vesicles) for X=5-Methyl- and 5-Methoxysalicylate Ions. *J. Phys. Chem. B* **2012**, *116*, 2065-2074.

Zana, R.; Kaler, E. W. *Giant Micelles: Properties and Applications*. CRC Press: Boca Raton, FL, 2007, ISBN: 9780849373084.

Zdziennicka, A.; Szymczyk, K.; Krawczyk, J.; and Jańczuk, B. Critical Micelle Concentration of Some Surfactants and Thermodynamic Parameters of Their Micellization. *Fluid Phase Equilibria* **2012**, *322-323*, 126-134.

- Zhang, C.; Wei, J. Mesoscale Simulation Study of the Structure and Rheology of Dilute Solutions of Flexible Micelles. *Chem. Eng. Sci.* **2013**, *102*, 544-550.
- Zhao, Y.; Haward, S. J.; Shen, A. Q. Rheological Characterizations of Wormlike Micellar Solutions Containing Cationic Surfactant and Anionic Hydrotropic Salt. *J. Rheol.* **2015**, *59*, 1229-1259.
- Zhou, W.; Zhu, L. Solubilization of Polycyclic Aromatic Hydrocarbons by Anionic-nonionic Mixed Surfactant. *Colloids Surf. A Physicochem. Eng. Asp.* **2005**, *255*, 145–152.
- Zilman, A. G.; and Safran, S. A. Thermodynamics and Structure of Self-assembled Networks. *Phys. Rev. E* **2002**, *66*, 051107.
- Zilman A.; Safran, S. A.; Sottmann, T.; and Strey, R. Temperature Dependence of the Thermodynamics and Kinetics of Micellar Solutions. *Langmuir* **2004**, *20*, 2199-2207.
- Zou, W.; Larson, R. G. A Mesoscopic Simulation Method for Predicting the Rheology of Semi-dilute Wormlike Micellar Solutions. *J. Rheol.* **2014**, *58*, 681–721.
- Zou, W.; Tang, X.; Weaver, M.; Koenig, P.; Larson, R. G. Determination of Characteristic Lengths and Times for Wormlike Micelle Solutions from Rheology Using a Mesoscopic Simulation Method. *J. Rheol.* **2015**, *59*, 903-934.